Sacks, I.S., Suyehiro, K., Acton, G.D., et al., 2000
Proceedings of the Ocean Drilling Program, Initial Reports Volume 186

5. Site 1151[1]

Shipboard Scientific Party[2]

BACKGROUND AND OBJECTIVES

The two drilling sites of Leg 186 are located at the deep-sea terrace of the Japan Trench (Fig. **F1**). Although sharing similar geological goals of the previous Deep Sea Drilling Project (DSDP) Legs 56, 57, and 87 in this area (Scientific Party, 1980; Kagami, Karig, Coulbourn, et al., 1986), the main objective of this leg was to establish borehole geophysical observatories to monitor active processes in a plate subduction zone. This site being only 48 km south of Site 1150 and along the strike of the Japan Trench, the general geological background is the same as that of Site 1150 (see **"Background and Objectives,"** p. 1, in the "Site 1150" chapter).

Site 1151 was drilled about 200 m north of shotpoint 4556 on seismic Line KH90-1 (Fig. **F2**). The seismic characteristics are similar to those at Site 1150 (Fig. **F2**). Along this line, the seismic stratigraphic features remain constant with a prominent reflector about 1.5 s below seafloor in two-way traveltime. This reflector most likely marks the Cretaceous unconformity and can be traced west to the end of the seismic line at the continental slope. Seismic Line KH96-3, Line 2, shows that the undulation of sedimentary layering has a much shorter wavelength in the north-south direction in accordance with the bathymetry change (Fig. **F3**). For the same reason as at Site 1150, we planned to drill to a depth of about 1000 m, given the available length of time and space for casing on the drillship.

In contrast to Site 1150, which is situated in a seismically active zone, Site 1151 is located in a seismically quiescent area. This means that there is no historical record that a significant earthquake that caused either large tremors or tsunamis to the coastal area of northern Japan occurred within this area. Also, few microearthquakes have been located within the area by the land seismic network, in operation since the 1970s. Except for this prominent seismic feature, no significant dif-

F1. Map of the Japan Trench area off northeast Japan, p. 42.

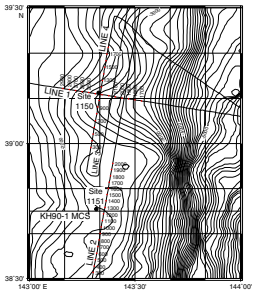

ferences in tectonics, geology, or structure have been identified between the two areas. The present seismic observational data can provide resolution in space of less than a few kilometers and less than a few tenths of a kilometer per second in velocity structure in the vicinity of the plate boundary. We are yet to identify the key parameter that is governing this difference.

The geophysical observatory is designed to record strain, tilt, seismic signals, and temperature change. The objectives are the same as for Site 1150. By comparing the data from two sites, it is further expected that the observatory will provide data of sufficiently high resolution to infer the key differences in static and/or dynamic features at the plate boundary.

Previous drilling results and seismic reflection surveys show that a tectonic erosion process is taking place in the Neogene at the Japan Trench region (Scientific Party, 1980; Kagami, Karig, Coulbourn, et al., 1986; von Huene et al., 1994). Together with Site 1150 results, the style of convergence and the forearc subsidence history will be detailed. Analyses of faults and fractures in the cores will be compared with the present-day deformation as the observatory data become available.

The ash records from this site are expected to become an important reference section near Japan. A more detailed analysis of ash layers that are observed to increase from near the end of the upper Miocene into the lower Pliocene is expected to provide important information about eruptive processes, volcanic hazards, and aspects of climate such as response to wind, sand, and volcanogenic input of greenhouse and related gases.

OPERATIONS

Transit to Site 1151

The 26-nmi distance between Site 1150 and Site 1151 (JT-2L) was covered in 2.8 hr at an average speed of 9.3 kt. The primary positioning beacon was deployed at 2200 hr on 28 July. The bottom-hole assembly (BHA) was assembled, core barrels were spaced out for rotary core barrel (RCB) coring, and the pipe was tripped to the seafloor. The depth estimated for this site from the precision depth recorder (PDR) was 2202.4 m; however, we determined our actual rig floor adjusted seafloor depth by using the vibration-isolated television (VIT) subsea camera to visually observe the bit tag the seafloor.

Hole 1151A

Hole 1151A was spudded at 0445 hr on 29 June 1999 at a depth of 2182.2 m (2193.7 meters below rig floor [mbrf]). Because this was to be a reentry site, we conducted a jet-in test to 78.0 meters below seafloor (mbsf) as our first operation. Because the RCB coring system was unlikely to recover much quantity or quality core in the upper sediments, we decided to conserve valuable time by initiating continuous RCB coring at the base of the jet-in hole rather than pulling back to the seafloor and starting a new hole. The first barrel recovered was considered a wash barrel (1W) because of the extended interval of advance.

The wash barrel was checked with the handheld hydrogen sulfide (H_2S) monitor, and it registered 4 ppm H_2S gas. This core was left on the catwalk after splitting until it had degassed. H_2S gas was not detected in

any of the subsequent cores. Methane varied from 3711 to 61,526 ppmv and ethane from 1.4 to 13.4 ppmv; both were similar to levels observed at Site 1150. The lowest C_1/C_2 ratio was 3374, and no higher molecular weight hydrocarbons were detected.

RCB coring in Hole 1151A began with Core 2R at a depth of 78.0 mbsf and continued through Core 109R to a depth of 1113.6 mbsf. Of the 1035.6 m cored, 707.57 m, or 68.3%, was recovered (Table **T1,** also available in **ASCII format**). Recovery was highly variable ranging from 0% to 102%. The average rate of penetration (ROP) for the cored interval was 61.3 m/hr, which is exceptionally high. Even at depth, the ROP was quite rapid with the last 48.3 m of hole advancing at a rate of 32.2 m/hr.

Coring was halted at that point because the formation was considered hard enough for a successful instrument emplacement, which was planned for Hole 1151B. Wireline logging was not conducted in this hole because all remaining time was to be used for the primary leg objective of installing the second instrument string.

At 1130 hr on 2 August we pulled the pipe to a depth of 600.0 mbsf and rigged the circulating head for setting a cement plug. The hole plugging operation was finished at 1345 hr on 2 August after we displaced a 15-bbl plug of 15.8 lb/gal cement into the hole. With the cementing operation completed, we continued to pull out of the hole, clearing the seafloor at 1430 hr. The bit was back at the rig floor by 1745 hr on 2 August, officially ending Hole 1151A.

T1. Site 1151 coring summary, p. 97.

Hole 1151B

Reentry Cone and 16-in Casing String Installation

Preparations began immediately for making up the 16-in casing string/reentry cone assembly (Fig. **F4**). While this was happening, we offset the ship 60 m to the west. At 1900 hr, the reentry cone was moved onto the moonpool doors and preparations began for running the six joints (73.7 m) of 16-in casing. Within 4.75 hr, the entire casing operation was completed. This included welding all casing couplings, making up the 16-in casing hanger, engaging the Dril-Quip running tool, lowering the casing into the reentry cone and verifying latch-in, disengaging the running tool, making up the stinger assembly and remaining BHA components, and reengaging the running tool. At 2345 hr on 2 August, we began tripping the drill string to the seafloor with its 30,000-lb load.

At 0300 hr on 3 August, we spudded Hole 1151B as the casing shoe tagged the seafloor at 2181.6 m (2193.7 mbrf). The jetting process took 10.5 hr (at an average rate of 7.3 m/hr), and at 1330 hr that same day we landed the reentry cone at the seafloor with the casing shoe positioned at 76.3 mbsf.

While recovering the VIT camera, we began to trip the drill string back to the rig floor to change out the jet nozzles in preparation for drilling the 14¾-in hole. By 2045 hr on 3 August, the ship and drill string were positioned for reentry. After only 15 min of maneuvering time, Hole 1151B was reentered for the first time at 2100 hr.

It took 29.5 hr to drill the 14¾-in diameter hole to a depth of 1081.3 mbsf, completing the drilling at 0315 hr on 5 August. A 34.1 m/hr net ROP was achieved. There were no mud sweeps pumped while drilling the hole. At total depth (TD) we circulated a 30-bbl sepiolite mud pill out of the hole and then made a wiper trip to 76.3 mbsf. The trip up

F4. Schematic of borehole installation at Site 1151, p. 45.

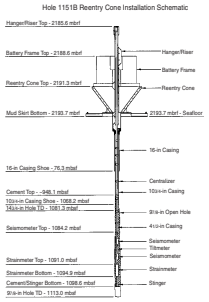

and back did not identify any trouble spots in the hole. On bottom we found ~12 m of fill that was circulated out of the hole while we pumped a 50-bbl sepiolite mud sweep. The hole was displaced with an additional 400 bbl of sepiolite, and the drill string was recovered back to the ship. The reentry cone was cleared at 1215 hr on 5 August, and the bit was back at the rig floor by 1500 hr.

The 10¾-in Casing String

The casing shoe joint, 79 joints (1065.8 m) of 10¾-in casing, and casing hanger were assembled in just over 7 hr. We lowered the 10¾-in casing to just above the seafloor, and after 30 min of positioning the ship Hole 1151B was reentered for the second time. The casing was run to 1023.3 m without resistance. The top drive was picked up and the remaining casing was lowered into the hole, placing the bottom of the casing string at 1068.2 mbsf. This is the longest casing string set in open hole (991.9 m of open hole) in the operation history of DSDP and the Ocean Drilling Program (ODP). Because of the excellent hole conditions, the casing slid into the hole with ease, making it also one of the fastest casing operations. After making up the cementing swivel we landed the 10¾-in casing hanger at 0615 hr on 6 August. Latch-in was verified with 15,000 lb of overpull.

We displaced 50 bbl of 15.8 lb/gal cement to bottom using the rig pumps, but there was no indication that the cement dart had properly landed or that the wiper plug sleeve had sheared. We overdisplaced the cement by a few barrels and then checked for backflow verifying that the check valve in the cementing shoe was holding. After releasing the running tool from the reentry cone, it was clear that the casing wiper plug was still attached to the launching sub. Further investigation of the cementing manifold verified that the dart had hung up in the sub and not released. We offset the ship 50 m and then pumped the cementing dart out, wiping the drill string and expelling the wiper plug assembly at the seafloor. The drill string was then tripped back to the drillship, clearing the rotary table by 1500 hr on 6 August.

The 9 7/8-in drilling assembly was assembled and run to bottom. Within 45 min of positioning the ship, the third reentry of Hole 1151B was made at 1930 hr on 6 August. The bit was run to bottom, and we tagged the cementing shoe at 1068.3 mbsf. Without the rubber wiper plug and dart in the hole, it only took an hour to drill out the cementing shoe and cement. By 0145 hr on 7 August, we had drilled the 9 7/8-in hole to a TD of 1113.0 mbsf. The hole was swept with 20 bbl of sepiolite mud, and a wiper trip was made to the 10¾-in casing shoe and back. No problems were experienced with the wiper trip and, once back on bottom, another 20-bbl sepiolite mud sweep was circulated out of the hole. After displacing the hole with an additional 30 bbl of sepiolite, the drill string was recovered back to the ship. The reentry cone was cleared at 0715 hr, and at 1030 hr on 7 August the bit was back at the rig floor.

Installation of the Borehole Instruments

Deployment of the instrumentation string went smoothly and even more efficiently than in Hole 1150D. After having run the instrument package, strapping/taping the cables, making up 93 joints (1082.4 m) of 4½-in casing, making up the riser/hanger, and installing the multiple-access expandable gateway (MEG), it was time to conduct the final in-

strument checks. Much to our dismay, only three of the four instruments responded correctly. One of the seismometers was not functioning properly. After removing the MEG, we isolated the problem in the MEG rather than the downhole instrument package or cabling. Within 3.75 hr the problem had been identified and corrected, and the MEG was mounted once again on the riser/hanger.

The trip to bottom was interrupted only to deploy the VIT sleeve and test it over the riser/hanger. The VIT camera was then positioned above the hanger and followed the drill string to bottom. By 2130 hr on 8 August, after maneuvering the ship for 30 min, Hole 1151B was reentered for the fourth and final time. The hanger landed at 0100 hr on 9 August, placing the end of the cementing stinger at a depth of 1098.6 mbsf. The instrument string was cemented into the hole with 80 bbl of 15.8 lb/gal cement.

Battery Pack Installation

The battery frame halves were moved onto the moonpool doors, and preparations began on the assembly and rigging of the battery platform at 0315 hr on 9 August. At 0645 hr, the battery frame was deployed through the moonpool on the logging line and run to bottom at ~3500 ft/hr. The frame landed in the reentry cone at 0900 hr and was immediately released, using the same acoustic release system as was used at Site 1150. We recovered the logging line and deployed the VIT to inspect the installation. At 1145 hr, we determined that the battery frame was resting in the correct position around the riser/hanger. The J-type running tool (J-tool) was released, and the drill string and VIT camera were both pulled out of the hole. The J-tool cleared the rig floor at 1745 hr on 9 August, completing Hole 1151B and ending the second successful instrument emplacement operation.

Hole 1151C

The running tool and associated subs were disassembled, and the advanced hydraulic piston corer/extended core barrel (APC/XCB) coring BHA was assembled while the ship was offset 200 m to the south of Hole 1151A. Bathymetric data indicated that the seafloor was about 10 m shallower than at Holes 1151A and 1151B, and a PDR reading indicated that the seafloor depth was about 6 m shallower. Based on this information, the bit was placed at a depth of 2179.0 m. Hole 1151C was spudded with the APC coring system at 0045 hr on 10 August, establishing a seafloor depth of 2174.2 m (2186.3 mbrf), about 8 m shallower than at Holes 1151A and 1151B.

APC coring continued through Core 11H to a depth of 97.2 mbsf. Nonmagnetic core barrels were run intermittently with the standard alloy steel barrels to evaluate the effectiveness of nonmagnetic components relative to the magnetic overprint seen in the cores. Coring was halted after experiencing an overpull of 70,000 lb on Core 11H. A single Adara temperature measurement was taken on Core 4H at a depth 30.7 mbsf. Because overpull on that core was 40,000 lb, we decided to abandon further Adara measurements to avoid possible loss of the hole or equipment. Core orientation was also begun with Core 4H. The drill string was pulled clear of the seafloor, and Hole 1151C was officially ended at 0945 hr. Of the 97.2 m penetrated with the APC, 101.75 m (104.7%) of core was recovered.

There were no hydrocarbon problems associated with this hole, though H_2S gas was measured in Core 4H at 20 ppm. Readings for all other cores never exceeded 4 ppm.

While coring operations were under way, a helicopter chartered through the Royal Japanese Helicopter Service landed at 0815 hr on 10 August. Kim Cheh (U.S. congressional staff), James Henry Hall and Edward Kloth (American Embassy, Tokyo), Timothy Clancy (National Science Foundation), Michael Woods (Pittsburgh *Post Gazette*), and Jeff Fox (ODP/Texas A&M University [TAMU]) came aboard for the day. The helicopter departed at 1500 hr with all passengers except for Michael Woods, who stayed aboard until the Yokohama port call.

Hole 1151D

With the drill string clear of the seafloor, the ship was offset 15 m further to the south, and Hole 1151D was spudded with the APC at 1030 hr on 10 August. We continued the nonmagnetic core barrel component evaluation on this hole. A calculated seafloor depth of 2179.9 m (2184.0 mbrf) was established with the first APC barrel, which was shot 3 m lower to stagger the core breaks. APC coring continued through Core 10H to a depth of 93.0 mbsf. Cores 4H through 10H were oriented with the Tensor tool. Overall, APC coring in this hole netted a recovery of 96.19 m, or 103.4%, of the formation cored.

Drilling resumed from 93.0 mbsf in Hole 1151D using an XCB center bit assembly. At 1800 hr on 11 August, we terminated the drilling operation at a depth of 3058.4 m, or 874.4 mbsf. After circulating a 40-bbl bentonite gel mud sweep out of the hole, the top drive was set back and we pulled the drill string to a logging depth of 100.4 mbsf.

At 2100 hr on 11 August, we installed the logging sheaves and began rigging up for wireline logging. The first tool string consisted of the Formation MicroScanner (FMS) and the dipole sheer sonic imager (DSI) tools. This string was deployed to TD of 874.0 mbsf. After logging up to the bit, a second pass with the FMS-DSI tool was made, again reaching TD. The second tool string consisted of the triple combination logging tool (triple combo), which also reached TD. By 1515 hr, after 18.25 hr of logging, all tools were out of the hole and the sheaves were rigged down.

The drill string was lowered to TD, and the hole was displaced with 260 bbl of barite-weighted (10.5 lb/gal) mud. The string was then recovered back to the drillship. The bit cleared the seafloor at 1830 hr, and the positioning beacon was released and recovered aboard at 1915 hr on 12 August. At 2330 hr on 12 August, the last thruster was secured, and we were under way for the transit to Yokohama, Japan.

Transit to Yokohama, Japan

Almost immediately after departing Site 1151, the transit propulsion motor overheated because of a water cooling problem. Because the propulsion motors are coupled, we had to take a second propulsion motor off line. An opposing current further slowed our overall speed for a good portion of the trip, though we still managed to maintain an average speed of 8.6 kt over the 346-nmi distance. The bay pilot came aboard at 1400 hr, the harbor pilot came aboard at 1540 hr, and the vessel was tied up with the first line ashore at 1615 hr on 14 August 1999, officially ending Leg 186.

Weather

Weather on site and during transits was exceptionally good. Calm seas, scattered clouds, and a gentle wind typified each day. A southerly swell generated some heave, but it rarely exceeded 0.6 m.

LITHOSTRATIGRAPHY

Introduction

A 1113-m thick sedimentary section of Holocene to middle Miocene age was cored in Holes 1151A, 1151C, and 1151D (Fig. F5). The common major lithology of the recovered sediments is olive green diatomaceous silty clay and diatomaceous silty claystone, similar to that at Site 1150. The similarity in lithogies is such that the upper 950 m of section at Site 1151 correlates well with the Site 1150 section, although the two sections differ slightly in degree of lithification and other physical properties.

The major lithology is composed mainly of siliciclastic, volcaniclastic, and biogenic components, whose relative proportions vary with depth. The siliciclastic component ranges from 30% to 60% of the total composition based on smear-slide observations but is more often the dominant component, comprising 50%–60% of the composition. The siliciclastic component is composed predominantly of clay minerals with lesser amounts of quartz, feldspar, hornblende, and mica. Small grains of clinopyroxene are more common at this site than at Site 1150, although they are still rare in smear-slide observation. The biogenic component is the next most abundant, comprising on average 26%–30% of the composition and ranging between 15% and 45%. The dominant fossils are fragments of diatom tests and siliceous sponge spicules. Nannofossils, radiolarians, foraminifers, and silicoflagellates, though rare, are also observed. In general, calcareous tests are better preserved at this site than at Site 1150. The volcaniclastic component consists of volcanic glass shards and rare palagonite, accounting for 5%–30% of the composition and averaging 12%. Other components include carbonaceous grains, iron oxides, iron sulfides, and opaque minerals.

Lithification increases with depth from soft through firm to hard. Brittle deformational structures dominate below 400 mbsf. Bioturbation can be seen in most cores below 300 mbsf and causes patchy color variations of the usual olive green.

Lithologic Units

The division of the cored sedimentary column into lithologic units (Fig. F5) is based mainly on the composition of the major lithology and the degree of lithification. Quantitative color of sediments and sedimentary rock, frequency of brittle deformational structures, occurrence of minor lithologies, and physical properties analyses are also used. Occurrences of minor lithologies such as ash layers, fractures, and silty layers are referred to as sparse or low (<0.4 occurrences/m), common or intermediate (<1.0 occurrences/m), and abundant or high (>1 occurrence/m). The degree of lithification is determined by visual core description (VCD) (see "Lithostratigraphy," p. 3, in the "Explanatory Notes" chapter) and by resistivity logs.

F5. Site 1151 lithologic units, p. 46.

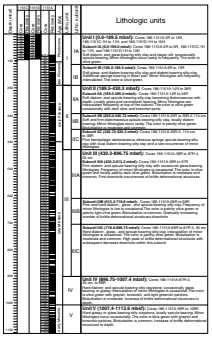

Lithologic Unit I

Interval: Cores 186-1151A-2R through 13R; 186-1151C-1H through 11H; and 186-1151D-1H through 10H
Depth: 0–189.5 mbsf
Age: Holocene to late Pliocene
Description: Hemipelagic diatom-bearing silty clay, glass- and diatom-bearing silty clay, and diatom- and siliceous sponge spicule-bearing silty clay or diatomaceous silty clay. Minor lithologies (sand, silt, ash, and pumice) are abundant to sparse.

Subunit IA

Interval: Cores 186-1151A-2R through 5R; 186-1151C-1H through 11H; and 186-1151D-1H through 10H
Depth: 0–106.0 mbsf
Description: Soft hemipelagic diatom-bearing silty clay, diatom- and glass-bearing silty clay, and clayey silt, with sparse to abundant occurrence of minor lithologies.

Subunit IB

Interval: Cores 186-1151A-6R through 13R
Depth: 106.0–189.5 mbsf
Description: Soft hemipelagic glass- and diatom-bearing silty clay and diatom-bearing silty clay, with sponge-bearing silty clay in the lower part. Minor lithologies are commonly intercalated.

Unit I consists predominantly of homogeneous diatom-bearing silty clay and diatomaceous silty clay (Fig. F5). Volcanic glass and siliceous sponge spicules comprise between 10% and 24% of the total composition; therefore, we use the suffix "-bearing" for these components. Unit I is olive green in color, with intercalated variations between light and dark olive green at a 1- or 2-m scale. The color is more green compared to Units II and III (Fig. F6).

Primary tephra layers, reworked tephra layers, and bioturbated ash patches are present and may be intercalated with diatomaceous silty clay (Fig. F7). More than 50 of these ash intervals are correlatable between Holes 1151C and 1151D.

Sandy and silty layers and accumulations are more common in this unit than in the other units at this site, though they are still a minor component. These layers and accumulations are common to abundant in Subunit IA, which contains as many as 22 occurrences per core (Fig. F8). The high abundance of these minor lithologies produces a relative high in magnetic susceptibility (Fig. F7).

Subunit IA is composed of hemipelagic diatom-bearing silty clay and diatom- and glass-bearing silty clay. Siliciclastic components occupied ~50% in smear slides (Fig. F9A) in this subunit, corresponding to high peaks of clay minerals by X-ray diffraction (XRD) analysis (Fig. F10). The biogenic component, mainly consisting of diatoms, is ~30% of the total composition in Subunit IA. Volcanic glass and siliceous sponge spicules comprise between 10% and 24% of the total composition.

Subunit IB consists of hemipelagic diatom-bearing silty clay and diatom- and glass-bearing silty clay. Siliciclastic components in this subunit are high (as much as 60%) and show a gradual decrease downhole. In contrast, the biogenic component decreases relative to Subunit IA to ~20% of the total composition. The volcaniclastic component is relatively high at ~20%. The siliciclastic and volcaniclastic components are

F6. Variation of L*, a*, and b* values from handheld color reflectance measurement, p. 48.

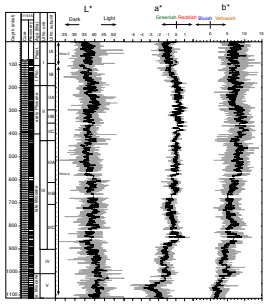

F7. Occurrence of volcanogenic minor lithologies, p. 49.

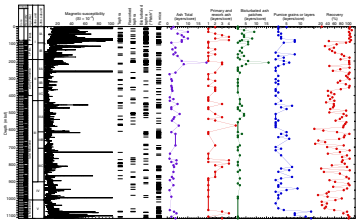

F8. Number of sandy and silty layers and patches at Site 1151, p. 51.

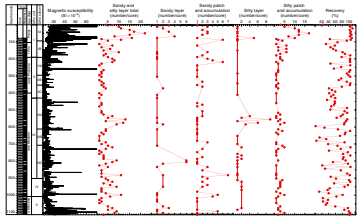

F9. Variations of components from smear-slide observations, Site 1151, p. 52.

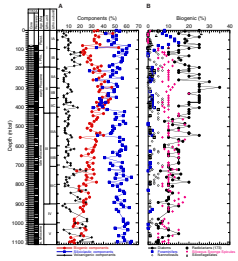

F10. Variations of major minerals by XRD analysis, Site 1151, p. 53.

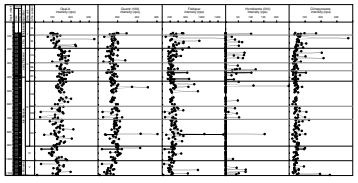

rich in Subunit IB compared to Subunit IA. In Subunit IB, occurrences of sandy and silty layers as well as volcanic ash and its reworked layers and patches are less common than at Subunit IA, although more common than in other units.

The Subunit IA/IB boundary is determined to be where the occurrence of minor lithologies such as ash layers and sandy/silty layers significantly decreases downhole, with a corresponding lack of abrupt peaks of magnetic susceptibility in Subunit IB. The base of Unit I is placed at the point where magnetic susceptibility decreases below about 1.5×10^{-5} SI units (~25 raw meter units) (Fig. F7) and where opal-A increases (Fig. F10).

Lithologic Unit II

Interval: Cores 186-1151A-14R through 38R
Depth: 189.5–430.3 mbsf
Age: early Pliocene to late Miocene
Description: Soft and firm hemipelagic siliceous sponge spicule-bearing diatomaceous silty clay, diatom-bearing silty clay, and diatomaceous silty clay. The major lithology is locally glass and nannofossil bearing. Common intercalation of minor lithologies occurs at the top of the subunit, but minor lithologies otherwise have sparse occurrence.

Subunit IIA

Interval: Cores 186-1151A-14R through 24R
Depth: 189.5–295.0 mbsf
Description: Soft hemipelagic diatom- and siliceous sponge spicule-bearing silty clay that becomes diatomaceous with depth. Locally glass bearing and nannofossil bearing. Common intercalation of minor lithologies occurs at the top of the subunit.

Subunit IIB

Interval: Core 186-1151A-25R through Section 30R-2, 114 cm
Depth: 295.0–346.72 mbsf
Description: Soft and firm hemipelagic siliceous sponge spicule-bearing diatomaceous silty clay and diatom-bearing silty clay, locally diatom bearing, with sparse occurrence of minor lithologies.

Subunit IIC

Interval: Section 186-1151A-30R-2, 114 cm, through Core 38R
Depth: 346.72–430.3 mbsf
Description: Firm hemipelagic diatomaceous siliceous sponge spicule-bearing silty clay with local diatom-bearing silty clay and sparse occurrence of minor lithologies.

Unit II is composed of hemipelagic siliceous sponge spicule-bearing diatomaceous silty clay, diatom-bearing silty clay, and diatomaceous silty clay. Relative to other units, this unit has the highest amount of the biogenic component, mainly in the form of opal-A. On the other hand, siliciclastic components, such as quartz and clay minerals, decrease in this unit (Fig. F10). The 14-Å minerals decrease at the lowest level between ~300 and 350 mbsf. The major lithology is locally glass and nannofossil bearing. Lithification of sediments is soft in Subunit IIA, becoming firmer downhole in Subunits IIB and IIC (see shallow resistivity logs in Fig. F5). Sandy and silty layers and patches are common at the top of

the subunit, but otherwise are sparse. The unit has an olive-green color with some brownish and dark olive regions in Subunit IIA, with the color becoming more patchy in Subunits IIB and IIC. Bioturbation is moderate to common in this unit.

Subunit IIA consists of soft hemipelagic diatom- and siliceous sponge spicule-bearing silty clay that becomes diatomaceous with depth. Primary and reworked ash layers, bioturbated ash, and pumice accumulation are common. The Subunit IIA/IIB boundary is determined to be where the color of the sediments becomes slightly dark and more yellowish, based on L* and b* value, respectively (Fig. **F6**), and where 14-Å minerals abruptly increase (Fig. **F10**).

The sediments of lithologic Subunits IIB and IIC consist mainly of diatomaceous siliceous sponge spicule-bearing silty clay. Clay minerals are richer than in Subunit IIA and increase slowly downhole. Minor lithologies such as ash and sandy layers are rare. The Subunit IIB/IIC boundary is determined to be where lithification starts to increase, as shown by resistivity logs (Fig. **F5;** see **"Physical Properties,"** p. 27).

Lithologic Unit III

Interval: Core 186-1151A-39R through Section 87R-4, 35 cm
Depth: 430.3–896.75 mbsf
Age: late Miocene
Description: Firm hemipelagic diatom-bearing silty clay, with volcanic glass and siliceous sponge spicule bearing, and common intercalations of minor lithologies. The unit is marked by the first downhole occurrence of brittle deformational structures, which reach their peak occurrence within the unit.

Subunit IIIA

Interval: Cores 186-1151A-39R through 57R
Depth: 430.3–613.2 mbsf
Description: Firm hemipelagic diatom- and siliceous sponge spicule-bearing silty clay with common glass-bearing minor components and sparse intercalations of other minor lithologies. The first downhole occurrence of brittle deformational structures is within this subunit.

Subunit IIIB

Interval: Cores 186-1151A-58R through 68R
Depth: 613.2–718.8 mbsf
Description: Firm and hard hemipelagic diatom-, glass-, and siliceous sponge spicule-bearing silty clay, with common occurrences of minor lithologies. The number of brittle deformational structures increases gradually downhole within this subunit.

Subunit IIIC

Interval: Core 186-1151A-69R through Section 87R-4, 35 cm
Depth: 718.8–896.75 mbsf
Description: Hard diatom-, glass-, and siliceous sponge spicule-bearing silty claystone, with sparse occurrences of minor lithologies. Brittle deformational structures reach their peak in this subunit and then decrease downhole to the base of this subunit.

Lithologic Unit III consists mainly of firm diatom-bearing silty clay. Volcanic glass and siliceous sponge spicule typically comprise 10%–24% of the composition. The top interval of the unit is determined by the first

downhole occurrence of brittle deformational structures (Fig. F5). The frequency of structures increases downhole to a high peak value followed by a rapid decrease.

The sediments have a predominantly olive-green color with patchy variations due to moderate to common bioturbation. Subunit IIIB is a slightly lighter olive green relative to the other subunits (Fig. F6). In Subunits IIIB and IIIC, sediments are more greenish in some intervals and become yellowish to bluish with depth. The siliciclastic components generally increase downhole in this unit (Fig. F10), with the exception of 10-Å minerals, which are low in Subunit IIIA, increase at the top of Subunit IIIB, and then decrease with depth in Subunits IIIB and IIIC. Opal-A, in contrast, decreases with depth and has peaks at ~550, 790, and 859 mbsf. These peaks correspond to lows in siliciclastic minerals and natural gamma radiation (NGR).

Minor lithologies have common or abundant occurrences in this unit. The occurrence of reworked ash layer and pumice accumulation is relatively low overall, although slightly more common in Subunits IIIA and IIIC (Fig. F7). Sand and silt accumulations are common to abundant. Silty layers are rich at ~550 mbsf in Subunit IIIA, and sandy layers are rich at ~800 mbsf in Subunit IIIC (Fig. F8).

Lithification increases with depth (Fig. F5), with the sediments becoming firm in Subunit IIIA and transitioning from firm to hard in Cores 186-1151A-62R, 63R, and 64R in Subunit IIIB. In Subunit IIIC, the core becomes hard enough to be called "stone."

The Subunit IIIA/IIIB boundary is determined to be at the interval where color of the sediments become less yellowish (Fig. F6), siliciclastic components increase (Fig. F10), and lithification starts to increase as constrained by resistivity logs (Fig. F6). The Subunit IIIB/IIIC boundary is determined to be where resistivity logs reached almost constant level, which occurs at the top of the interval classified as "stone." The base of Unit III is determined to be at the interval where 10-Å minerals decrease (Fig. F10) and the lightness of sedimentary rocks increases (Fig. F6) and at the boundary between where the sediments are considered consolidated and overconsolidated (see "Physical Properties," p. 27).

Lithologic Unit IV

Interval: Section 186-1151A-87R-4, 35 cm, through Core 98R
Depth: 896.75–1007.4 mbsf
Age: late to middle Miocene
Description: Hard hemipelagic diatom- and siliceous sponge spicule-bearing silty claystone. Minor lithologies have sparse to common occurrence. Brittle deformational structures increase downhole through this unit.

Lithologic Unit IV consists of hard diatom- and siliceous sponge spicule-bearing silty claystone, which is commonly glass bearing. The sedimentary rocks have an olive-green color with grayish and brownish patches caused by moderate bioturbation. In this unit the color is lighter and more blue greenish than in Units II and III. The biogenic component, represented mainly by opal-A, is low in the top of the section and increases from ~970 mbsf to the bottom.

Minor lithologies have sparse to common occurrences, with ash occurrence being very low. Pumice grains and layers are common (Fig. F7). Sandy and silty layers and accumulations are common, with silt-

sized grains being dominant. The frequency of brittle deformational structures increases with depth.

The base of Unit IV is determined to be at the interval where quartz, 14-Å, and 7-Å mineral abundances decrease (Fig. F10), where the color becomes lighter and more greenish and bluish (Fig. F6), and where magnetic susceptibility and NGR begin to increase.

Lithologic Unit V

Interval: Cores 186-1151A-99R through 109R
Depth: 1007.4–1113.6 mbsf
Age: middle Miocene
Description: Hard hemipelagic glassy or glass-bearing silty claystone that is locally siliceous sponge spicule bearing. Bioturbation is common. Brittle deformational structures increase with depth.

Lithologic Unit V consists of glassy or glass-bearing silty claystone that is locally siliceous sponge spicule bearing and diatom bearing, although less so than in other units. Opal-A is relatively high in this unit (Fig. F10). XRD intensities of quartz and clay minerals are low and decrease with depth (Fig. F10).

The color of the sedimentary rocks of this unit is quite characteristic relative to the other units, with a more bluish green with gray color rather than olive green (Fig. F6). Brownish patches caused by common bioturbation are also present.

Pumice grains and layers occur together, especially in the bottom part of the unit (Fig. F7). Sandy and silty accumulations are also high in the bottom of the unit. Feldspars, hornblende, and clinopyroxene, coarser grains of which are included in silty or sandy layers and accumulations, increase with depth. These high occurrences may explain the high values of magnetic susceptibility. The frequency of brittle deformational structures increases with depth (see "Structural Geology," p. 37).

Major Lithology

The major lithologies are described following the scheme of three main constituting components of siliciclastic, biogenic, and volcanogenic origin. The percentages of their occurrence were determined by smear-slide analysis, and quasiquantitative variations with depth were derived from XRD analysis (Table T2, also available in ASCII format).

T2. XRD data, Site 1151, p. 100.

Siliciclastic Components

The siliciclastic components are the main constituent of the major sediments and sedimentary rocks of Sites 1151 and 1150. Clay minerals are the dominant siliciclastic constituent, with feldspars, quartz, pyroxenes, hornblende, and mica (brown biotite) present in much lower percentages. Clay mineral content varies between 25% and 50%. Between 200 and 400 mbsf, the values are slightly lower; below 700 mbsf, the values are slightly higher. Mica, hornblende, and pyroxene are present only in trace amounts in major lithologies and range from accessory (<1%) to maxima of 2% in minor lithologies such as sand or silt layers. Quartz and feldspar grains are present in almost all cores with values between 1% and 7%. The siliciclastic component decreases with

depth from the top of the section down to ~300 mbsf and then increases down to ~800 mbsf. A correlation between the increase of siliciclastic components and grain density is observed below 400 mbsf (see "Physical Properties," p. 27).

The siliciclastic components are divided into quartz, feldspars, hornblende, clinopyroxene, and clay minerals based on XRD identification (Table T2; Fig. F10). Variations of XRD intensities with depth of quartz, feldspars, and 14- and 7-Å minerals show similar patterns downhole, decreasing from the top of the section down to ~300 mbsf, then increasing from ~300 to ~600 mbsf, and finally decreasing downhole with ~100-m scale variation. Quartz and 14- and 7-Å minerals decrease in Units IV and V. The 10-Å minerals, which include glauconite and the illite group, behave differently from other minerals, decreasing with depth from the top of the section down to ~500 mbsf, abruptly increasing at ~610 mbsf (Fig. F10), and then decreasing with depth down to the bottom of the hole.

Biogenic Components

The biogenic components represent the second most common constituent of the sediments. Biogenic components are mainly represented by diatoms, siliceous sponge spicules, and their fragments with small amount of radiolarians and siliceous silicoflagellate. The sum of these biogenic components is constant at 35% from 0 to 80 mbsf and then increases, albeit with large scatter, from ~20% at 80 mbsf to 40% at 350 mbsf. Below that, the sum decreases to values of ~15% at the bottom of the hole (Fig. F9). The percentages lie between 5% and 35% for diatoms and between 5% and 19% for siliceous sponge spicules in smear-slide observation. Minor calcareous components of nannofossils and foraminifers are more abundant than at Site 1150. Foraminifers show a peak abundance between 0 and 100 mbsf, where they reach up to 15% but then decrease to below 2% of the total composition. Siliceous sponge spicule aggregates (Fig. F11), which are often found in the core during visual core description, are abundant to common above Core 186-1151A-87R and very rare or absent below Core 88R.

F11. Photograph showing typical siliceous sponge aggregates, p. 56.

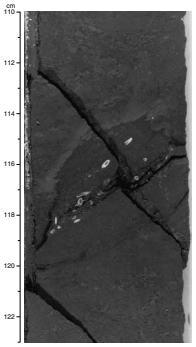

Diatoms have an average value of 20% from 0 to 80 mbsf (Cores 186-1151C-1H to 9H) and then change, with large scatter, to an average of 15% below 80 mbsf, increasing subsequently to a maximum of 25%–30% at 300 mbsf (Cores 186-1151A-25R and 26R) (Fig. F9). From 500 to 650 mbsf (Cores 186-1151A-46R to 61R), biogenic content stays at an average of 15% and then decreases to <10% in the bottom of the sedimentary section.

Opal-A, as measured by a hump in the XRD intensities, increases from the top of the section down to 350 mbsf (Fig. F10) with a small-scale variation. Below 350 mbsf, opal-A decreases with depth and may have a 100-m scale variation. At the bottom of the section, the opal-A hump increases. This is probably related to an increase in volcanic glass associated with the common accumulation of pumiceous grains and layers (Fig. F7).

Volcaniclastic Components

The volcaniclastic component has the lowest abundance of the three main components. The volcaniclastic component is composed mainly of volcanic glass shards of clay to sand grain size, with a predominance of silt grain size. The majority of the ash shards in the major lithology

are colorless, but rare dark altered shards are also present. The grains are highly angular, typically with sharp broken edges and clear surfaces. The dark shards are of the same habit as the translucent shards but show different amounts of brown and black fine inclusions. The dark glass is far more common in minor lithologies (see "Minor Lithologies," p. 14). Very minor amounts of palagonite grains can be found as alteration products of the volcanic glass. The overall proportion of volcaniclastic components lies between 5% and 30%. Between 0 and 90 mbsf, as well as between 200 and 380 and between 420 and 700 mbsf, the values stay at intermediate levels slightly below or above 10%.

Other Components

Minor minerals in order of decreasing abundance are glauconite, pyrite, calcite, hematite, and dolomite. As mentioned above, for simplicity, the iron minerals and calcite are included in the sum of siliciclastic components for the triangle diagram. The very minor and sporadic amounts of minerals in the major lithology or related to minor lithologies normally range below 3%.

Glauconite is often found in smear slides from this site at <5%, reaching values up to 10% in the major lithology only in three intervals. Glauconite shows two different kinds of grain size depending on its detrital or authigenic origin. The detrital glauconite occurs either as sand grain size in the major lithology (Fig. F12) or as layers of minor lithology within the major lithology (Fig. F13). It is most abundant in interval 186-1151A-78R-4, 70 cm, to 79R-4, 120 cm, where a dense scattering of sand-sized glauconite grains occurs. The authigenic glauconite, found in both the major and minor lithologies, is of fine-silt grain size. The detrital glauconite is always found in association with the finer grained authigenic glauconite, but the latter may occur in the absence of the former. Alteration to limonite often occurs below 300 mbsf in brownish bioturbated patches.

Pyrite and hematite are ubiquitous, with pyrite accounting for 2%–4% and hematite usually <1%. Both are of medium- to fine-silt grain size. Pyrite is rarely shapeless and mainly framboidal and is common in diatom, radiolarian, and siliceous sponge spicule tests.

Inorganic calcite is present as sporadic accumulations of very fine grained aggregates and remains below an average of 3%. Within certain layers of the minor lithology, calcite and dolomite reach higher values.

Minor Lithologies

The minor lithologies are volcaniclastic ash layers and patches, commonly of gray to light gray color; sand and silt layers and patches, commonly dark gray and black; and distributed sand grains, commonly of black or white color (Tables T3, T4, both also available in ASCII format). Further, there are some rare carbonate layers consisting of dolomite or calcite (Table T5). The NGR data (see "Physical Properties," p. 27) show these intercalated lithologies well with clear peaks.

Primary and Reworked Tephra, and Pumice Grains and Accumulations

Volcaniclastic material can be divided into primary and reworked tephra layers, their bioturbated patches, and accumulated grains and layers of granule- and pebble-sized pumice. Primary tephra layers (Fig. F14)

F12. Photograph showing typical glauconitic sand-scattering intervals recovered at Site 1151, p. 57.

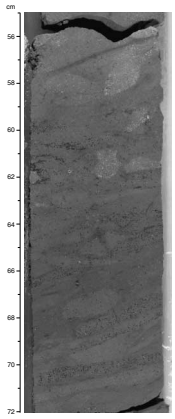

F13. Photograph showing glauconitic sand-rich intervals recovered from Hole 1151A, p. 58.

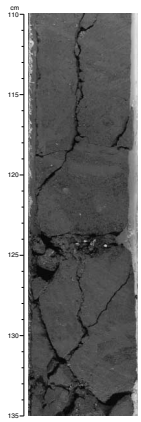

T3. Sand and silt layers and patches/accumulations in recovered core, p. 101.

T4. Number and types of ash layers, p. 102.

T5. Calcareous minor lithologies and evidence of calcitic or dolomitic composition from XRD data, p. 104.

and bioturbated patches (Fig. F15) are light gray and white, and reworked layers and patches are dark gray, sometimes lightening upward in the layers. The layer thickness varies from 0.5 to 20 cm, and grain size varies from silt to coarse sand. Layer boundaries are commonly sharp, sometimes bioturbated and occasionally gradational. Where an erosional boundary occurs, a reworked origin can be inferred for the layer. The upper boundary is often gradational but can be sharp. Grading rarely occurs within each layer. Patches are typically a few centimeters in diameter with diffuse boundaries. Pumice grains occur singly or in layers. The grains are white, gray, or brownish gray in color and of granule to pebble size (Fig. F16). Pumice content peaks at 150–230, 440–490, and 600–660 mbsf, and from 800 mbsf to the base of the section. Overall pumice content increases below 800 mbsf.

Sandy and Silty Layers and Accumulations

Sand layers display a range of colors from black through dark gray to light gray and white. Layer thickness is typically at centimeter scale (1–2 cm), and both upper and lower boundaries can be sharp or gradational. Erosional lower boundaries are also found. The sand layers show a range of grain size from coarse to fine, and a fining-upward texture is occasionally present. Sand patches are similar in color and grain size to sand layers. Thicknesses are typically at a centimeter scale, with average values of 1–2 cm.

Silty layers range in color from dark gray through dark olive gray to light olive green. Layers are typically 0.5–2 cm thick with a gradational upper boundary and sharp lower boundary. A fining-upward texture is occasionally present, and bioturbation of the unit is common. Silt patches have the same color as the layers and are typically 0.5–3 cm in diameter with diffuse or sharp boundaries. Patches can occur singly and together.

Sandy and silty layers are rich in feldspars, hornblende, and pyroxene by smear-slide observation and XRD analysis. Glauconite is often found with sand-sized particles.

Sand frequency shows a slight decrease over the interval of 220–680 mbsf relative to that at shallower depths and a sharp increase at 680 mbsf with relatively high values. These high sand abundances continue to the base of the hole (Fig. F8). Silt frequency (Fig. F8) shows two major peaks between 100 and 160 mbsf and between 530 and 590 mbsf and a minor peak from 900 to 1000 mbsf.

Dolomitic and Calcareous Layers

Fourteen carbonaceous intervals were recovered (Table T5). The intervals are very hard and have a light gray, khaki, or white color. In smear slides from the major and minor lithologies, the carbonate grains occur both as aggregates of very fine grained (clay to silt size) and coarser grained detrital grains. The XRD data (Table T5) indicate that these intervals are predominantly composed of dolomite, though three intervals contain calcite as well. Only one thick limestone layer was recovered at interval 186-1151A-101R-2, 20–55 cm (Fig. F17). Another significant interval of carbonaceous concretions several centimeters in diameter and of oval shape was recovered in Core 186-1151A-109R (Fig. F18).

F14. Photograph showing typical primary tephra (ash) layer, p. 59.

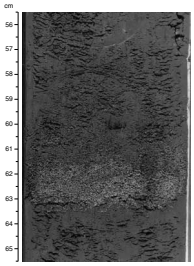

F15. Photograph showing typical bioturbated tephra ("ash patches"), p. 60.

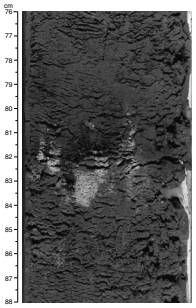

F16. Photograph showing a typical dark gray surrounded pebble-sized pumice grain, p. 61.

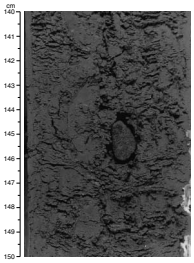

F17. Photograph showing calcareous layers in minor lithology, p. 62.

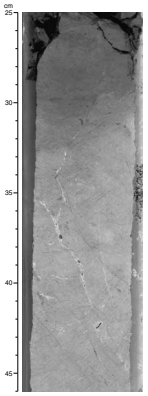

Color Variation

The color of the sediments in the homogeneous upper part of Site 1151 is dominantly olive green. In the lower bioturbated part of the section, the color is olive green and light greenish gray with light brownish gray or light gray patchy burrows that have green and dark gray rims. The color in the lowermost part of the section, lithologic Unit V, becomes bluish green with light brownish gray or light gray patchy burrows.

The quantitative color variation from spectrophotometric measurements shows a characteristic variation with depth (Fig. F6). L* values, which refer to the lightness of the sediment color, show three broad variations from 80 to 400 mbsf, from 400 to 870 mbsf, and from 870 mbsf to the base of the section. The lightness increases with depth down to ~280 mbsf and decreases rapidly at ~280–300 mbsf. The color from 280 to 520 mbsf is slightly darker. The lightness increases gradually from 480 to 720 mbsf, then the color becomes lighter in lithologic Units IV and V.

The a* values are dominantly negative, with positive and negative a* values corresponding to the degree of redness and greenness respectively. The a* values increase from the top of the section to ~200 mbsf and have an almost constant value of nearly zero between 200 and 600 mbsf with a slowly decreasing trend. From 700 down to 850 mbsf, a* increases with depth, corresponding to an increasing degree of bioturbation by light brownish gray and light gray patchy burrows. Below 850 mbsf, the color becomes greenish, as reflected by the decrease in a* values. A decrease of a* is also found between 1000 to 1080 mbsf. The color becomes bluish green in this interval.

The b* values are positive except for a few spikes, with positive and negative values corresponding to the degree of yellow and blue, respectively. Between 280 and 580 mbsf, b* is slightly higher, corresponding to the homogeneous olive-green sediments. Below 580 mbsf, yellow decreases with depth, but there are intervals with increasing values at ~800, 850, and 1000 mbsf. The lowest and only negative values occur in lithologic Unit V.

These color variations should be related to mineral and chemical compositional changes and physical properties variations within the recovered sediments and sedimentary rocks. The decreasing variation of a* values with depth shows a good correlation with grain density and/or porosity (see "Physical Properties," p. 27). The b* values also show a good correlation with void ratio. These similarities are not observed in Unit V.

Lithification

As is common, sediment lithification increases with depth with few exceptions (Fig. F5). Sediments from the top of the section to 350 mbsf in Units I and Subunits IIA and IIB are mainly unconsolidated. Below 285.9 mbsf, the recovered cores became firm enough in some intervals that we began splitting the cores with a saw rather than a wire. Between 350 and 430 mbsf, soft and firm sediments are intercalated, as noted by the small variations in the resistivity logs (Fig. F5). Between 613 and 720 mbsf, sediments are firm and much more lithified, as noted by the sediment surface, which becomes difficult to scratch by fingernail. Below 720 mbsf, the sediments are hard enough to warrant the use of the suffix "-stone" in the lithologic descriptions.

F18. Photograph showing nodule-like white and light gray calcareous concretions, p. 63.

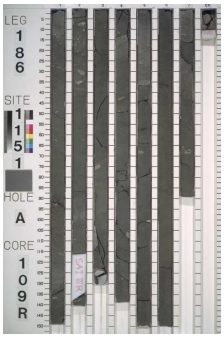

These lithification boundaries correspond well to the changes in resistivity logs and physical properties (see "Physical Properties," p. 27). In some cases these logs indicate downhole decreases in resistivity, which we might expect to be associated with downhole decreases in lithification. Though counter to the general increase of lithification with depth, these decreases in resistivity are still likely indicative of decreases in lithification. For example, resistivity logs show a decreasing trend with depth at Units IB, IIB, and IIIC (Fig. F5). Dolomitic layers, however, are found at the top those intervals and are generally more lithified than surrounding lithologies.

BIOSTRATIGRAPHY

A generally continuous sequence of middle Miocene through Pleistocene sediments and sedimentary rocks was recovered from Site 1151. The 1113-m-thick section consists mainly of diatomaceous silty clay. Calcareous nannofossils are generally barren to abundant throughout, with variable preservation. Except for some ash and dolomite layers, the sequence contains few to dominant diatoms throughout. Diatoms are moderately well preserved. Because the first occurrence (FO) of the diatom *Denticulopsis praelauta* was not recognized, we interpret the base of the section to be younger than 16.3 Ma.

Calcareous Nannofossils

Hole 1151A

We recovered 108 RCB cores from Holes 1151A (Cores 2R–109R; no recovery for 1W), from 78.0 to 1113.46 mbsf. Calcareous nannofossils at this hole were dated primarily from core-catcher (CC) samples.The nannofossil biostratigraphy suggests the sequence represents a record from the Pleistocene to the lower Miocene (Table T6).

T6. Datum levels of calcareous nannofossils, p. 105.

Cores 2R to 5R were assigned to the Pleistocene. Detailed samples were examined in each of these five cores because, except for Sample 186-1151A-2R-CC, all the core-catcher samples were either barren or contained only trace nannofossils that were poorly preserved. The last occurrence (LO) of *Pseudoemiliania lacunosa* was not observed. The FO of *Gephyrocapsa parallela,* observed in Sample 186-1151A-3R-1, 10–11 cm, and the FO of *Gephyrocapsa caribbeanica,* observed in Sample 186-1151A-4R-3, 10–11 cm, were used to define the bases of Subzones CN14a and CN13b, respectively.

The boundary of the Pleistocene and Pliocene lies between Samples 186-1151A-4R-3, 10–11 cm, and 6R-CC, in which the FO of *Discoaster brouweri* was observed. The FO of *D. brouweri* defines the base of Subzone CN13a. The Pliocene and Miocene assemblage was dominated by *Gephyrocapsa* and *Coccolithus pelagicus,* and the warm-water *Discoaster* spp. were also common. The FO of *Discoaster pentaradiatus* was observed in Sample 186-1151A-12R-CC. Because Samples 186-1151A-10R-CC and 11R-CC are barren, the base of Subzone CN12d was put between Samples 186-1151A-9R-CC and 12R-CC. The FO of *Discoaster tamalis* was observed in Sample 186-1151A-13R-CC, which indicates that both the boundary of Subzones CN12c/CN12b and CN12b/CN12a must lie in Core 13R. The LO of *Reticulofenestra pseudoumbilicus* was observed in Sample 186-1151A-15R-CC, which defines the base of Subzone CN12a. The LO of *Amaurolithus* spp., FO of *Ceratolithus rugosus,* and LO of *Tri-*

quetrorhabdulus rugosus, which mark the CN11/CN10c, CN10c/CN10b, and CN10b/CN10a boundaries, respectively, were not observed because of the sparsity of these nannofossils. The LO of *Discoaster quinqueramus,* which marks the base of Subzone CN10a, was observed in Sample 186-1151A-67R-CC. From Cores 59R through 66R, all core-catcher samples are either barren or only contain trace nannofossils, so the CN10a/CN9 boundary may lie within Section 186-1150A-58R-CC to 67R-CC. There are several intervals within Zone CN10 and CN11 that are barren or contain trace nannofossils: Samples 186-1150A-16R-CC, 17R-CC, 19R-CC, 23R-CC to 27R-CC, 39R-CC, 48R-CC to 50R-CC, and 59R-CC to 66R-CC. The base of Zone CN9 is defined by the FO of *Discoaster berggrenii,* which was observed in Sample 186-1151A-90R-CC. In Zone CN9, the samples from Section 67R-CC to 78R-CC contain common to abundant nannofossils. From Section 79R-CC to 88R-CC, the samples are either barren or contain only trace nannofossils. Zone CN7 was not recognized at this site; its top and base are marked by the LO and FO of *Discoaster hamatus,* and no *D. hamatus* was observed at this site. Section 91R-CC to 98R-CC were assigned to Zone CN6–CN8 because the FO of *Catinaster coalithus,* which defines the base of Zone CN6, was observed in Sample 186-1151A-98R-CC. In this interval, Samples 186-1151A-95R-CC to 97R-CC are either barren or contain only trace nannofossils. Sample 186-1151A-99R-CC was assigned to Zone CN5. Samples 186-1151A-100R-CC and 101R-CC are barren. Sample 186-1151A-102R-CC was assigned to Subzone CN5a since it contains *Cyclicargolithus floridanus* but no *Sphenolithus heteromorphus*. Samples 186-1151A-103R-CC to 107R-CC are barren. Sample 186-1151A-108R-CC was assigned to Zone CN3 since both *Discoaster deflandrei* and *S. heteromorphus* were observed in this sample. Sample 186-1151A-109R-CC is barren, although diatom data indicate that the bottom of this core is still in Zone CN3.

Zone CN9, which is defined by the total range of the two related taxa *D. quinqueramus* and *D. berggrenii,* gave younger ages than those indicated by the diatom datums. Since the ages were established mainly from the low-latitude area (Backman and Rafffi, 1997; Rio et al., 1990), they may be different in this area.

Holes 1151C and 1151D

A Pleistocene nannofossil assemblage was observed from the 11 APC cores recovered from Hole 1151C and the 10 APC cores from Hole 1151D (Table **T6**). The assemblage was marked by *Emiliania huxleyi, P. lacunosa, C. pelagicus, Calcidiscus leptoporus,* and *Gephyrocapsa* spp.

The CN15/CN14b boundary, which is marked by the FO of *E. huxleyi,* lies within Samples 186-1151C-2H-CC to 3H-CC and 186-1151D-2H-CC to 3H-CC. As mentioned in **"Biostratigraphy,"** p. 23, in the "Site 1150" chapter, postcruise scanning electron microscope study will be necessary for defining this boundary. The nannofossils in Zone 15 are common to abundant and well preserved in both sites. The LO of *P. lacunosa,* which marks the base of the Subzone CN14b, was observed in Samples 186-1151C-5H-3, 98 cm, and 186-1151D-4H-CC. Sample 186-1151C-4H-CC is barren. The FO of *G. parallela,* which marks the CN14/CN13 zonal boundary, was observed in Samples 186-1151C-8H-CC and 186-1151D-7H-CC. The nannofossils in the Zone 14 are rare to common. Sample 186-1151D-9H-CC is barren. *Gephyrocapsa caribbeanica* was observed in both Samples 186-1151C-11H-CC and 186-1151D-10H-CC, which indicated the bottoms of these two holes are still within the Subzone CN13b.

Diatoms

Hole 1151A

Most of our observations come from core-catcher samples. For determination of zonal boundaries and for the sequence of lower sedimentation rates (below 923 mbsf, see "Sedimentation Rates," p. 23), additional smear slides were prepared from other core intervals. Diatoms are generally few to abundant and moderately well preserved throughout the Pleistocene through middle Miocene section recovered at Site 1151. The abundance of diatoms is common to dominant above 580 mbsf, slightly decreases to common between 930 to 580 mbsf, and then decreases to few to common occurrence below that depth. A range chart showing the distribution of the index species and other selected species is shown in Tables T7 and T8 (both also available in ASCII format). From the distribution of these species, 23 datum levels were identified (Table T9, also available in ASCII format).

T7. Distribution and relative abundances of selected diatom species, Hole 1151A, p. 106.

T8. Distribution and relative abundances of selected diatom species, Holes 1151C and 1151D, p. 110.

T9. Datum levels of diatoms, p. 111.

The top of Hole 1151A contains *Proboscia curvirostris,* indicating that the age is older than 0.3 Ma. Because the other late Pleistocene diatoms such as *Thalassiosira jouseae* and *Neodenticula seminae* also are continuously present, the top of Hole 1151A apparently corresponds to the *P. curvirostris* Zone (North Pacific diatom [NPD] 11).

The last common occurrence (LCO) of *Actinocyclus oculatus* (1.01–1.46 Ma), which defines the boundary between the upper Pleistocene *P. curvirostris* Zone and the lower Pleistocene *A. oculatus* Zone (NPD 11/10), is clearly identified between Sections 186-1151A-3R-CC and 4R-2 in Hole 1151A. The FO of the Pleistocene diatom *P. curvirostris* lies between Sections 186-1151A-4R-CC and 5R-CC.

The base of the *A. oculatus* Zone (NPD 10) and the top of the underlying *Neodenticula koizumii* Zone (NPD 9) is defined by the LO of *N. koizumii*. This latest Pliocene event occurs between Sections 186-1151A-5R-CC and 6R-1. In the upper part of NPD9, *Nitzschia fossilis* and *Thalassiosira antiqua* are rare.

The LCO of *Neodenticula kamtschatica* (2.61–2.68 Ma) between Sections 186-1151A-11R-CC and 12R-3 marks the top of the *N. koizumii–N. kamtschatica* Zone (NPD 8). As at Site 1150, the FO of *N. seminae* is observed in the upper part of this zone (Section 186-1151A-12R-CC), together with its closed copula (see "Biostratigraphy," p. 23, in the "Site 1150" chapter).

The FO of *N. koizumii* (3.53–3.95 Ma), which defines the boundary between the upper Pliocene *N. koizumii–N. kamtschatica* Zone and the lower Pliocene *Thalassiosira oestrupii* Zone (NPD 8/7B boundary), is clearly identified between Sections 14R-CC and 15R-4 in Hole 1151A. Within NPD 7B, the FO of *Thalassiosira latimarginata* (5.07 Ma) lies between Sections 186-1151A-29R-CC and 30R-CC.

The FO of *T. oestrupii* sensu lato defines the top of the upper Miocene *N. kamtschatica* Zone of Koizumi (1992). This datum exists between Sections 38R-1 and 38R-CC of Hole 1151A. Though the abundance is very rare, *Rouxia californica* appears continuously below Section 186-1151A-66R-CC, suggesting that the boundary of NPD 7Ba/7A (6.65 Ma) exists between Sections 186-1151A-66R-1 and 66R-CC. The presence of the LO of *Cavitatus jouseanus* (6.7–6.8 Ma) between Sections 186-1151A-69R-CC and 70R-CC supports this zonal boundary. The FO of *Pyxidicula* (= *Thalassiosira*) *zabelinae* falls in the bottom of this zone.

The upper Miocene *R. californica* Zone of Koizumi (1992) is situated on the lower part of NPD 7A. The top of this zone is defined by the FO

of *N. kamtschatica* (7.3–7.4 Ma). In this site, however, this species has a sporadic occurrence down to the underlying *Thalassionema schraderi* Zone (see below). Thus this datum is documented as the first common occurrence (FCO) between Sections 186-1151A-77R-CC and 78R-1. In this zone, *R. californica* is continuously present, and *Ikebea tenuis* appears sporadically.

The LO of *T. schraderi* (7.6 Ma) is between Sections 186-1151A-79R-CC and 80R-1 and marks the top of the upper Miocene *T. schraderi* Zone (NPD 6B). As at Site 1150, *Actinocyclus ingens* appears continuously from the lower part of this zone. The LO of *Denticulopsis katayamae* occurs between Sections 186-1151A-89R-CC and 90R-CC. The distinction of *N. kamtschatica* from its ancestor *Nitzschia rolandii* is difficult because of its gradual evolutionary change (Yanagisawa and Akiba, 1998), but according to Yanagisawa and Akiba (1990), *N. kamtschatica* can be distinguished from *N. rolandii* by broader spacing of pseudosepta or costae (5–8 in 10 µm). In this sense, *N. kamtschatica* occurs sporadically in the upper part of this zone. Koizumi and Tanimura (1985) also reported such phenomena at DSDP Site 581; thus, the datum level of the FO of *N. kamtschatica* should be redefined as the FCO.

The zonal boundary between the *T. schraderi* Zone and the *D. katayamae* Zone (NPD 6A) is determined by the LCO of *Denticulopsis simonsenii* (8.6 Ma), as between Sections 186-1151A-91R-3 and 91R-5.

The top of the *Denticulopsis dimorpha* Zone (NPD 5D) is defined by the LO of *D. dimorpha* (9.16 Ma). This datum is recognized between Sections 186-1151A-91R-CC and 92R-2, together with the FO of *T. schraderi*. Below this depth, the FO of *D. katayamae* (9.26 Ma) is observed (between Sections 186-1151A-93R-CC and 94R-CC). The base of this zone is defined by the FO of *D. dimorpha* (9.9 Ma).

The FO of *D. dimorpha* (9.9 Ma), which defines the top of *Thalassiosira yabei* Zone (NPD 5C), is clearly identified between Sections 186-1151A-95R-CC and 96R-1. But its nominate species, *T. yabei,* is very rare. The bottom of this zone is determined by the LCO of *Denticulopsis praedimorpha* (11.5 Ma) between Sections 186-1151A-99R-CC and 100R-1.

The middle Miocene *D. praedimorpha* Zone (NPD 5B) at this site contains four important marker species: *Crucidenticula nicobarica, Denticulopsis hyalina, D. simonsenii,* and the nominate species *D. praedimorpha*. The LO of *C. nicobarica* (12.5 Ma) lies at the top of this zone, suggesting that there is possibly a redeposition of this species, coring gap, or a hiatus (<1.0 m.y.) between Sections 186-1151A-99R-CC and 100R-1. The bottom of this zone is defined by the FO of *D. praedimorpha* (12.9 Ma) between the Samples 186-1151A-101R-1, 71–73 cm, and 101R-1, 90–91 cm.

The underlying *C. nicobarica* Zone (NPD 5A) was not identified because the FCO of *D. simonsenii* (13.1 Ma), which defines the bottom of NPD 5A, is found at the same interval as the FO of *D. praedimorpha* (the top of NPD 5A). Yanagisawa and Akiba (1998) proposed that the LCO of *D. hyalina* can be also used as the base of NPD 5A, and this datum is also recognized between 71–73 and 90–91 cm of Section 186-1151A-101R-1. Thus there must be a short hiatus which wiped out the zone NPD 5A (>0.2 m.y.) within this interval.

The FO of *D. simonsenii* (14.4–14.6 Ma), defining the base of *Denticulopsis hustedtii* Zone (NPD 4Bb), is recognized between Sections 186-1151A-102R-1 and 102R-2. The carbonate nodule layer in this zone (Sample 186-1151A-102R-2, 62–64 cm) contains well-preserved abundant diatoms such as *A. ingens, C. nicobarica, D. hyalina, Denticulopsis lauta,* and *T. yabei*.

The underlying *D. hyalina* Zone (NPD 4Ba) is marked by the continuous occurrence of *D. hyalina* and few *D. lauta*. Its base is defined by the FO of *D. hyalina* (14.9 Ma) between Sections 186-1151A-104R-1 and 104R-CC.

Within the *D. lauta* Zone (NPD 4A), the abundance becomes few to common, with sporadic poor preservation intervals. Nevertheless, the marker species *D. lauta* occurs continuously down to Section 186-1151A-108R-4, which defines the bottom of this zone.

The *D. praelauta* Zone (NPD 3B) is the oldest zone of Hole 1151A because its bottom horizon defined by the FO of *D. praelauta* (16.3 Ma) is not identified in this hole. Extrapolation of the 43 m/m.y. sedimentation rate (see **"Sedimentation Rates,"** p. 23) between the FO of *D. hyalina* (14.9 Ma) and FO of *D. lauta* (15.9 Ma) would give a slightly younger age of 16.2 Ma for the sediments at the bottom of the hole and is, therefore, acceptable.

Diatom assemblages from all samples consist almost entirely of oceanic species. They are mainly of the subarctic North Pacific Ocean, although such warm-water taxa as *Nitzschia reinholdii* and *Hemidiscus cuneiformis* are more frequent than those of Site 1150. Neritic species such as *Actinoptychus senarius, Paralia sulcata,* and *Cocconeis* spp. vary from few to trace, but they are recognized in most samples. Freshwater species such as *Aulacoseira* spp. are rare, but there is continuous appearance between the upper NPD 4A and the lower NPD 4Ba. As at Site 1150, resting spores of *Chaetoceros* spp. are mostly few to abundant between NPD 10 to 12 and rare to few in lower zones.

Holes 1151C and 1151D

The boundary between the upper Pleistocene *N. seminae* and *P. curvirostris* Zones (NPD 12/11) is indicated by the LO of *P. curvirostris* (0.30 Ma) between Sections 186-1151C-3H-CC and 4H-4, and 186-1151D-3H-4 and 3H-CC. The continuous occurrence of *T. jouseae,* the LO of which corresponds to 0.30–0.41 Ma, is observed in this depth in Hole 1151C but is slightly shallower in Hole 1151D (between Sections 2H-CC and 3H-4). The warm-water species *N. reinholdii,* the LO of which corresponds to 0.62 Ma in the equatorial Pacific (Shackleton et al., 1995), is found in Sections 186-1151C-5H-CC to 6H-CC and 186-1151D-4H-CC to 5H-CC.

The LCO of *A. oculatus* (1.01–1.46 Ma), which defines the boundary between the upper Pleistocene *P. curvirostris* Zone and the lower Pleistocene *A. oculatus* Zone (NPD 11/10), is clearly identified between Sections 186-1151C-9H-5 and 9H-CC, and between Cores 186-1151D-8H and 9H. *Thalassiosira antiqua,* which has its LO from 1.52 to 1.8 Ma, is scarce in the lower part of this zone (Section 186-1151D-10H-CC).

The base of the *A. oculatus* Zone (NPD 10) and the top of the underlying *N. koizumii* Zone (NPD 9) is defined by the LO of *N. koizumii*. This latest Pliocene event occurs between Sections 186-1151C-11H-4 and 11H-CC, and 186-1151D-9H-CC and 10H-CC.

The latter two datums are about 20 m shallower than those in Hole 1151A, which may be caused by possible coring gaps and/or sedimentation rate variations influenced by local topographical features between Hole 1151A and Holes 1151C and 1151D.

PALEOMAGNETISM

Split-Core and Whole-Core Measurements

The magnetic remanence of all archive halves of APC cores from Holes 1151C and 1151D (0.0–97.2 mbsf and 0.0–93.0 mbsf, respectively) and all RCB cores from Hole 1151A (78.0–1113.6) were measured at 5-cm intervals. Following measurement of the natural remanent magnetization, each section was subjected to stepwise alternating-field (AF) demagnetization. Sections from Hole 1151A were demagnetized at 10, 20, and 30 mT, with the exception that the 10-mT step was skipped for Cores 186-1151A-16R through 77R (Fig. F19). Because of time limitations, sections from Holes 1151C and 1151D were AF demagnetized at 20 mT only (Figs. F20, F21). Magnetic susceptibility was measured on whole-core sections every 2 cm for Hole 1151A and every 5 cm for Holes 1151C and 1151D (Figs. F19, F22). Both remanence and susceptibility data for these sections are available from the ODP (Janus) database.

The lithology and sedimentation rates at Site 1151 were very similar to those at Site 1150, so it is not surprising that the paleomagnetic and rock magnetic properties also appear to mimic those at Site 1150. As at the previous site, before demagnetization, the inclinations display a very strong tendency toward large positive values (~60°–90°) over the entire cored interval, indicating the presence of a steep downward-directed drill-string overprint. The radial bias is not as evident at this site, but we have not evaluated its presence to the same degree as for Site 1150 (see "Paleomagnetism," p. 27, in the "Site 1150" chapter).

The magnetization remaining after demagnetization at 20 or 30 mT reflects the characteristic remanent magnetization (ChRM), a term we use to refer to the high coercivity or high unblocking temperature component that records the ancient magnetization of the sediments. As at Site 1150, in some cases the ChRM at Site 1151 is not a primary magnetization that was acquired at or near the time of deposition but is instead a secondary magnetization probably acquired during subsequent chemical and mechanical remagnetization.

Examination of inclinations after 20 or 30 mT AF demagnetization (Figs. F19, F20) illustrates that both normal and reversed polarities are recorded in at least the upper 700 m, though with a considerable amount of noise. Below 700 m, however, virtually the entire section has very stable positive inclinations, with mean inclinations of 56° to 60°. This would indicate that the sediments are of normal polarity, with the exception of a few short intervals. This conflicts with biostratigraphic information, which instead indicates that about half of the section should be reversed polarity. Given the abundance and good preservation of diatoms, and the resulting high quality of the biostratigraphy (see "Biostratigraphy," p. 17), it seems unlikely that the sedimentary section below 700 mbsf has a primary remanence. Remagnetization appears to be required and is supported by other evidence (see "Paleomagnetism," p. 27, in the "Site 1150" chapter).

The remagnetization process that has replaced all or nearly all of the primary remanence in the lower 700 mbsf has probably also partially replaced the magnetization in the section above. The noise in the interval below ~80 mbsf we attribute to the low intensities and to partial remagnetization of the sedimentary section. Assuming that either chemical remagnetization, mechanical remagnetization, or both increase progressively downhole, then it is not surprising that below 700

F19. Split-core inclination and intensity of magnetization after AF demagnetization, and whole-core susceptibility for Hole 1151A, p. 64.

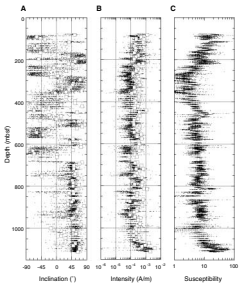

F20. Split-core inclinations for Holes 1151C and 1151D after AF demagnetization, p. 65.

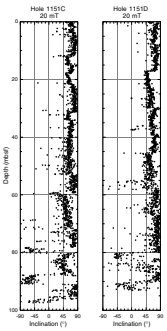

F21. Split-core intensity of magnetization for Holes 1151C and 1151D after AF demagnetization, p. 66.

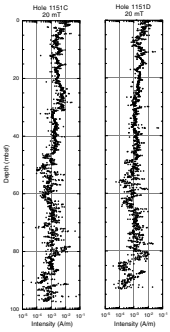

F22. Whole-core susceptibility for Holes 1151C and 1151D, p. 67.

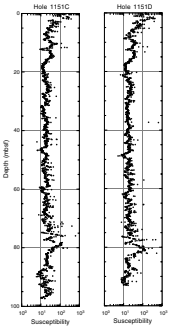

mbsf there is relatively little evidence of reversed polarity and that in the interval from 700 to 80 mbsf polarity identification is difficult. Given that the field has had a normal polarity for the past 780,000 yr, there would be ample opportunity of the net bias of the sedimentary section to be in a normal polarity direction.

In contrast, the sediments above 80 mbsf likely contain a primary magnetization acquired at or near the time of deposition. The magnetization of this interval appears to be unaffected by reduction diagenesis as evidenced by the intensity and susceptibility data, which again are about an order of magnitude higher than sediment lower in the section. The presence of pyrite in the upper cores may indicate that some level of reduction takes place shortly after deposition, but not enough to consume completely magnetic minerals carrying a primary remanence. Unlike the lower part of the sedimentary section, there has been little time for mechanical deformation to remagnetize the sediment in the upper 80 mbsf, and evidence from ash layers and burrows suggests deformation is absent. Finally, inclinations within this interval are very stable and consistent with a Brunhes normal polarity direction (Fig. **F20**). The stability of these sediments is further confirmed by consistent directions, intensities, and susceptibilities obtained for Holes 1151C and 1151D (Figs. **F20, F21, F22**).

Discrete Samples

Discrete samples measured with the NP2 (Fig. **F23;** Table **T10,** also available in **ASCII format**) agree well with the split-core results (Fig. **F19**). On average, the intensities from the NP2 are slightly higher than those from the cryogenic magnetometer, which mainly is a result of using the 20-mT AF demagnetization results for the NP2 magnetometer and the 30-mT AF demagnetization results for the cryogenic magnetometer.

F23. Discrete sample results from the NP2 spinner magnetometer, p. 68.

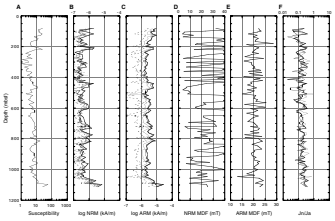

T10. NRM and ARM results from the NP2 magnetometer before and after AF demagnetization, p. 112.

Magnetostratigraphy

Magnetostratigraphic interpretation is hampered by the large amount of overprinting caused by drilling, reduction diagenesis, coring disturbance, and structural deformation. The location of the Brunhes/Matuyama reversal would appear to be well resolved by the abrupt downhole change to negative inclinations at about 78.2 mbsf in Hole 1151C, 80.1 mbsf in Hole 1151D, and at 82–84 mbsf (between Cores 186-1151A-2R and 3R) in Hole 1151A. However, the reversals lower in the section are not easily correlated with the geomagnetic polarity time scale. As at Site 1150, diatom datums provide the main age control for the sediments at Site 1151. Given the overall age constraints provided by the diatoms, the few prominent reversals can be used to make slight adjustments to the age estimates for the sediments, particularly between diatom datums (see **"Sedimentation Rates,"** p. 23).

SEDIMENTATION RATES

The sedimentation rates of Site 1151 were estimated using a combination of biostratigraphy and magnetostratigraphy as at Site 1150 (see **"Sedimentation Rates,"** p. 35, in the "Site 1150" chapter). This estimation is based primarily on datums of diatom zonal boundaries because diatom valves were well preserved and the datums were continuously

recognized. The magnetostratigraphy is poorly constrained and at best provides a few reversal boundaries that can be used to adjust the age estimates predicted between diatom datums. A magnetostratigraphy derived from the diatom datums does, however, accurately predict several of the more prominent observed reversal boundaries, and so we consider the two to be in good agreement above 680 mbsf. Below ~680 mbsf, however, the inclination indicates a long interval with normal polarity, which is interpreted as an overprint (see "Paleomagnetism," p. 22).

As discussed in "Biostratigraphy," p. 17, calcareous nannofossil datums between 90 and 940 mbsf indicate younger ages than those from diatom biostratigraphy. The age assignments based on calcareous nannofossils at Site 1151 are uncertain for reasons discussed in the previous chapter.

The control points for age assignment were thus chosen from 16 diatom datums and four geomagnetic chron boundaries above 610 mbsf (Table T11, also available in ASCII format). Ages of diachronous events were averaged, but the age of the FO of *N. koizumii* (diatom) was defined as its youngest value (3.53 Ma) because the bottom of Gauss (C2An / C2Ar, 3.58 Ma) was recognized immediately below this datum. Instead of the LCO of the diatom *D. simonsenii* (8.6 Ma), the LO of *D. katayamae* (8.5 Ma) was used because the presence of the latter species was clearer (see "Biostratigraphy," p. 17). Since the FO of the diatom *D. praelauta* was not found, the lowermost depth (1113.46 mbsf) is slightly younger than 16.3 Ma, which is calculated as 16.18 Ma by using the 43-m/m.y. sedimentation rate of the *D. lauta* Zone.

Sedimentation rates for the upper 100 m of the site are complicated by offsets between diatom datums. In particular, two diatom datums from Holes 1151C and 1151D (LCO of *A. oculatus* and LO of *N. koizumii*) are about 20 m shallower than in Hole 1151A (see "Biostratigraphy," p. 17). We have used the datums from Hole 1151A because they are more consistent with the location of the Brunhes/Matuyama boundary, which is located at ~78.2 mbsf in Hole 1151C, 80.1 mbsf in Hole 1151D, and at 82–84 mbsf (between Cores 186-1151A-2R and 3R) in Hole 1151A. In these holes, the reversal is defined by a clear change from steep positive to steep negative inclination, though the reversal sequence lower in the section does not follow a standard magnetostratigraphy. Postcruise study will be needed to resolve the conflicting ages.

The average sedimentation rate is 24 m/m.y over the entire interval, though it is 99 m/m.y. over the past 9.5 m.y. This latter value is slightly lower than the 120 m/m.y. rate found for Site 1150 over the past 9.5 m.y. (Fig. F24).

An age-depth plot for Site 1151 indicates that the upper 200 m has a relatively low rate (18 to 152 m/m.y.). As at Site 1150, the sedimentation rate is especially low between 110 and 86 mbsf, which corresponds to the early to mid-Pleistocene. At a depth of between 200 and 920 mbsf the sedimentation rate increases, with the highest values (~240 m/m.y.) between 450 and 800 mbsf. Below this the rate gradually decreases. In the interval at 1027 mbsf there is a hiatus ranging more than 0.2 m.y., and then the sedimentation rate increases gradually downhole to 43 m/m.y.

Similar to Site 1150, Site 1151 has high rates in the uppermost Miocene and low rates below and above this (Fig. F25). The intervals of low rates correspond to the early late Miocene (prior to 8.5 Ma) and the early to mid-Pleistocene (2.0 to 0.78 Ma), respectively.

T11. Age control points for datum events and sedimentation rates, p. 113.

F24. Age-depth relationship, p. 69.

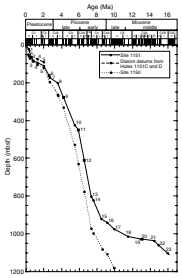

F25. Sedimentation rate vs. age, p. 70.

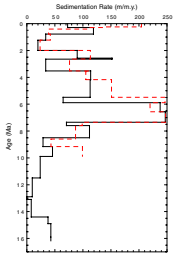

GEOCHEMISTRY

The shipboard geochemistry program at Site 1151 included (1) analyses of volatile hydrocarbons; (2) determinations of abundances of inorganic carbon, total carbon, total sulfur, total nitrogen in sediments; and (3) measurements of salinity, alkalinity, pH, and concentrations of some dissolved anionic species in interstitial waters (for description of methods see "Geochemistry," p. 15, in the "Explanatory Notes" chapter.)

Volatile Hydrocarbons

Headspace gas analyses at Site 1151 indicate that methane concentrations are between 0.4% to 6% with an average concentration of ~2%. Ethane concentrations fluctuate between 1 and 13 ppmv and typically are ~4 ppmv. Methane/ethane ratios are consistent throughout the studied interval with values of ~4400 (Fig. F26; Table T12, also available in ASCII format). Other hydrocarbon gases are below the detection limit.

Carbonate Content

No trend is present in the distribution of carbonate abundances with depth at Site 1151 (Fig. F27). Abundances range from 0.08 to 79 wt%, with an average value of 3.3 wt%. Most values, however, fall between 2 and 4 wt% with excursions having peak values up to 15 wt%. Low carbonate abundances are in agreement with trace to few occurrences of calcareous nannofossils in the sediments (see "Biostratigraphy," p. 17).

Organic Carbon, Total Nitrogen, and Total Sulfur

Abundance of organic carbon (C_{org}) fluctuates between 0.2 and 1.4 wt%, with an average value of about 0.9 wt% (Fig. F27). C_{org} values tend to decrease with depth in the studied interval from 1.2 wt% at the top to about 0.4 wt%. C_{org}/N ratios range from 2.5 to 11.5 with typical values of ~7 (Fig. F27). The distribution of C_{org}/N shows an irregular pattern with depth, although a general decreasing trend is observed. Values decrease from ~9 at the top to ~4 at the final depth. Total sulfur abundances irregularly fluctuate between 0.35 and 1.5 wt%, with an average value of 0.85 wt% (Fig. F27).

Salinity and Chlorinity

Salinity and chlorinity exhibit, in general, a similar decreasing trend with depth (Fig. F28). Salinity gradually decreases with depth from a value of ~32 at the top of the borehole to a value of 18 at ~900 mbsf. Below this depth, salinity remains constant at 18 to the final depth (Table T13, also available in ASCII format). Chlorinity concentrations remain constant at ~500 mM in the upper 200 m of the borehole and then steadily decrease to 320 mM at the final depth.

Alkalinity, and Dissolved Sulfate and Ammonium

Alkalinity values gradually decrease downhole in the upper 200 m from 31 to 17 mM and then increase to 25 mM at ~450 mbsf (Fig. F28). Below this depth, values decrease steadily downhole to 2 mM at the

F26. Distribution with depth of headspace concentrations of C_1 and C_2, and C_1/C_2 ratios, p. 71.

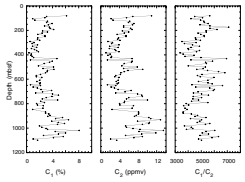

T12. Headspace concentrations of light hydrocarbons, p. 114.

F27. Distribution of carbonate, C_{org}, and S abundances and C_{org}/N ratios with depth, p. 72.

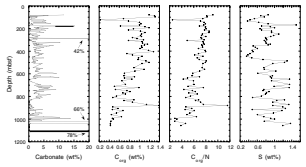

F28. Distribution with depth of pore-water geochemical concentrations, p. 73.

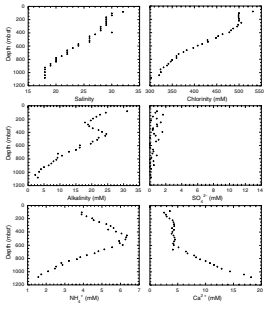

T13. Results of interstitial water analyses, p. 115.

bottom of the borehole. Dissolved sulfate (SO_4^{2-}) concentrations exhibit values lower than 2 mM throughout the borehole (Fig. F28). Values probably higher than 1 mM are the result of seawater contamination. Ammonium (NH_4^+) concentrations increase downhole from 3.9 to 6.4 mM in the upper 450 m and then gradually decrease to about 1.5 mM at the final depth of the borehole (Fig. F28).

Dissolved Calcium, Magnesium, and Strontium

Concentrations of dissolved calcium (Ca^{2+}) in pore waters slightly increase downhole from values of ~3 mM at the top to ~4 mM at 600 mbsf (Fig. F28). Below this depth, Ca^{2+} concentrations steadily increase to 18 mM at the bottom of the borehole.

Concentrations of dissolved magnesium (Mg^{2+}) remain constant at ~25 mM in the upper 400 m of the borehole and then steadily decrease to 4 mM at the bottom of the borehole (Fig. F28).

Concentrations of dissolved strontium (Sr^{2+}) increase from ~115 to ~130 µM in the upper 250 m of the borehole and then decline to 100 µM at 550 mbsf. Below this depth, Sr^{2+} concentrations increase downhole to reach a maximum value of 232 µM at the bottom of the borehole (Fig. F28).

Dissolved Sodium, Potassium, and Lithium

Concentrations of dissolved sodium (Na^+) remain relatively constant at a value of 425 mM in the upper 300 m of the borehole and then decrease to ~240 mM at the bottom of the borehole (Fig. F28). Concentrations of dissolved potassium (K^+) steadily decrease downhole from ~10.5 mM at the top of the borehole to ~5 mM at the final depth.

Concentrations of dissolved lithium (Li^+) gradually increase from 20 to 480 µM in the upper 850 m of the borehole and then decrease to ~280 µM at the bottom of the borehole (Fig. F28).

Discussion

Several geochemical parameters exhibit similar distributions with depth. K^+, Na^+, Mg^{2+}, chlorinity, and salinity show a characteristic decreasing trend with depth. Decreasing K^+ concentrations are probably the result of the incorporation of potassium during the diagenetic formation of illite from smectite. Depletion of Mg^{2+} concentrations with depth are probably caused by dolomite formation and/or diagenetic transformation of volcanic ash.

The cause for the decreasing trend in salinity and chlorinity at Site 1151 is still unknown. Several hypothesis can, however, explain the observed trend. Influx of modern meteoric waters is unlikely since the shoreline is more than 100 km from the site. Similarly, influx from aquifers with ancient meteoric waters is also unlikely because sediments deposited in shallow environments are absent at Site 1151. Hemipelagic accumulation is characteristic throughout the entire studied stratigraphic sequence (see "Lithostratigraphy," p. 7). Another possible source of freshwater causing dilution of pore-water salts is in situ dewatering of smectite and biogenic opal. This possibility is also unlikely because the amount of smectites and opal present in sediments at Site 1151 is not enough to account for the observed 60% decrease in chlorinity. The only plausible scenario causing a decreasing trend in salinity

and chlorinity is an upwelling of less-saline waters probably formed as a result of compaction dewatering at deep intervals.

Sediments at Site 1151 exhibit relatively high abundances of organic matter (OM) with characteristic low (<10) C_{org}/N ratios suggesting that most of the OM is marine in origin (Tyson, 1995). It is possible, however, that these ratios are higher since total nitrogen in sediments includes both organic and inorganic sources. The contribution of these inorganic sources to the total nitrogen content is generally low and typically corresponds to inorganic ammonium incorporated in the interlayer position of smectites (e.g., Muller, 1977). High abundances of marine OM in the studied sediments are the result of high productivity rates prevailing in the eutrophic Oyashio Current (Handa and Tanoue, 1980) and enhanced preservation caused by the high sedimentation rates estimated at the site (see **"Sedimentation Rates,"** p. 23). Degradation of OM is rapid under the oxic conditions usually prevailing at the seafloor. High sedimentation rates promote the rapid removal of OM from the oxic zone and limit pore waters from exchanging oxygen with bottom waters, thereby enhancing the amount of OM present in the sediments.

Sulfate concentrations at Site 1151 are very low (<2 mM) in the studied sediments. A characteristic exponential decreasing trend observed in most marine sediments is not observed at Site 1151, probably because the upper 70 m was not cored with a RCB system in Hole 1151A and there was not sufficient time to analyze samples from the APC-cored holes. As at Site 1150 (see **"Geochemistry,"** p. 37, in the "Site 1150" chapter), sulfate concentrations are probably rapidly depleted in the sediments at Site 1151 as a result of active sulfate-reducing bacterial activity induced by an abundant supply of labile OM. A shallow sulfate-reducing zone can additionally be caused by limited infiltration of sulfate into the sediments under high sedimentation rates as a result of the rapid removal of sediments from the water/sediment interface (Berner, 1980). The presence of significant amounts of methane in the first core retrieved is evidence for a shallow sulfate-reducing zone at Site 1151 because methane is generated by methanogens immediately below the sulfate-reducing zone (e.g., Claypool and Kaplan, 1974). The bacterial origin of the methane is supported by the relatively high methane/ethane ratios present at Site 1151. Ratios higher than 1000 are typical of sediments with large methanogen activity (Claypool and Kaplan, 1974).

PHYSICAL PROPERTIES

Measurements on whole-round core sections taken in Hole 1151A included magnetic susceptibility, gamma-ray attenuation (GRA) bulk density, NGR activity, and thermal conductivity. *P*-wave velocity and index properties measurements were made on what appeared to be the least-disturbed portions of split core sections. Hence, sampling was biased in favor of indurated sections. The *P*-wave logger (PWL) and vane shear apparatus were not used in Hole 1151A because RCB sediments are not of appropriate quality. Only multisensor track (MST) data were acquired on whole-round core sections from Holes 1151C and 1151D. Thermal conductivity, *P*-wave velocity, shear strength, and index properties were not measured because of time constraints, which also forced us to conduct the MST measurements before the cores had equilibrated to ambient laboratory room temperature. Descriptions of the experimental

methods are in "Physical Properties," p. 18, in the "Explanatory Notes" chapter.

Multisensor Track

Magnetic susceptibility was measured with a 2-cm sampling interval on all cores recovered in Hole 1151A and with a 5-cm sampling interval on cores from Holes 1151C and 1151D. The results of magnetic susceptibility measurements are discussed in "Paleomagnetism," p. 22. GRA bulk density was measured with a 2-cm sampling interval on all cores from Hole 1151A, and with a 5-cm sampling interval on cores recovered in Holes 1151C and 1151D. In addition, a number of whole-round core sections from Hole 1151A (i.e., Sections 186-1151A-69R-4, 105R-2, 106R-5, and 108R-2) were rerun with a 1-cm sampling interval to aid the selection of suitable whole-round core samples for postcruise laboratory tests. Preliminary shipboard analyses included editing of density data by removing values <1.0 g/cm³. The maximum GRA bulk density is reported here because it is assumed to provide the best estimate of bulk density.

The maximum GRA bulk density in Hole 1151A has a total range from ~1.3 to 2.0 g/cm³ (Fig. F29). Corresponding ranges for the variation in Holes 1151C and 1151D are 1.2 to 1.8 g/cm³ and 1.2 to 2.1 g/cm³, respectively. Density increases from 1.2 g/cm³ at the mudline to 1.7 g/cm³ at 15 mbsf. After this local maximum, density decreases to ~1.4 g/cm³ at 190 mbsf. Lithologic Unit II (190–430 mbsf; see "Lithostratigraphy," p. 7) is characterized by rather constant values, averaging at ~1.4 g/cm³. Density varies from 1.3 to 1.7 g/cm³ along an oscillating trend in lithologic Unit III (430–911 mbsf). Local peaks occur at ~450, 570, 590, 810, and 900 mbsf, and local troughs occur at ~530, 670, 800, and 850 mbsf. Similar oscillating trends are observed in lithologic Units IV and V (911–1007 mbsf and 1007–1113 mbsf, respectively). However, the range of values is greater in lithologic Unit IV (1.3–1.8 g/cm³) and greater and more scattered in lithologic Unit V (1.4–2.0 g/cm³).

P-wave velocity in the horizontal direction was acquired with the PWL on full sections for Holes 1151C and 1151D. The cores in this interval were severely disturbed by gas expansion, which resulted in mechanical stretching and micro- to macrofracturing of the cores. As a result, PWL measurements generally are of poor quality. After the preliminary shipboard processing (see "Physical Properties," p. 18, in the "Explanatory Notes" chapter), the results of PWL measurements included data from the upper 20 and 22 m of Holes 1151C and 1151D, respectively. *P*-wave velocity ranges from 1450 to more than 5000 m/s, although most values vary between 1450 and 1600 m/s (Fig. F30). Higher velocities generally are obtained near the edges and voids of core sections and are assumed to be artificial.

NGR activity was measured every 20 cm with 20-s-long counting periods on all cores recovered at Site 1151 and reported in counts per second (cps) with the total background radiation subtracted (12.27 cps). The maximum values at each depth of NGR activity are reported here.

NGR activity has an overall range from 5 to 29 cps in Hole 1151A. Corresponding ranges for the variation in Holes 1151C and 1151D are 9–36 and 10–40 cps, respectively. The downhole variation generally has a width of scatter of ~5 cps (Fig. F31). The downhole trend correlates with that of GRA bulk density. NGR activity increases from 15 to 27 cps

F29. Bulk density from GRA measurements, p. 75.

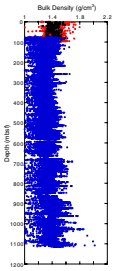

F30. Horizontal *P*-wave velocity from PWL measurements, p. 76.

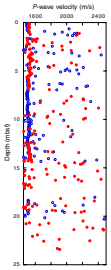

F31. NGR activity, p. 77.

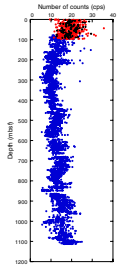

in the upper 15 m of Holes 1151C and 1151D and then begins a decreasing trend to 12 cps at 190 mbsf. From ~250 to 1114 mbsf, NGR activity generally increases with depth. NGR activity generally ranges from 10 to 15 cps in lithologic Unit II (190–430 mbsf). Lithologic Units III through V are characterized by oscillating trends. The former unit has lower and somewhat less scattered values that generally range from 11 to 21 cps compared to the two latter ones, for which the NGR activity ranges from 13 to 25 cps.

Thermal Conductivity

Thermal conductivity was measured at a frequency of one measurement per core from 79 to 413 mbsf in Hole 1151A using the full-space configuration. The mean error associated with these measurements is assumed to be 0.2 W/(m·K). The average thermal conductivity, which was obtained from three measurements, ranges from <0.4 to ~0.9 W/(m·K) (Fig. **F32;** Table **T14,** also available in **ASCII format**). The maximum and minimum values were obtained in the first two measurements of Hole 1151A cores. Below, a generally fluctuating downhole trend is measured, with breaks in the slope at ~150 and 300 mbsf. A poor correlation is obtained for thermal conductivity vs. porosity and bulk density, indicating that the quality of data is deteriorated by drilling disturbances.

F32. Thermal conductivity variation with depth, Hole 1151A, p. 78.

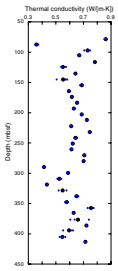

T14. Thermal conductivity measurements, Hole 1151A, p. 116.

T15. *P*-wave velocity and anisotropy, Hole 1151A, p. 117.

P-Wave Velocity

P-wave velocity was mainly measured in split cores from Hole 1151A with the PWS3 system. We aimed at a sampling frequency of one measurement per section. However, because of scattering and attenuation of the signal in the sediment specimen, the PWS1 system yielded good data for only two measurements at ~80 mbsf (Table **T15,** also available in **ASCII format**), and the PWS3 system was used downhole only from ~250 mbsf. *P*-wave velocity values <1450 m/s were omitted. PWS3 measurements were made on indurated pieces (305–413 mbsf) and on cylindrical minicores (247 and 422–1113 mbsf). For the latter, *P*-wave velocity was measured in three directions, allowing estimation of acoustic anisotropy. *P*-wave velocity and index properties data were measured on the same sample.

In Hole 1151A, horizontal and vertical velocity has overall ranges from ~1540 to 5290 m/s and ~1450 to 5010 m/s, respectively (Fig. **F33;** Table **T15**). However, the majority of measurements indicate *P*-wave velocities <2150 m/s. Greater velocities were measured in thin beds of dolomite, dolomite concretions, and carbonate-rich sediments. Three measurements of horizontal and vertical velocity at ~80 mbsf yield the lowest values of Hole 1151A (<1480 m/s). Horizontal velocity increases from ~1550 at 305 mbsf to 1640 m/s at 425 mbsf in lithologic Unit II (Fig. **F33A**). Lithologic Unit III (430–911 mbsf) is characterized by steadily increasing horizontal velocity from ~1600 to 1800 m/s. Below 600 mbsf, the values generally are scattered by ~200 m/s. The vertical velocity shows a similar trend, but with lower values than the horizontal velocity, and generally increases from 1580 to 1750 m/s in lithologic Unit III (Fig. **F33B**). Below 911 mbsf, somewhat fluctuating trends in horizontal and vertical velocity were measured. Horizontal and vertical velocities increase to ~2100 and 2000 m/s, respectively, at the base of Hole 1151A. There are two zones with increased scatter and higher velocity values, namely from 893 to 970 mbsf, and from 1058 to 1113

F33. *P*-wave velocity vs. depth from measurements on split cores, Hole 1151A, p. 79.

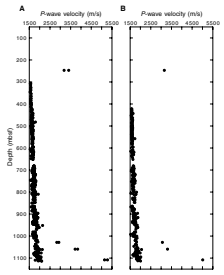

mbsf. Maximum horizontal and vertical velocities in Hole 1151A (5290 and 5010 m/s, respectively) were measured on a dolomite concretion at 1108 mbsf.

Acoustic anisotropy was calculated from measurements of *P*-wave velocity in the x, y, and z directions on cylindrical minicores (see "Physical Properties," p. 18, in the "Explanatory Notes" chapter). Three anisotropy values were determined, namely maximum vs. minimum horizontal velocity (A_{Hh}), maximum horizontal vs. vertical velocity (A_{HV}), and minimum horizontal vs. vertical velocity (A_{hV}). Anisotropy in the horizontal direction (A_{Hh}) ranges from 0 to 0.15, although the majority of values are less than 0.05 (Fig. F34A). Furthermore, the A_{Hh} anisotropy tends to become more scattered with depth. The ranges of A_{HV} and A_{hV} are –0.05–0.19 and –0.08–0.12, respectively. However, the vast majority of these measurements (>90%) have positive values. The results suggest that the sediments at minimum are transverse isotropic but that they probably are anisotropic. The preliminary shipboard analyses did not include investigations of the variation of horizontal anisotropy (A_{XY}) with azimuth using paleomagnetic declination data.

F34. Anisotropy vs. depth from measurements of vertical and horizontal *P*-wave velocities, Hole 1151A, p. 80.

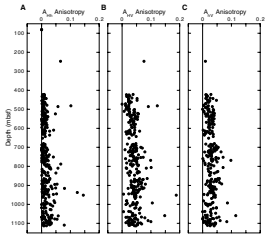

Index Properties

Index properties were determined on discrete samples recovered from Hole 1151A using gravimetric methods. A dedicated program calculates the index properties from wet and dry mass and dry volume, using a salinity of 0.035 and a pore-water density of 1.024 g/cm³. At this site, the salinity and density of the pore water were significantly different (0.032–0.018 and 1.023–1.012 g/cm³, respectively). Index properties were recalculated using in situ values of salinity and pore-water density from linear extrapolation of 34 measurements on interstitial pore-water samples (see "Geochemistry," p. 25; see also "Physical Properties," p. 18, in the "Explanatory Notes" chapter). Figure F35 shows variation with depth of the ratio of index properties corrected for in situ salinity and pore-water density over those determined with standard salinity and pore-water density. The different salinity and pore-water density values have only a minor influence on bulk density and grain density (the ratio ranges from 0.98 to 1.02); however, they have intermediate influence on dry density, porosity, and void ratio (the ratio ranges from 0.96 to 1.04), and significant influence on water content of total mass, and water content of mass of solids (the ratio ranges from 0.93 to 1.07). Index properties determined from in situ variations of salinity and density of pore water are reported here. Note that index properties included in the Janus database are calculated from standard values of salinity and pore-water density.

F35. Corrections for in situ salinity and pore-water density, Hole 1151A, p. 81.

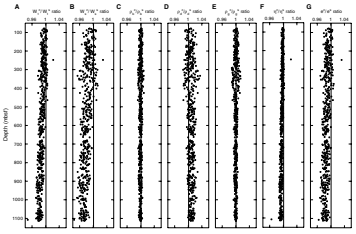

To cross-examine the internal quality of the data, porosity, dry density, and void ratio were calculated indirectly from the other index properties (see "Physical Properties," p. 18, in the "Explanatory Notes" chapter). The direct and indirect calculations of dry density, porosity (i.e., Equation 9, p. 23, in the "Explanatory Notes" chapter) and void ratio overlap perfectly (i.e., 0% difference), whereas the difference between direct and indirect determination of porosity (i.e., Eq. 10, p. 23, in the "Explanatory Notes" chapter) is <2%. These differences lie within the estimated uncertainty of index properties measurements (±2%), which implies good quality of index properties measurements.

The overall plots of index properties vs. depth indicate that sediments at this site are porous and poorly consolidated. Exceptions from

these trends are obtained from measurements of dolomite samples that appear to be well consolidated. The main results of the downhole variation in porosity, bulk density, and grain density are presented below. Water content and void ratio have downhole trends similar to that of porosity, and dry density has a downhole trend similar to that of bulk density (Fig. **F36;** Table **T16,** also available in **ASCII format**).

The overall ranges of porosity, bulk density, and grain density in Hole 1151A are 10%–77%, 1.32–2.42 g/cm³, and 2.09–3.91 g/cm³, respectively. Generally, samples with low porosity (<40%) and high bulk density (>1.8 g/cm³) consist of dolomite or carbonate-rich sediment. The section from 78 to 347 mbsf has scattered but slightly inverse trends of porosity and bulk density; porosity and bulk density generally range from 57% to 77% and from 1.3 to 1.6 g/cm³, respectively. At 190 mbsf, there is a small decrease in the width of the scatter of porosity and bulk density values and some of the measurements indicate slightly increasing porosity and decreasing bulk density from 190 to 347 mbsf (Fig. **F36;** Table **T16**). Grain density variation from 78 to 347 mbsf is more scattered and ranges from 2.09 to 2.67 g/cm³. Between 347 and 430 mbsf, index properties show normal downhole trends. Porosity decreases from ~76% to 65%, bulk density and grain density increase from 1.34 to 1.65 g/cm³ and 2.31 to 2.42 g/cm³, respectively. There is a drop to slightly more scattered and lower porosity and higher bulk density in the section from ~410 to 450 mbsf. Below ~450 mbsf, the trends of index properties show normal and uniform changes with depth. At 719 mbsf, porosity is ~60% and bulk density is ~1.6 g/cm³. Rather constant values of porosity (58%–65%) and bulk density (1.46–1.65 g/cm³) are measured from 719 to 812 mbsf. Index properties change significantly in the interval from 812 to 897 mbsf. Porosity reaches a local minimum of 50% at 812 mbsf and a local maximum of 69% at 849 mbsf. Bulk density and grain density values mirror the trend of porosity and show a local maximum at 812 mbsf (1.58 and 2.40 g/cm³, respectively) and a local minimum at 849 mbsf (1.38 and 2.20 g/cm³, respectively). Yet another section of constant index properties values is measured from 897 to 962 mbsf; porosity and bulk density averages are 58% and 1.6 g/cm³, respectively. This is followed by more scattered values. The section from 962 to 1007 mbsf has higher porosity, whereas the section from 1007 to 1114 mbsf has lower porosity. At the base of Hole 1151A, porosity, bulk density, and grain density are 49%, 1.75 g/cm³, and 2.46 g/cm³, respectively.

F36. Index properties vs. depth, Hole 1151A, p. 82.

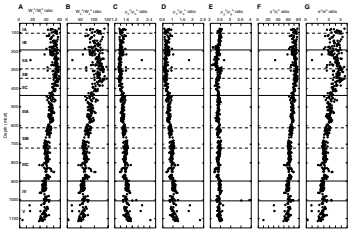

T16. Index properties, Hole 1151A, p. 118.

Vertical Stress

The total and effective vertical stress were calculated from bulk density and porosity data following **Equation 13,** p. 23, and **Equation 8,** p. 23, in the "Explanatory Notes" chapter. The bulk density data consisted of GRA bulk density data from 0 to 97 mbsf, discrete measurements of bulk density in cores from 78 to 1113 mbsf, and hostile environment lithodensity sonde (HLDS) bulk density from 111 to 858 mbsf. GRA and HLDS bulk density data were converted into porosity using **Equation 9,** p. 23, in the "Explanatory Notes" chapter. Grain density values were estimated from linear extrapolation of discrete grain density measurements in cores, and pore-water density was assumed to be 1.024 g/cm³. The total and effective vertical stresses increase uniformly with depth to 16.8 and 9.8 MPa at 1113 mbsf, respectively. The

downhole trends of vertical stresses are rather linear, with subtle changes in the slope at ~100 and 730 mbsf (Fig. F37).

F37. Vertical stress vs. depth, Site 1151, p. 83.

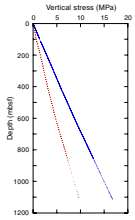

Discussion

Quality of Data

In general, the various shipboard analyses of physical properties show similar downhole trends. There is a good fit between GRA and discrete bulk density measurements in the upper 700 mbsf, whereas GRA measurements are 0.1 to 0.2 g/cm^3 lower than discrete measurements below 700 mbsf. This could result in part from biased sampling of index properties samples. However, the discrepancy between GRA and discrete values probably also results from the fact that the deeper RCB cores did not completely fill the core liner. This would result in underestimation of GRA bulk density (Blum, 1997). The shallow RCB cores were disturbed by drilling and often comprised drilling biscuits. This has resulted in low quality of thermal conductivity data, which is confirmed by the poor correlation between thermal conductivity vs. porosity and bulk density. In Holes 1151C and 1151D, the quality of *P*-wave velocity (PWL measurements) is degraded by the presence of micro- and macrofractures in many of the APC cores. These fractures were formed by gas expansion in the cores when they were recovered to the drill floor. The remaining physical properties appear to correlate well with each other. Tests of internal consistency of index property data confirm the good-quality index properties.

Downhole Variation of Physical Properties

Site 1151 is characterized by minor to moderate variations in physical properties reflecting the generally homogeneous lithology, with the exception of a few large excursions in the data. Apart from the excursions, which were taken from dolomite or other carbonate-rich layers or nodules, the downhole variations of physical properties are generally similar at Sites 1150 and 1151. Lithology in Site 1151 is dominated by varying amounts of greenish hemipelagic diatom-bearing clay and silt that become indurated with depth. The variation of physical properties data with depth is marked with anomolous values and/or changes in the downhole trend that generally can be correlated with lithologic units (see **"Lithostratigraphy,"** p. 7). The breaks in physical properties data appear mainly to signal variations in mechanical conditions (i.e., induration of sediments) (Figs. **F29, F31, F33, F36**).

The upper 78 mbsf of the section was cored only in Holes 1151C and 1151D and not in Hole 1151A. Lithologic Unit I (0–190 mbsf) is largely composed of soft Pleistocene and Pliocene diatom-bearing silty clays. GRA bulk density variation in the upper 15 mbsf of this interval suggests decreasing values with depth, whereas increasing values are measured below 15 mbsf (Fig. **F29**). The base of lithologic Unit I coincides with a distinct change to higher NGR activity and a small decrease in the width of scatter of index properties data (Figs. **F31, F36**).

Lithologic Unit II (190–430 mbsf) consists of soft diatomaceous and spicule-bearing to diatomaceous silty clay. The unit is divided into three subunits based on the induration of the sediment (see **"Lithostratigraphy,"** p. 7), of which NGR activity and index properties data (Figs. **F31, F36**) signal the boundary between Subunits IIA and IIB (295 mbsf) and index properties data signal the boundary between Subunits IIB and IIC

(347 mbsf). The section from 78 to 347 mbsf generally has constant index properties, suggesting that the section is underconsolidated. Below 347 mbsf, normal trends (decreasing porosity and increasing bulk density) are measured.

The top of lithologic Unit III (430–897 mbsf) is marked by a local drop of porosity, which is followed by a small change to higher porosity; bulk density shows the inverse trend to that of porosity. This is followed by normal trends to 719 mbsf (i.e., boundary between lithologic Subunits IIIB and IIIC) where the induration of cores changes from a mix of soft and firm sediment to firm sediment. The gradients of downhole change of index properties is similar in the sections from 347 to 430 mbsf and ~450 to 719 mbsf, suggesting that the section from 347 to 719 mbsf is normally consolidated. This sequence is mainly composed of firm diatom-, spicule-, and glass-bearing silty clay of early Pliocene to late Miocene age. Existing *P*-wave velocity data in this interval show uniformly increasing values to ~600 mbsf (Fig. **F33**). *P*-wave velocity becomes significantly more scattered below, probably reflecting increasing influence of brittle deformational structures (see **"Lithostratigraphy,"** p. 7). Lithologic Subunit IIIC (719–897 mbsf) is mainly composed of upper Miocene diatom-, glass-, and spicule-bearing silty claystone. The porosity and bulk density is rather constant throughout the unit, suggesting that this section is underconsolidated. Dewatering of the section is probably hindered by the rapid deposition (250 m/m.y.) and impermeable nature of the overlying sediment section (see **"Sedimentation Rates,"** p. 23).

Sediments of lithologic Unit IV (897–1007 mbsf) are classified as hard, and they are mainly composed of upper Miocene silty claystone that is diatom-, glass-, and/or spicule-bearing (see **"Lithostratigraphy,"** p. 7). The upper 63 m of the unit is characterized by almost constant porosity and bulk density, whereas the sediment is less consolidated (higher porosity, lower bulk density) in the lower section of lithologic Unit IV. The interval between 962 and 1007 mbsf does not correspond to changes in lithology, chemistry, or biostratigraphy. However, the core recovery was very low (1.1-m-long core), and the bedding dips increase significantly near this depth (see **"Bedding,"** p. 40). This indicates that there is an unconformity at this depth.

Lithologic Unit V (1007–1114 mbsf) is characterized by significantly lower porosity and higher bulk density and *P*-wave velocity (Figs. **F33, F36**).

DOWNHOLE MEASUREMENTS

Introduction

Downhole measurements were used to determine in situ physical properties, geologic structure, and thermal structure, especially in sections where core recovery was poor. Logs also provide high-resolution records that will be used to study the paleoceanographic history in the western Pacific region and the nature of compaction, lithification, and deformation processes in the drilled forearc region.

Operation

Hole 1151D was drilled with an XCB bit with a diameter (bit size) of 29 cm (11 7/16 in). Logging operations at Site 1151 are summarized in

Table T17. Two logging runs were performed on 11 and 12 August 1999. The FMS/long-spaced sonic imager (LSS) string was run from 871 mbsf to the mudline, and the triple combo tool string was run from 868 to 49 mbsf. The bottom of the drill pipe was at 105 mbsf.

T17. Summary of Hole 1151D logging operations, p. 119.

Data Quality

The wireline logs recorded in Hole 1151D are shown in Figure F38; they are generally of high quality except for the neutron porosity log. Density, resistivity, sonic, and FMS data recorded in the drill pipe are not interpretable. The NGR logs in the drill pipe are highly attenuated and should be interpreted only qualitatively.

The hole diameter was elongated in the interval of 105–320 mbsf with a short axis of 27–30 cm and a log axis of 30–38 cm. The elongation may be stress-induced and/or be washouts within high-porosity zones. The FMS calipers revealed that the hole generally has a circular shape with a 30-cm diameter in the interval of 320–868 mbsf. The downhole variation of the calipers shows spikes in the borehole diameter each nine meters. This is especially apparent for caliper C2 in the upper 320 m of the hole. These spikes are caused by the pipe-tripping operation. The compressional velocity data from the LSS log are of high quality. A minor amount of cycle skipping is present in the raw data, but shipboard processing of the traveltime eliminated these excursions. Thin intervals of especially abrupt velocity changes corresponded to hard, thin layers.

F38. Summary of logs from Hole 1151D compared with the lithologic units, p. 84.

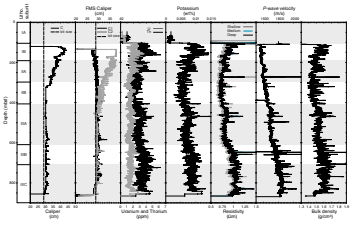

Results

Natural Gamma Ray

In situ NGR measurements were collected from 67 to 844 mbsf by the hostile environment spectral natural gamma-ray sonde (Fig. F38). Potassium and thorium values show similar trends throughout the logged section. Potassium values typically fluctuate in the range of 0.002–0.005 wt% and change between 0.003 and 0.015 wt%. Vertical variations of potassium and thorium are similar to that of density.

Electric Resistivity

In situ electric resistivity measurements were collected from 108 to 865 mbsf by the dual induction tool as part of the triple combo string. The deep-, medium-, and shallow-resistivity logs in Figure F38 show similar trends throughout the logged intervals, indicating good hole conditions. Resistivity values typically fluctuate in the range of 0.1–0.2 Ωm, and background values change between 0.75 and 1.15 Ωm. Large excursions occur at ~110, 275, 648, 658, and 830 mbsf, which can be correlated to dolomite layers (see Table T5).

Sonic Velocity

In situ sonic velocity was acquired from 107 to 856 mbsf in two passes with the LSS tool, which is part of the FMS/sonic tool string (Fig. F38). The downhole trend of log and core *P*-wave velocity measurements are similar, but the log measurements are generally ~100 m/s higher and less scattered than the discrete core measurements. *P*-wave velocity generally increases from 1540 to 1850 m/s across the logged in-

terval of Hole 1151D, although higher values are commonly observed across dolomite layers, for example at 273 and 648 mbsf. The maximum *P*-wave velocity (3800 m/s) of Hole 1151D is measured at 648 mbsf. The width of scatter in *P*-wave velocity increases from ~600 mbsf, which probably reflects the increasing number of brittle structures in the logged sequence.

Bulk Density

In situ bulk density was measured from 111 to 858 mbsf with the HLDS, which is part of the triple combo string (Fig. F38). The downhole trends of log and core density measurements are closely correlated, but log measurements are generally ~0.1–0.2 g/cm³ higher than the discrete core measurements in the upper part of the hole with soft lithologies. This discrepancy is expected because of core decompaction and drilling disturbance. Consequently, the difference between log and core measurements decreases gradually with depth as sediments become more indurated, and log and core values have similar magnitudes from ~700 mbsf.

Bulk density generally ranges from 1.4 to 1.7 g/cm³ in Hole 1151D, but spike values up to 2.5 g/cm³ are occasionally measured (Fig. F38). Bulk density decreases with depth across lithologic Unit I, from about 1.6 g/cm³ at the base of the drill pipe to 1.4 g/cm³ at 296 mbsf. A small excursion from this trend (i.e., slightly increasing values) occurs between 200 and 240 mbsf. A shift to rather constant values occurs across lithologic Unit II (296–407 mbsf), and bulk density generally ranges from 1.4 to 1.6 g/cm³. Infrequent higher values (<1.8 g/cm3) are measured in the upper section of the unit.

Bulk density values in lithologic Subunit IIIA generally fluctuate between 1.5 and 1.6 g/cm³. A significant excursion with bulk density ranging between 1.4 and 1.8 g/cm³ occurs from 452 to 467 mbsf. The width of the scatter in bulk density increases from about 1.5 to 1.6 g/cm³ in this subunit. At 647 mbsf, the maximum bulk density (2.5 g/cm³) of Hole 1151D is measured in a dolomite layer. Bulk density values fluctuate around 1.6 g/cm³ in lithologic Subunit IIIC (719–817 mbsf) with a range of ±0.1 g/cm³. This interval also includes a spike value in bulk density (<1.9 g/cm³) at 768 mbsf. Only the upper 40 m of lithologic Unit IV was logged, and bulk density values generally decrease from 1.7 to 1.5 g/cm³ in this interval.

Temperature Measurements

Equilibrium temperatures obtained from the Adara temperature tool and the Davis-Villinger temperature probe are shown in Table T18 and Figure F39 and are also shown as a function of depth in Figure F40. The errors were determined subjectively, based on the stability of the equilibration record and tool performance. The geothermal gradients at Holes 1151A and 1151D are 28°C/km in the interval from 0 to 372.9 mbsf. Extrapolation of this gradient suggests an in situ temperature of ~34°C at the instrument depth (~1200 mbsf).

T18. Summary of in situ temperature measurements, p. 120.

F39. Temperature data vs. time from the Adara temperature tool and the DVTP, p. 85.

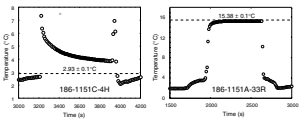

F40. Temperature vs. depth, p. 86.

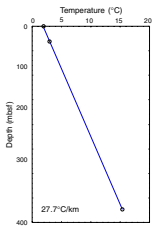

BOREHOLE INSTRUMENT STATUS

Introduction

Site 1151 is ~48 km south of Site 1150 along the direction of the Japan Trench axis in a seismically inactive zone (Fig. F41). The contrast in seismic activity is the main reason for establishing a second borehole observatory for comparison at this spatial separation. Because many aspects and features of the two observatories are identical, we will describe the chief differences between Site 1151 and the Site 1150 observatory and avoid repetition of "Borehole Instruments Status," p. 57, in the "Site 1150" chapter.

More than 1000 global positioning systems stations are distributed on Japanese islands, but there are no geodetic observatories offshore. The two observatories of strain, tilt, and seismic waves are expected to reveal the previously unknown nature of plate coupling at the seismogenic zone.

F41. Logging data of *P*-wave velocity and bulk density near the instrument installation depth, p. 87.

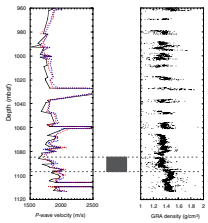

Operation

The installation of a geophysical observatory at Hole 1151B proceeded as shown in Table T19. Based on core recovery and lab measurements from Hole 1151A, we decided to emplace the strainmeter at 1097 mbsf (Fig. F41), where the core recovery was good in a relatively constant, higher density (~1.9 g/cm³) and *P*-wave velocity (~2000 m/s) section. The target depth is slightly shallower, but physical properties data suggest a more competent rock environment than at Site 1151.

T19. Instrument package deployment, p. 121.

Based on the first experience, some changes were made to expedite the operation, which are detailed in "Operations," p. 2. The strapping of the cables proceeded much more quickly than at Site 1150. Only one centralizer was attached at every joint except at critical sections. Seas were calmer than during the first installation, which prompted this decision. To reach the target depth, 93 joints of 4½-in casing pipes were used.

The four cables were terminated in the subsea shop as before. Connectors were attached to cables cut 30 cm longer than the required lengths. This extra length is half of that used at Site 1150. Less excess length makes it easier to strap the cable onto the hanger below the MEG. All cable sections must maintain full contact with the pipe wall. ODP engineers and borehole researchers worked overnight to complete the terminations.

A final check of the MEG module connected to the cables via the underwater mateable connectors indicated that the power-up test failed on the CMG-1T ocean borehole seismometer (OBHS). Other sensors were functional; therefore, the MEG was retrieved from the hanger and checked in the downhole lab. The defective part of the power switching circuit distributing power to the OBHS was modified so that this problem will not recur. A surge protector was added to the circuit to damp large transient voltages. After about 3 hr the MEG was reseated in the frame attached to the hanger. After a final successful check, the casing hanger was lowered through the moonpool. The moonpool door opening had to be adjusted several times for the casing hanger to pass through safely.

Because we encountered difficulty in lowering the instrument at Site 1150, some modifications were made to the drilling plan. The open

hole was shortened to 43 m and the upper part of the hole was reamed with the 14¾-in bit before setting the 10¾-in casing. Because it is critical for the strainmeter to have a good bonding to the surrounding rock, the bottom portion was not reamed. The instrument string was successfully inserted on the first attempt.

The bottom of the hole was filled with cement with a density of 1.9 g/cm^3 and a volume of 12.7 m^3 without displacing with mud beforehand. That volume will fill to above the open-hole section into the cased-hole section.

After successfully cementing the instruments, the power/access terminal (PAT) battery frame was made up in the moonpool. The assembly is the same as before, but improvements were made to take fewer steps to start lowering the PAT hung by the logging line. There was no time loss due to waiting for daylight. The ship's heave was smaller than before, at ~0.5 or less m.

The relative position of the MEG top connector plug to the remotely operated vehicle connector parking position on the PAT was similar but slightly nearer than at Site 1150. The disconnection of the J-tool to decouple the drill string went smoothly.

Borehole Instruments

The array of emplaced instruments from the bottom to the top of Hole 1151B consists of the volumetric strainmeter, three-component broadband PMD-2123 seismometer sensor, two-component tiltmeter, and three-component CMG seismometer sensor (T1020) (see **"Borehole Instruments,"** p. 5, in the "Borehole Instrument Package" chapter). A 3-m-long stinger pipe with centralizers was attached to the strainmeter bottom. We had a spare unit for each sensor but all functioned well.

Seafloor Instruments

All the components were successfully emplaced. These are the power supply, data recorder, and the MEG to merge and digitize data and control the observatory (see **"Seafloor Instruments,"** p. 11, in the "Borehole Instrument Package" chapter). The MEG at this site has two fewer sets of 24-bit digitizer boards than those at Site 1150. This is because the strainmeter at this site has just one component.

Summary

The second seafloor borehole geophysical observatory, 'Neath Seafloor Equipment for Recording Earth's Internal Deformation (NEREID-2), was successfully installed. The vision of establishing borehole observatories beneath the seafloor has become a reality. Though only a first step, the two observatories installed during Leg 186 and the data that will obtained from them are expected to accelerate efforts for establishing similar observatories worldwide.

STRUCTURAL GEOLOGY

Description of Structures

In this section we describe the brittle structures, focusing on those with lengths that are greater than core diameter. Numerous smaller-

scale structures are also visible, particularly when the core surface has dried, but detailed description of these is beyond the scope of the shipboard analyses. The occurrence of brittle deformational structures is restricted to the cored section below 300 mbsf, with the number of structures becoming much more abundant below 400 mbsf. The depth of apparent faulting begins at the top of lithologic Unit II, which is also the depth at which the sediment lithification changes from soft to firm. Faults are rare, however, down to the top of lithologic Unit III, which is where we commenced counting faults (Table T20, also available in ASCII format).

T20. Deformation structures, Hole 1151B, p. 122.

For the large-scale structures, we have assessed the abundance and type of structures that occur. For abundances, we have divided fractures into two types: open and healed. Most of the brittle structures were healed and filled with fine-grained dark gray clayey gauge. The width of the infill varies from 2 mm to a few tenths of a millimeter. No secondary mineralization or recrystallization (fibrous crystal growth) were observed. Open structures, though not as common as healed structures, were also abundant. These were probably drilling induced, although they were often formed along pre-existing weakness planes. These fractures were not considered in the structural interpretation unless they were partially filled.

Within the healed fracture category, we have further assessed the abundance of faults and joints. The distinction between faults and joints is based on the visible apparent displacement. Because sedimentary layering was rarely observed, the displacement was estimated primarily from the offset of burrows, carbonate nodule-like accumulations, and dissolution and precipitation rims around manganese or iron. As a result, the number of faults per meter is probably underestimated and the number of joints is overestimated. The fault planes, if accessible by open fracturing, usually show slickenside striation and structures indicating the direction of relative movement on the fault plane.

In addition, we measured the apparent dip of the large-scale structures with a conventional contact goniometer. The apparent dip is less than or equal to the real dip of any plane; therefore, dip angles that are reported here are minimum values. For curved fault traces (e.g., listric faults) the predominant apparent dip was measured. True dip measurements of faults are presented in "Downhole Measurements," p. 33. Finally, we reconstructed the orientation of healed and open fractures and bedding planes relative to geographical north using paleomagnetic directions.

Observation of Structures

Faults and Joints

The types of observed faults are similar to those described for Site 1150 (See "Structural Geology," p. 60, in the "Site 1150" chapter). Also similar to Site 1150, displacements recorded for the different types of faults range from some few millimeters to tens of centimeters. However, large displacements are visible only for normal faults and were more common than at Site 1150. The displacements along strike-slip faults is difficult to estimate, but the intense slickenside formation with deep grooves on polished surfaces and long mineral fibers indicate displacements of considerable size (several centimeters to decimeters).

F42. Photograph showing a compaction-related steep normal fault, initiating below a dark gray discontinuous silt layer, p. 88.

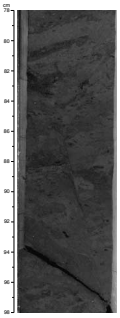

An example of a steep normal fault is shown in Figure F42. The tip of this fault begins below a coarse-grained dark intercalation of a discontinuous sand/silt layer, and the vertical displacement amount increases downward along the fault. A specific feature of the hard sedimentary rocks in Hole 1151A is the sets of small pinnate fractures, parallel and S-shaped, commonly occurring as precursors of larger shear fractures. These tension gashes are so abundant that counting them was not feasible (Fig. F43). Some fractures consist of broad zones of anastomosing and branching joints, which resemble dewatering zones (Fig. F44).

Black and brown precipitation rims adjacent to fault planes and joint planes are very common, possibly indicating that past fluid movement occurred along the faults and joints. Usually, these rims extend in a cloud-like shape above the fracture planes, possibly indicating that the main flow direction was mainly parallel to the fractures, but with an upward component.

Frequency of Fractures

The different kinds of structures were counted, and the total number was divided by recovered length in meters (Fig F45; Table T20). The open fractures are most common. Significant numbers of joints are present below 500 mbsf but are rare above 500 mbsf. The values essentially show peaks from 650 to 720 mbsf, at 800 mbsf, and from 920 to 980 mbsf, with the amplitude of the peaks decreasing with depth. The number of normal faults is low, with one sharp peak at 680 mbsf and some small but broad peaks at 700–800 mbsf, 840–930 mbsf, and 1000–1110 mbsf. Strike-slip and reverse faults are very rare, with the strike-slip faults restricted to depths below 750 mbsf. Unidentified faults (i.e., those where the sense of motion could not be determined) occur predominantly in lithologic Unit V. This is probably caused by the changing lithology with completely different bioturbation that obscures features of fault motion. The pattern found at Hole 1150B, where the number of faults showed an overall increase with depth, does not occur at Site 1151.

Reconstruction of Orientation of Structures

Healed Fractures

We measured the orientations of healed fractures from recovered cores and then reoriented these into geographic coordinates using paleomagnetic declinations (Table T21, also available in ASCII format). Histograms of azimuths and dip angles are shown in Figure F46. The clusters of reoriented dip azimuths are weakly concentrated in 40°–160° and 260°–340° directions, with small peaks at 0°–20° and 200°–220°. The distribution of dip angles shows a unimodal pattern. Most angles range between 40° and 80°, which is the same distribution observed for Hole 1150B.

From the downhole variation of dip azimuth, we subdivided the data into domains (Fig. F47):

1. The upper domain, spanning the interval between 400 and 950 mbsf, shows a bimodal clustering of directions.
2. The middle domain, spanning the interval between 950 and 1040 mbsf, also has a bimodal clustering but it is more focused than the upper domain.

F43. Photograph showing typical S-shaped tension gashes that indicate dextral shearing, p. 89.

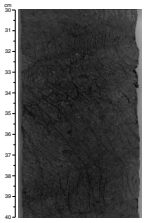

F44. Photograph showing large anastomosing and branching zone of steep joints and faults, p. 90.

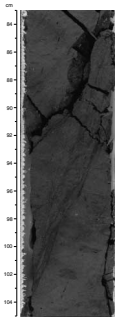

F45. Number of faults, joints, and open fractures at Site 1151, p. 91.

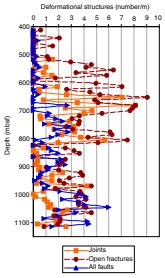

T21. Orientations of healed fractures, Hole 1151A, p. 123.

F46. Frequency of healed fractures and distribution of dip azimuth and dip angle of healed fracture planes after reorientation, Hole 1151A, p. 92.

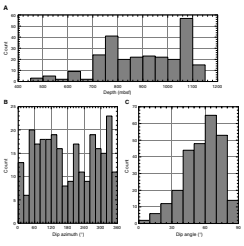

3. The lower domain, spanning the interval between 1040 and 1113 mbsf, has scattered directions.

The poles to the fracture planes typically have bimodal distributions for all three domains (Fig. F48). In the upper domain these poles are concentrated in the southeast and northwest, whereas the poles for the other two domains are concentrated to the east and west.

Two dominant fracture directions, northwest-southeast and east-west, are also recognized in Hole 1150B. In Hole 1150B, however, the lower domain (1050–1180 mbsf) has the northwest-southeast orientation rather than the upper domain as in Hole 1151A. The middle domains are similar at both sites.

Variations of structural orientations with age as well as with depth will need to be investigated postcruise, in addition to the statistical significance of these variations. At both sites the overall combined poles give a west-northwest–east-southeast dominant direction (see "Accomplishments and Interesting Observations," p. 15, in the "Leg 186 Summary" chapter).

Open Fractures

Open fractures were reoriented in the same manner as healed fractures (Table T22, also available in ASCII format). The poles to the open fractures have been divided into the same domains as discussed above (Fig. F49). The orientations of the open fractures are more scattered than those for the healed fractures, although dip angles are concentrated at about 20°.

Bedding

The tilt of bedding planes at Site 1151 differs from that of those observed below ~800 mbsf at Site 1150. Above this depth the bedding is nearly horizontal. Below 900 mbsf most bedding planes dip more than 10°, with the dip increasing gradually downhole (Fig. F50B; Table T23, also available in ASCII format). The reoriented dip azimuths of the bedding plane point dominantly to the east (Fig. F50A). Above 900 mbsf no dominant dip direction is evident, but below 900 mbsf the strata dip to the east.

Striation

We recognized clear striations that indicate the direction of fault movement on a few fracture planes. The number of planes with striations represents only a small fraction of all the fracture planes, and the planes with striations are more common below Core 186-1151A-94R, where the recovery rate of core decreased. In most cases the striations indicate that the motion along the fault is in the reverse sense.

F47. Downhole variation in dip azimuths of healed fracture planes in Hole 1151A, divided into three subdomains, p. 93.

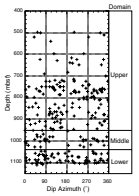

F48. Contour diagram of poles of healed fracture planes in Hole 1151A, p. 94.

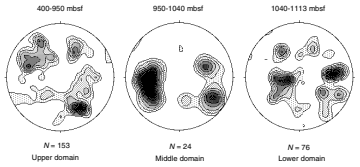

T22. Orientations of open fractures, Hole 1151A, p. 124.

F49. Contour diagram of poles to the open fracture planes in Hole 1151A, p. 95.

F50. Bedding orientation from Hole 1151A, p. 96.

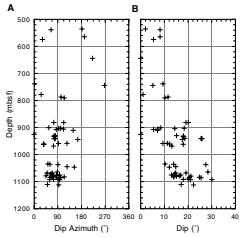

T23. Orientations of bedding planes, Hole 1151A, p. 125.

REFERENCES

Backman, J., and Raffi, I., 1997. Calibration of Miocene nannofossil events to orbitally tuned cyclostratigraphies from Ceara Rise. *In* Shackleton, N.J., Curry, W.B., Richter, C., and Bralower, T.J. (Eds.), *Proc. ODP, Sci. Results,* 154: College Station, TX (Ocean Drilling Program), 83–99.

Berner, R.A., 1980. *Early Diagenesis: A Theoretical Approach:* Princeton, NJ (Princeton Univ. Press).

Blum, P., 1997. Physical Properties Handbook–A guide to the shipboard measurement of physical properties of deep-sea cores by the Ocean Drilling Program, *ODP Technical Note,* 26.

Claypool, G.E., and Kaplan, I.R., 1974. The origin and distribution of methane in marine sediments. *In* Kaplan, I.R. (Ed.), *Natural Gases in Marine Sediments:* New York (Plenum), 99–139.

Handa, N., and Tanoue, E., 1980, Organic matter in the Bering Sea and adjacent areas. *In* Hood, D.W., and Calder, J.A. (Eds.), *The Eastern Bering Sea Shelf: Oceanography and Resources* (Vol. 1): Seattle (NOAA), 359–381.

Kagami, H., Karig, D.E., Coulbourn, W.T., et al., 1986. *Init. Repts. DSDP,* 87: Washington (U.S. Govt. Printing Office).

Koizumi, I., 1992. Diatom biostratigraphy of the Japan Sea: Leg 127. *In* Pisciotto, K.A., Ingle, J.C., Jr., von Breymann, M.T., Barron, J., et al., *Proc. ODP, Sci. Results,* 127/128 (Pt. 1): College Station, TX (Ocean Drilling Program), 249–289.

Koizumi, I., and Tanimura, Y., 1985. Neogene diatom biostratigraphy of the middle latitude western North Pacific, Deep Sea Drilling Project Leg 86. *In* Heath, G.R., Burckle, L.H., et al., *Init. Repts. DSDP,* 86: Washington (U.S. Govt. Printing Office), 269–300.

Müller, P.J., 1977. C/N ratios in Pacific deep sea sediments: effect of inorganic ammonium and organic nitrogen compounds sorbed by clays. *Geochim. Cosmochim. Acta,* 41:765–776.

Rio, D., Fornaciari, E., and Raffi, I., 1990. Late Oligocene through early Pleistocene calcareous nannofossils from western equatorial Indian Ocean (Leg 115). *In* Duncan, R.A., Backman, J., Peterson, L.C., et al., *Proc. ODP, Sci. Results,* 115: College Station, TX (Ocean Drilling Program), 175–235.

Scientific Party, 1980. *Init. Repts. DSDP,* 56, 57: Washington (U. S. Govt. Printing Office).

Shackleton, N.J., Crowhurst, S., Hagelberg, T., Pisias, N.G., and Schneider, D.A., 1995. A new late Neogene time scale: application to Leg 138 sites. *In* Pisias, N.G., Mayer, L.A., Janecek, T.R., Palmer-Julson, A., and van Andel, T.H. (Eds.), *Proc. ODP, Sci. Results,* 138: College Station, TX (Ocean Drilling Program), 73–101.

Tyson, R.V., 1995. *Sedimentary Organic Matter: Organic Facies and Palynofacies:* London (Chapman & Hall).

von Huene, R., Klaeschen, D., Cropp, B., and Miller, J., 1994. Tectonic structure across the accretionary and erosional parts of the Japan Trench margin. *J. Geophys. Res.,* 99:22349–22361.

Yanagisawa, Y., and Akiba, F., 1990. Taxonomy and phylogeny of the three marine diatom genera, *Crucidenticula, Denticulopsis* and *Neodenticula. Bull. Geol. Surv. Jpn.,* 41:197–301.

————, 1998. Refined Neogene diatom biostratigraphy for the northwest Pacific around Japan, with an introduction of code numbers for selected diatom biohorizons. *J. Geol. Soc. Jpn.,* 104:395–414.

Figure F1. Map of the Japan Trench area off northeast Japan.

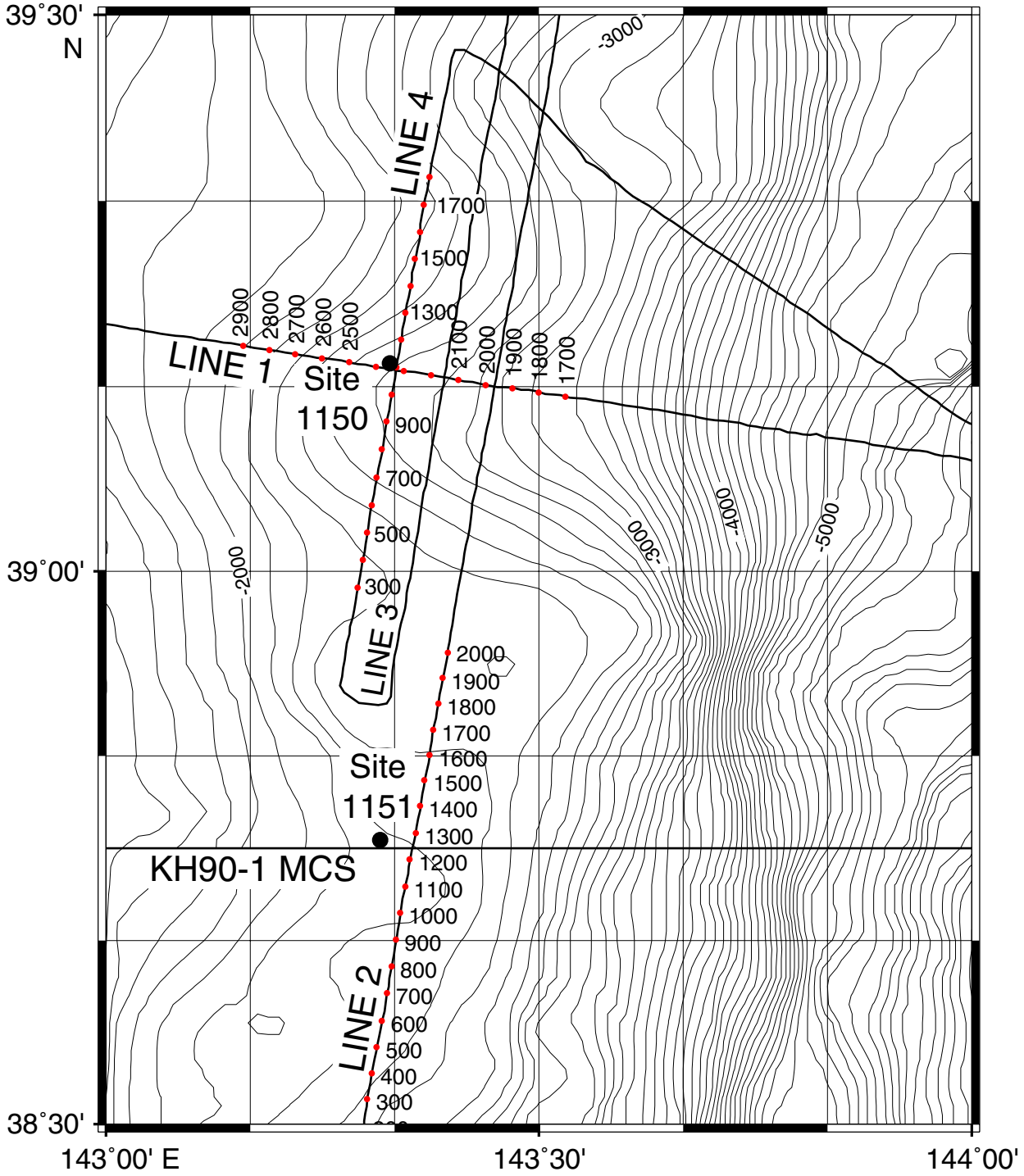

Figure F2. Seismic reflection profile section crossing near Site 1151 in an east-west direction.

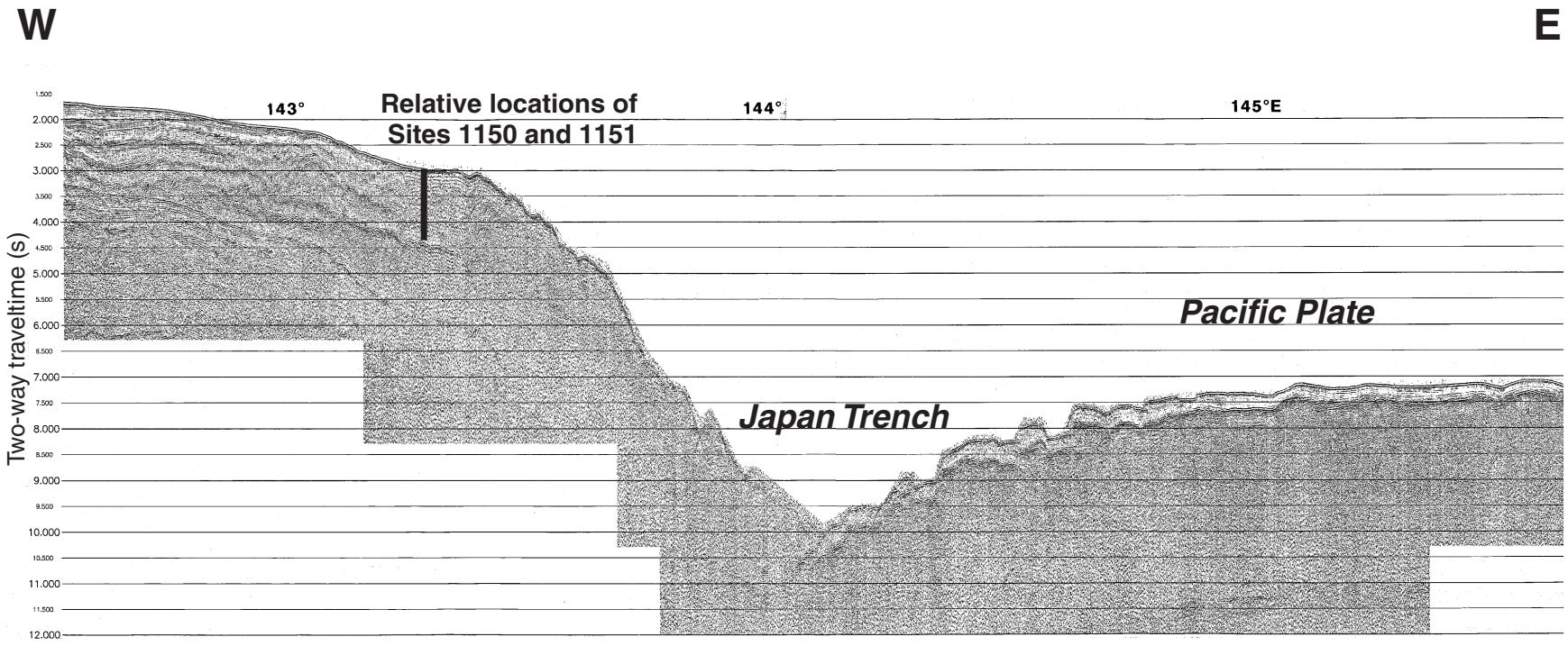

Figure F3. Seismic reflection profile section from seismic Line KH96-3, Line 2, crossing near Site 1151 in a north-south direction.

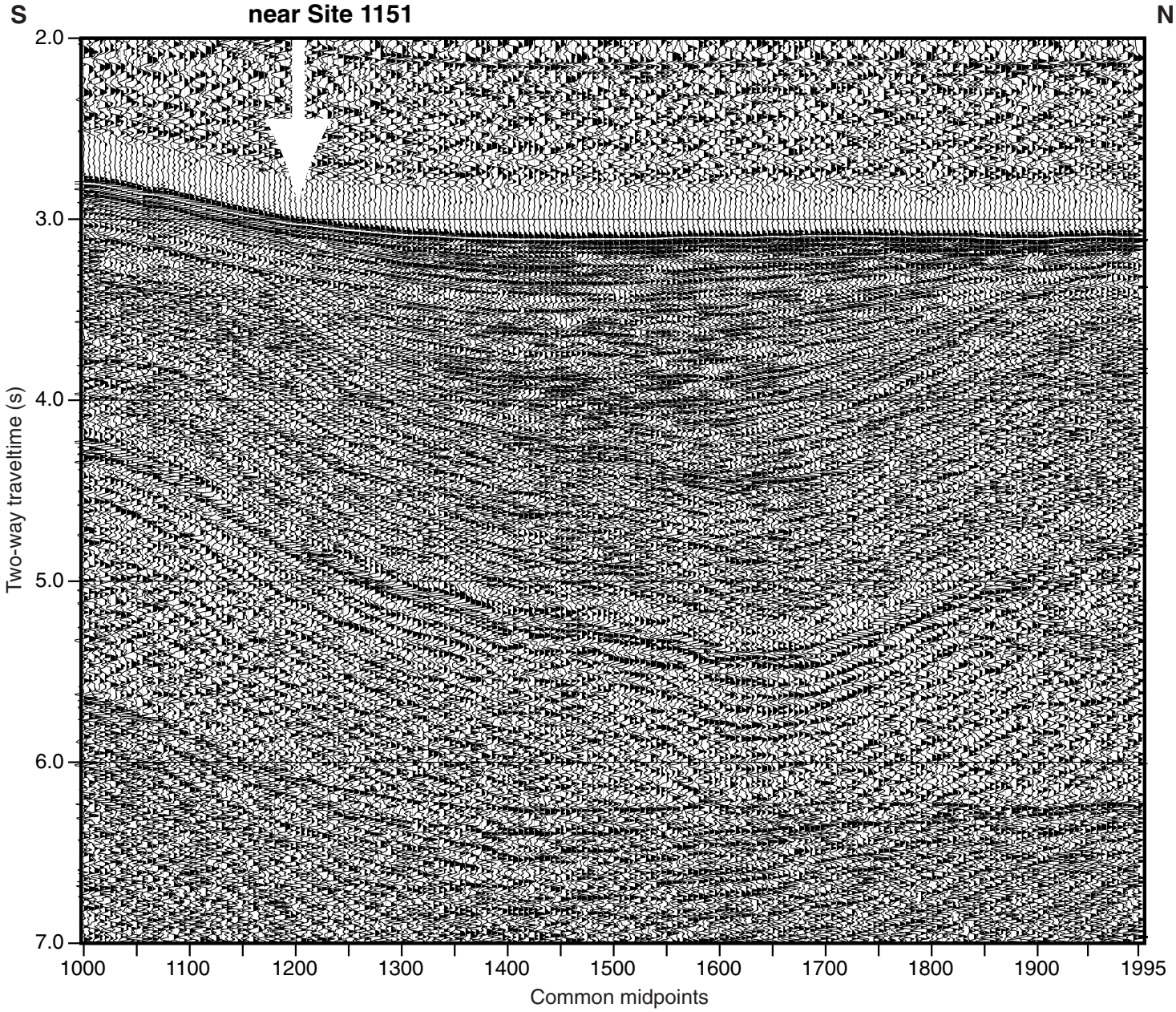

Figure F4. Schematic of borehole installation at Site 1151. The depths listed are those of the final installation in Hole 1151B.

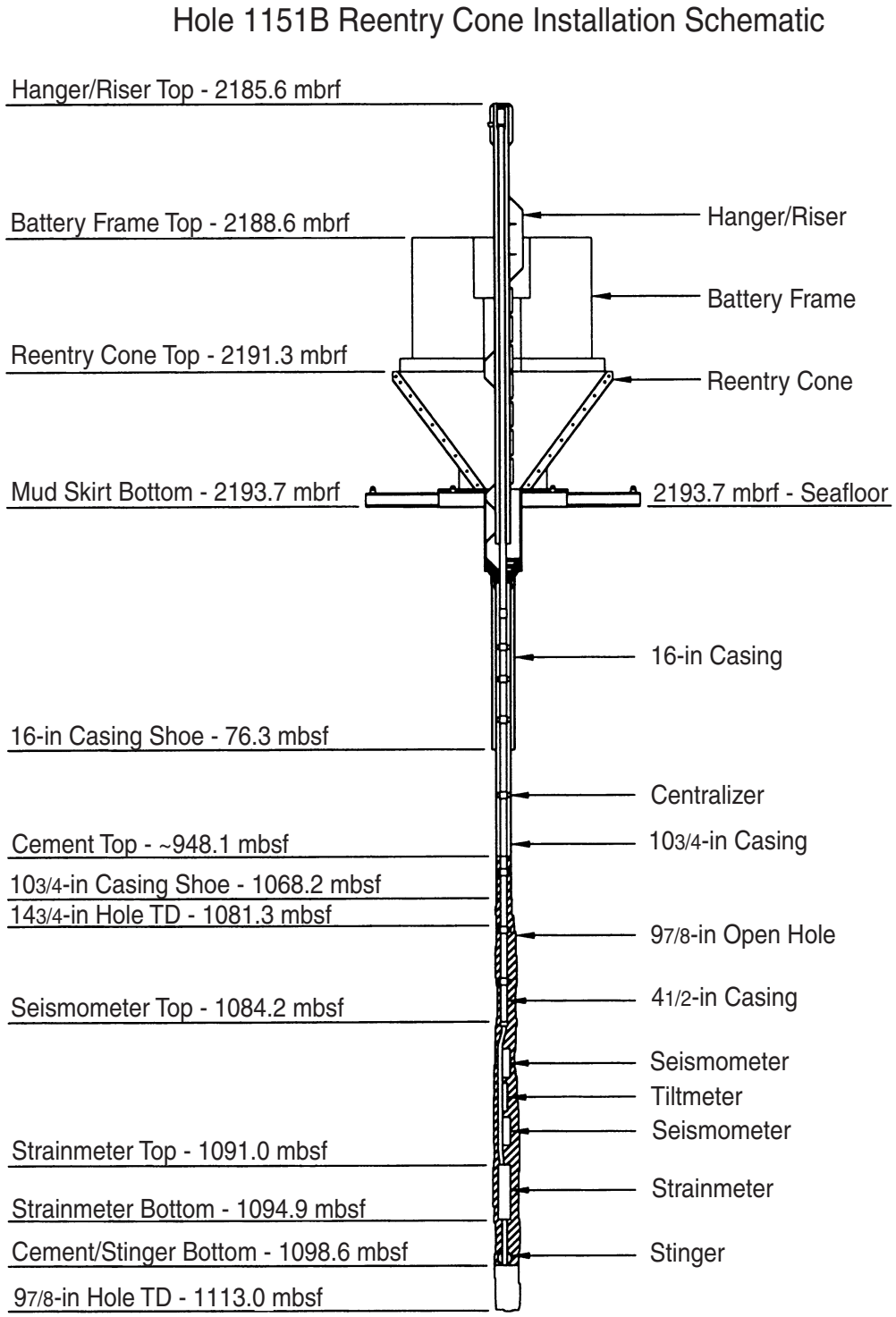

Figure F5. Site 1151 lithologic units. (Continued on next page.)

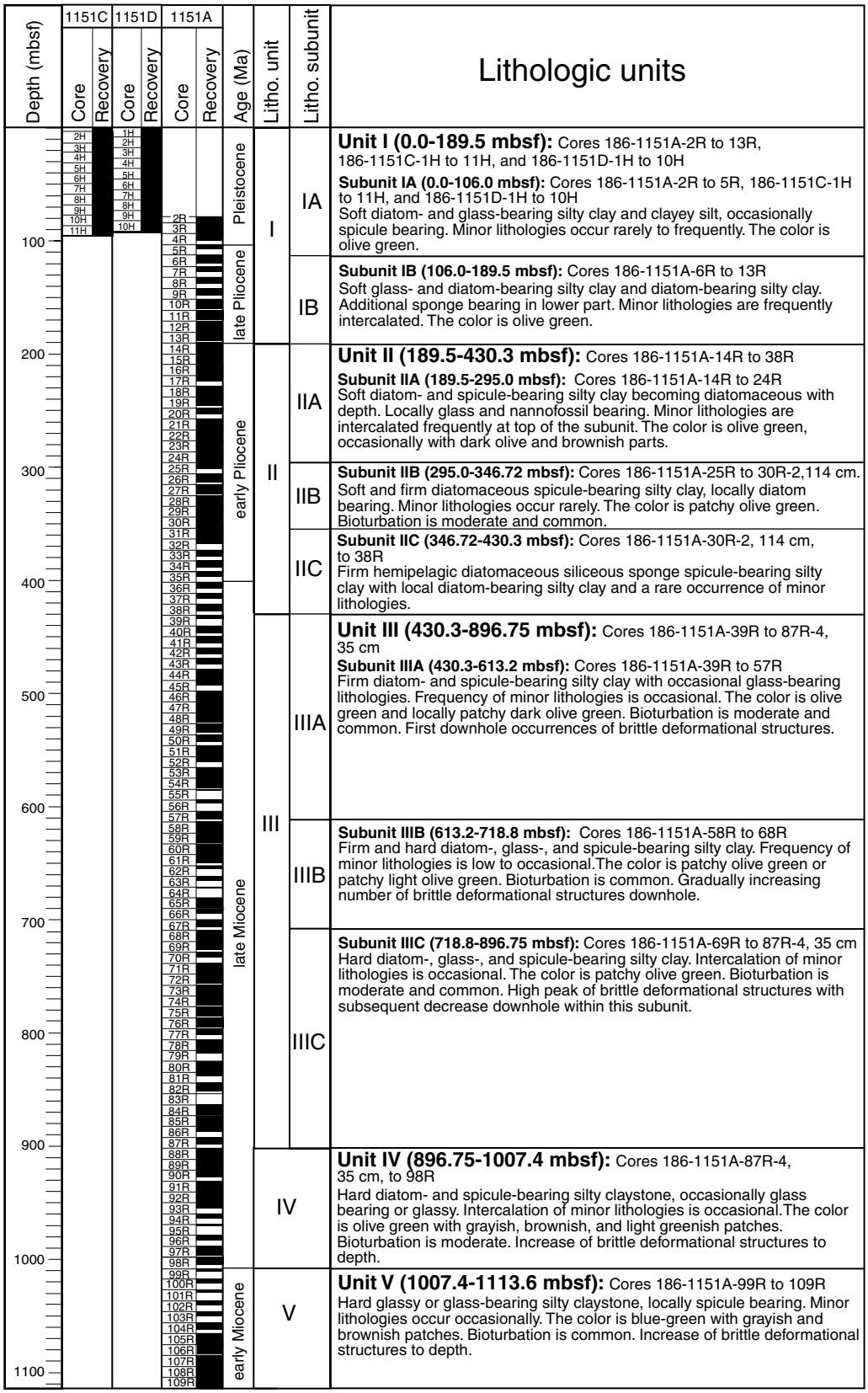

Figure F5 (continued).

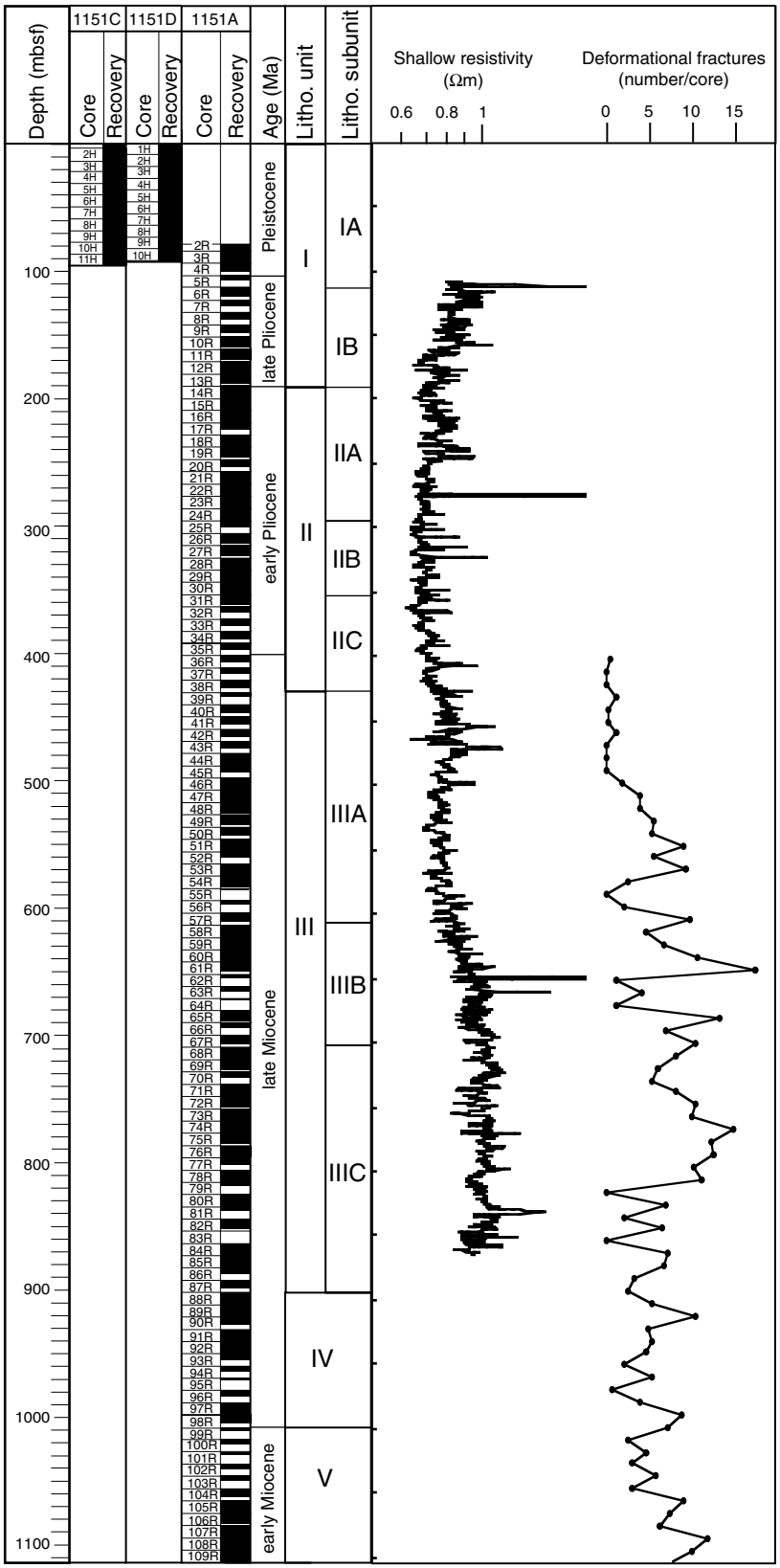

Figure F6. Variation of L*, a*, and b* values from handheld color reflectance measurement.

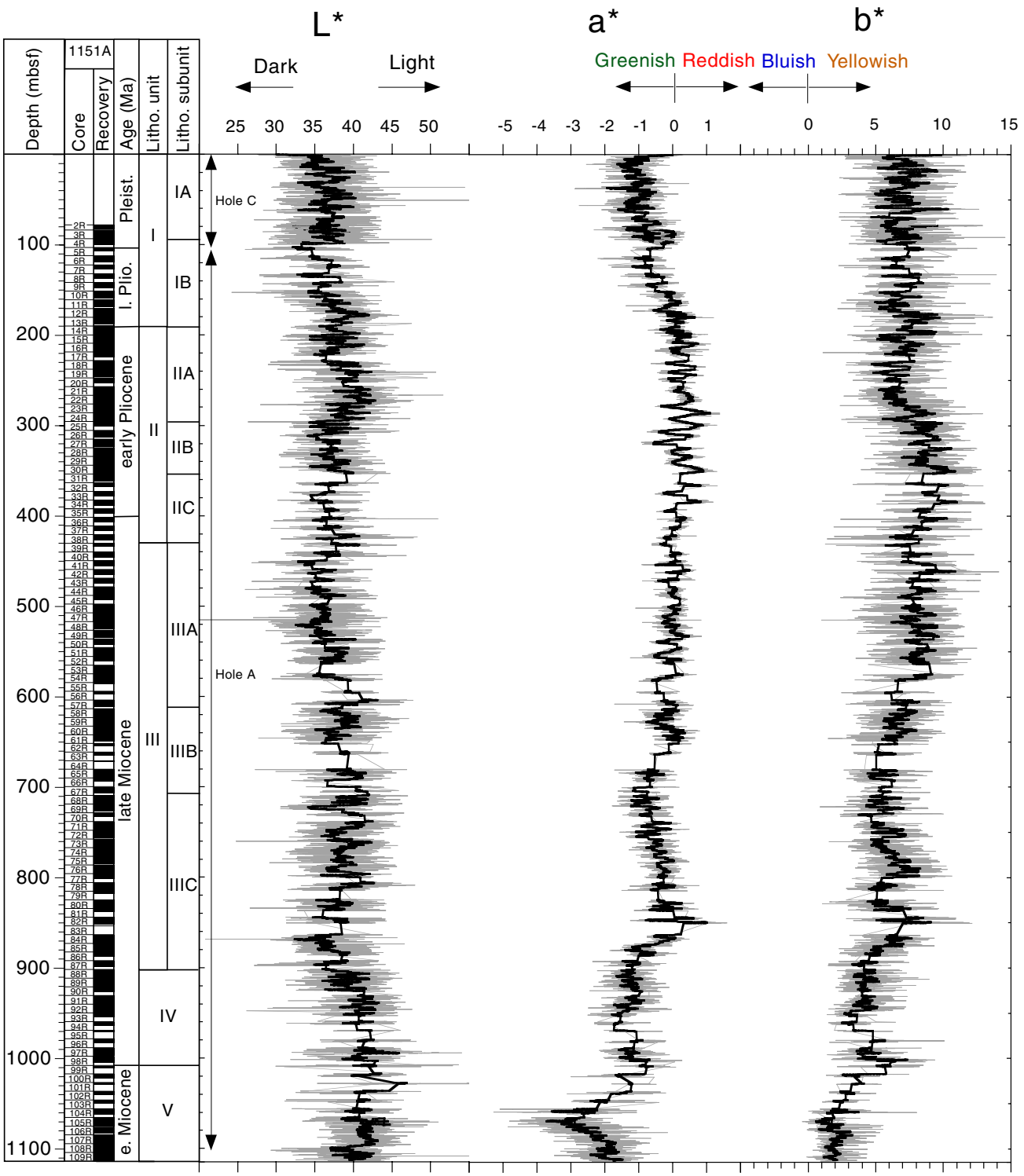

Figure F7. Occurrence of volcanogenic minor lithologies at Site 1151. From left, columns include magnetic susceptibility; recovered intervals of tephra, reworked tephra, bioturbated tephra patches, and pumice grains and layers (each bar shows recovered interval in mbsf); number of ash occurrences per recovered core without pumiceous grains and layers; number of primary and reworked ash layers per recovered core; number of bioturbated ash layers per recovered core; numbers of pumiceous grains and layers per recovered core, and core recovery. (**Figure shown on next page.**)

Figure F7. (Caption on previous page.)

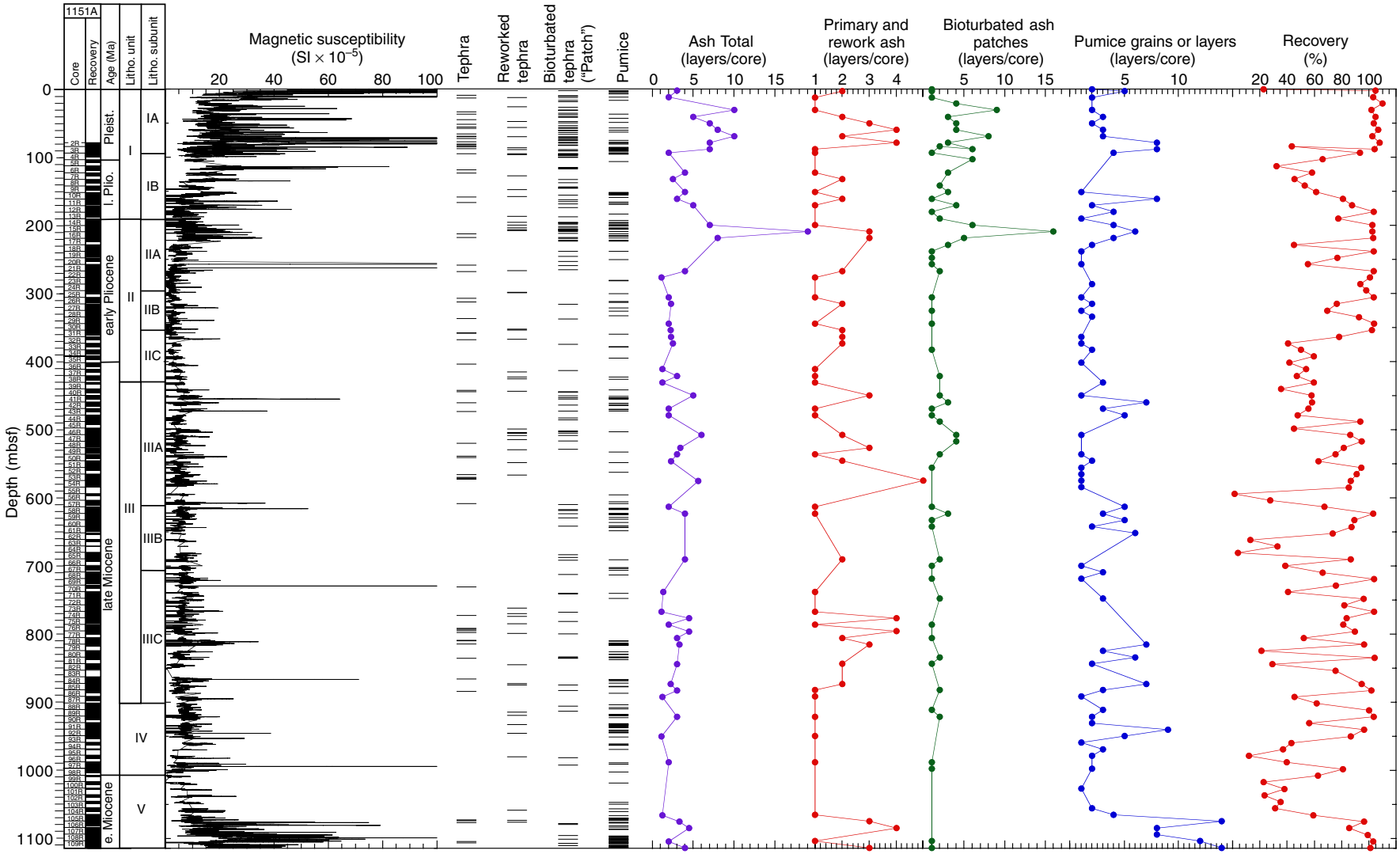

Figure F8. Number of sandy and silty layers and patches at Site 1151. From left, columns include magnetic susceptibility, total number of sandy and silty layers per recovered core, number of sandy layers per recovered core, number of sandy patches and accumulations per recovered core, number of silty layers per recovered core, number of silty patches and accumulations per recovered core, and core recovery.

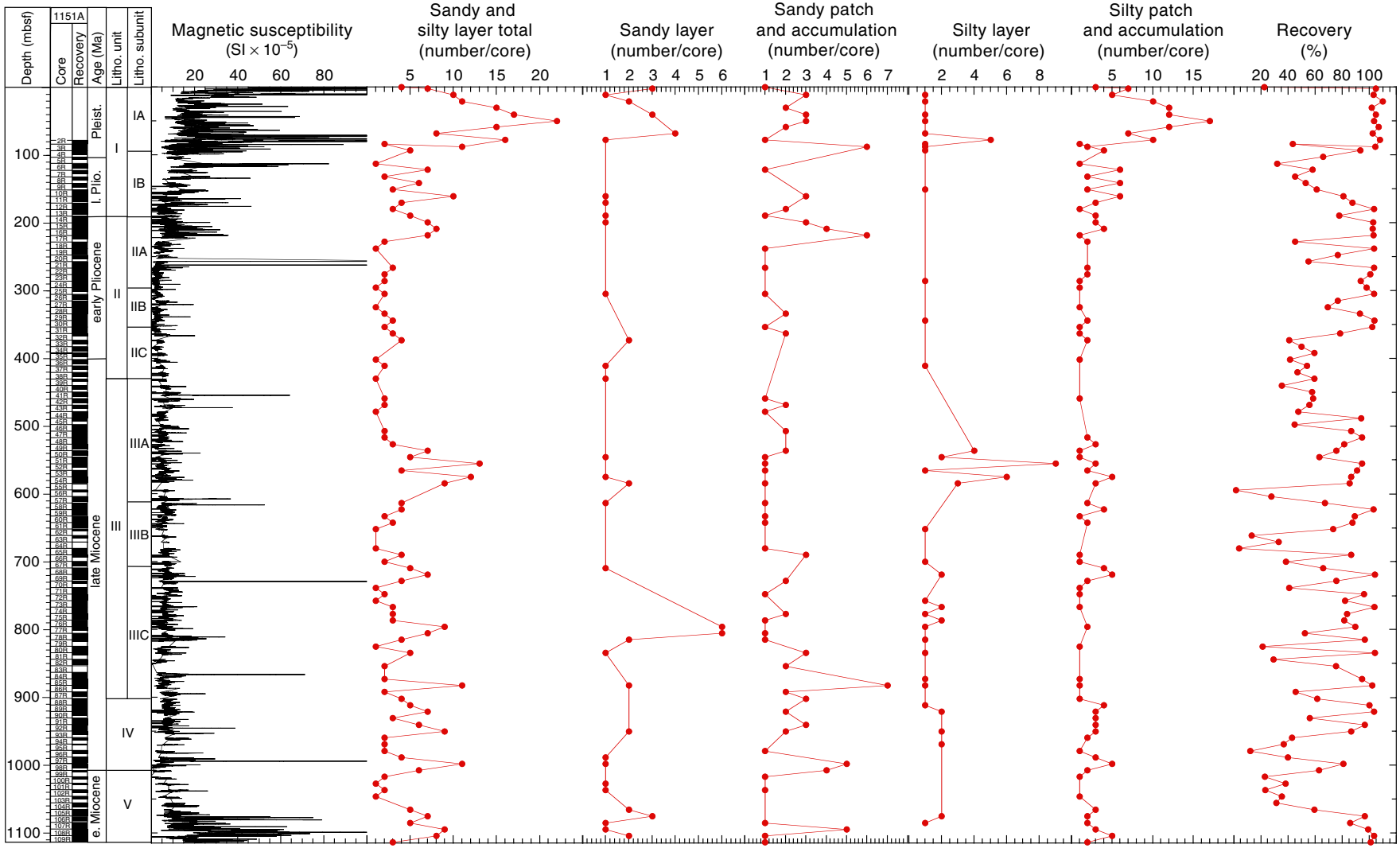

Figure F9. Downhole variations of components from smear-slide observations. **A.** Percentages of the three main constituent components (biogenic, siliciclastic, and volcaniclastic) in major lithologies at Site 1151. **B.** Variations of biogenic components of major lithologies estimated by smear-slide observation.

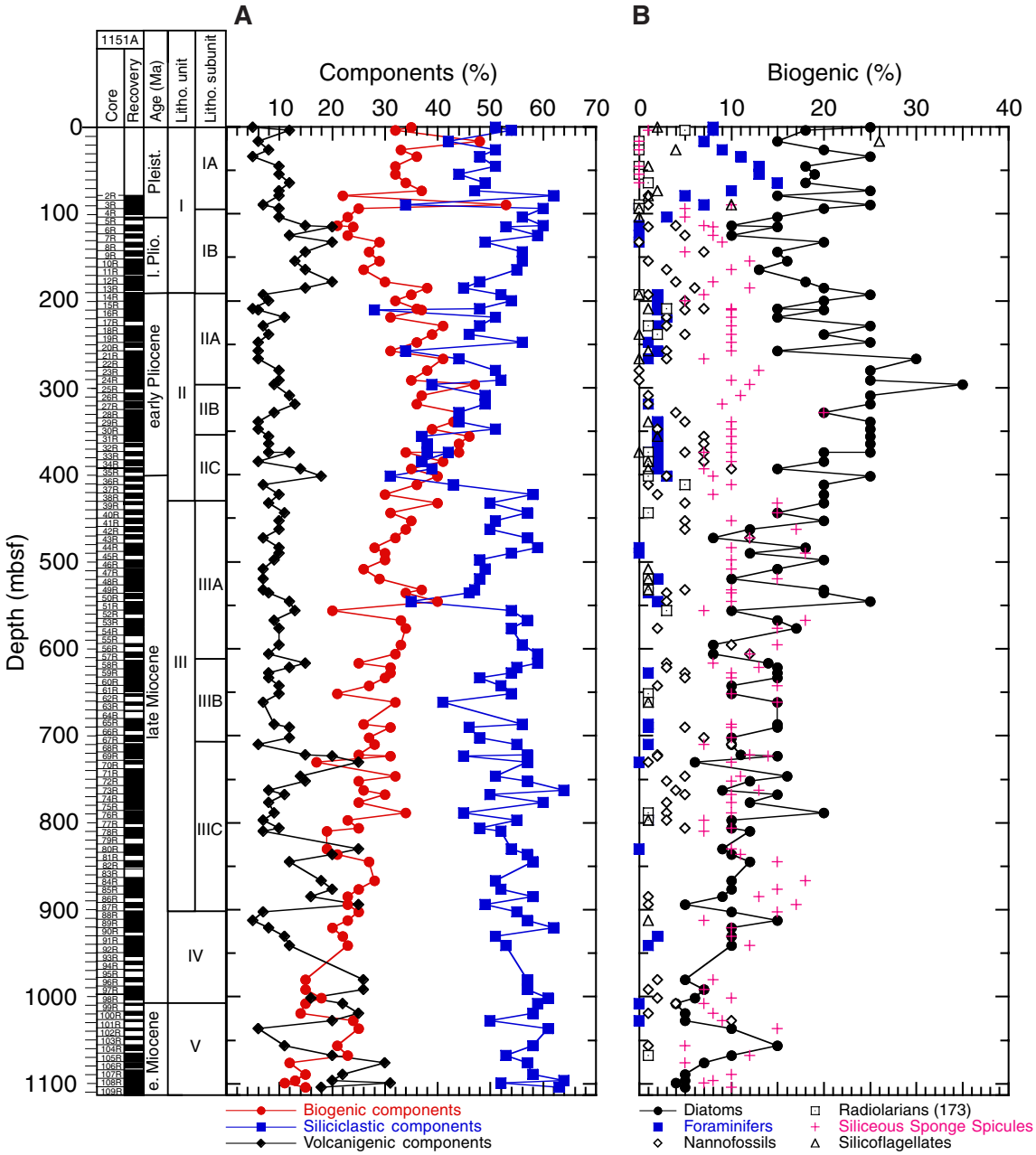

Figure F10. The variations of major minerals by XRD analysis. Depth-series data are compiled as XRD intensities for each mineral. (Continued on next two pages.)

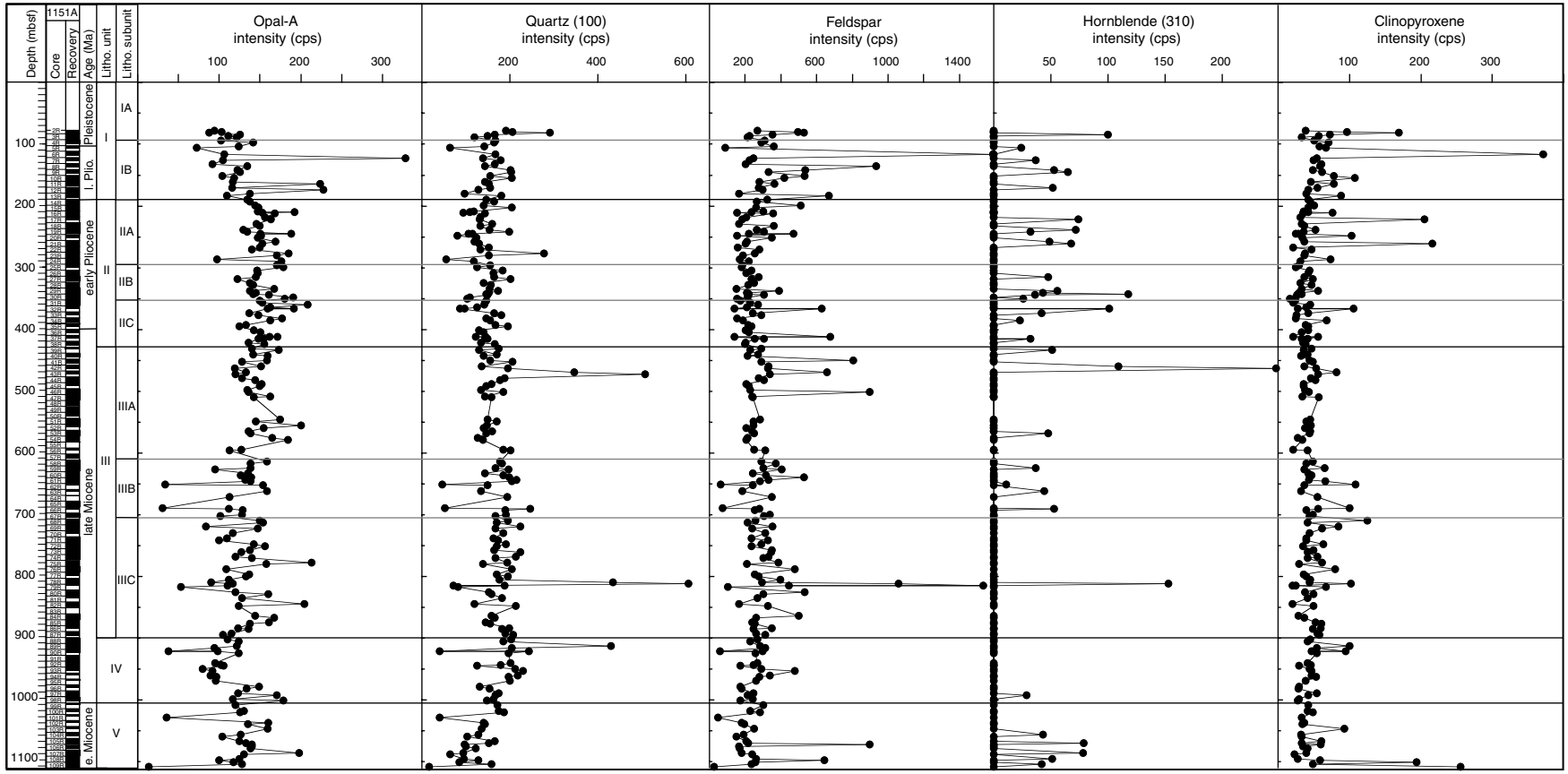

Figure F10 (continued).

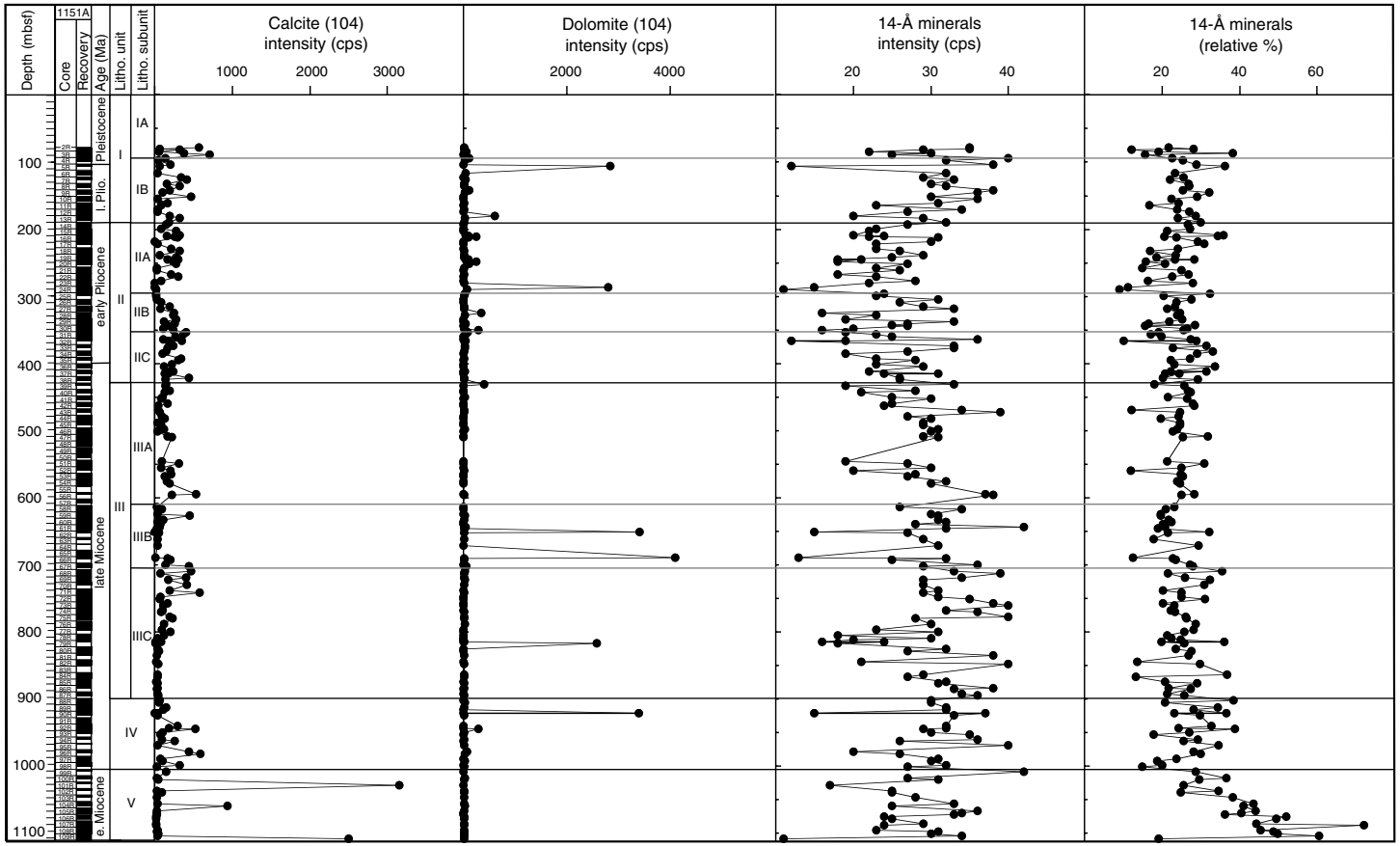

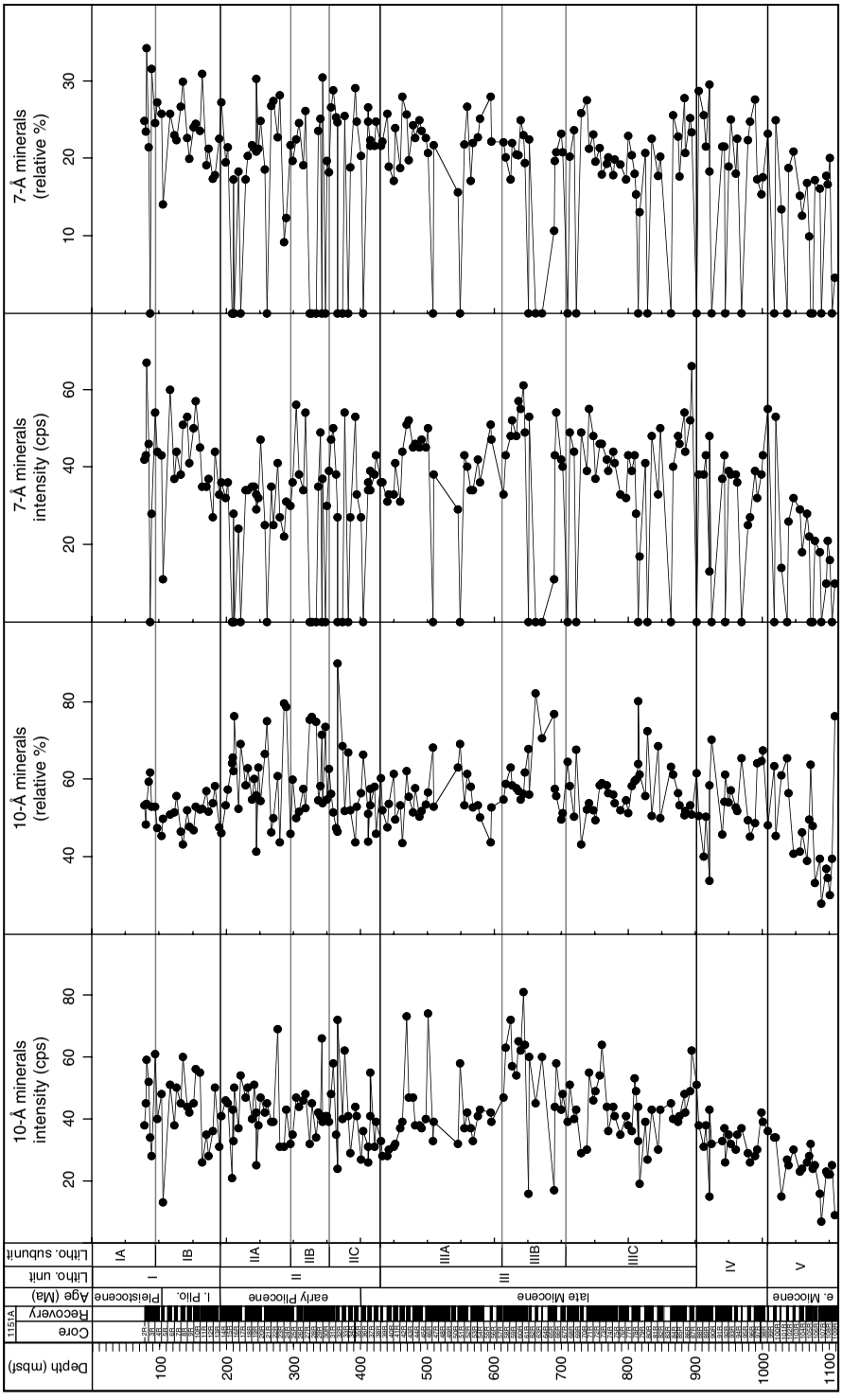

Figure F10 (continued).

Figure F11. Photograph showing typical siliceous sponge aggregates (interval 186-1151A-80R-3, 110–123 cm).

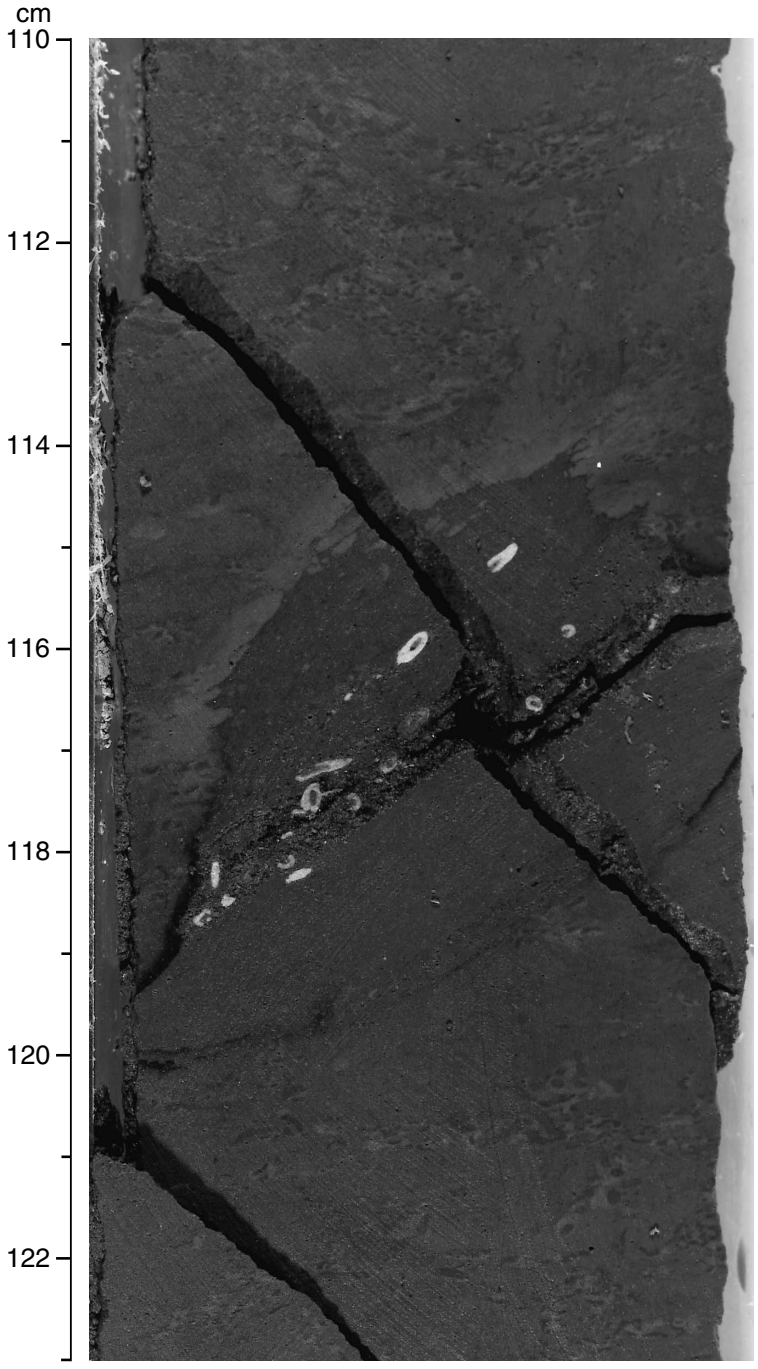

Figure F12. Photograph showing typical glauconitic sand-scattering intervals recovered at Site 1151. In this case, glauconitic grains are found in burrows (interval 186-1151A-92R-4, 55–72 cm).

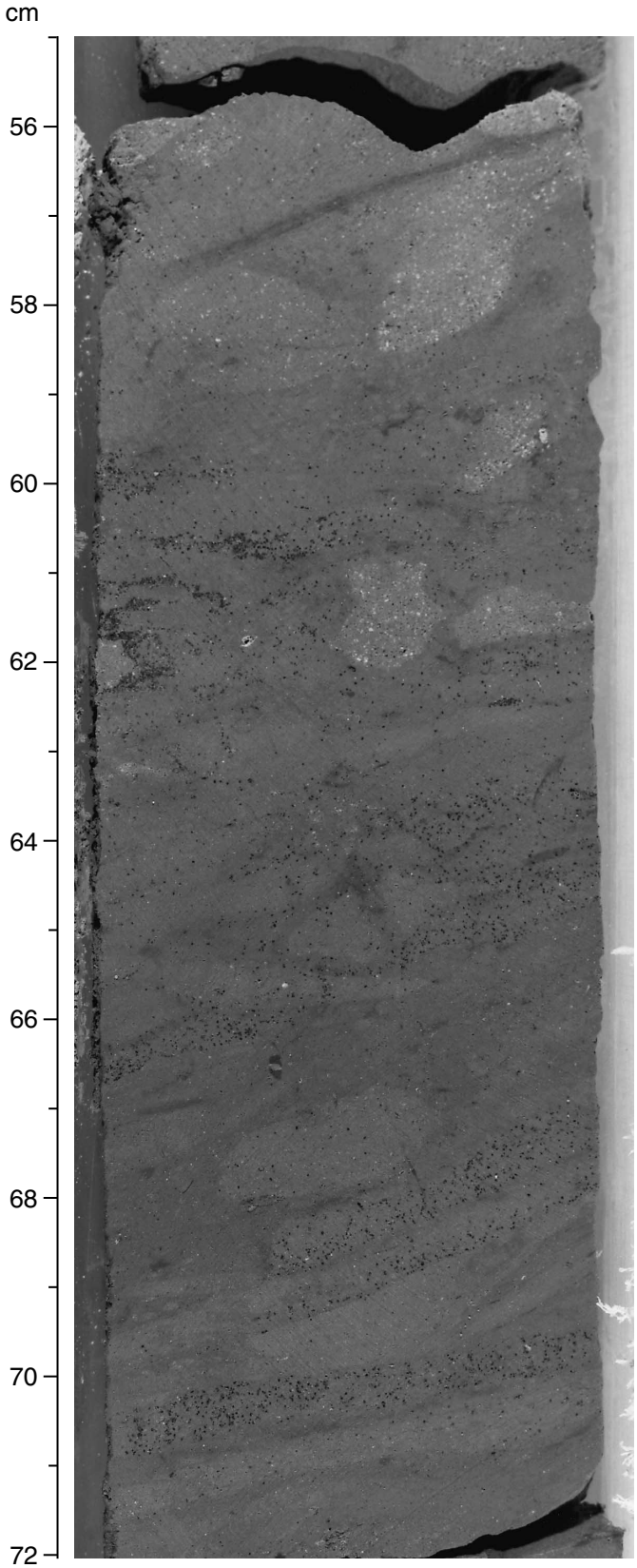

Figure F13. Photograph showing glauconitic sand-rich intervals (interval 186-1151A-78R-4, 110–135 cm).

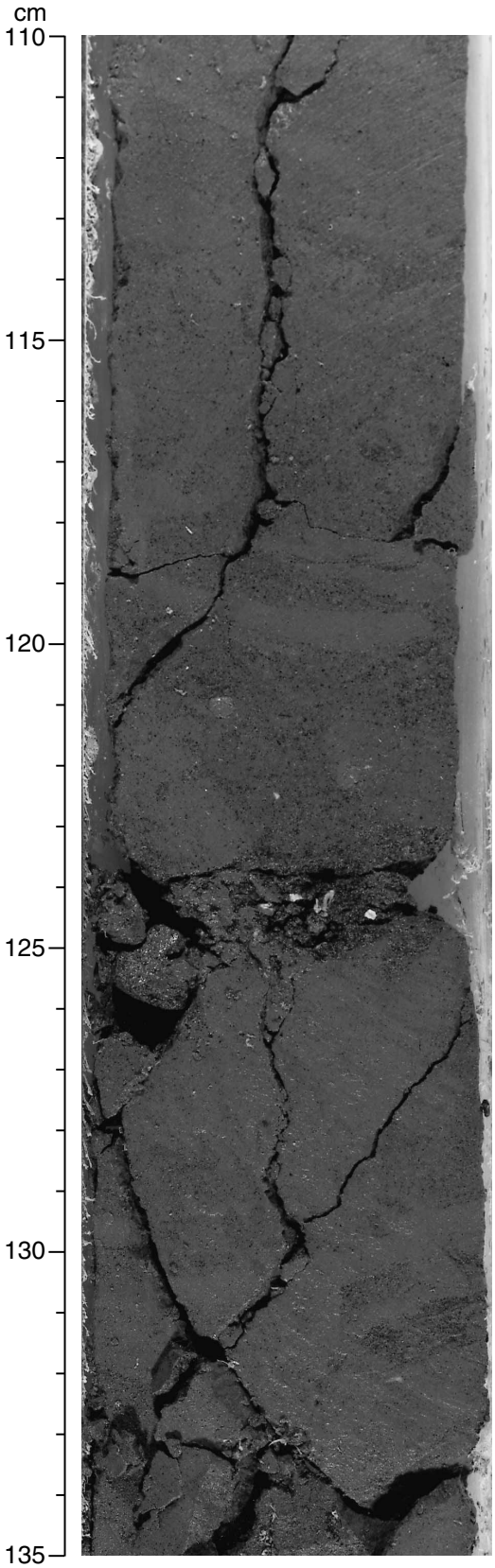

Figure F14. Photograph showing typical primary tephra (ash) layer (interval 186-1151A-6R-4, 56–65 cm).

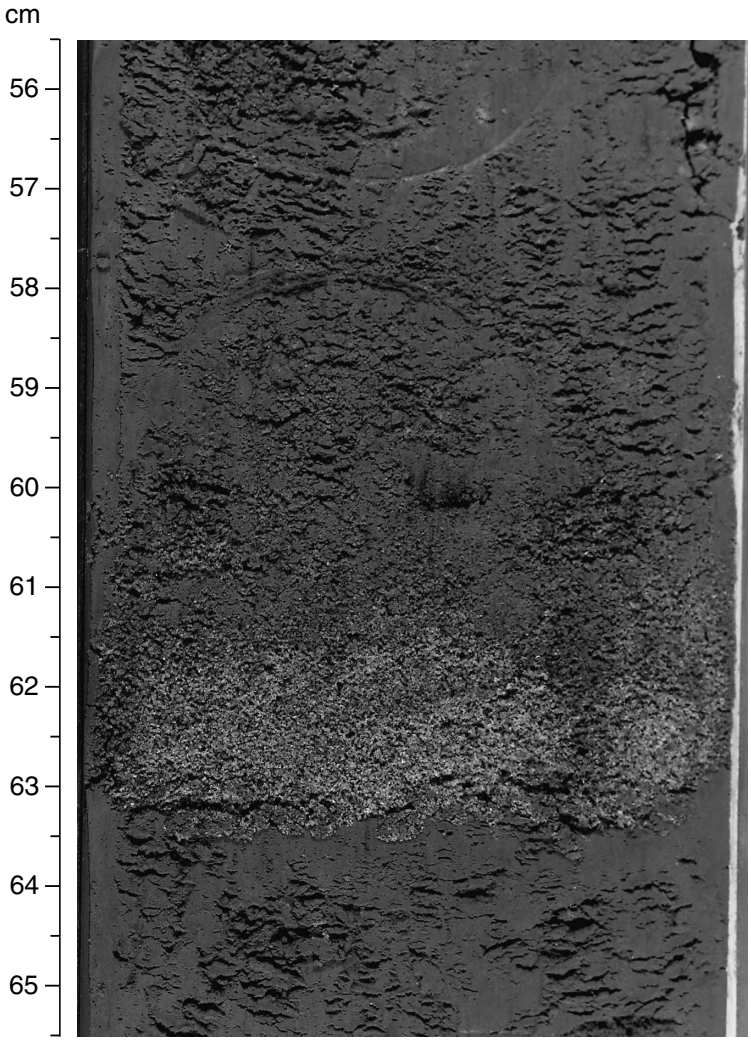

Figure F15. Photograph showing typical bioturbated tephra ("ash patches") (interval 186-1151A-11R-3, 76–88 cm).

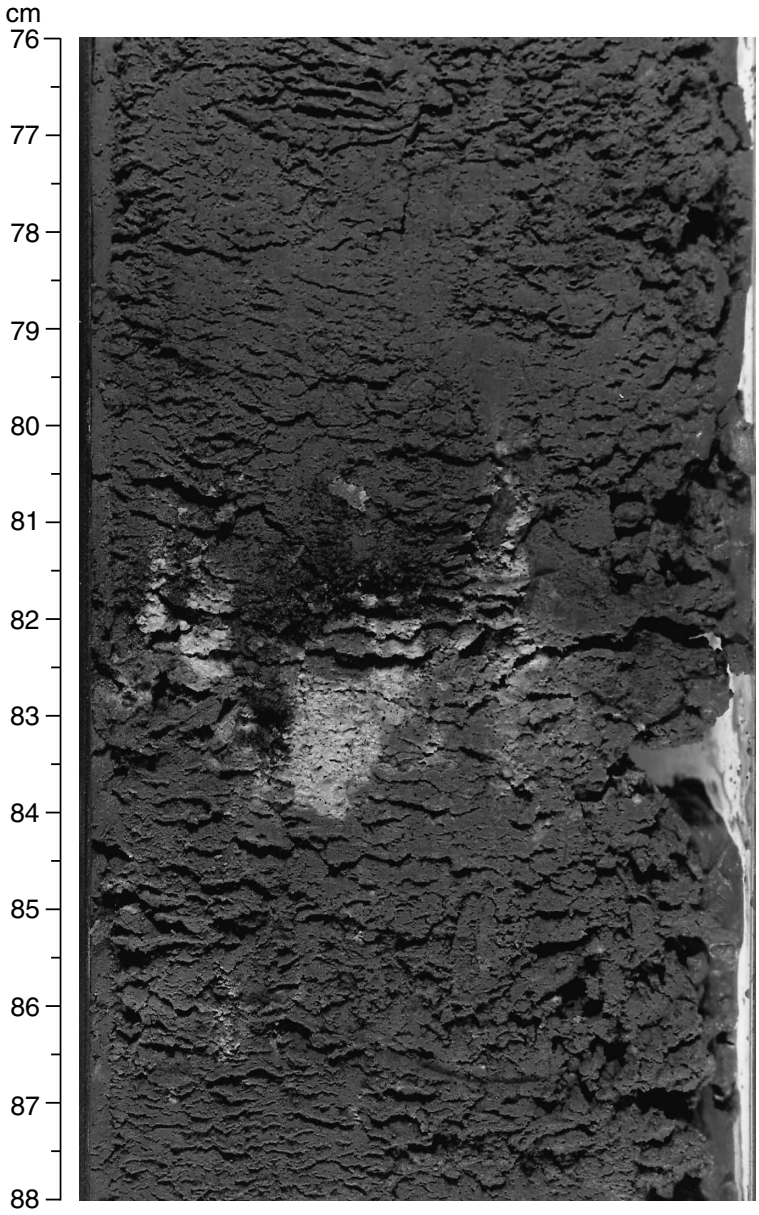

Figure F16. Photograph showing a typical dark gray surrounded pebble-sized pumice grain (interval 186-1151A-3R-4, 140–150 cm).

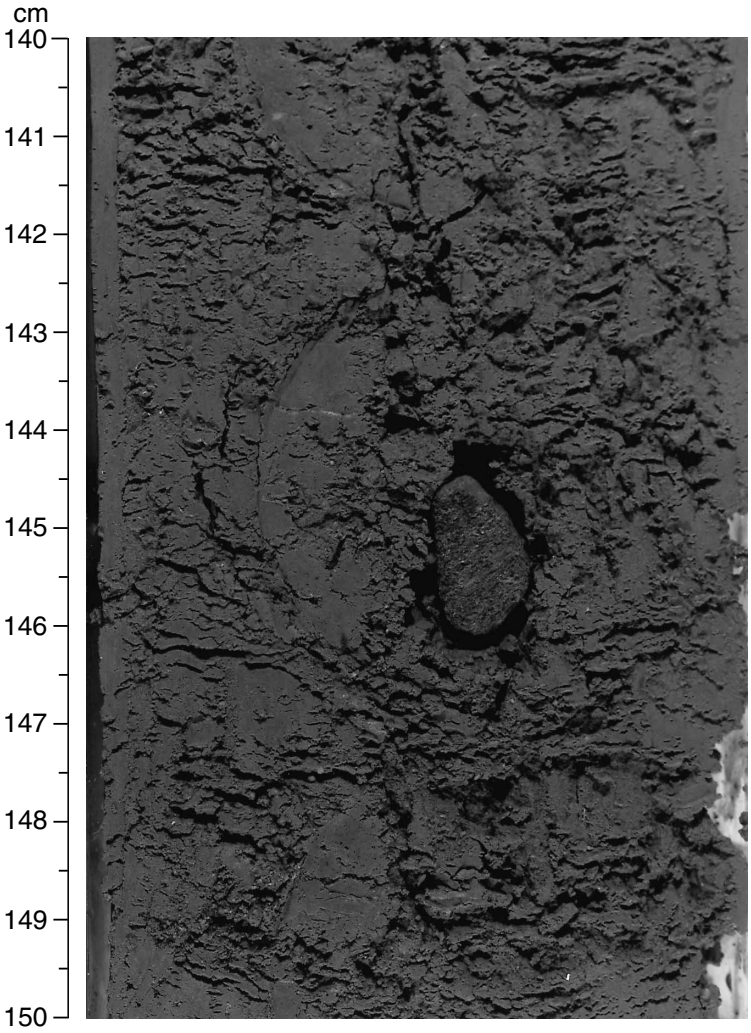

Figure F17. Photograph showing calcareous layers in minor lithology, including an upper gradational boundary of a pure calcareous layer that consists of 95% inorganic calcite based on smear-slide observation. XRD of collected samples in this interval shows that the main constituent carbonate is calcite. Several faults and joints are visible, some filled with white calcite crystals (interval 186-1151A-101R-2, 25–46 cm).

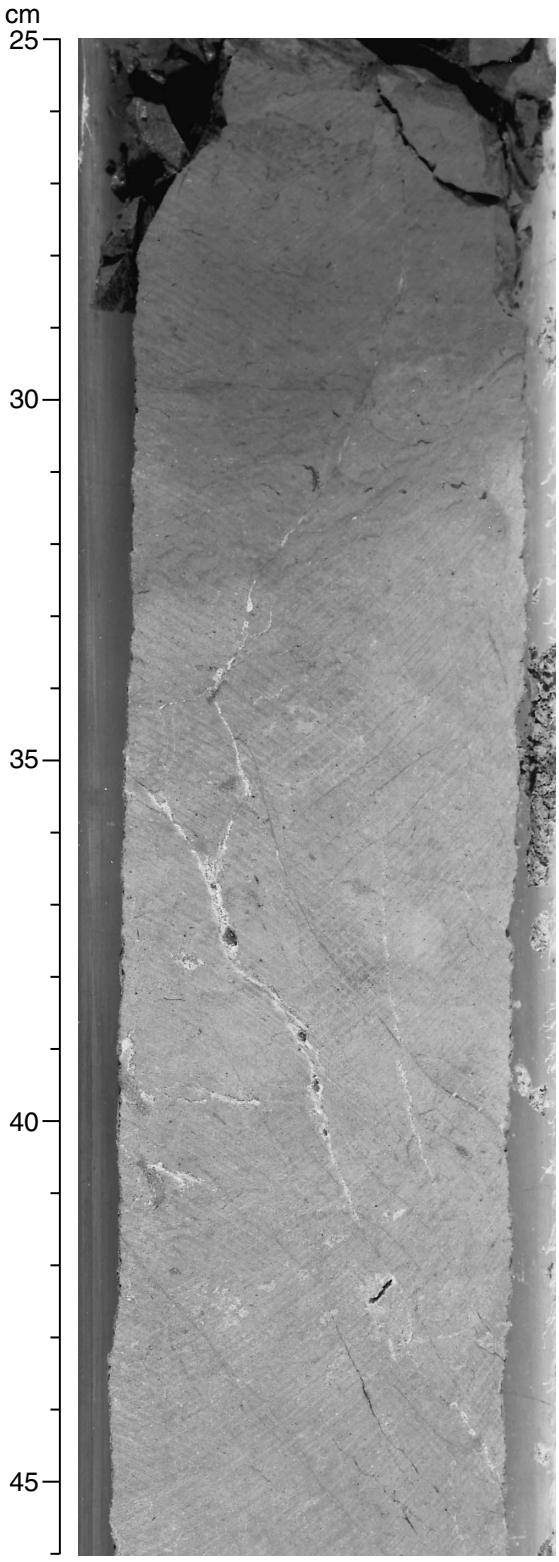

Figure F18. Photograph showing nodule-like white and light gray calcareous concretions. XRD of selected samples shows constituent minerals are calcite and dolomite (Core 186-1151A-109R).

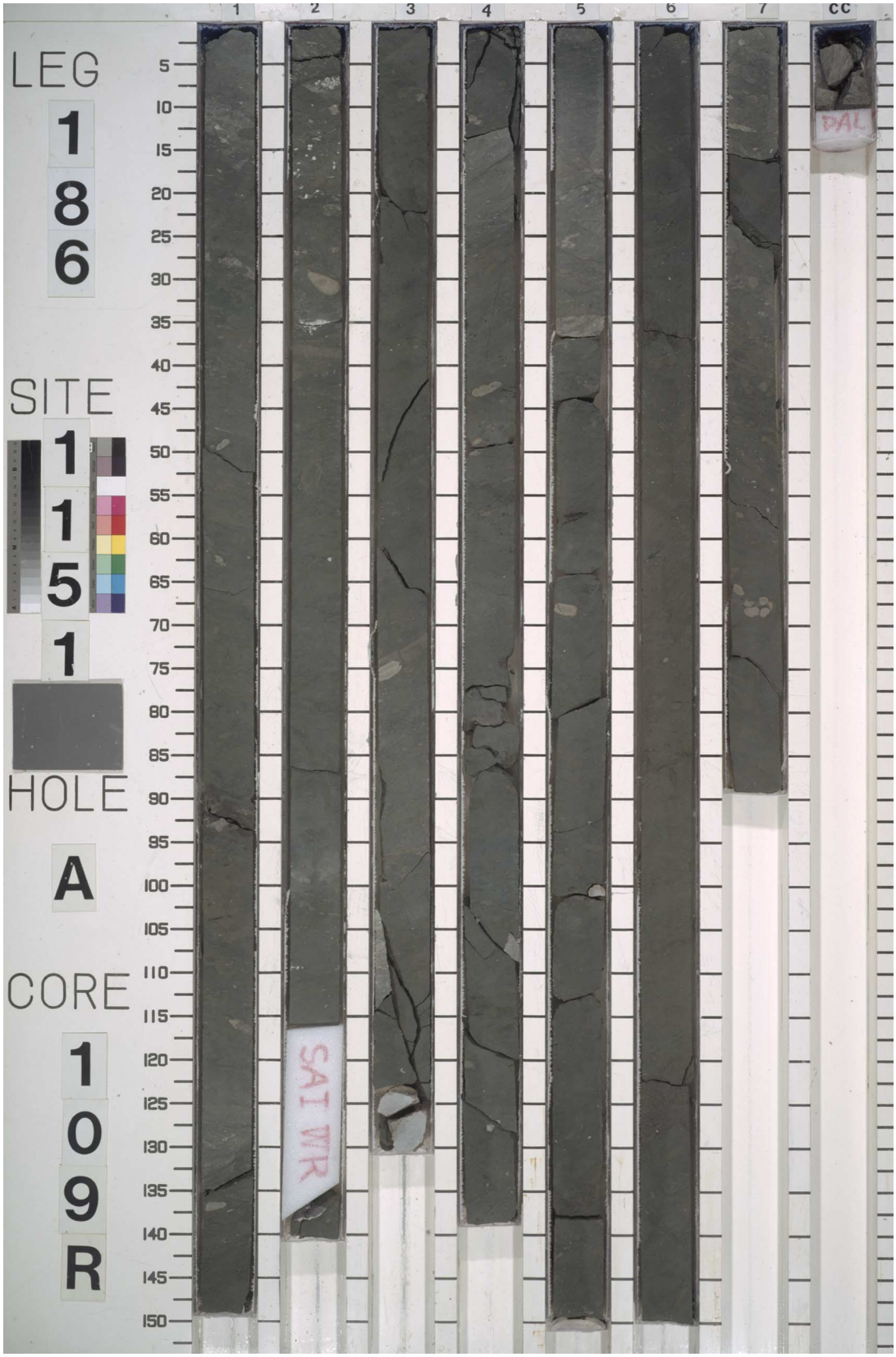

Figure F19. (**A**) Split-core inclination and (**B**) intensity of magnetization after 30 mT AF demagnetization, and (**C**) whole-core susceptibility for Hole 1151A (given in raw meter units, which can be converted to SI units by multiplying by ~0.7 × 10^{-5}). Also shown are the discrete samples (open squares) after 20 mT demagnetization.

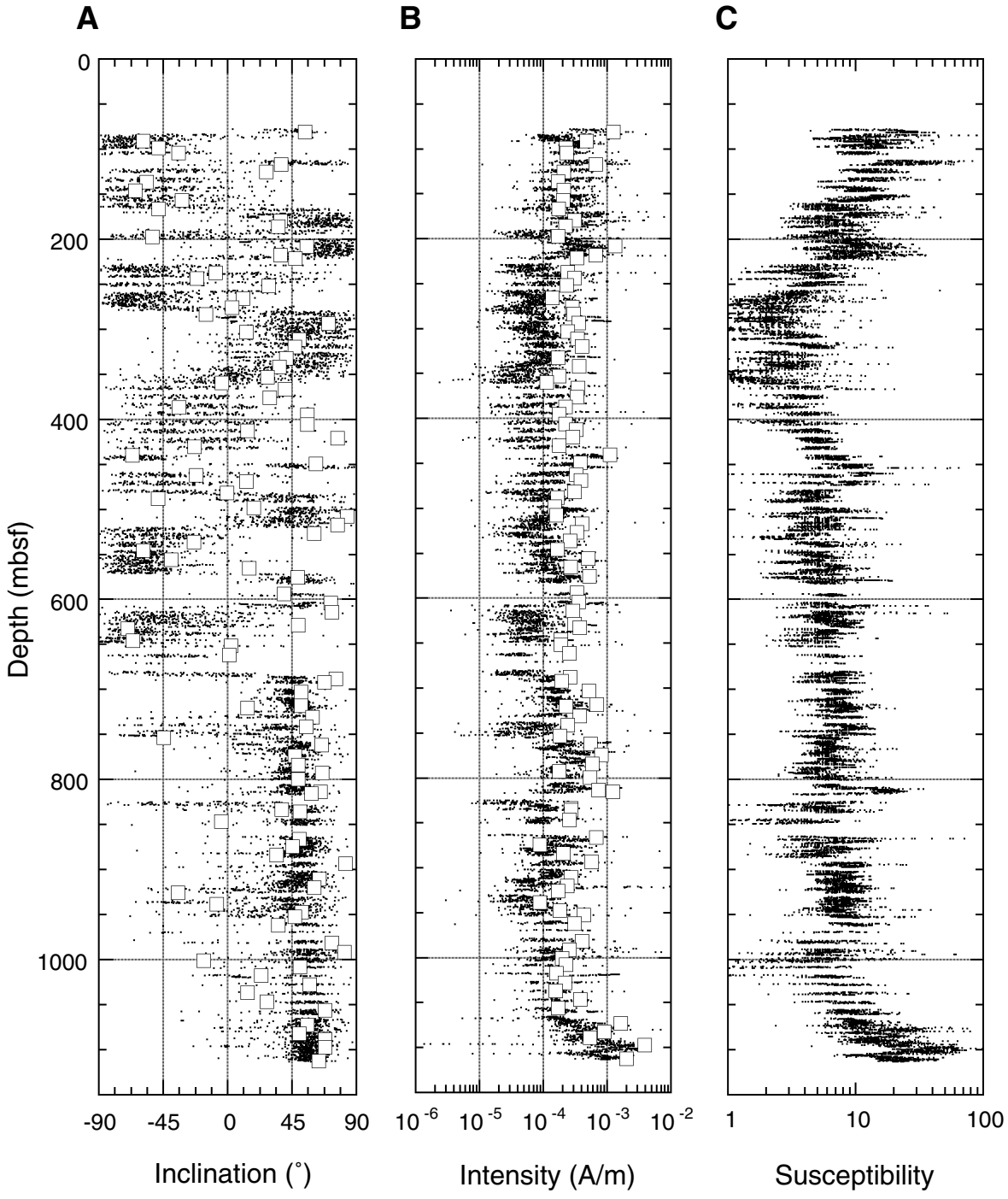

Figure F20. Split-core inclinations for Holes 1151C and 1151D after AF demagnetization at 20 mT.

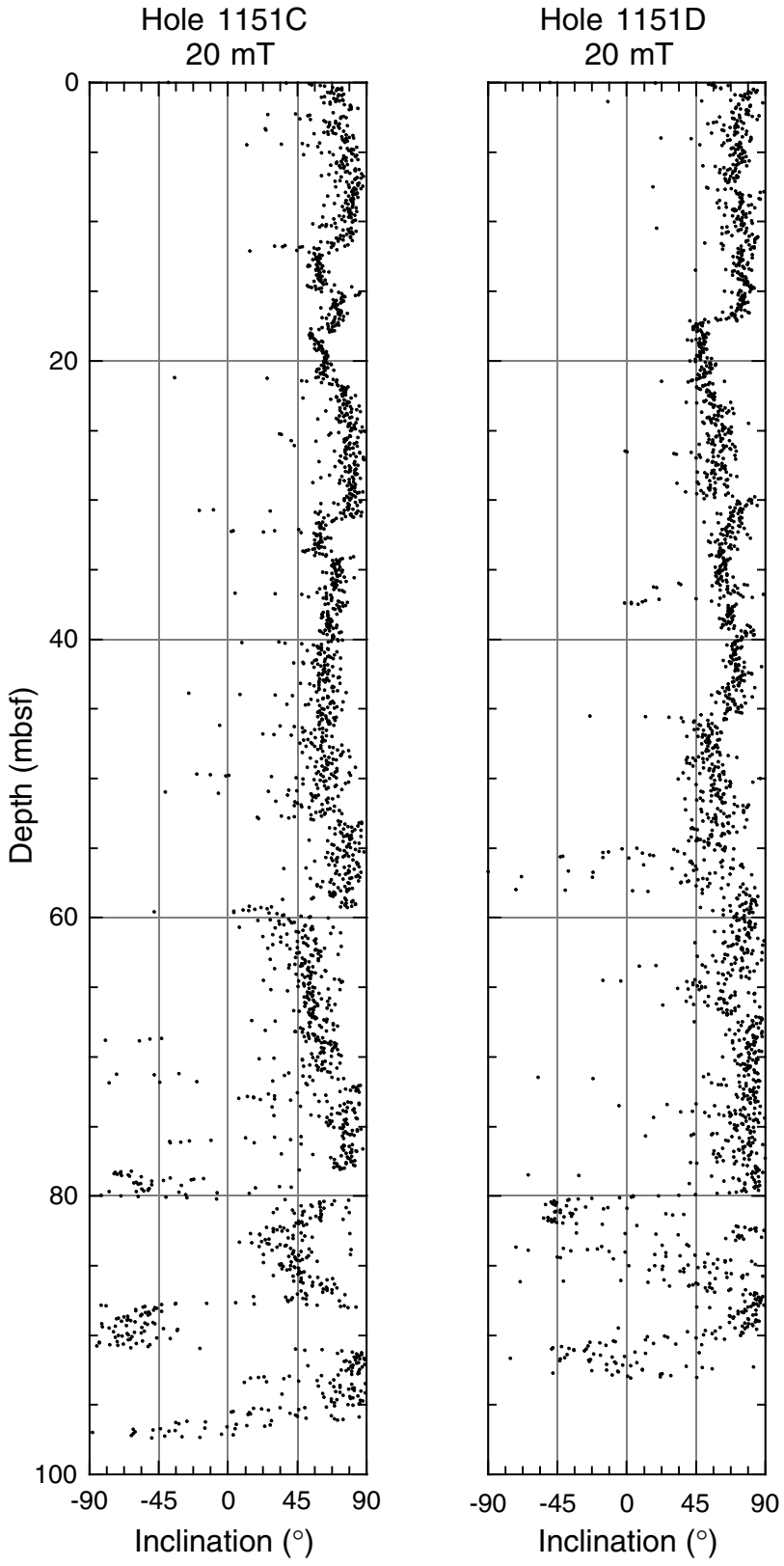

Figure F21. Split-core intensity of magnetization for Holes 1151C and 1151D after AF demagnetization at 20 mT.

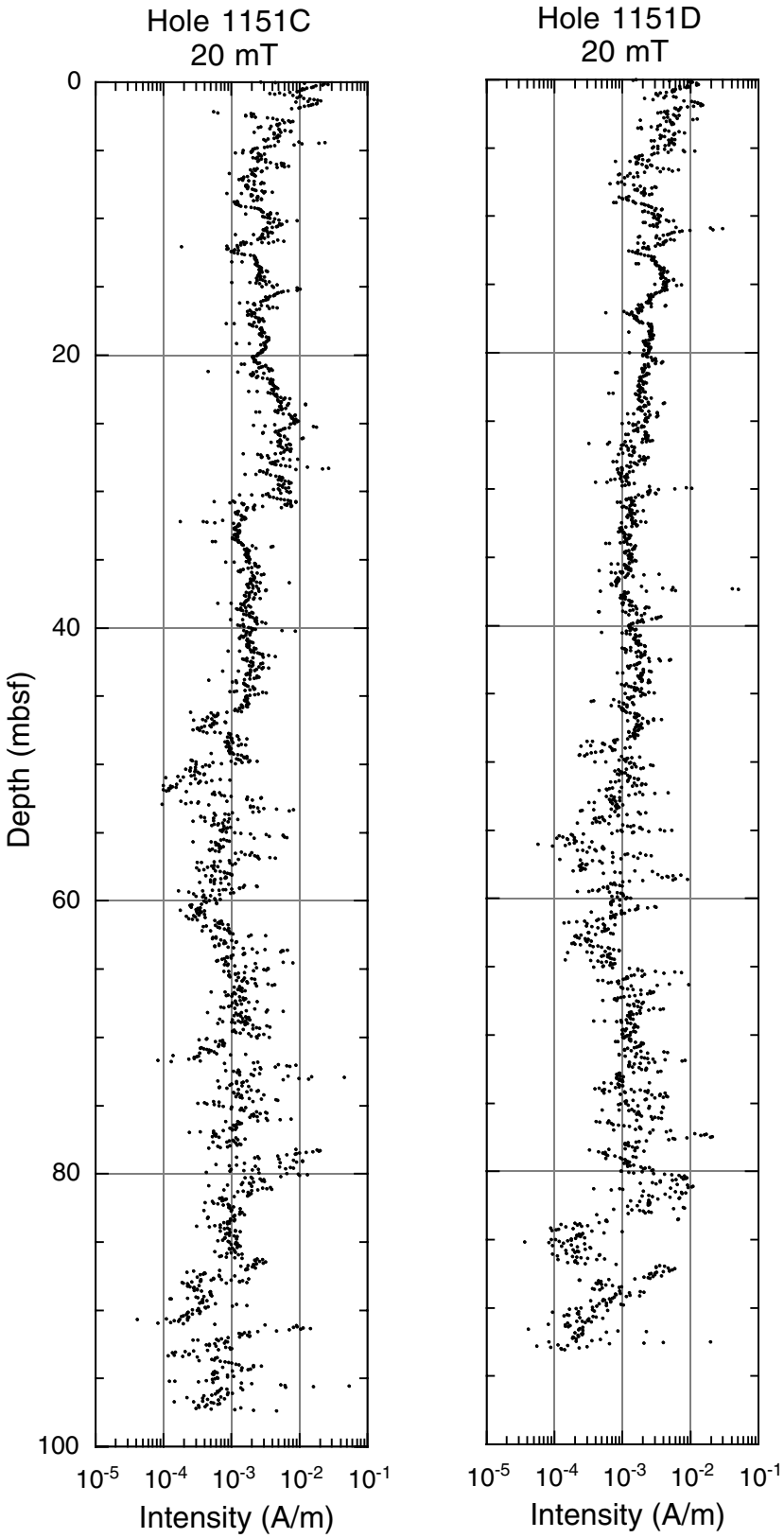

Figure F22. Whole-core susceptibility for Holes 1151C and 1151D (given in raw meter units, which can be converted by SI units by multiplying by ~0.7 × 10^{-5}).

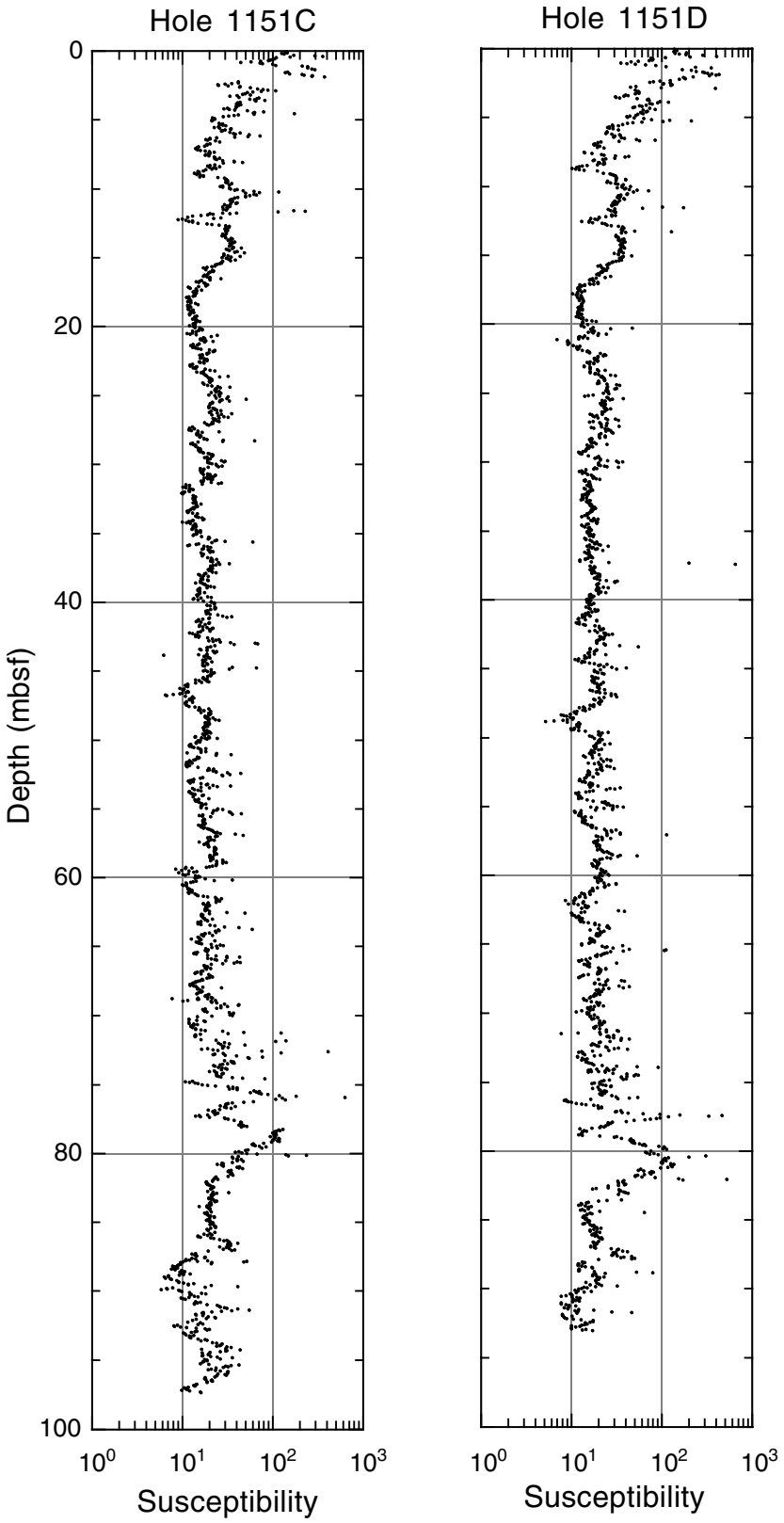

Figure F23. Discrete sample results from the NP2 spinner magnetometer. **A.** Susceptibility (raw meter values). **B.** Natural remanent magnetization (NRM) intensity. **C.** Anhysteretic remanent magnetization (ARM) intensity. **D.** Median destructive field (MDF) of the NRM. **E.** MDF of the ARM. **F.** The NRM intensity (Jn) divided by the ARM intensity (Ja). In the plots with multiple lines, the bold line is prior to demagnetization, the medium-thick line is after 10 mT demagnetization, the thin line is after 20 mT demagnetization, the thick dashed line is after 30 mT demagnetization, and thin dashed line is after 40 mT demagnetization.

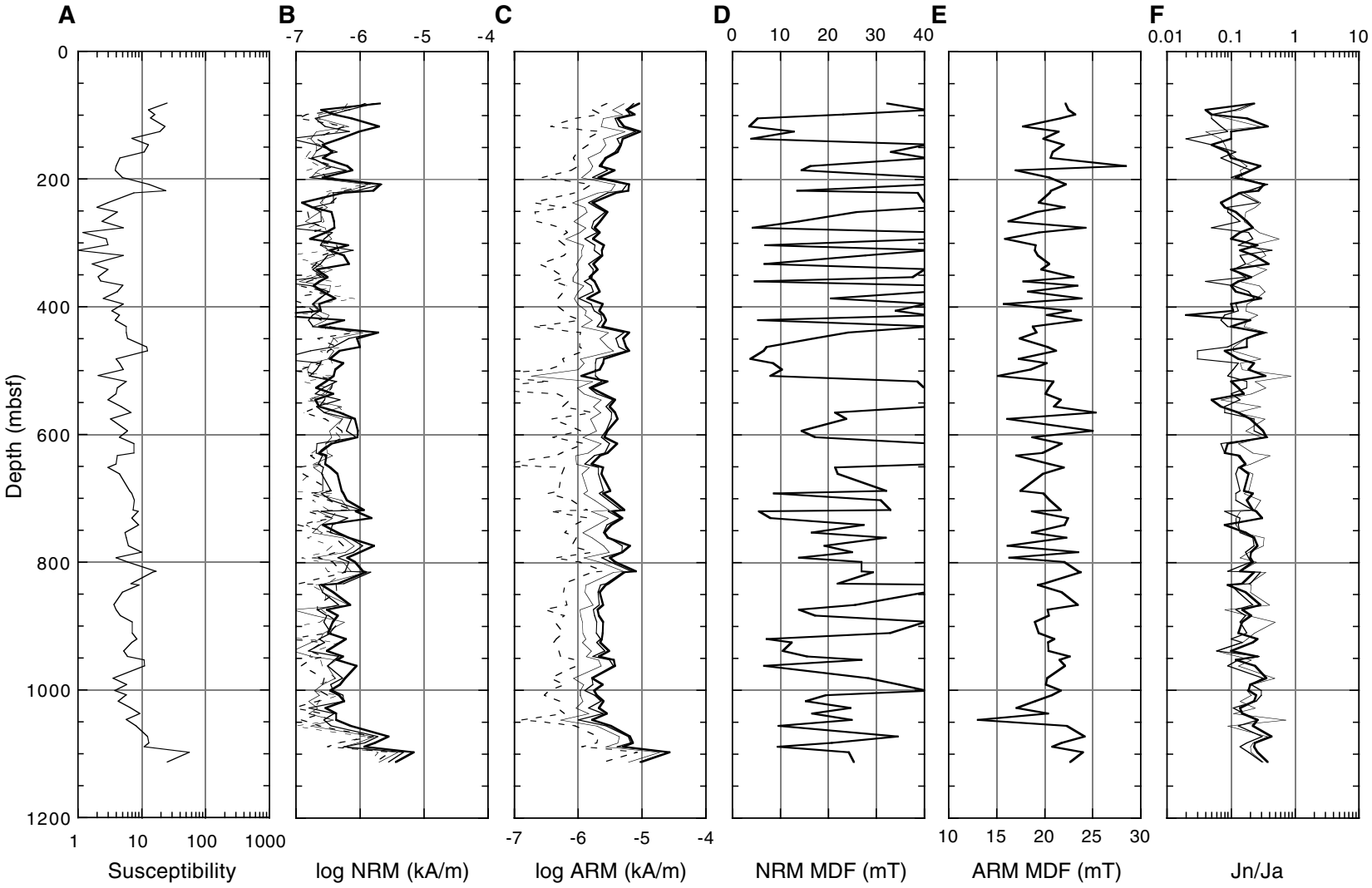

Figure F24. Age-depth relationship for Site 1151 (bold line) and for diatom datums from Holes 1151C and 1151D (bold dashed line), based on diatom (solid circle) and geomagnetic reversal boundaries (solid square), compared with that of Site 1150 (thin dashed lines). Numbers at the age control points correspond to datum events of Table **T11,** p. 113.

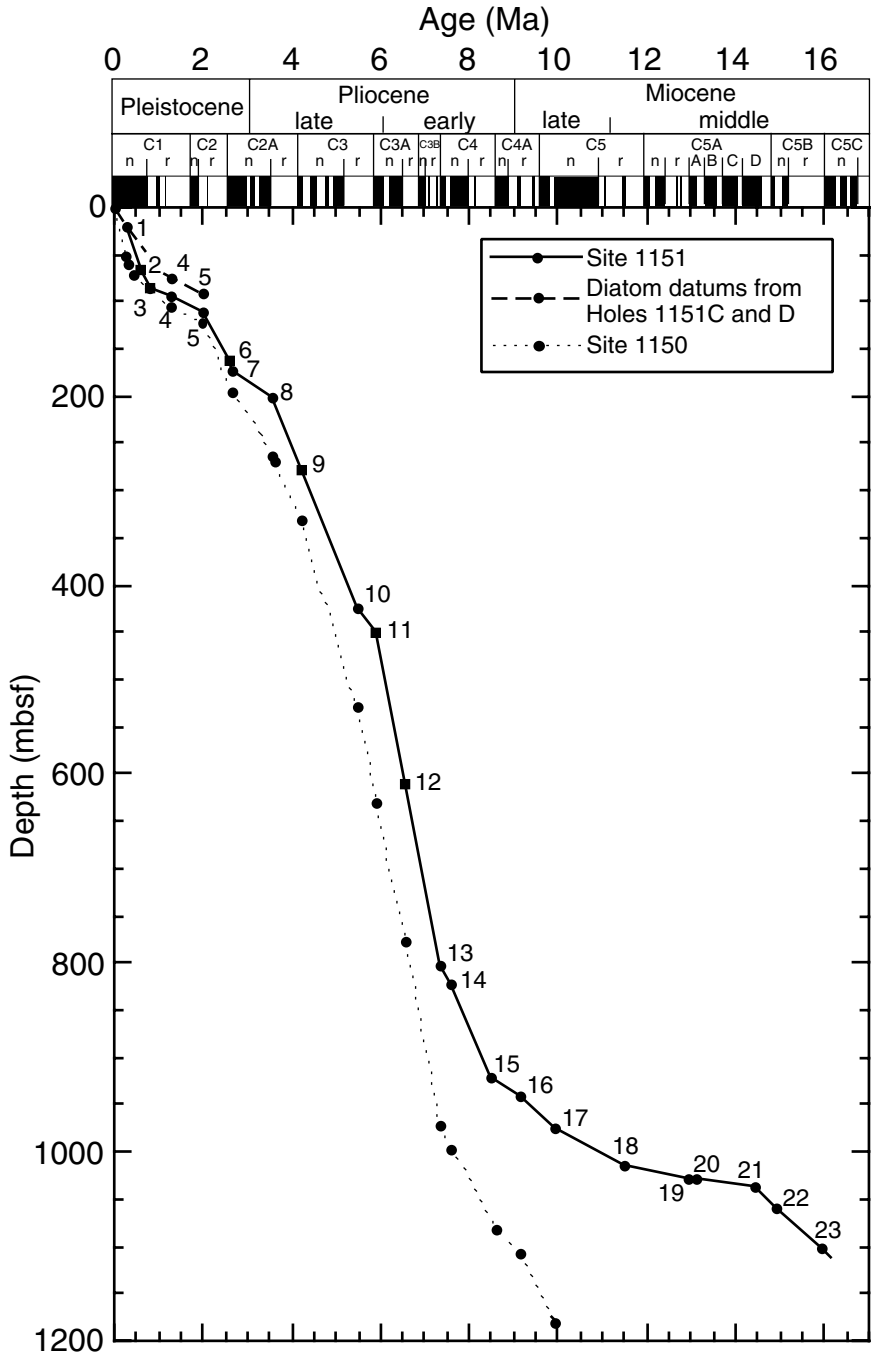

Figure F25. Sedimentation rate vs. age of Site 1151 (bold line) and Site 1150 (dashed line).

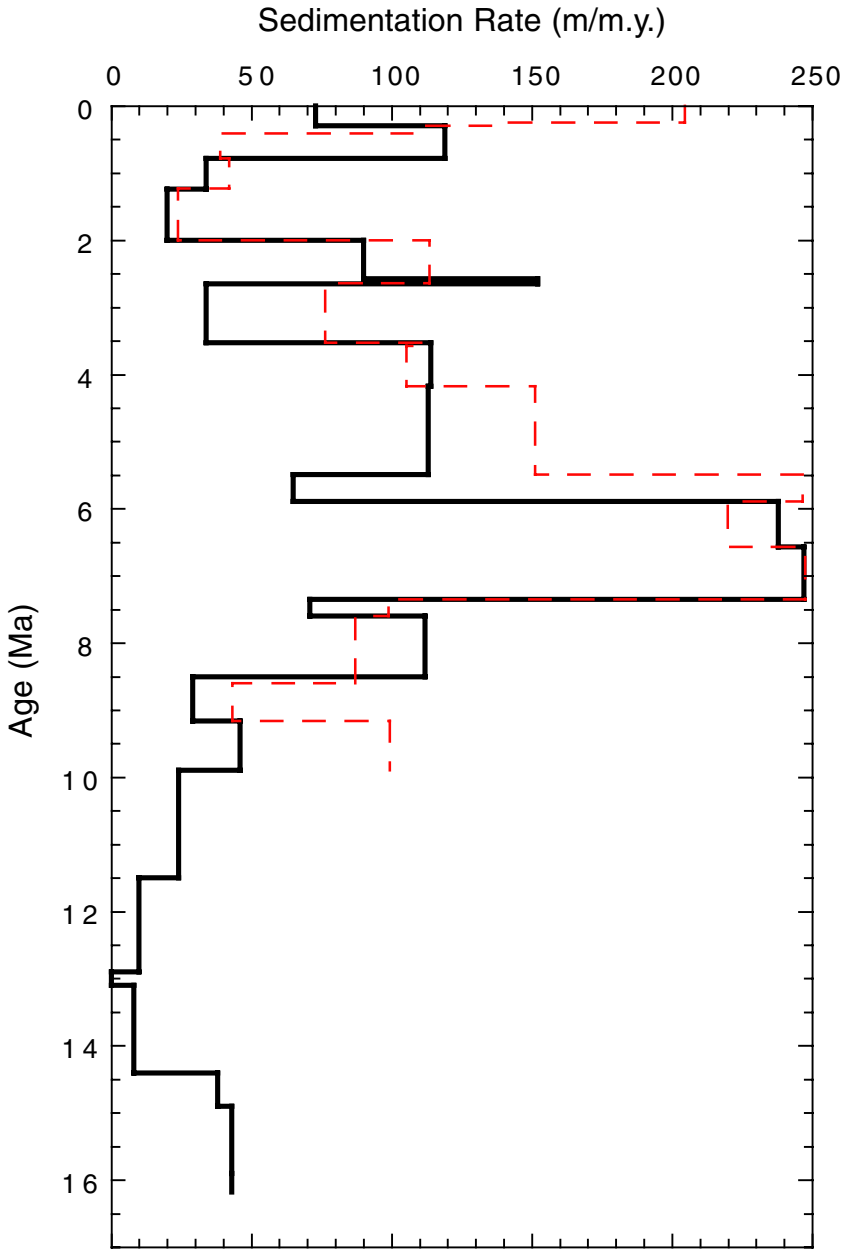

Figure F26. Distribution with depth of headspace concentrations of methane (C_1) and ethane (C_2), and C_1/C_2 ratios at Site 1151.

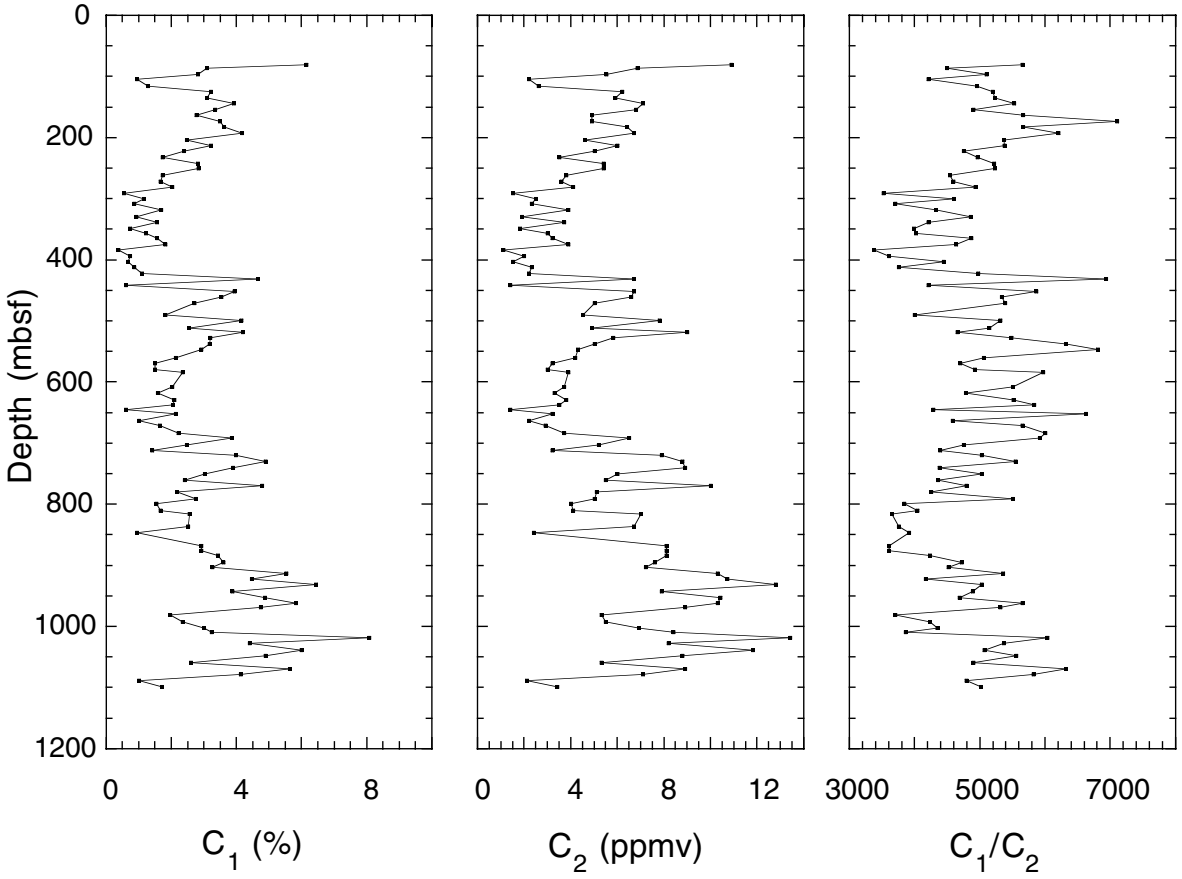

Figure F27. Distribution of carbonate, organic carbon (C_{org}), and sulfur (S) abundances and organic carbon/nitrogen (C_{org}/N) ratios with depth in sediments at Site 1151. Arrows indicate values of excursions.

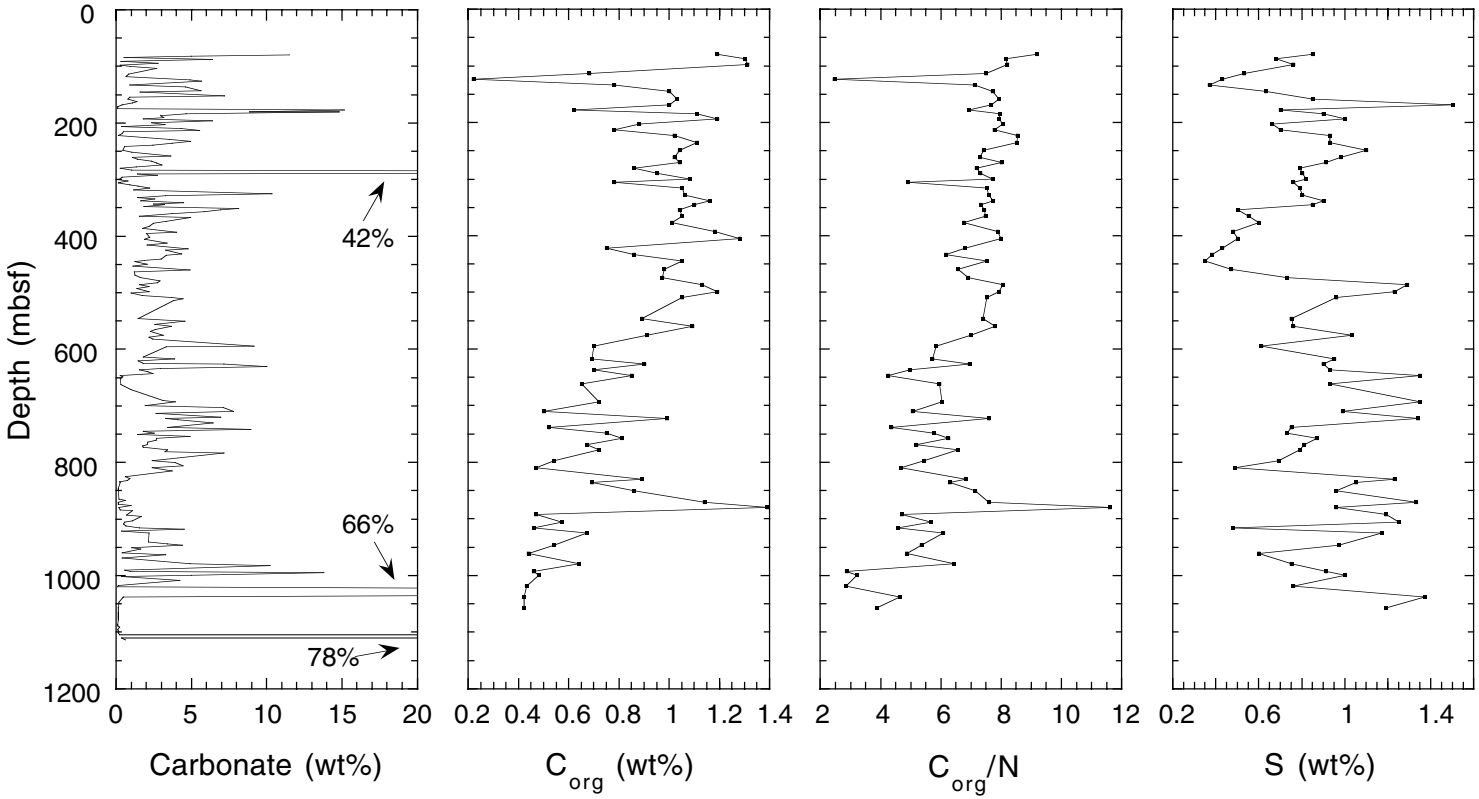

Figure F28. Pore-water salinity, chlorinity, and alkalinity, and pore-water concentrations of dissolved sulfate (SO_4^{2-}), ammonium (NH_4^+), calcium (Ca^{2+}), magnesium (Mg^{2+}), strontium (Sr^{2+}), sodium (Na^{2+}), potassium (K^+), and lithium (Li^+) at Site 1151. (Continued on next page.)

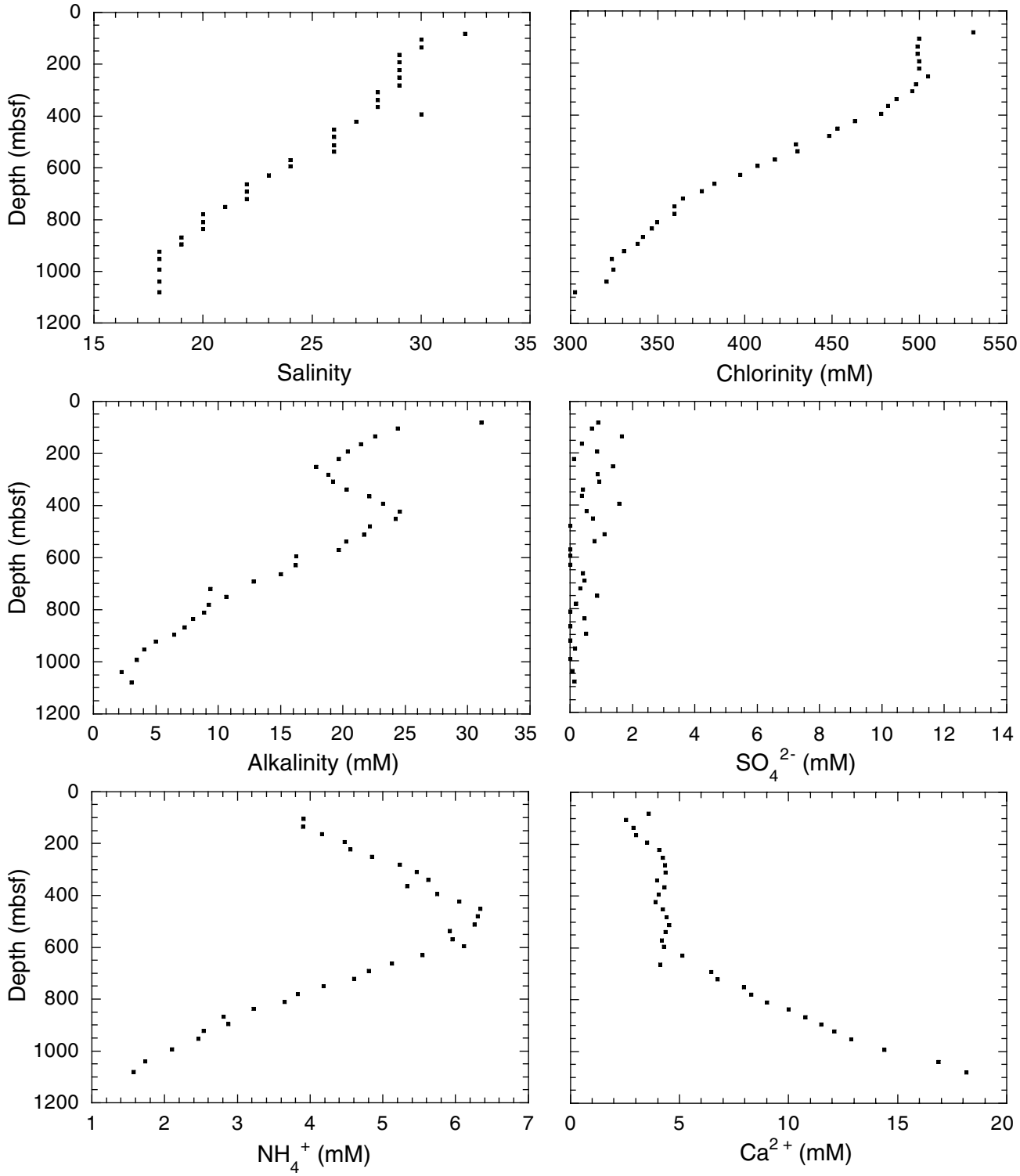

Figure F28 (continued).

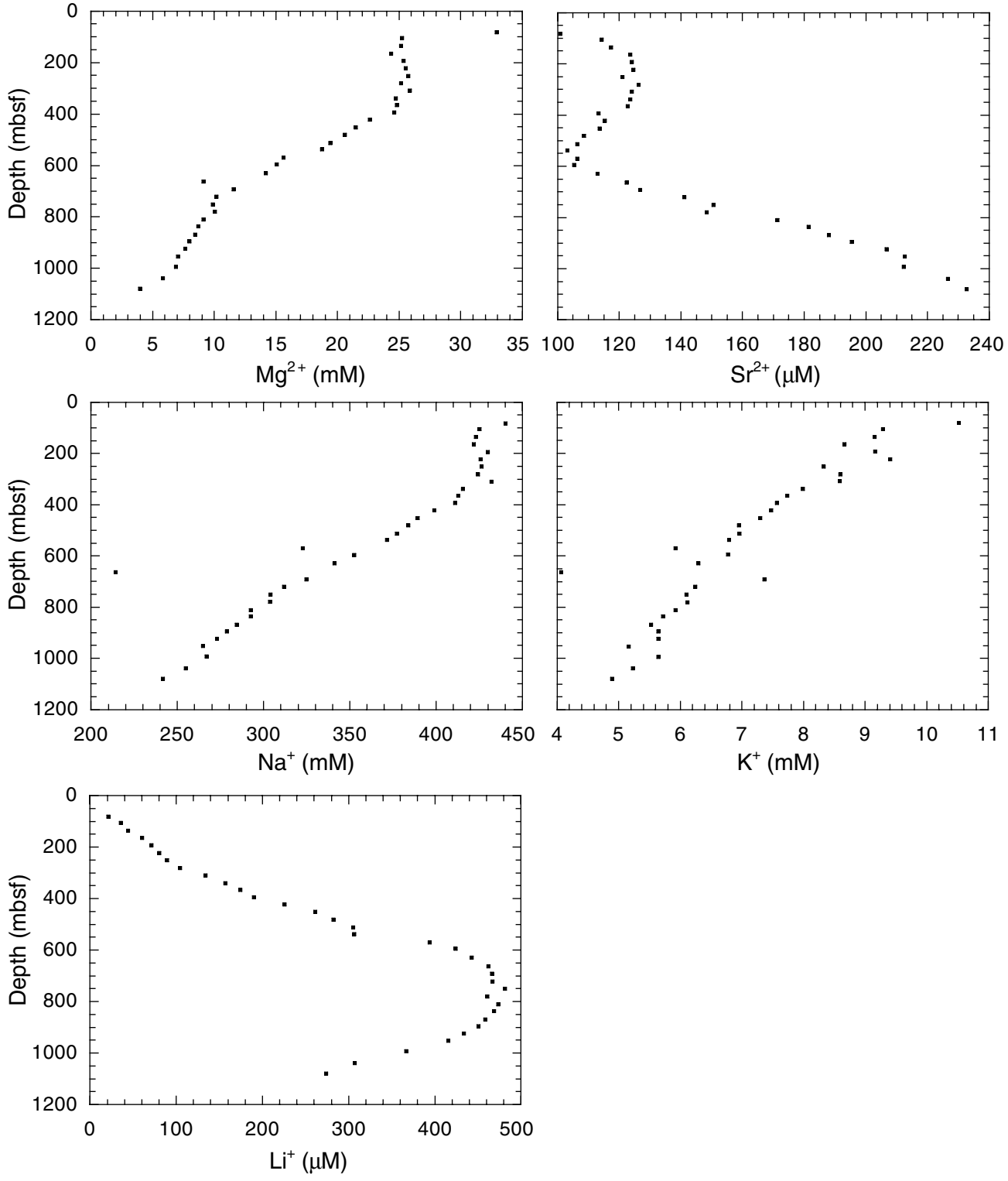

Figure F29. Bulk density from GRA measurements on cores at Site 1151. Open blue circles = data from Hole 1151A; solid red circles = data from Hole 1151C; crosses = 10% of the data from Hole 1151D.

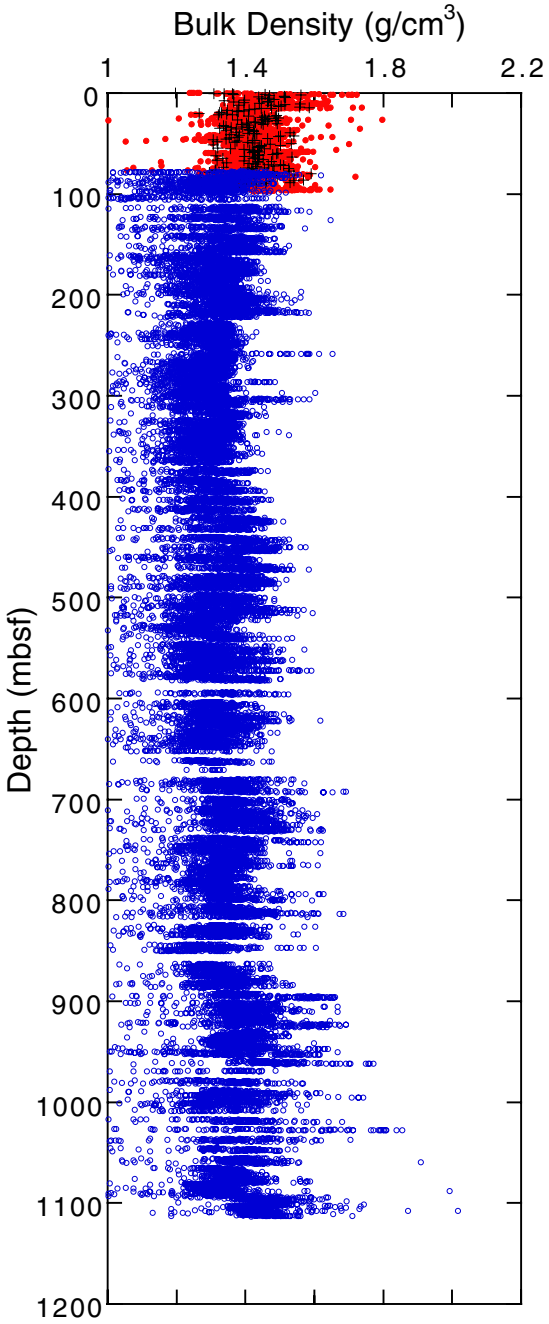

Figure F30. Horizontal *P*-wave velocity from PWL measurements on cores at Site 1151. Open blue circles = data from Hole 1151C; solid red circles = data from Hole 1151D.

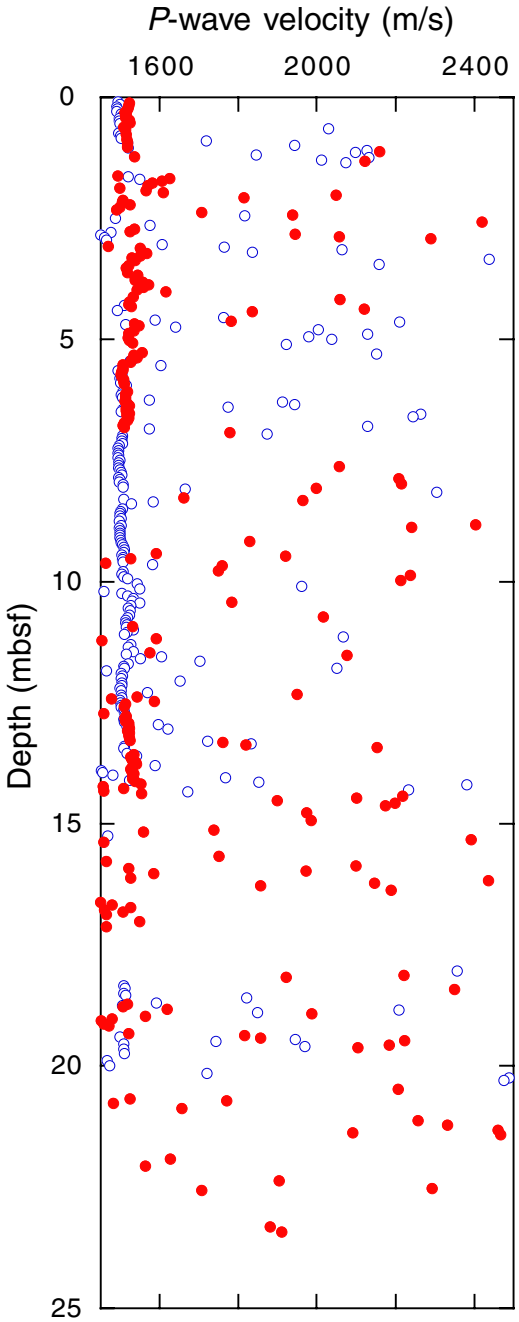

Figure F31. NGR activity of cores at Site 1151. Open blue circles = data from Hole 1151A; solid red circles = data from Hole 1151C; crosses = 20% of the data from Hole 1151D.

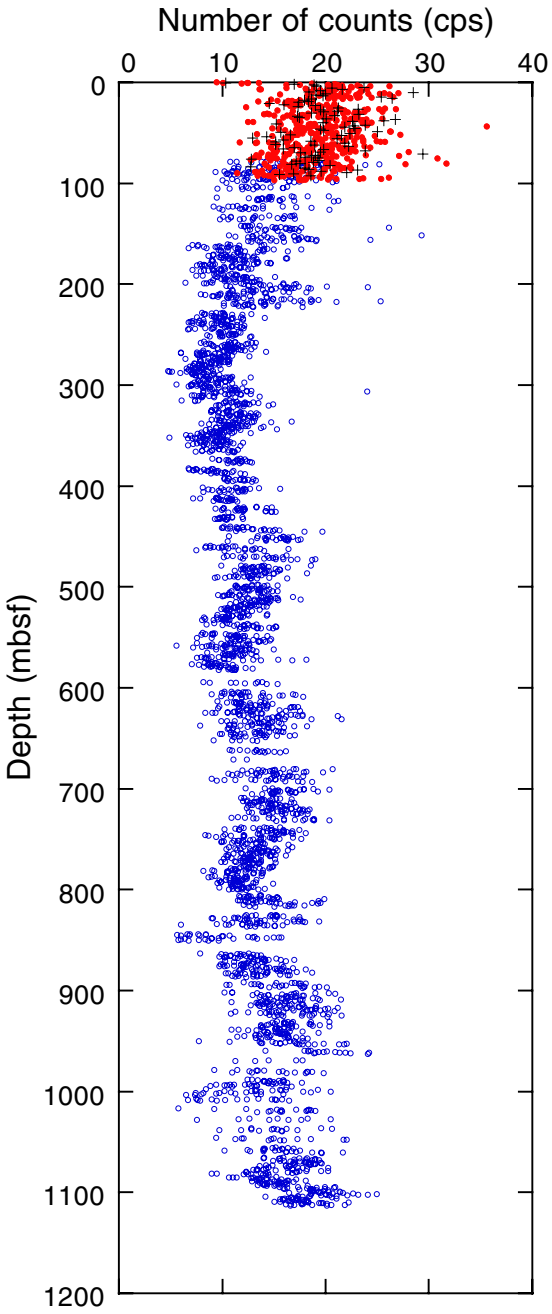

Figure F32. Thermal conductivity variation with depth in Hole 1151A. Large solid circles = average thermal conductivity; small open circles = individual thermal conductivity measurements.

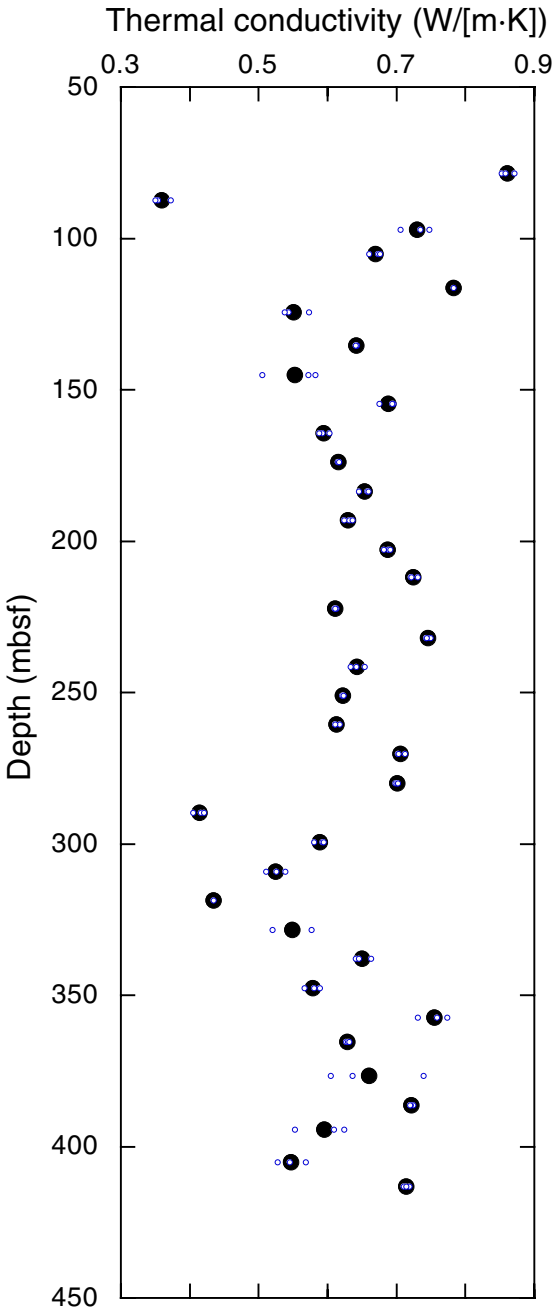

Figure F33. *P*-wave velocity vs. depth from measurements on split cores in Hole 1151A. **A.** *P*-wave velocity in horizontal directions (V_X and V_Y). **B.** *P*-wave velocity in vertical direction (V_Z).

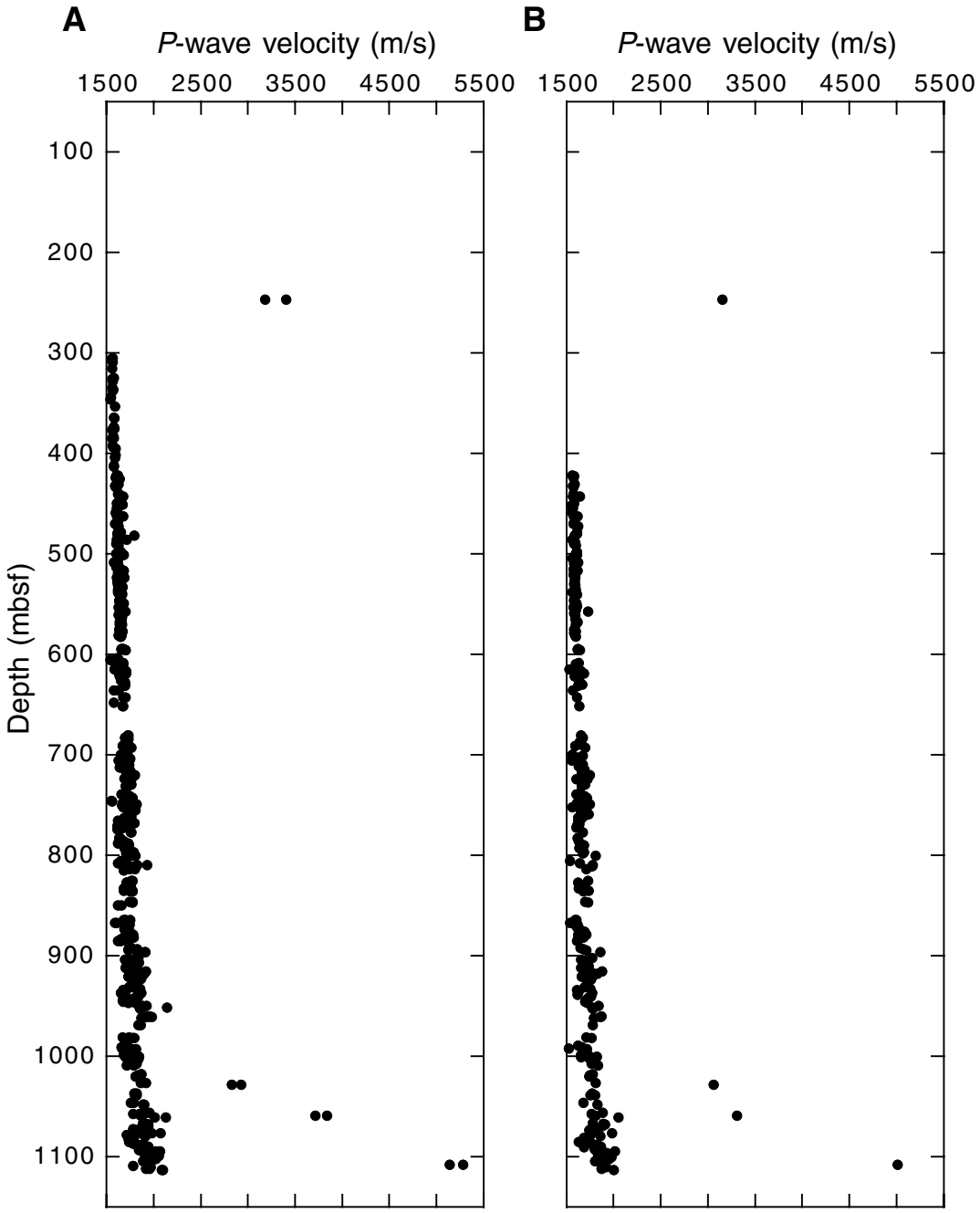

Figure F34. Anisotropy vs. depth from measurements of vertical and horizontal *P*-wave velocities in Hole 1151A. **A.** Anisotropy of maximum vs. minimum horizontal *P*-wave velocity. **B.** Anisotropy of maximum horizontal vs. vertical *P*-wave velocity. **C.** Anisotropy of minimum horizontal vs. vertical *P*-wave velocity.

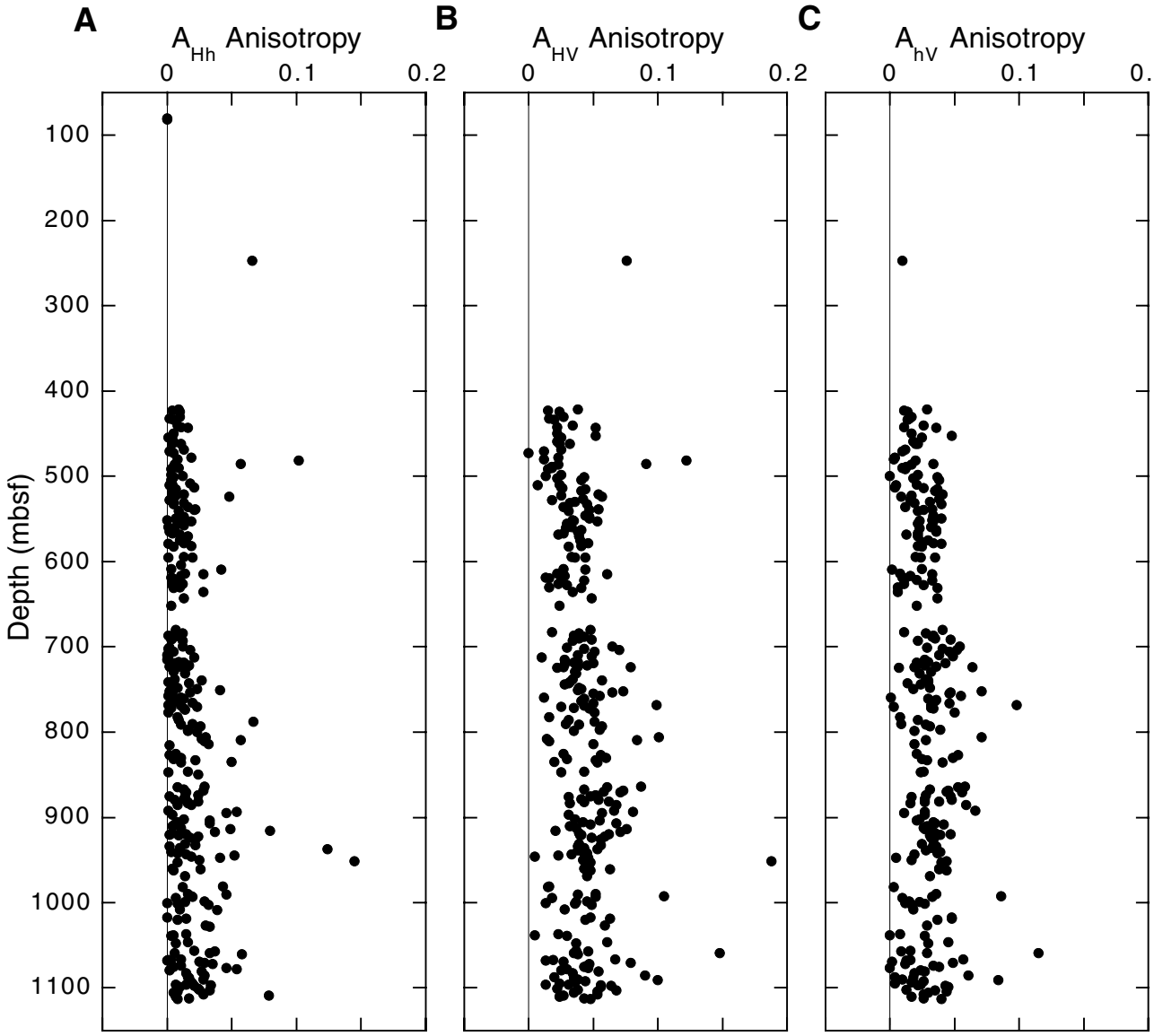

Figure F35. Corrections for in situ salinity and pore-water density in Hole 1151A. The variation vs. depth of the ratio of index properties calculated (c) from in situ values over index properties calculated from ODP standard values (s) (Blum, 1997) are plotted in the diagrams. **A.** Water content of total mass (W_t^c/W_t^s) ratio. **B.** Water content of mass of solids (W_s^c/W_s^s) ratio. **C.** Bulk density (ρ_b^c/ρ_b^s) ratio. **D.** Dry density (ρ_d^c/ρ_d^s) ratio. **E.** Grain density (ρ_g^c/ρ_g^s) ratio. **F.** Porosity (η^c/η^s) ratio. **G.** Void (e^c/e^s) ratio.

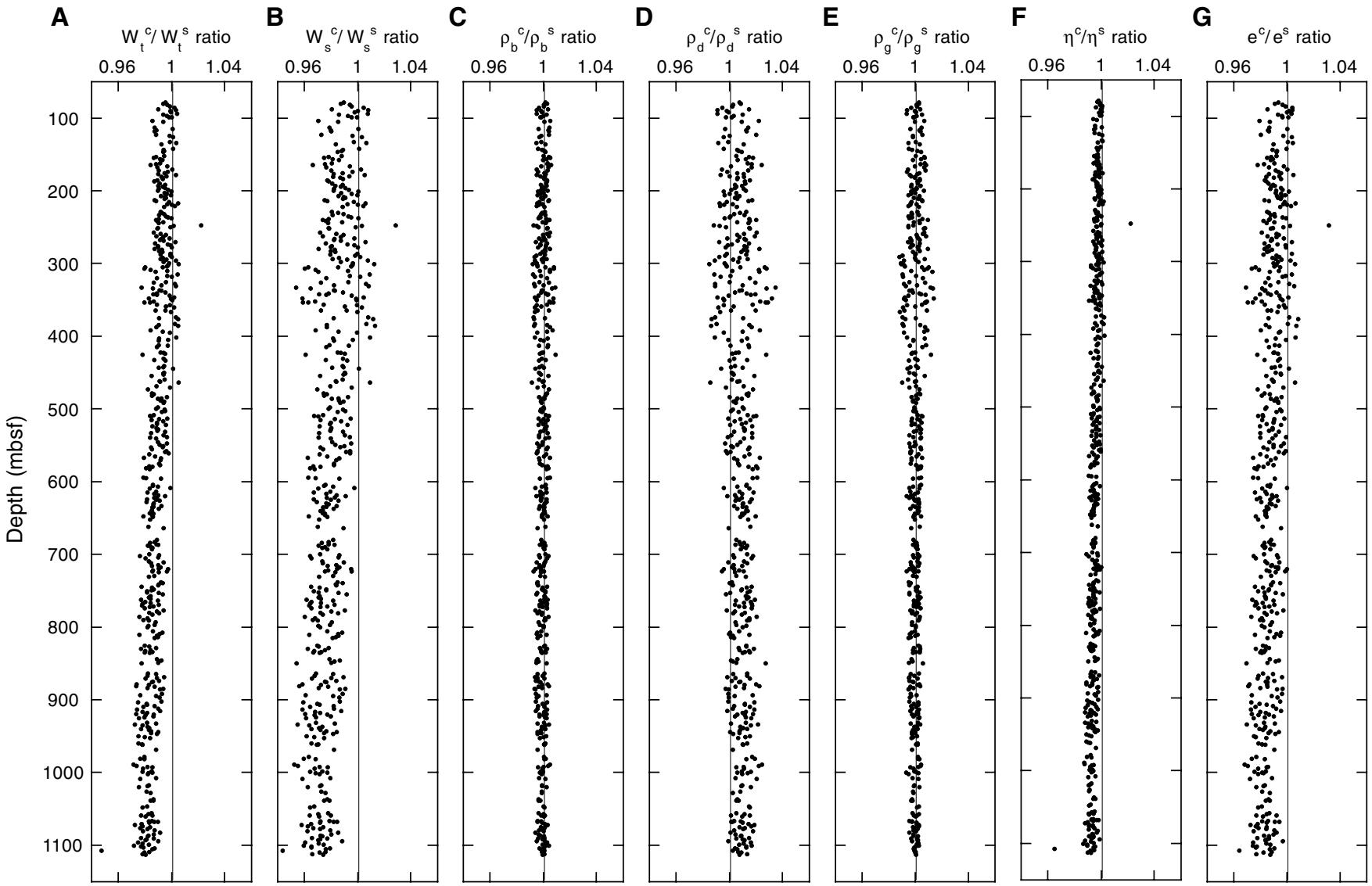

Figure F36. Index properties vs. depth in Hole 1151A. The calculation of index properties is based on in situ values of salinity and density of pore water. Solid lines = lithologic units, dashed lines = lithologic subunits. **A.** Water content of total mass (W_t^c/W_t^s) ratio, and lithologic units/subunits. **B.** Water content of mass of solids (W_s^c/W_s^s) ratio. **C.** Bulk density (ρ_b^c/ρ_b^s) ratio. **D.** Dry density (ρ_d^c/ρ_d^s) ratio. **E.** Grain density (ρ_g^c/ρ_g^s) ratio. **F.** Porosity (η^c/η^s) ratio. **G.** Void (e^c/e^s) ratio.

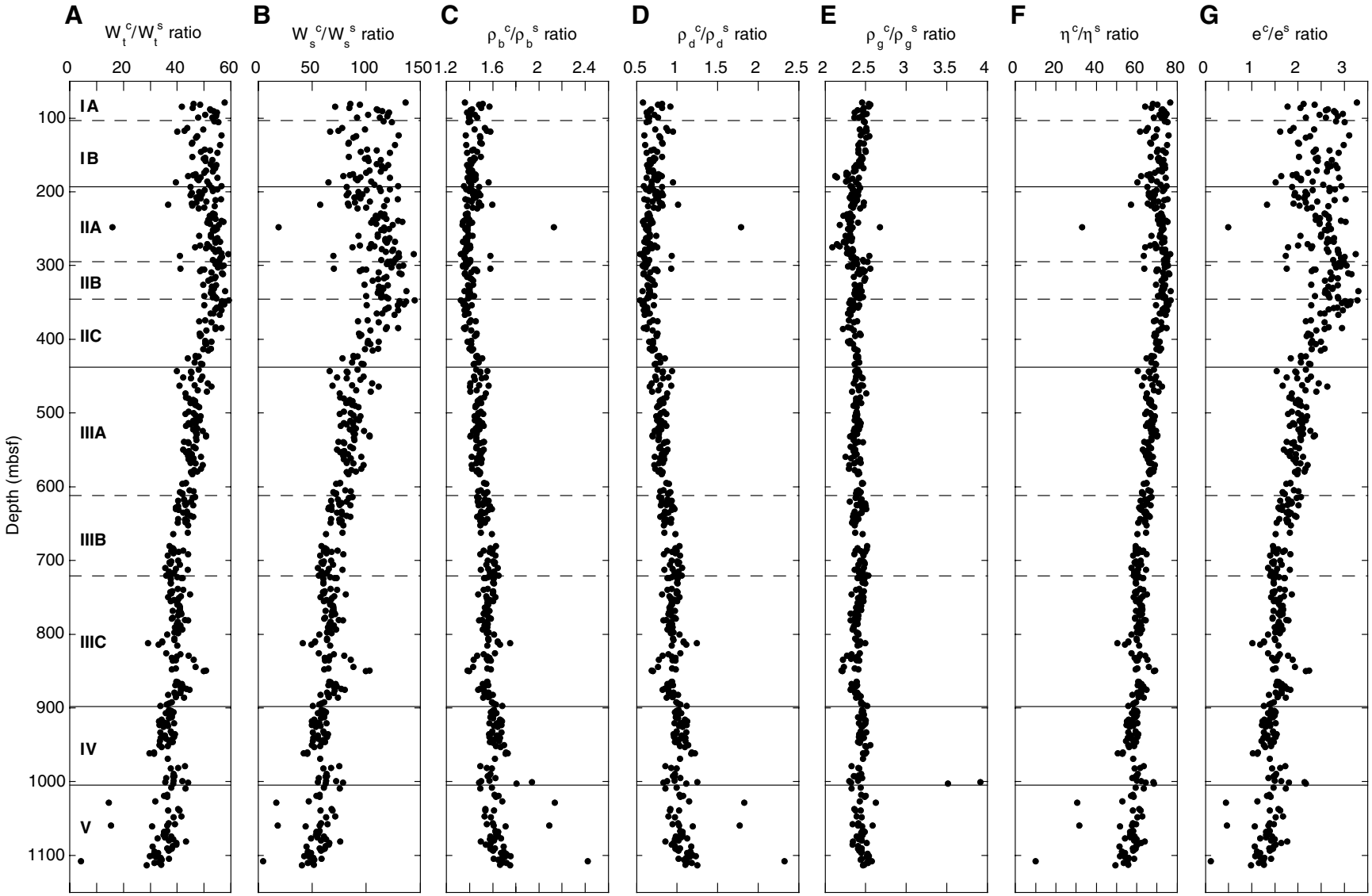

Figure F37. Total and effective vertical stress vs. depth at Site 1151. Linear fit of the data shows that the total and effective vertical stresses have the following depth relationships: $\delta_v = -0.09218 + 0.014823 \times z$ (R > 0.999) and $s_v' = -0.15056 + 0.0083804 \times z$ (R = 0.999), where z = depth. The weight of seawater (22.0 MPa) was excluded when the total vertical stress was calculated. Blue solid line = total vertical stress (s_v), dotted red line = effective vertical stress (s_v')

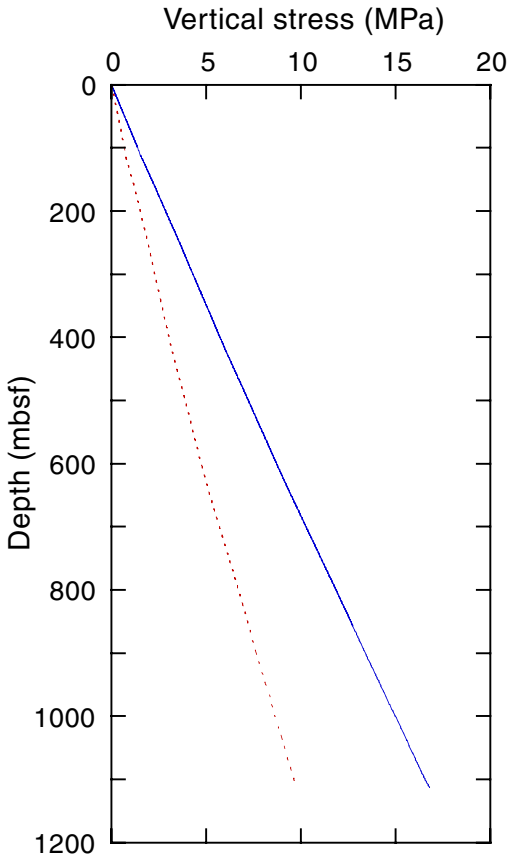

Figure F38. Summary of logs from Hole 1151D compared with the lithologic units (see "Lithostratigraphy," p. 7).

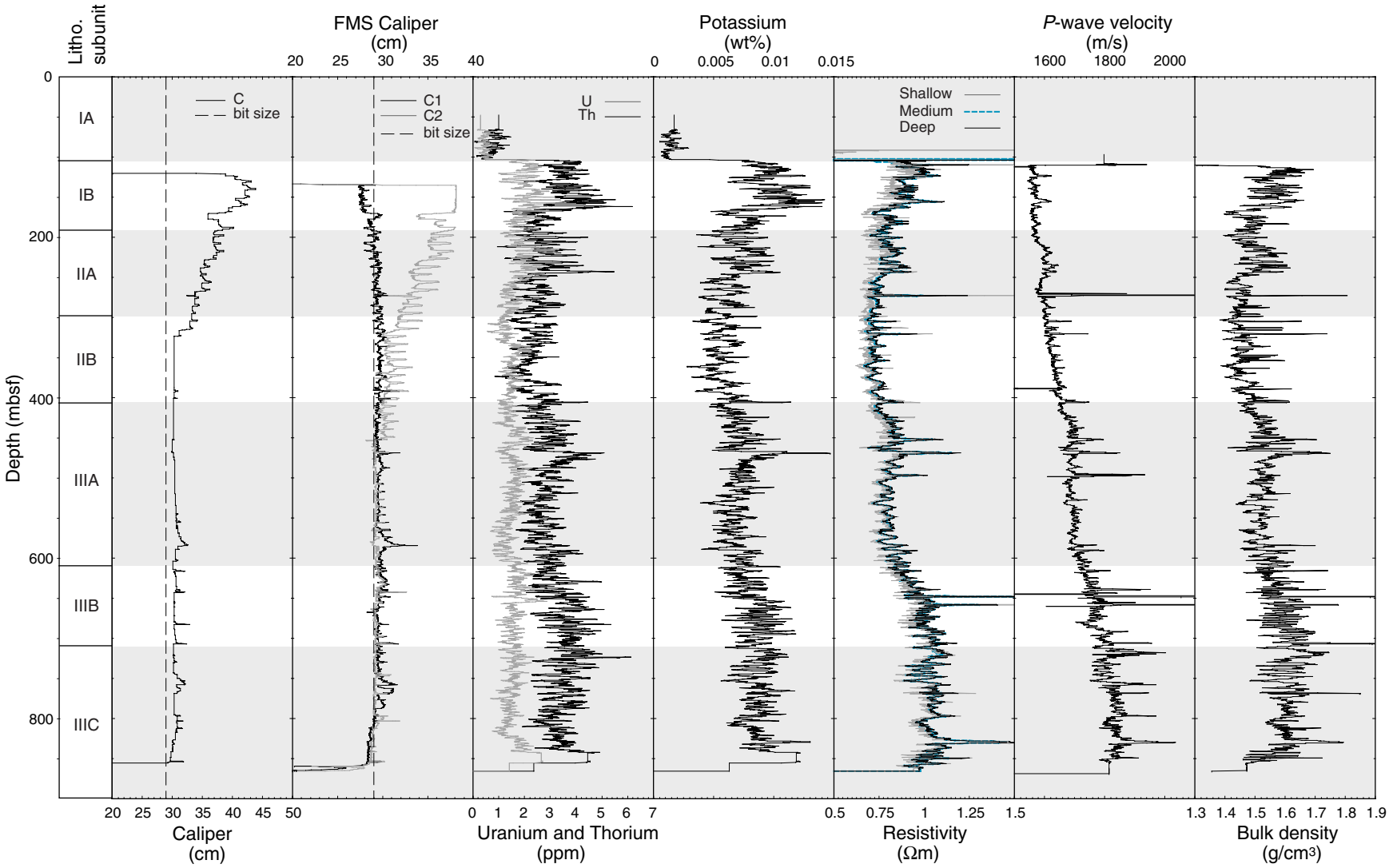

Figure F39. Temperature data vs. time from the APC Adara temperature tool and the DVTP at Site 1151. The dashed line in each panel indicates the estimated equilibrium temperature determined by curve fitting to the equilibration record. The portion of the equilibrium curve used for the curve fitting is indicated with solid circles.

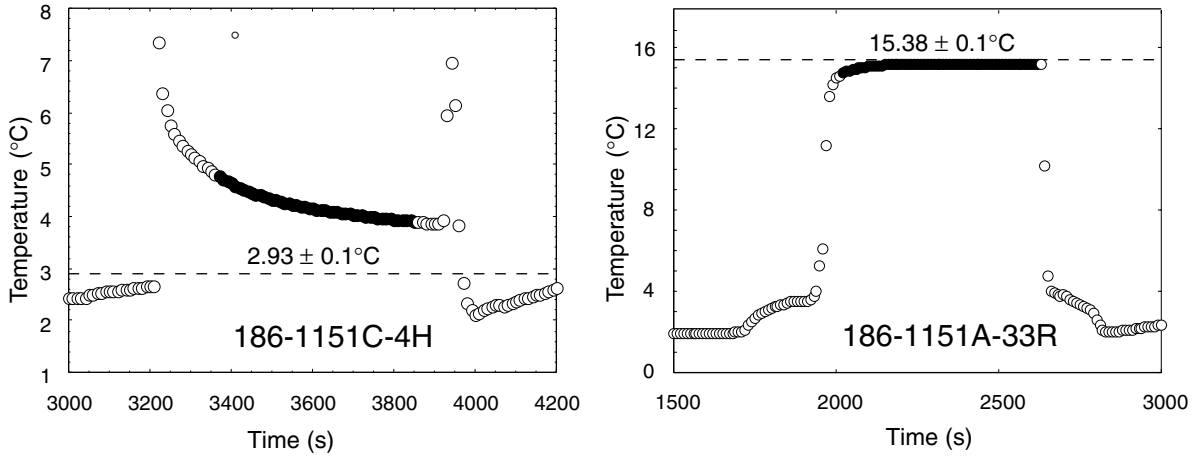

Figure F40. Temperature vs. depth at Site 1151, with a best-fit line through the three observations giving a gradient of 27.7°C/km.

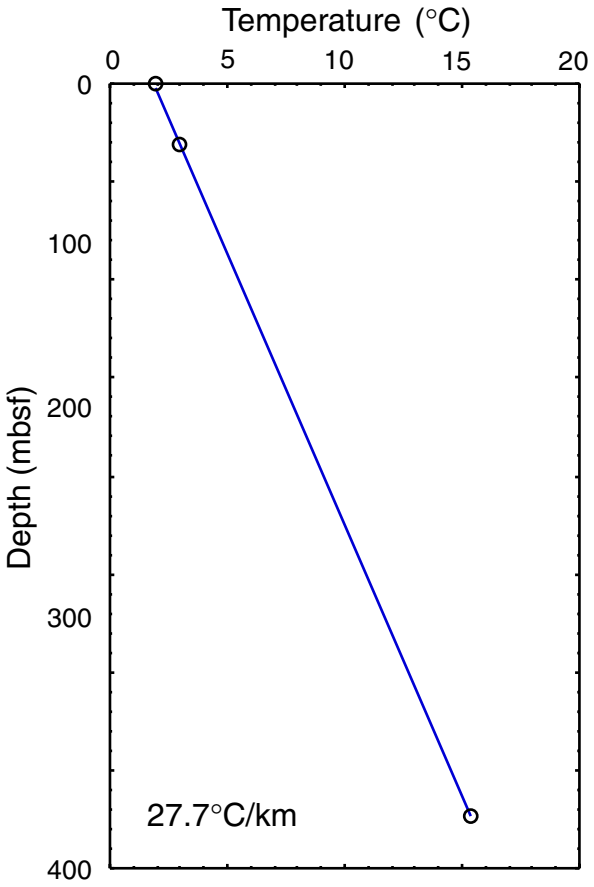

Figure F41. Logging data of *P*-wave velocity and GRA bulk density near the instrument installation depth. Shaded square shows the entire length of the sensor section.

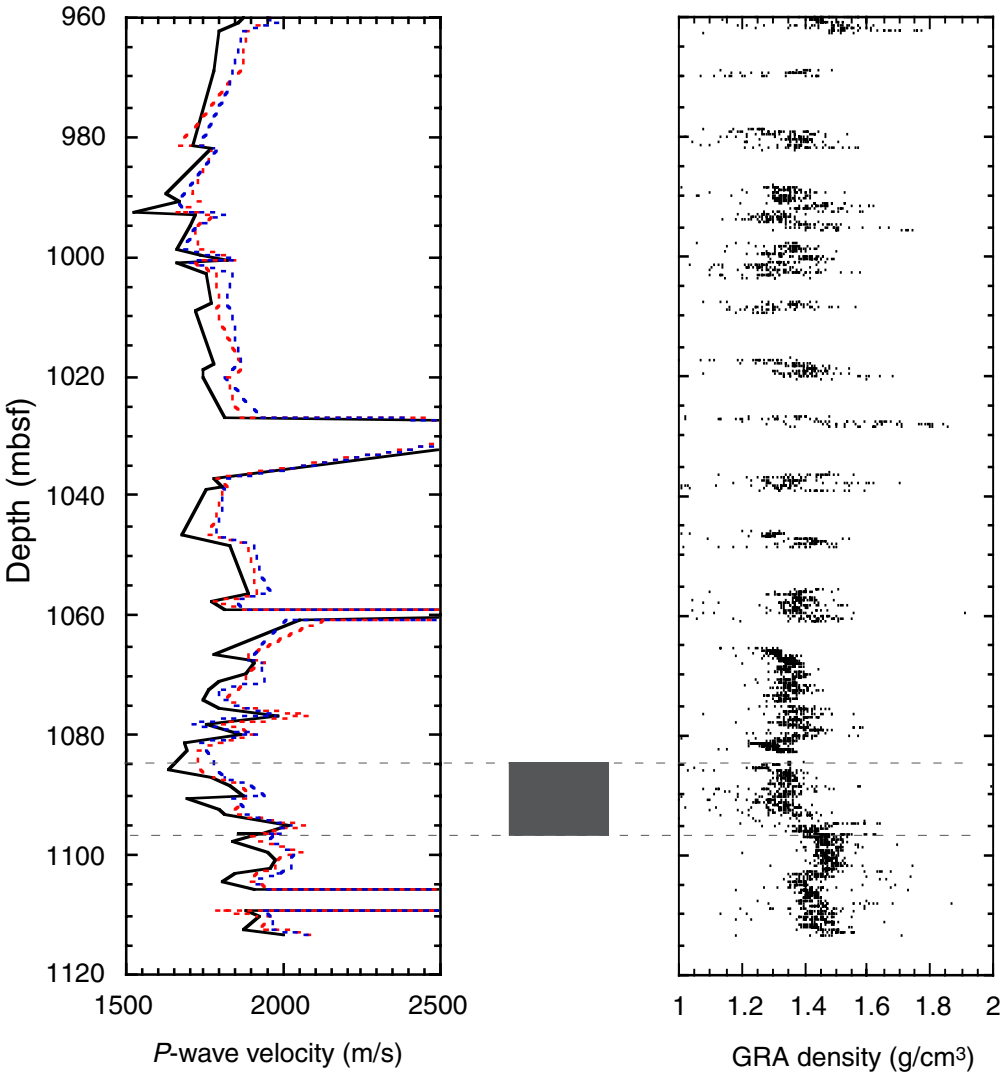

Figure F42. Photograph showing a compaction-related steep normal fault initiating below a dark gray discontinuous silt layer at 83 cm. Bioturbation and the intercalated minor lithologies indicate an increase in displacement with depth. The fault is typically anastomosing on a small scale and filled with gray clayey material. A minor normal fault dipping in opposite direction is offset by the major fault at 86 cm for about 1 cm (interval 186-1151A-108R-7, 78–98 cm).

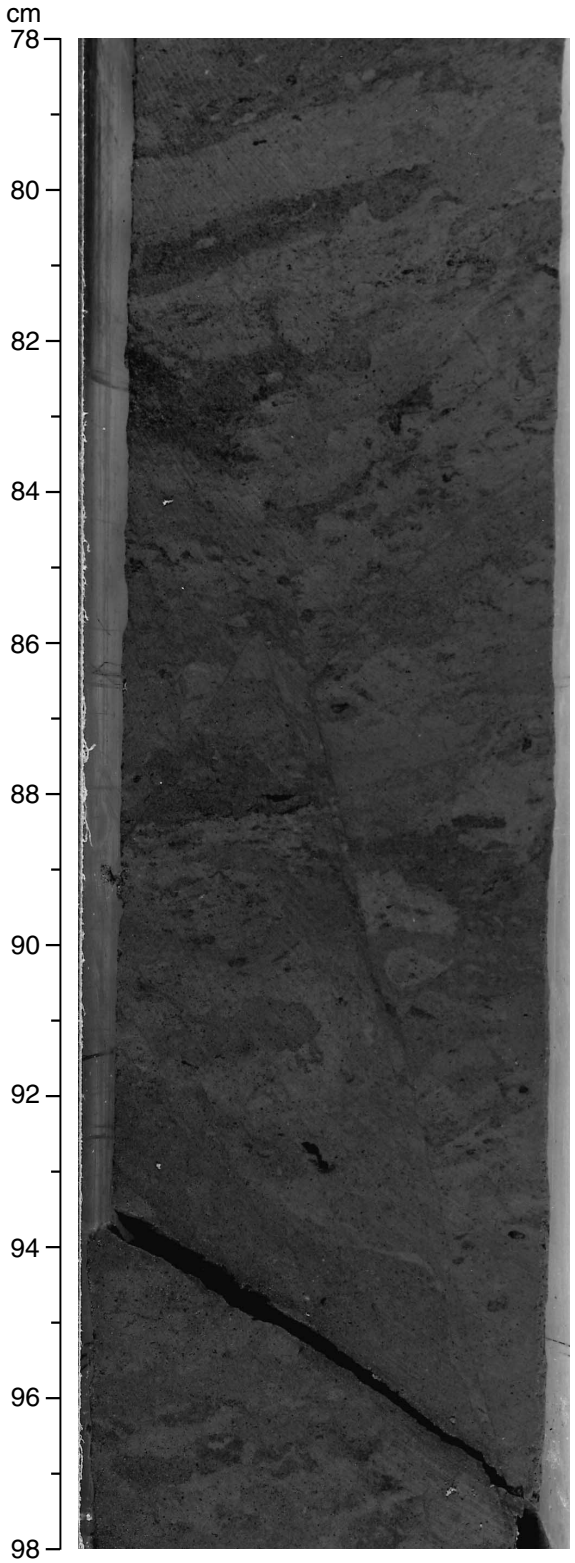

Figure F43. Photograph showing sets of typical S-shaped tension gashes that indicate dextral shearing (interval 186-1151A-103R-2, 30–40 cm).

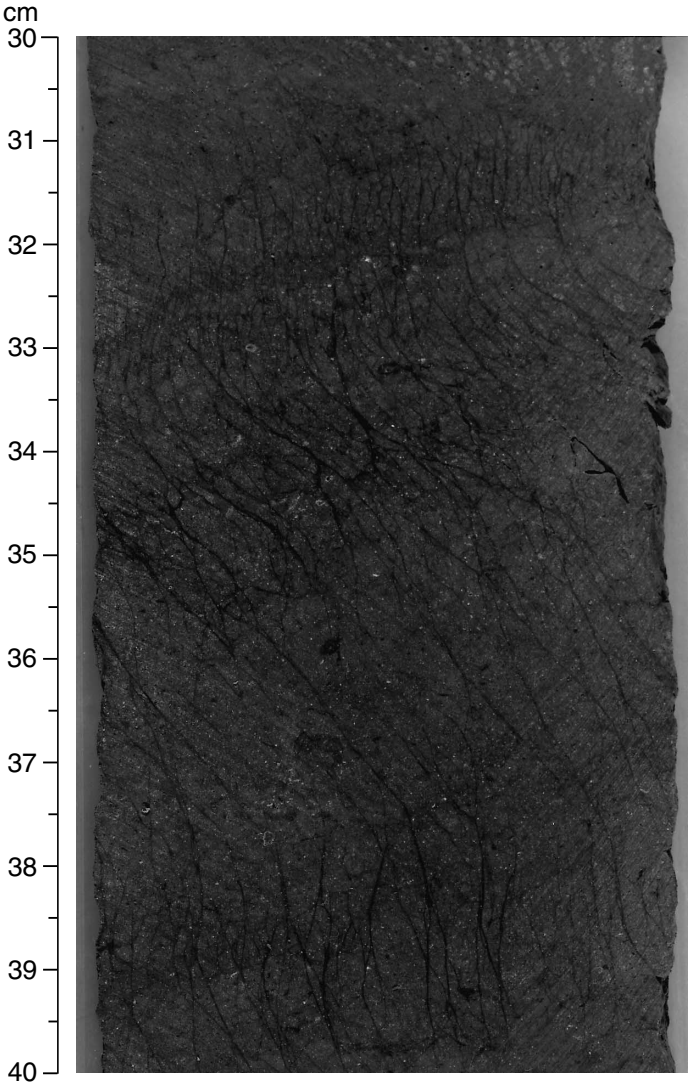

Figure F44. Photograph showing large anastomosing and branching zone of steep joints and faults with dark-colored interfracture lithology, which is supposed to be colored by precipitated material from circulating fluids (interval 186-1151A-100R-2, 83–105 cm).

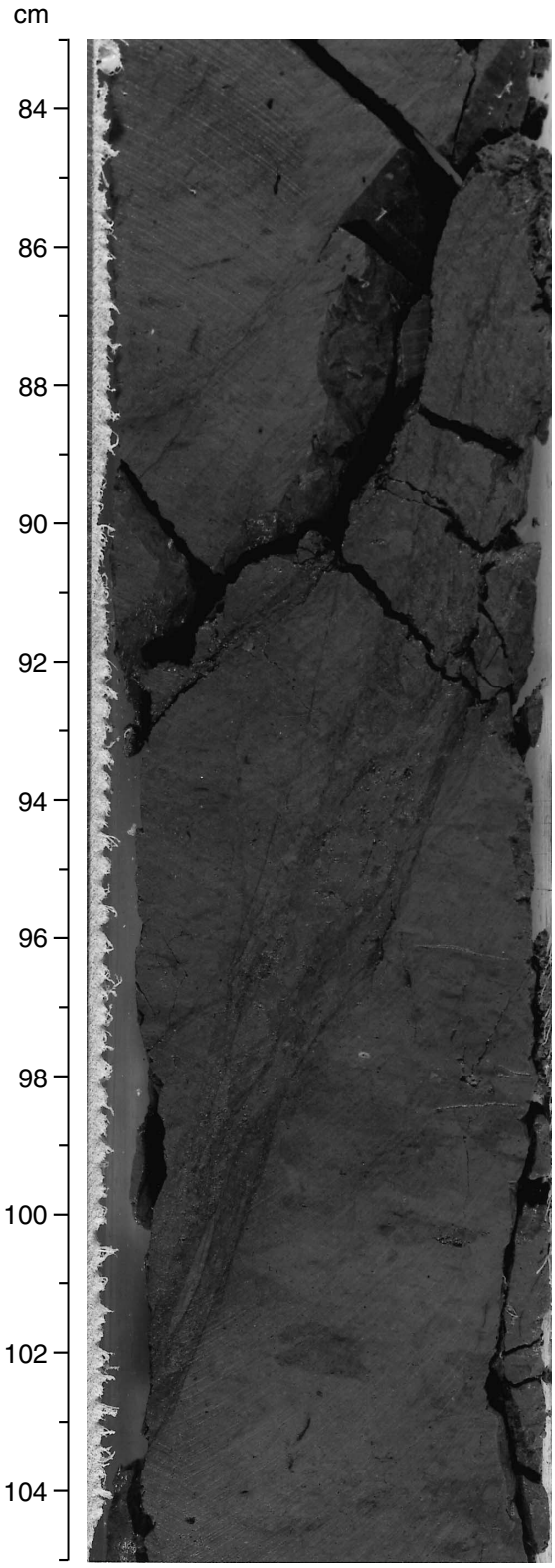

Figure F45. Number of all faults, joints, and open fractures between 400 and 1150 mbsf at Site 1151. Frequencies are plotted by numbers per recovered meter of each core.

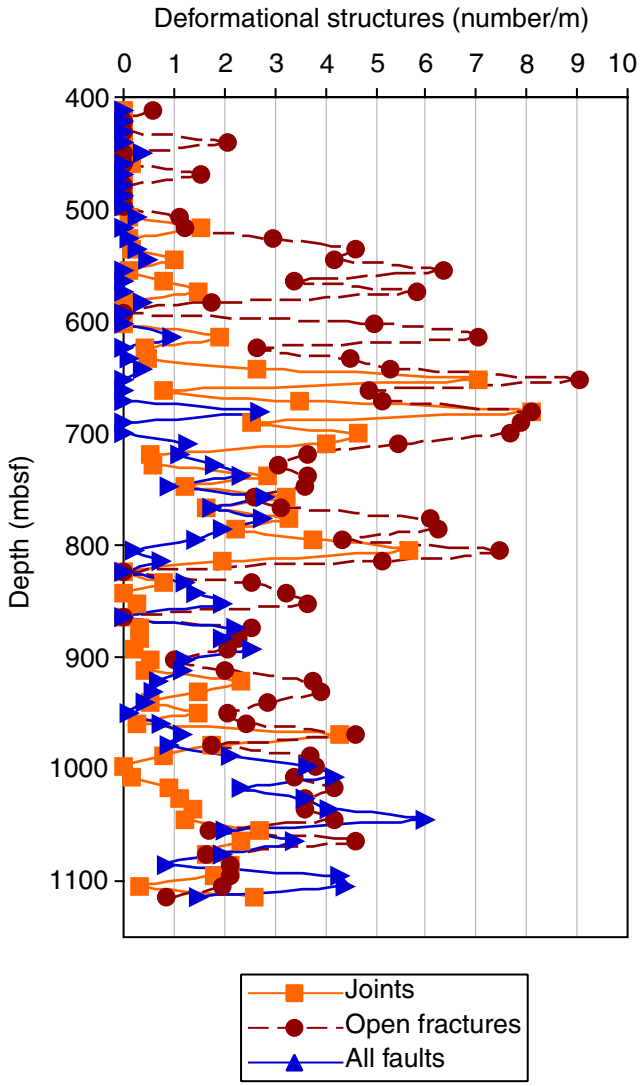

Figure F46. **A.** Frequency of measured healed fractures through Hole 1151A. **B.** Distribution of dip azimuth of healed fracture planes after reorientation. **C.** Distribution of dip angle of healed fracture planes after reorientation.

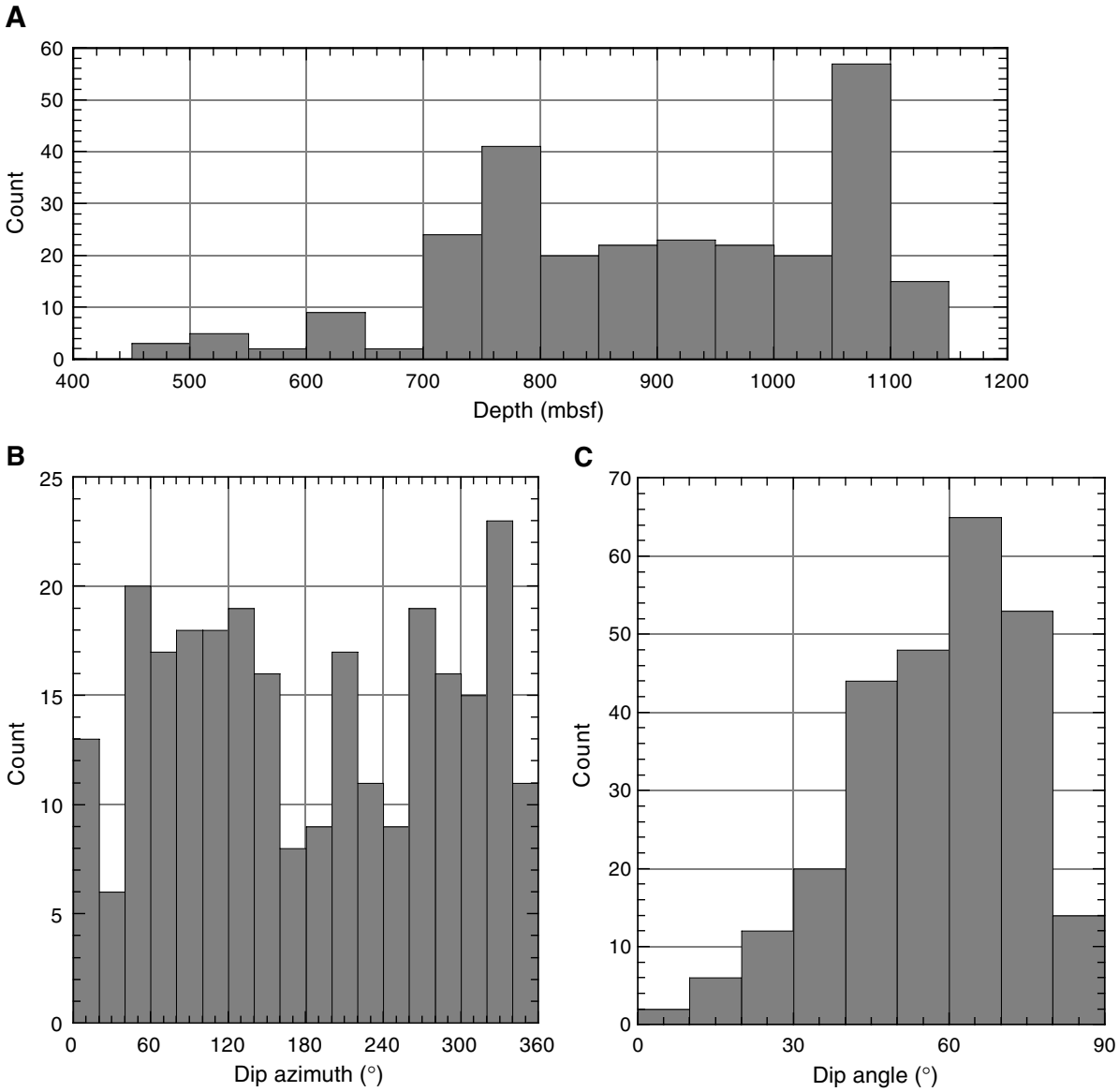

Figure F47. Downhole variation in dip azimuths of healed fracture planes in Hole 1151A, divided into three subdomains.

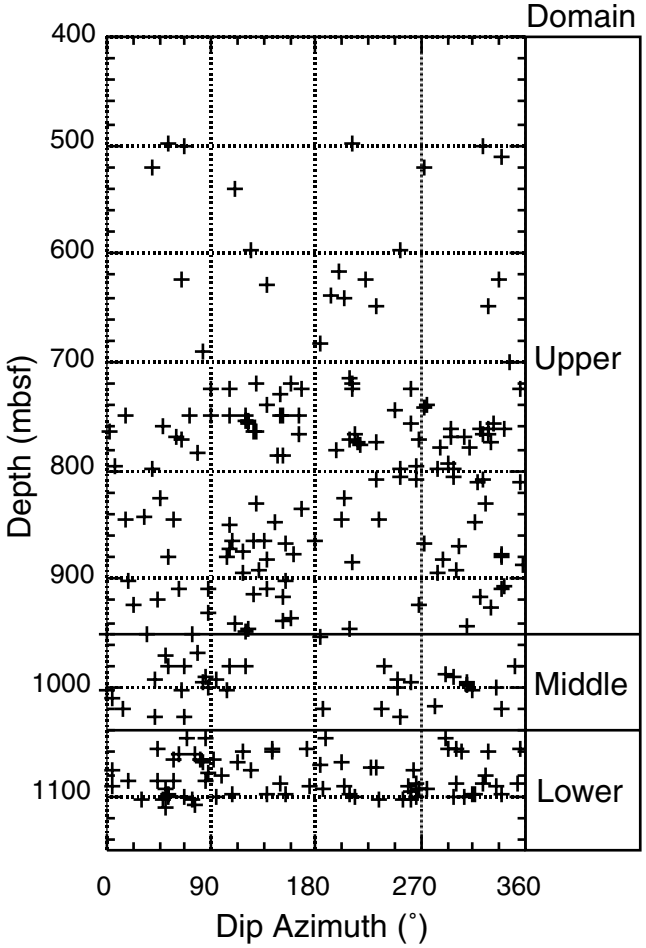

Figure F48. Contour diagram of poles of healed fracture planes in Hole 1151A. Contour interval is every 0.5 starting from a pole density of 1.

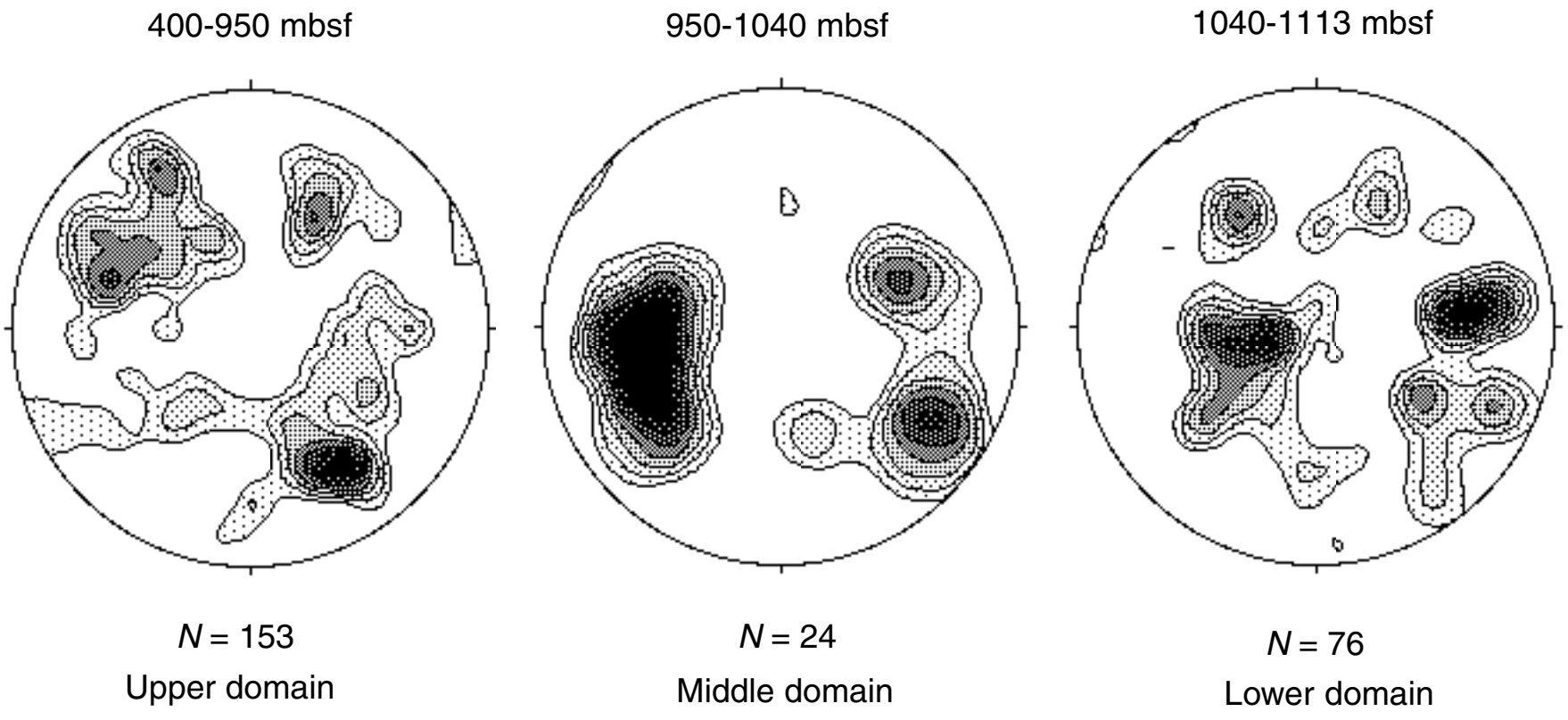

Figure F49. Contour diagram of poles to the open fracture planes in Hole 1151A. Contour interval is every 0.5 starting from a pole density of 1.

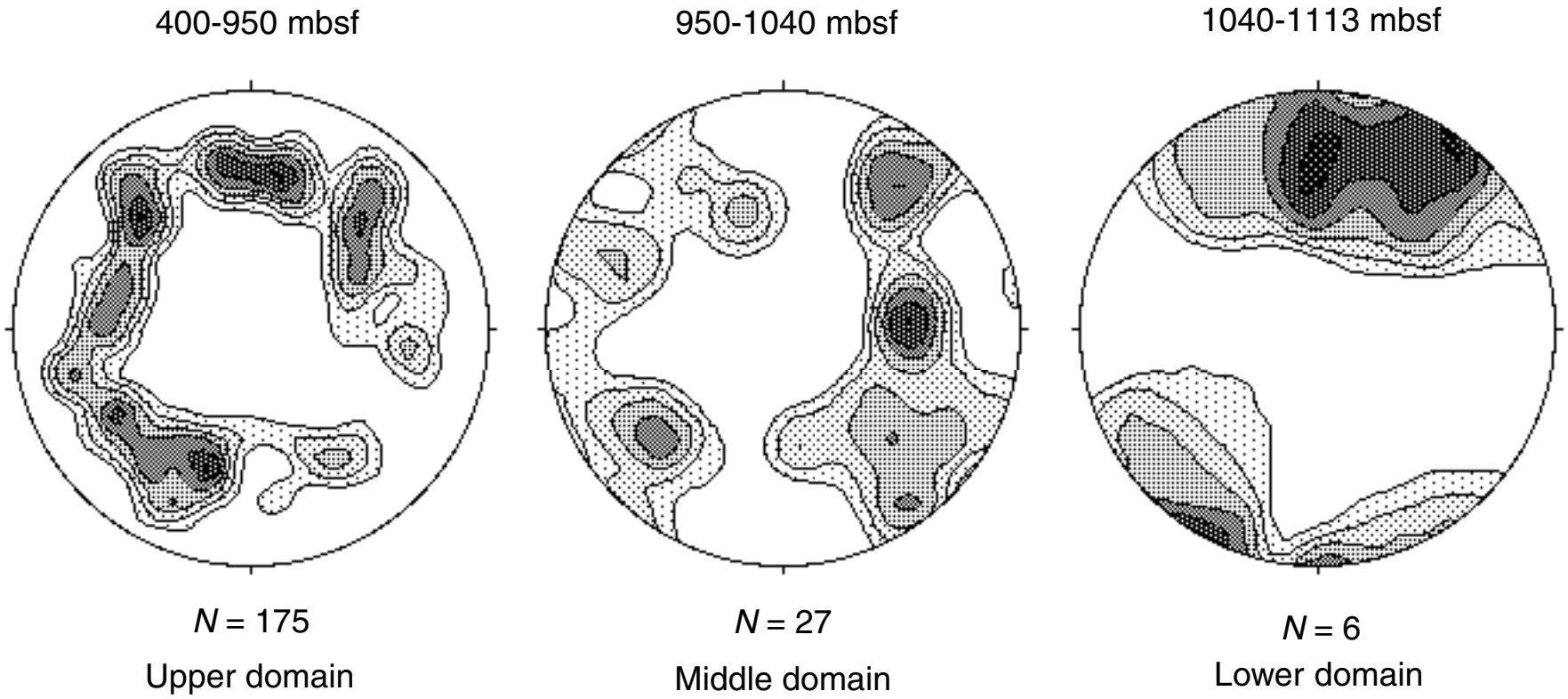

Figure F50. Bedding orientation from Hole 1151A. **A.** Dip azimuth of bedding. **B.** Dip angle of bedding.

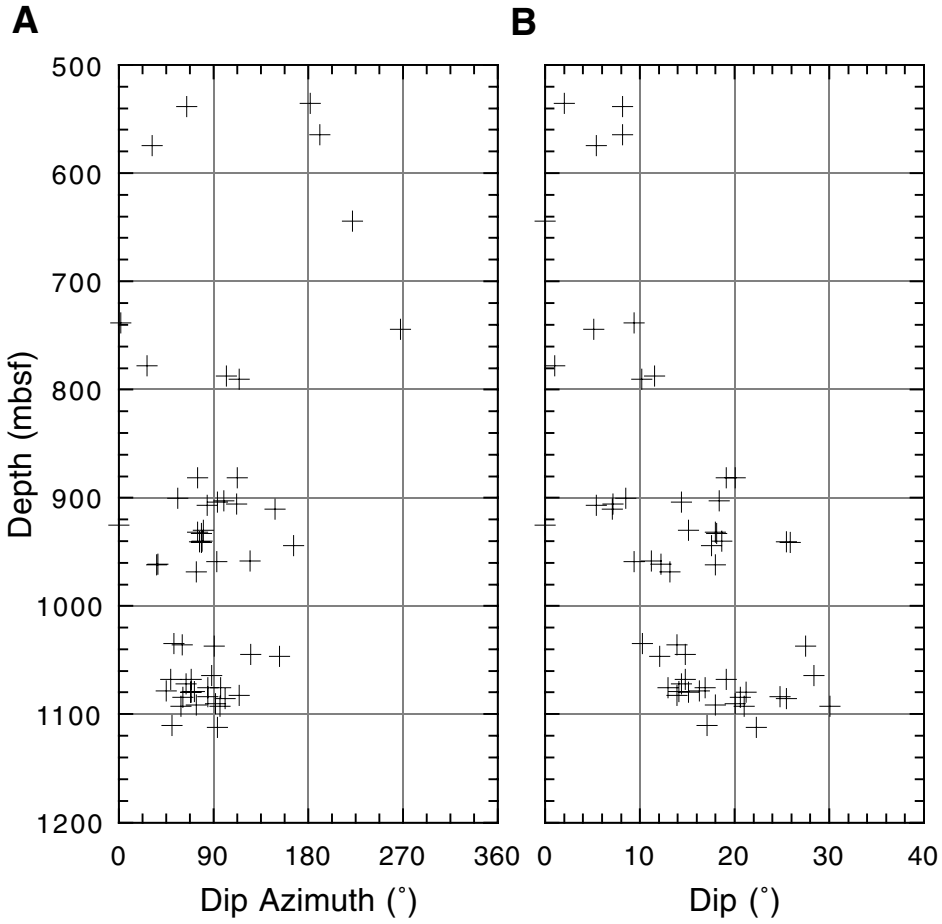

Table T1. Site 1151 coring summary. (See table notes. Continued on next two pages.)

Hole 1151A
Latitude: 38.7519913° (38°45.1195′N)
Longitude: 143.334403° (143°20.0642′E)
Time on hole: 115.75 hr (2200 hr, 28 July 1999–1745 hr, 2 August 1999)
Time on site: 361.50 hr
Seafloor (drill-pipe measurement from rig floor, mbrf): 2193.7
Distance between rig floor and sea level (m): 11.50
Water depth (drill-pipe measurement from sea level, m): 2182.2
Total depth (from rig floor, mbrf): 3307.3
Total penetration (mbsf): 1113.6
Total length of cored section (m): 1035.6
Total length of drilled intervals (m): 78.0
Total core recovered (m): 707.57
Core recovery (%): 68.3
Total number of cores: 108
Total number of drilled intervals: 1

Hole 1151B
Latitude: 38.752073° (38°45.1244′N)
Longitude: 143.3335783° (143°20.0147′E)
Time on hole: 168 hr (1745 hr, 2 August 1999–1745 hr, 9 August 1999)
Seafloor (drill-pipe measurement from rig floor, mbrf): 2193.7
Distance between rig floor and sea level (m): 12.1
Water depth (drill-pipe measurement from sea level, m): 2181.6
Total depth (from rig floor, mbrf): 3306.7
Total penetration (mbsf): 1113.0
Total length of cored section (m): 0.0
Total length of drilled intervals (m): 1113.00
Drilling, casing, emplacement of downhole instrument. No coring.

Hole 1151C
Latitude: 38.750337° (38°45.0202′N)
Longitude: 143.3340417° (143°20.0425′E)
Time on hole: 16 hr (1745 hr, 9 August 1999–0945 hr, 10 August 1999)
Seafloor (drill-pipe measurement from rig floor, mbrf): 2186.3
Distance between rig floor and sea level (m): 12.1
Water depth (drill-pipe measurement from sea level, m): 2174.2
Total depth (from rig floor, mbrf): 2283.5
Total penetration (mbsf): 97.2
Total length of cored section (m): 97.2
Total core recovered (m): 101.75
Core recovery (%): 104.7
Total number of cores: 11

Hole 1151D
Latitude: 38.75023° (38°45.0138′N)
Longitude: 143.3340683° (143°20.0441′E)
Time on hole: 61.75 hr (0945 hr, 10 August 1999–2330 hr, 12 August 1999)
Seafloor (drill-pipe measurement from rig floor, mbrf): 2184.0
Distance between rig floor and sea level (m): 12.1
Water depth (drill-pipe measurement from sea level, m): 2171.9
Total depth (from rig floor, mbrf): 3058.0
Total penetration (mbsf): 874.0
Total length of cored section (m): 93.0
Total length of drilled intervals (m): 781.0
Total core recovered (m): 96.19
Core recovery (%): 103.4
Total number of cores:10

Core	Date (1999)	Time (local)	Depth (mbsf) Top	Depth (mbsf) Bottom	Length (m) Cored	Length (m) Recovered	Recovery (%)	Comments
186-1151A-								
1W			*****Drilled from 0 to 78.0 mbsf*****					Drilled. Jet in.
2R	29 July	1130	78.0	83.7	5.7	4.11	72.1	
3R	29 July	1200	83.7	93.3	9.6	8.85	92.2	
4R	29 July	1225	93.3	102.9	9.6	6.25	65.1	
5R	29 July	1255	102.9	112.6	9.7	3.05	31.4	
6R	29 July	1330	112.6	122.2	9.6	5.52	57.5	
7R	29 July	1355	122.2	131.8	9.6	4.30	44.8	
8R	29 July	1425	131.8	141.4	9.6	5.02	52.3	
9R	29 July	1455	141.4	151.0	9.6	5.81	60.5	
10R	29 July	1525	151.0	160.6	9.6	7.67	79.9	
11R	29 July	1550	160.6	170.2	9.6	8.30	86.5	

Table T1 (continued).

Core	Date (1999)	Time (local)	Depth (mbsf) Top	Depth (mbsf) Bottom	Length (m) Cored	Length (m) Recovered	Recovery (%)	Comments
12R	29 July	1625	170.2	179.8	9.6	9.81	102.2	
13R	29 July	1650	179.8	189.5	9.7	7.36	75.9	
14R	29 July	1720	189.5	199.2	9.7	9.74	100.4	
15R	29 July	1755	199.2	208.9	9.7	9.72	100.2	
16R	29 July	1830	208.9	218.5	9.6	9.78	101.9	
17R	29 July	1900	218.5	228.1	9.6	4.29	44.7	
18R	29 July	1940	228.1	237.7	9.6	9.82	102.3	
19R	29 July	2110	237.7	247.3	9.6	7.29	75.9	DVTP after Core 18R
20R	29 July	2145	247.3	256.9	9.6	5.23	54.5	
21R	29 July	2310	256.9	266.6	9.7	9.82	101.2	DVTP after Core 20R
22R	29 July	2345	266.6	276.2	9.6	9.57	99.7	
23R	30 July	0015	276.2	285.9	9.7	8.88	91.6	
24R	30 July	0045	285.9	295.6	9.7	9.30	95.9	
25R	30 July	0115	295.6	305.3	9.7	9.82	101.2	
26R	30 July	0145	305.3	314.9	9.6	7.27	75.7	
27R	30 July	0215	314.9	324.6	9.7	6.57	67.7	
28R	30 July	0245	324.6	334.2	9.6	8.81	91.8	
29R	30 July	0315	334.2	343.9	9.7	9.84	101.4	
30R	30 July	0345	343.9	353.6	9.7	9.69	99.9	
31R	30 July	0415	353.6	363.2	9.6	7.42	77.3	
32R	30 July	0445	363.2	372.9	9.7	3.87	39.9	
33R	30 July	0615	372.9	382.5	9.6	4.74	49.4	DVTP after Core 32R
34R	30 July	0645	382.5	392.1	9.6	5.64	58.8	
35R	30 July	0715	392.1	401.4	9.3	3.95	42.5	
36R	30 July	0745	401.4	411.0	9.6	5.12	53.3	
37R	30 July	0820	411.0	420.6	9.6	4.46	46.5	
38R	30 July	0850	420.6	430.3	9.7	5.64	58.1	
39R	30 July	0925	430.3	439.9	9.6	3.37	35.1	
40R	30 July	0955	439.9	449.5	9.6	5.49	57.2	
41R	30 July	1025	449.5	459.2	9.7	5.53	57.0	
42R	30 July	1100	459.2	468.8	9.6	5.28	55.0	
43R	30 July	1130	468.8	478.4	9.6	4.52	47.1	
44R	30 July	1205	478.4	488.0	9.6	8.90	92.7	
45R	30 July	1245	488.0	497.6	9.6	4.26	44.4	
46R	30 July	1325	497.6	507.2	9.6	8.20	85.4	
47R	30 July	1410	507.2	516.8	9.6	8.98	93.5	
48R	30 July	1450	516.8	526.4	9.6	7.73	80.5	
49R	30 July	1520	526.4	536.0	9.6	7.17	74.7	
50R	30 July	1625	536.0	545.7	9.7	5.98	61.7	
51R	30 July	1700	545.7	555.4	9.7	8.97	92.5	
52R	30 July	1740	555.4	565.1	9.7	8.63	89.0	
53R	30 July	1825	565.1	574.7	9.6	8.22	85.6	
54R	30 July	1900	574.7	584.3	9.6	8.10	84.4	
55R	30 July	1940	584.3	593.9	9.6	0.13	1.4	
56R	30 July	2045	593.9	603.5	9.6	2.61	27.2	
57R	30 July	2125	603.5	613.2	9.7	6.38	65.8	
58R	30 July	2205	613.2	622.9	9.7	9.79	100.9	
59R	30 July	2310	622.9	632.5	9.6	8.47	88.2	
60R	31 July	0005	632.5	642.1	9.6	8.29	86.4	
61R	31 July	0110	642.1	651.6	9.5	6.96	73.3	
62R	31 July	0200	651.6	661.2	9.6	1.23	12.8	
63R	31 July	0300	661.2	670.8	9.6	3.13	32.6	
64R	31 July	0400	670.8	680.2	9.4	0.37	3.9	
65R	31 July	0525	680.2	689.8	9.6	8.22	85.6	
66R	31 July	0630	689.8	699.4	9.6	3.65	38.0	
67R	31 July	0730	699.4	709.0	9.6	6.25	65.1	
68R	31 July	0830	709.0	718.6	9.6	9.87	102.8	
69R	31 July	0930	718.6	728.3	9.7	7.19	74.1	
70R	31 July	1100	728.3	738.0	9.7	3.86	39.8	
71R	31 July	1200	738.0	747.7	9.7	9.12	94.0	
72R	31 July	1300	747.7	757.3	9.6	7.78	81.0	
73R	31 July	1400	757.3	766.9	9.6	9.85	102.6	
74R	31 July	1515	766.9	776.5	9.6	7.92	82.5	
75R	31 July	1620	776.5	786.1	9.6	7.72	80.4	
76R	31 July	1750	786.1	795.7	9.6	8.50	88.5	
77R	31 July	1850	795.7	805.4	9.7	4.96	51.1	
78R	31 July	1950	805.4	815.0	9.6	9.16	95.4	
79R	31 July	2100	815.0	824.6	9.6	2.00	20.8	

Table T1 (continued).

Core	Date (1999)	Time (local)	Depth (mbsf) Top	Depth (mbsf) Bottom	Length (m) Cored	Length (m) Recovered	Recovery (%)	Comments
80R	31 July	2230	824.6	834.2	9.6	9.89	103.0	
81R	31 July	2330	834.2	843.8	9.6	2.77	28.9	
82R	1 Aug	0030	843.8	853.4	9.6	7.15	74.5	
83R	1 Aug	0130	853.4	863.1	9.7	0.00	0.0	
84R	1 Aug	0230	863.1	872.8	9.7	8.98	92.6	
85R	1 Aug	0335	872.8	882.3	9.5	9.68	101.9	
86R	1 Aug	0515	882.3	891.9	9.6	4.32	45.0	
87R	1 Aug	0625	891.9	901.6	9.7	5.83	60.1	
88R	1 Aug	0730	901.6	911.2	9.6	9.49	98.9	
89R	1 Aug	0830	911.2	920.8	9.6	9.82	102.3	
90R	1 Aug	0940	920.8	930.4	9.6	5.33	55.5	
91R	1 Aug	1120	930.4	940.1	9.7	9.16	94.4	
92R	1 Aug	1220	940.1	949.7	9.6	8.03	83.7	
93R	1 Aug	1340	949.7	959.3	9.6	4.07	42.4	
94R	1 Aug	1450	959.3	968.9	9.6	3.49	36.4	
95R	1 Aug	1600	968.9	978.6	9.7	1.13	11.7	
96R	1 Aug	1750	978.6	988.2	9.6	3.77	39.3	
97R	1 Aug	1850	988.2	997.8	9.6	7.66	79.8	
98R	1 Aug	2005	997.8	1007.4	9.6	5.95	62.0	
99R	1 Aug	2115	1007.4	1017.0	9.6	2.16	22.5	
100R	1 Aug	2220	1017.0	1026.6	9.6	3.60	37.5	
101R	1 Aug	2340	1026.6	1036.2	9.6	2.21	23.0	
102R	2 Aug	0140	1036.2	1045.9	9.7	3.34	34.4	
103R	2 Aug	0300	1045.9	1055.6	9.7	2.97	30.6	
104R	2 Aug	0405	1055.6	1065.3	9.7	5.63	58.0	
105R	2 Aug	0520	1065.3	1075.0	9.7	9.16	94.4	
106R	2 Aug	0635	1075.0	1084.6	9.6	8.13	84.7	
107R	2 Aug	0830	1084.6	1094.3	9.7	9.39	96.8	
108R	2 Aug	0940	1094.3	1103.9	9.6	9.80	102.1	
109R	2 Aug	1110	1103.9	1113.6	9.7	9.59	98.9	
Coring total:					1035.6	707.57	68.3	
Drilled total:					78.0			
Total:					1113.6			
186-1151C-								
1H	10 Aug	0100	0	2.2	2.2	2.15	97.73	
2H	10 Aug	0145	2.2	11.7	9.5	9.95	104.74	
3H	10 Aug	0225	11.7	21.2	9.5	9.79	103.05	
4H	10 Aug	0330	21.2	30.7	9.5	10.43	109.79	Adara
5H	10 Aug	0425	30.7	40.2	9.5	9.66	101.68	
6H	10 Aug	0510	40.2	49.7	9.5	9.95	104.74	
7H	10 Aug	0555	49.7	59.2	9.5	9.81	103.26	
8H	10 Aug	0640	59.2	68.7	9.5	10.15	106.84	
9H	10 Aug	0720	68.7	78.2	9.5	9.73	102.42	
10H	10 Aug	0800	78.2	87.7	9.5	10.23	107.68	
11H	10 Aug	0845	87.7	97.2	9.5	9.9	104.21	
Total:					97.2	101.75	104.68	
186-1151D-								
1H	10 Aug	1040	0.0	7.5	7.5	7.56	100.8	
2H	10 Aug	1115	7.5	17.0	9.5	9.99	105.2	
3H	10 Aug	1200	17.0	26.5	9.5	9.93	104.5	
4H	10 Aug	1235	26.5	36.0	9.5	9.96	104.8	
5H	10 Aug	1325	36.0	45.5	9.5	9.76	102.7	
6H	10 Aug	1400	45.5	55.0	9.5	9.92	104.4	
7H	10 Aug	1445	55.0	64.5	9.5	9.61	101.2	
8H	10 Aug	1520	64.5	74.0	9.5	10.18	107.2	
9H	10 Aug	1600	74.0	83.5	9.5	9.47	99.7	
10H	10 Aug	1700	83.5	93.0	9.5	9.81	103.3	
			*****Drilled from 93.0 to 874.0 mbsf*****					
Coring total:					93	96.19	103.43	
Drilled total:					781.0			
Total:					874.0			

Notes: DVTP = Davis-Villinger temperature probe, Adara = Adara temperature tool. This table is also available in **ASCII format**.

Table T2. X-ray diffraction data, Site 1151.

						Interval (cm)				Intensity (cps)						
Leg	Site	Hole	Core	Type	Section	Top	Bottom	Depth (mbsf)	Janus Code	Quartz (100)	Quartz (101)	Feldspars	Clinopyroxene	Calcite (104)	Dolomite (104)	Halite (200)
186	1151	A	2	R	1	77	79	78.77	1335533	192	736	268	39	570	11	284
186	1151	A	2	R	2	96	97	80.46	1335534	206	841	497	97	63	19	207
186	1151	A	2	R	3	82	83	81.82	1335538	292	1373	529	169	327	23	144
186	1151	A	3	R	1	66	67	84.36	1335563	166	1191	353	73	54	58	189
186	1151	A	3	R	3	66	67	87.36	1335612	149	763	226	57	378	17	235
186	1151	A	3	R	4	20	21	88.40	1335582	119	424	215	33	711	0	246
186	1151	A	4	R	1	71	72	94.01	1335677	168	750	311	51	136	113	214
186	1151	A	4	R	3	71	72	97.01	1335678	165	1009	291	71	44	29	299

						Interval (cm)				14-Å minerals			10-Å minerals		
Leg	Site	Hole	Core	Type	Section	Top	Bottom	Depth (mbsf)	Janus Code	Peak intensity (cps)	Area intensity (cps)	Relative (%)	Peak Intensity (cps)	10-Å minerals area intensity (cps)	Relative (%)
186	1151	A	2	R	1	77	79	78.77	1335533	35	2230	22	38	1365	53
186	1151	A	2	R	2	96	97	80.46	1335534	35	2607	28	45	1118	48
186	1151	A	2	R	3	82	83	81.82	1335538	29	1210	12	59	1329	54
186	1151	A	3	R	1	66	67	84.36	1335563	22	2001	19	52	1547	59
186	1151	A	3	R	3	66	67	87.36	1335612	30	2521	38	34	1013	62
186	1151	A	3	R	4	20	21	88.40	1335582	25	1073	16	28	911	53
186	1151	A	4	R	1	71	72	94.01	1335677	40	2566	23	61	1499	53
186	1151	A	4	R	3	71	72	97.01	1335678	32	2295	25	40	1072	47

						Interval (cm)				7-Å minerals					
Leg	Site	Hole	Core	Type	Section	Top	Bottom	Depth (mbsf)	Janus Code	Peak intensity (cps)	7-Å minerals area intensity (cps)	Relative (%)	Opal-A hump (cps)	Opal-CT area (cps)	CT/A ratio
186	1151	A	2	R	1	77	79	78.77	1335533	42	1272	25	94.0825	2157.02	22.93
186	1151	A	2	R	2	96	97	80.46	1335534	43	1083	23	102.7675	1756.65	17.09
186	1151	A	2	R	3	82	83	81.82	1335538	67	1697	34	88.0725	1423.385	16.16
186	1151	A	3	R	1	66	67	84.36	1335563	46	1119	21	125.2050	1892.475	15.12
186	1151	A	3	R	3	66	67	87.36	1335612	0	0	0	111.3825	2589.820	23.25
186	1151	A	3	R	4	20	21	88.40	1335582	28	1086	32	121.2050	3121.000	25.75
186	1151	A	4	R	1	71	72	94.01	1335677	54	1393	25	102.2125	3075.065	30.09
186	1151	A	4	R	3	71	72	97.01	1335678	44	1228	27	141.2975	3472.185	24.57

Note: Only a portion of this table appears here. The complete table is available in **ASCII format.**

Table T3. Number of sand and silt layers and patches/accumulations in recovered core, Site 1151.

							Sandy layer						Silty layer						Sandy and silty layers	
							Layer		Patch and accumulation		Total		Layer		Patch and accumulation		Total		Total	
Leg	Site	Hole	Core	Type	Depth (mbsf)	Recovered length (m)	(Number/ core)	(Number/ recovered m)	(Number/ core)	(Number/ recovered m)	(Number/ core)	(Number/ recovered m)	(Number/ core)	(Number/ recovered m)	(Number/ core)	(Number/ recovered m)	(Number/ core)	(Number/ recovered m)	(Number/ core)	(Number/ recovered m)
186	1151	C	1	H	0	2.15			1	0.2	1	0.5			3	0.7	3	0.7	4	1.9
186	1151	C	2	H	2.20	9.95	3	0.7			3	0.3			7	1.7	7	1.7	10	1.0
186	1151	C	3	H	11.70	9.79	1	0.2	3	0.7	4	0.4	1	0.2	5	1.2	6	1.5	10	1.0
186	1151	C	4	H	21.20	10.43	2	0.5			0		1	0.2	10	2.4	11	2.7	13	1.2
186	1151	C	5	H	30.70	9.66			2	0.5	2	0.2			12	2.9	12	2.9	14	1.5
186	1151	C	6	H	40.20	9.95	3	0.7	3	0.7	6	0.6	1	0.2	12	2.9	13	3.2	19	1.9
186	1151	C	7	H	49.70	9.81			3	0.7	3	0.3	1	0.2	17	4.1	18	4.4	21	2.1
186	1151	C	8	H	59.20	10.15			2	0.5	2	0.2			12	2.9	12	2.9	14	1.4
186	1151	C	9	H	68.70	9.73	4	1.0			4	0.4	1	0.2	7	1.7	8	1.9	12	1.2
186	1151	C	10	H	78.20	10.23	1	0.2	1	0.2	1	0.2	5	1.2	10	2.4	15	3.6	17	1.7
186	1151	C	11	H	87.70	9.90			6	1.5	6	0.6	1	0.2	2	0.5	3	0.7	9	0.9
186	1151	A	2	R	83.70	4.11							1	0.2	1	0.2	2	0.5	2	0.5
186	1151	A	3	R	93.30	8.85							1	0.2	4	1.0	5	1.2	5	0.6
186	1151	A	4	R	102.90	6.25														
186	1151	A	5	R	112.60	3.05									1	0.2	1	0.2	1	0.3
186	1151	A	6	R	122.20	5.52			1	0.2	1	0.2			6	1.5	6	1.5	7	1.3
186	1151	A	7	R	131.80	4.30									2	0.5	2	0.5	2	0.5
186	1151	A	8	R	141.40	5.02									6	1.5	6	1.5	6	1.2
186	1151	A	9	R	151.00	5.81							1	0.2	2	0.5	3	0.7	3	0.5
186	1151	A	10	R	160.60	7.67	1	0.2	3	0.7	4	1.0			6	1.5	6	1.5	10	1.3
186	1151	A	11	R	170.20	8.30	1	0.2			1	0.2			3	0.7	3	0.7	4	0.5
186	1151	A	12	R	179.80	9.81			2	0.5	2	0.5			1	0.2	1	0.2	3	0.3
186	1151	A	13	R	189.50	7.36	1	0.2	1	0.2	2	0.5			3	0.7	3	0.7	5	0.7
186	1151	A	14	R	199.20	9.74	1	0.2	3	0.7	4	1.0			3	0.7	3	0.7	7	0.7
186	1151	A	15	R	208.90	9.72			4	1.0	4	1.0			4	1.0	4	1.0	8	0.8
186	1151	A	16	R	218.50	9.78			6	1.5	6	1.5			1	0.2	1	0.2	7	0.7
186	1151	A	17	R	228.10	4.29									2	0.5	2	0.5	2	0.5
186	1151	A	18	R	237.70	9.82			1	0.2	1	0.2							1	0.1
186	1151	A	19	R	247.30	7.29														
186	1151	A	20	R	256.90	5.23														
186	1151	A	21	R	266.60	9.82			1	0.2	1	0.2			2	0.5	2	0.5	3	0.3
186	1151	A	22	R	276.20	9.57									2	0.5	2	0.5	2	0.2
186	1151	A	23	R	285.90	8.88							1	0.2	1	0.2	2	0.5	2	0.2
186	1151	A	24	R	295.60	9.30									1	0.2	1	0.2	1	0.1
186	1151	A	25	R	305.3	9.82	1	0.2	1	0.2	2	0.5							2	0.2
186	1151	A	26	R	314.9	7.27														
186	1151	A	27	R	324.6	6.57									1	0.2	1	0.2	1	0.2
186	1151	A	28	R	334.2	8.81			2	0.5	2	0.5							2	0.2
186	1151	A	29	R	343.9	9.84							1	0.2	2	0.5	3	0.7	3	0.3
186	1151	A	30	R	353.6	9.69			1	0.2	1	0.2			1	0.2	1	0.2	2	0.2
186	1151	A	31	R	363.2	7.42			2	0.5	2	0.5			1	0.2	1	0.2	3	0.4
186	1151	A	32	R	372.9	3.87	2	0.5			2	0.5			2	0.5	2	0.5	4	1.0

Notes: Blank = No data. Only a portion of this table appears here. The complete table is available in **ASCII format**.

Table T4. Number of pumice and primary, reworked, and bioturbated ash layers, Site 1151. (**See table notes.** Continued on next page.)

Leg	Site	Hole	Core	Type	Depth top (mbsf)	Recovered length (m)	Primary and reworked ash		Bioturbated ash patches		Pumice grains or layers	
							(Layers/core)	(Layers/m)	(Layers/core)	(Layers/m)	(Layers/core)	(Layers/m)
186	1151	C	1	H	0.00	2.15			1	0.5	2	0.9
186	1151	C	2	H	2.20	9.95	2	0.2	1	0.1	5	0.5
186	1151	C	3	H	11.70	9.79	1	0.1	1	0.1	2	0.2
186	1151	C	4	H	21.20	10.43			4	0.4		
186	1151	C	5	H	30.70	9.66	1	0.1	9	0.9	2	0.2
186	1151	C	6	H	40.20	9.95	2	0.2	3	0.3	3	0.3
186	1151	C	7	H	49.70	9.81	3	0.3	4	0.4	2	0.2
186	1151	C	8	H	59.20	10.15	4	0.4	4	0.4	3	0.3
186	1151	C	9	H	68.70	9.73	2	0.2	8	0.8	3	0.3
186	1151	C	10	H	78.20	10.23	4	0.4	3	0.3	8	0.8
186	1151	C	11	H	87.70	9.90	1	0.1	6	0.6	8	0.8
186	1151	A	2	R	83.70	4.11			2	0.5		
186	1151	A	3	R	93.30	8.85	1	0.1	1	0.1	4	0.5
186	1151	A	4	R	102.90	6.25			6	1.0		
186	1151	A	5	R	112.60	3.05						
186	1151	A	6	R	122.20	5.52	1	0.2	3	0.5		
186	1151	A	7	R	131.80	4.30	2	0.5				
186	1151	A	8	R	141.40	5.02			2	0.4		
186	1151	A	9	R	151.00	5.81	1	0.2	3	0.5	1	0.2
186	1151	A	10	R	160.60	7.67	2	0.3	1	0.1	8	1.0
186	1151	A	11	R	170.20	8.30	1	0.1	4	0.5	2	0.2
186	1151	A	12	R	179.80	9.81			1	0.1	4	0.4
186	1151	A	13	R	189.50	7.36			2	0.3	1	0.1
186	1151	A	14	R	199.20	9.74	1	0.1	6	0.6	4	0.4
186	1151	A	15	R	208.90	9.72	3	0.3	16	1.6	6	0.6
186	1151	A	16	R	218.50	9.78	3	0.3	5	0.5	4	0.4
186	1151	A	17	R	228.10	4.29			3	0.7	2	0.5
186	1151	A	18	R	237.70	9.82			1	0.1	1	0.1
186	1151	A	19	R	247.30	7.29			1	0.1		
186	1151	A	20	R	256.90	5.23			1	0.2	1	0.2
186	1151	A	21	R	266.60	9.82	2	0.2	2	0.2		
186	1151	A	22	R	276.20	9.57	1	0.1				
186	1151	A	23	R	285.90	8.88					2	0.2
186	1151	A	24	R	295.60	9.30						
186	1151	A	25	R	305.30	9.82	1	0.1	1	0.1	1	0.1
186	1151	A	26	R	314.90	7.27	2	0.3			2	0.3
186	1151	A	27	R	324.60	6.57			1	0.2	1	0.2
186	1151	A	28	R	334.20	8.81					2	0.2
186	1151	A	29	R	343.90	9.84	1	0.1	1	0.1		
186	1151	A	30	R	353.60	9.69	2	0.2				
186	1151	A	31	R	363.20	7.42	2	0.3			1	0.1
186	1151	A	32	R	372.90	3.87	2	0.5			1	0.3
186	1151	A	33	R	382.50	4.74			1	0.2	2	0.4
186	1151	A	34	R	392.10	5.64						
186	1151	A	35	R	401.40	3.95					1	0.3
186	1151	A	36	R	411.00	5.12	1	0.2				
186	1151	A	37	R	420.60	4.46	1	0.2	2	0.4		
186	1151	A	38	R	430.30	5.64	1	0.2			3	0.5
186	1151	A	39	R	439.90	3.37						
186	1151	A	40	R	449.50	5.49	3	0.5	2	0.4	1	0.2
186	1151	A	41	R	459.20	5.53			3	0.5	7	1.3
186	1151	A	42	R	468.80	5.28	1	0.2	1	0.2	3	0.6
186	1151	A	43	R	478.40	4.52	1	0.2	1	0.2	5	1.1
186	1151	A	44	R	488.00	8.90			2	0.2		
186	1151	A	45	R	497.60	4.26						
186	1151	A	46	R	507.20	8.20	2	0.2	4	0.5	1	0.1
186	1151	A	47	R	516.80	8.98			4	0.4		
186	1151	A	48	R	526.40	7.73	3	0.4				
186	1151	A	49	R	536.00	7.17	1	0.1	2	0.3	1	0.1
186	1151	A	50	R	545.70	5.98	2	0.3			2	0.3
186	1151	A	51	R	555.40	8.97			1	0.1	1	0.1
186	1151	A	52	R	565.10	8.63					1	0.1
186	1151	A	53	R	574.70	8.22	5	0.6			1	0.1
186	1151	A	54	R	584.30	8.10					1	0.1
186	1151	A	55	R	593.90	0.13						
186	1151	A	56	R	603.50	2.61						
186	1151	A	57	R	613.20	6.38	1	0.2	1	0.2	5	0.8

Table T4 (continued).

Leg	Site	Hole	Core	Type	Depth top (mbsf)	Recovered length (m)	Primary and reworked ash		Bioturbated ash patches		Pumice grains or layers	
							(Layers/core)	(Layers/m)	(Layers/core)	(Layers/m)	(Layers/core)	(Layers/m)
186	1151	A	58	R	622.90	9.79	1	0.1	3	0.3	3	0.3
186	1151	A	59	R	632.50	8.47			1	0.1	5	0.6
186	1151	A	60	R	642.10	8.29			1	0.1	2	0.2
186	1151	A	61	R	651.60	6.96					6	0.9
186	1151	A	62	R	661.20	1.23						
186	1151	A	63	R	670.80	3.13						
186	1151	A	64	R	680.20	0.37						
186	1151	A	65	R	689.80	8.22	2	0.2	2	0.2		
186	1151	A	66	R	699.40	3.65			1	0.3	1	0.3
186	1151	A	67	R	709.00	6.25					3	0.5
186	1151	A	68	R	718.60	9.87			1	0.1	1	0.1
186	1151	A	69	R	728.30	7.19						
186	1151	A	70	R	737.90	3.86	1	0.3				
186	1151	A	71	R	747.60	9.12			2	0.2	3	0.3
186	1151	A	72	R	757.30	7.78						
186	1151	A	73	R	766.90	9.85	1	0.1				
186	1151	A	74	R	776.50	7.92	4	0.5				
186	1151	A	75	R	786.10	7.72	1	0.1	1	0.1		
186	1151	A	76	R	795.70	8.50	4	0.5		0.0		
186	1151	A	77	R	805.40	4.96	2	0.4	1	0.2		
186	1151	A	78	R	815.00	9.16	3	0.3			7	0.8
186	1151	A	79	R	824.60	2.00					3	1.5
186	1151	A	80	R	834.20	9.89			2	0.2	6	0.6
186	1151	A	81	R	843.80	2.77	2	0.7	1	0.4	2	0.7
186	1151	A	82	R	853.40	7.15						0.0
186	1151	A	84	R	872.80	8.98	2	0.2			7	0.8
186	1151	A	85	R	882.30	9.68	1	0.1	2	0.2	3	0.3
186	1151	A	86	R	891.90	4.32	1	0.2			1	0.2
186	1151	A	87	R	901.60	5.83						
186	1151	A	88	R	911.20	9.49			1	0.1	3	0.3
186	1151	A	89	R	920.80	9.82	1	0.1	2	0.2	2	0.2
186	1151	A	90	R	930.40	5.33					2	0.4
186	1151	A	91	R	940.10	9.16					9	1.0
186	1151	A	92	R	949.70	8.22	1	0.1			5	0.6
186	1151	A	93	R	959.30	4.07					1	0.2
186	1151	A	94	R	968.90	3.49					3	0.9
186	1151	A	95	R	978.60	1.13					2	1.8
186	1151	A	96	R	988.20	3.77	1	0.3	1	0.3		
186	1151	A	97	R	997.80	7.66			1	0.1	2	0.3
186	1151	A	98	R	1007.40	5.95						
186	1151	A	99	R	1017.00	2.16						
186	1151	A	100	R	1026.60	3.60					1	0.3
186	1151	A	101	R	1036.20	2.21						0.0
186	1151	A	102	R	1045.90	3.34						
186	1151	A	103	R	1055.60	2.97					2	0.7
186	1151	A	104	R	1065.30	5.63	1	0.2			4	0.7
186	1151	A	105	R	1075.00	9.16	3	0.3			14	1.5
186	1151	A	106	R	1084.60	8.13	4	0.5			8	1.0
186	1151	A	107	R	1094.30	9.39					8	0.9
186	1151	A	108	R	1103.90	9.80	1	0.1	1	0.1	12	1.2
186	1151	A	109	R	1113.60	9.59	3	0.3	1	0.1	14	1.5

Notes: Blank = no data. This table is also available in **ASCII format**.

Table T5. Occurrences of calcareous minor lithologies and evidence of calcitic or dolomitic composition from X-ray diffraction data, Site 1151.

Number	Leg, hole, core, section	Interval (cm)		Depth (mbsf)		Occurrence in VCD	XRD identification
		Top	Bottom	Top	Bottom		
1151-D-1	186-1151A-5R-CC	5	8	105.95	105.98	Dolomitic fragment	Dolomite
1151-D-2a	186-1151A-19R-CC	11	15	244.91	244.95	Dolomitic fragment	Calcite + dolomite
1152-D-2b	186-1151A-20R-1	0	5	247.30	247.35	Dolomitic fragment	Calcite + dolomite
1151-D-3	186-1151A-21R-1	0	3	256.90	256.93	Dolomitic fragment	NS
1151-D-4	186-1151A-62R-1	0	3	651.60	651.63	Dolomitic fragment	Dolomite
1151-D-5a	186-1151A-66R-1	0	5	689.80	689.85	Dolomitic small fragment	Dolomite
1152-D-5b	186-1151A-67R-1	0	5	699.40	699.45	Dolomitic fragment	Dolomite
1151-D-6a	186-1151A-79R-2	26	45	816.76	816.95	Dolomitic layer	Dolomite
1152-D-6b	186-1151A-79R-CC	5	8	817.00	817.03	Dolomitic fragment	Dolomite
1151-D-7	186-1151A-90R-1	25	90	921.05	921.70	Dolomitic small fragment	Dolomite
1151-D-8	186-1151A-92R-4	0	80	944.34	945.14	Carbonate layer	Calcite + dolomite
1151-D-9	186-1151A-92R-CC	20	21	948.02	948.03	Dolomitic small fragment	NS
1151-D-10	186-1151A-95R-CC	3	6	982.40	982.43	Dolomitic fragment	NS
1151-D-11	186-1151A-101R-2	20	55	1027.91	1028.26	Limestone layer	Calcite
1151-D-12	186-1151A-102R-1	0	2	1036.20	1036.22	Dolomitic fragment	NS
1151-D-13	186-1151A-104R-3	89	95	1059.49	1059.55	Carbonate layer	NS
1151-D-14	186-1151A-109R-3	124	130	1108.04	1108.10	Carbonate concretion	Calcite

Note: VCD = visual core description, XRD = X-ray diffraction, NS = no sample.

Table T6. Stratigraphic occurrences and chronology of datum levels of calcareous nannofossils, Site 1151.

	Datum event	Zone (base)	Age (Ma)	Upper sample		Lower sample		Upper sample		Lower sample		Upper sample		Lower sample	
				Core, section, interval (cm)	Depth (mbsf)	Core, section, interval (cm)	Depth (mbsf)	Core, section, interval (cm)	Depth (mbsf)	Core, section, interval (cm)	Depth (mbsf)	Core, section, interval (cm)	Depth (mbsf)	Core, section, interval (cm)	Depth (mbsf)
				186-1151A-		186-1151A-		186-1151C-		186-1151C-		186-1151D-		186-1151D-	
FO	*Emiliania huxleyi*	CN15	0.248					2H-CC	12.10	3H-CC	21.44	2H-CC	17.44	3H-CC	26.88
LO	*Pseudoemiliania lacunosa*	CN14b	0.408					4H-2, 98	23.69	5H-3, 98	34.68	3H-CC	26.88	4H-CC	36.42
FO	*Gephyrocapsa parallela*	CN14a	0.94	3R-1, 10-11	84.45	3R-3, 10-11	86.80	8H-CC	69.30	9H-5, 70-77	75.40	7H-CC	64.56	8H-CC	74.63
FO	*Gephyrocapsa oceanica*							11H-2, 42	89.62	11H-CC	97.55				
FO	*Gephyrocapsa caribbeanica*	CN13b	1.71	4R-3, 10-11	96.40	4R -CC	99.51								
LO	*Discoaster brouweri*	CN13a	1.95	5R-CC	105.90	6R-CC	118.07								
LO	*Discoaster pentaradiatus*	CN12d	2.36	9R-CC	147.17	12R-5, 10-11	176.30								
LO	*Discoaster tamalis*	CN12b	2.82	12R-CC	192.01	13R-CC	202.94								
LO	*Reticulofenestra pseudoumbilicus*	CN12a	3.83	14R-CC	199.19	15R-CC	208.87								
FO	*Discoaster berggrenii*	CN9a	8.28	90R-CC	926.10	91R-CC	939.54								
FO	*Catinaster coalitus*	CN 6	10.794	98R-CC	1003.72	99R-CC	1009.53								

Note: FO = First occurrence, LO = last occurrence.

Table T7. Distribution and relative abundances of selected diatom species from Hole 1151A. (See table notes. Continued on next three pages.)

Leg	Site	Hole	Core	Type	Section	Top (cm)	Bottom (cm)	Depth (mbsf)	Diatom zones	NPD	Geological Age	Group abundance	Preservation	*Actinocyclus ellipticus*	*Actinocyclus ingens*	*Actinocyclus oculatus*	*Actinoptychus senarius*	*Aulacoseira* spp.	*Cavitatus jouseanus*	*Cocconeis costata*	*Coscinodiscus marginatus*	*Crucidenticula nicobarica*	*Delphineis simonsenii*	*Denticulopsis dimorpha*	*Denticulopsis hyalina*	*Denticulopsis katayamae*	*Denticulopsis lauta*	*Denticulopsis praedimorpha*	*Denticulopsis praelauta*	*Denticulopsis simonsenii*	*Fragilariopsis doliolus*	*Hemidiscus cuneiformis*	*Ikebea tenuis*	*Kieselviella carina*	*Koizumia tatsunokuchiensis*	*Neodenticula kamtschatica*	*Neodenticula koizumii*	*Neodenticula seminae*	*Nitzschia fossilis*	*Nitzschia reinholdii*	*Nitzschia rolandii*	*Paralia sulcata*	*Proboscia barboi*	*Proboscia curvirostris*	*Pyxidicula zabelinae*	*Rhizosolenia hebetata* f. *hiemalis*	*Rouxia californica*	*Stephanopyxis horridus*	*Stephanopyxis turris*	*Thalassionema nitzschioides*	*Thalassionema schraderi*	*Thalassiosira antiqua*	*Thalassiosira gravida*	*Thalassiosira jouseae*	*Thalassiosira latimarginata*	*Thalassiosira nidulus*	*Thalassiosira oestrupii*	*Thalassiosira praeoestrupii*	*Thalassiosira yabei*	*Thalassiothrix longissima*	*Chaetoceros* spp. (resting spores)
186	1151	A	2	R	1	70	73	78.70	*P. curvirostris*	11	Pleistocene	G	A																		R							C				R	R	R					F	F				R	F		R			R	F
186	1151	A	2	R	CC	5	8	82.08	*P. curvirostris*	11	Pleistocene	G	A							R																		C						R					R	C			F	C			R				A
186	1151	A	3	R	CC	0	5	92.50	*P. curvirostris*	11	Pleistocene	G	A								C																r	R						R						F			C	F							A
186	1151	A	4	R	2	138	142	96.18	*A. oculatus*	10	Pleistocene	VG	A			F					F																	C											F	F			F	F							C
186	1151	A	4	R	CC	15	19	99.51	*A. oculatus*	10	Pleistocene	G	A			R				R	F																	C		R			R	R					F												C
186	1151	A	5	R	CC	0	5	105.90	*A. oculatus*	10	late Pliocene	G	C			R		T		F												R						F	R	F										F				R			F				C
186	1151	A	6	R	1	70	72	113.30	*N. koizumii*	9	late Pliocene	G	A				R				F																F	C											F	F			F	R			R				C
186	1151	A	6	R	CC	8	13	118.07	*N. koizumii*	9	late Pliocene	G	A			R	R															R				r	C	C	T	C			R							F		T	F	F			F				A
186	1151	A	7	R	1	70	73	122.90	*N. koizumii*	9	late Pliocene	G	C			F																R						C					R					R	F	F										R	C
186	1151	A	7	R	CC	14	19	126.45	*N. koizumii*	9	late Pliocene	G	A			F					R															r		F	R				F						C	F			F	C							C
186	1151	A	8	R	CC	18	22	136.78	*N. koizumii*	9	late Pliocene	G	A			R																					C						R		R					F				F			R				C
186	1151	A	9	R	CC	7	11	147.17	*N. koizumii*	9	late Pliocene	G	A			R				R	R																C					T	T		C				R	F				R							A
186	1151	A	10	R	CC	18	21	158.64	*N. koizumii*	9	late Pliocene	M	A								F																F	F					C		F				C					R							F
186	1151	A	11	R	CC	12	16	168.86	*N. koizumii*	9	late Pliocene	G	A			R																					C						F						C	F				F							
186	1151	A	12	R	3	140	144	174.60	*N. koizumii-N. kamtschatica*	8	late Pliocene	G	A			R					C							r								F	C	R											R	C			R				F				
186	1151	A	12	R	CC	7	12	179.96	*N. koizumii-N. kamtschatica*	8	late Pliocene	G	A								F											R				F	C	R					R		R					F				F			R				
186	1151	A	13	R	CC	11	16	187.11	*N. koizumii-N. kamtschatica*	8	late Pliocene	G	C								F									r						R	C			R			R							F		R			R		F				C
186	1151	A	14	R	CC	9	14	199.19	*N. koizumii-N. kamtschatica*	8	early Pliocene	G	A								C											F				C	R							R						F				R			R			R	F
186	1151	A	15	R	4	72	74	204.42	*T. oestrupii*	7Bb	early Pliocene	G	A								F					r		r								C									C					F					F						F
186	1151	A	15	R	CC	0	5	208.87	*T. oestrupii*	7Bb	early Pliocene	G	C				R				F											R				C			R						F				C	F			R	R	R		F				
186	1151	A	16	R	CC	8	12	218.64	*T. oestrupii*	7Bb	early Pliocene	G	C				R															R				C				R					F					F				R			R				R
186	1151	A	17	R	CC	0	4	222.75	*T. oestrupii*	7Bb	early Pliocene	G	A								F															A													R	C				R	R						F
186	1151	A	18	R	CC	11	14	237.89	*T. oestrupii*	7Bb	early Pliocene	G	C								C															C							R		R				T	F		F			F		F				F
186	1151	A	19	R	CC	16	19	244.96	*T. oestrupii*	7Bb	early Pliocene	G	A				R				R															C									R					A		F		R			R				F
186	1151	A	20	R	CC	12	15	252.50	*T. oestrupii*	7Bb	early Pliocene	G	C				R			R	C															C						T								F		F					T				
186	1151	A	21	R	CC	12	15	266.69	*T. oestrupii*	7Bb	early Pliocene	G	A				R				C															C			R										F	F				R	R						C
186	1151	A	22	R	CC	12	15	276.14	*T. oestrupii*	7Bb	early Pliocene	VG	C								C														F	C			R											F			R	R	R						R
186	1151	A	23	R	CC	14	17	285.05	*T. oestrupii*	7Bb	early Pliocene	M	A								C															C			R						R					F		R		R			R				F
186	1151	A	24	R	CC	11	14	295.17	*T. oestrupii*	7Bb	early Pliocene	G	C				R																			C									R					F		F		R							F
186	1151	A	25	R	CC	12	15	305.39	*T. oestrupii*	7Bb	early Pliocene	M	C																							C			T						F					C		F				R					C
186	1151	A	26	R	CC	14	17	312.54	*T. oestrupii*	7Bb	late Miocene	G	C				F				F															C							T		F				R	F		T		R							F
186	1151	A	27	R	CC	17	20	321.44	*T. oestrupii*	7Bb	late Miocene	G	C				R																			C							R		F	R			F	F		F									C
186	1151	A	28	R	CC	14	17	333.38	*T. oestrupii*	7Bb	late Miocene	G	A				R				F															C														C		F			R	R	R				F
186	1151	A	29	R	CC	14	17	344.01	*T. oestrupii*	7Bb	late Miocene	G	A				F				F															C									F					F		F		R	R	T					F
186	1151	A	30	R	CC	10	13	353.56	*T. oestrupii*	7Bb	late Miocene	G	A								F															C							R						F	C							F				F
186	1151	A	31	R	CC	14	17	360.99	*T. oestrupii*	7Bb	late Miocene	G	C								F															C							F						R	C				T			R				F

Table T7 (continued).

Leg	Site	Hole	Core	Type	Section	Top (cm)	Bottom (cm)	Depth (mbsf)	Diatom zones	NPD	Geological Age	Group abundance	Preservation	*Actinocyclus ellipticus*	*Actinocyclus ingens*	*Actinocyclus oculatus*	*Actinoptychus senarius*	*Aulacoseira* spp.	*Cavitatus jouseanus*	*Cocconeis costata*	*Coscinodiscus marginatus*	*Crucidenticula nicobarica*	*Delphineis simonsenii*	*Denticulopsis dimorpha*	*Denticulopsis hyalina*	*Denticulopsis katayamae*	*Denticulopsis lauta*	*Denticulopsis praedimorpha*	*Denticulopsis praelauta*	*Denticulopsis simonsenii*	*Fragilariopsis doliolus*	*Hemidiscus cuneiformis*	*Ikebea tenuis*	*Kieselviella carina*	*Koizumia tatsunokuchiensis*	*Neodenticula kamtschatica*	*Neodenticula koizumii*	*Neodenticula seminae*	*Nitzschia fossilis*	*Nitzschia reinholdii*	*Nitzschia rolandii*	*Paralia sulcata*	*Proboscia barboi*	*Proboscia curvirostris*	*Pyxidicula zabelinae*	*Rhizosolenia hebetata* f. *hiemalis*	*Rouxia californica*	*Stephanopyxis horridus*	*Stephanopyxis turris*	*Thalassionema nitzschioides*	*Thalassionema schraderi*	*Thalassiosira antiqua*	*Thalassiosira gravida*	*Thalassiosira jouseae*	*Thalassiosira latimarginata*	*Thalassiosira nidulus*	*Thalassiosira oestrupii*	*Thalassiosira praeoestrupii*	*Thalassiosira yabei*	*Thalassiothrix longissima*	*Chaetoceros* spp. (resting spores)
186	1151	A	32	R	CC	15	17	367.05	*T. oestrupii*	7Bb	late Miocene	M	C				R				C															C							F		R					F		R					R	T			F
186	1151	A	33	R	CC	19	22	377.61	*T. oestrupii*	7Bb	late Miocene	G	A				R				R															C													F	C		R				R	R				R
186	1151	A	34	R	CC	13	16	388.11	*T. Oestrupii*	7Bb	late Miocene	M	C				R			R	R		R												R	C														F						R	R				R
186	1151	A	35	R	CC	17	21	396.01	*T. oestrupii*	7Bb	late Miocene	M	F				R																			F						T				R				F		T				R	T				R
186	1151	A	36	R	CC	12	15	406.49	*T. oestrupii*	7Bb	late Miocene	G	C				T			R	C									r						C									C					F							R	R		R	F
186	1151	A	37	R	CC	11	14	415.43	*T. oestrupii*	7Bb	late Miocene	G	A				R			R	C															C				T			T		F				R	C		R					R				F
186	1151	A	38	R	1	70	73	421.30	*T. oestrupii*	7Bb	late Miocene	G	C				R				C		R												R	C			R						F					F							T				F
186	1151	A	38	R	CC	9	12	426.21	*N. kamtschatica*	7Ba	late Miocene	M	C								C															C			R						F				R			R		R							F
186	1151	A	39	R	CC	12	15	433.64	*N. kamtschatica*	7Ba	late Miocene	G	C								F		T													C									F				R	F							R				R	F
186	1151	A	40	R	CC	17	20	445.36	*N. kamtschatica*	7Ba	late Miocene	M	F								F															C									F					F							R					R
186	1151	A	41	R	CC	12	14	455.01	*N. kamtschatica*	7Ba	late Miocene	G	C				R																			C									F					F							R					R
186	1151	A	42	R	CC	11	13	464.46	*N. kamtschatica*	7Ba	late Miocene	G	A													r										A			R						F					C		R					T		T			
186	1151	A	43	R	CC	9	11	473.30	*N. kamtschatica*	7Ba	late Miocene	G	A				R				F															C									R					F				T				R			F
186	1151	A	44	R	CC	0	5	487.25	*N. kamtschatica*	7Ba	late Miocene	G	C								C															C									C				R	F							R					
186	1151	A	45	R	CC	15	20	492.21	*N. kamtschatica*	7Ba	late Miocene	G	A				R			T				r												A									F				R	F								R		T	R
186	1151	A	46	R	CC	12	17	505.75	*N. kamtschatica*	7Ba	late Miocene	G	A				R				C															C							R		F					F										R	R
186	1151	A	47	R	CC	13	18	516.13	*N. kamtschatica*	7Ba	late Miocene	G	A				R			F																A									R					F										R	F
186	1151	A	48	R	CC	11	15	524.49	*N. kamtschatica*	7Ba	late Miocene	M	A				R			T	F	r														C						F	R		C				R												
186	1151	A	49	R	CC	15	20	533.52	*N. kamtschatica*	7Ba	late Miocene	G	A				R				R				r										R	C									C					F							T					F
186	1151	A	50	R	CC	15	19	541.94	*N. kamtschatica*	7Ba	late Miocene	M	A				R			R	F											T				F							R		C					F											F
186	1151	A	51	R	CC	14	18	554.63	*N. kamtschatica*	7Ba	late Miocene	G	A							R	C															A				R		R			F							R					R					
186	1151	A	52	R	CC	18	22	563.99	*N. kamtschatica*	7Ba	late Miocene	VG	A				R	T		R	C															F									C					F											F
186	1151	A	53	R	CC	16	20	573.28	*N. kamtschatica*	7Ba	late Miocene	G	A				F			R	F															C			R						C					F							R					F
186	1151	A	54	R	CC	14	18	582.76	*N. kamtschatica*	7Ba	late Miocene	M	C				R				F															C									C					R											C
186	1151	A	55	R	CC	8	13	584.38	*N. kamtschatica*	7Ba	late Miocene	G	A				R			R	R															C			R						R					A							R				F	C
186	1151	A	56	R	CC	13	17	596.47	*N. kamtschatica*	7Ba	late Miocene	M	C				R				F															C									F					R											R
186	1151	A	57	R	CC	13	17	609.84	*N. kamtschatica*	7Ba	late Miocene	M	C				R				F											R				C				R										F							R					R
186	1151	A	58	R	CC	13	17	622.95	*N. kamtschatica*	7Ba	late Miocene	M	C				R				F											R			T	F				R					F																	F
186	1151	A	59	R	CC	12	15	631.34	*N. kamtschatica*	7Ba	late Miocene	G	C				R				F									r					F	C							R							F				R								F
186	1151	A	60	R	CC	21	24	640.76	*N. kamtschatica*	7Ba	late Miocene	M	C				R				F														T								R							F							R					
186	1151	A	61	R	CC	17	20	649.03	*N. kamtschatica*	7Ba	late Miocene	M	C								F														R	F														F							R					R
186	1151	A	62	R	CC	14	17	652.80	*N. kamtschatica*	7Ba	late Miocene	M	F		r						F									r						F			T			T			F					R											R
186	1151	A	63	R	CC	15	17	664.31	*N. kamtschatica*	7Ba	late Miocene	M	F								F				r											F			R			R								R											R
186	1151	A	64	R	1	35	37	671.15	*N. kamtschatica*	7Ba	late Miocene	M	C		r		R				F									r						R			T			R								R											
186	1151	A	65	R	CC	14	16	688.40	*N. kamtschatica*	7Ba	late Miocene	G	C		r		R				F									r						F									R					R							T					R
186	1151	A	66	R	1	70	73	690.50	*N. kamtschatica*	7Ba	late Miocene	M	C		r						F	r			r											F				R										F							R					R
186	1151	A	66	R	CC	19	21	693.43	*N. kamtschatica*	7A	late Miocene	M	C				R				C															R							R		R		T			F											R
186	1151	A	67	R	CC	9	11	705.63	*N. kamtschatica*	7A	late Miocene	M	F				F				R															F			R						R		T			R											R
186	1151	A	68	R	CC	22	25	718.84	*N. kamtschatica*	7A	late Miocene	G	C																	r		R				C					T						T			F											F
186	1151	A	69	R	CC	16	18	725.77	*N. kamtschatica*	7A	late Miocene	G	C		r		R				F					r										F					R						R			R											R

Table T7 (continued).

Leg	Site	Hole	Core	Type	Section	Top (cm)	Bottom (cm)	Depth (mbsf)	Diatom zones	NPD	Geological Age	Group abundance	Preservation	*Actinocyclus ellipticus*	*Actinocyclus ingens*	*Actinocyclus oculatus*	*Actinoptychus senarius*	*Aulacoseira* spp.	*Cavitatus jouseanus*	*Cocconeis costata*	*Coscinodiscus marginatus*	*Crucidenticula nicobarica*	*Delphineis simonsenii*	*Denticulopsis dimorpha*	*Denticulopsis hyalina*	*Denticulopsis katayamae*	*Denticulopsis lauta*	*Denticulopsis praedimorpha*	*Denticulopsis praelauta*	*Denticulopsis simonsenii*	*Fragilariopsis doliolus*	*Hemidiscus cuneiformis*	*Ikebea tenuis*	*Kieselviella carina*	*Koizumia tatsunokuchiensis*	*Neodenticula kamtschatica*	*Neodenticula koizumii*	*Neodenticula seminae*	*Nitzschia fossilis*	*Nitzschia reinholdii*	*Nitzschia rolandii*	*Paralia sulcata*	*Proboscia barboi*	*Proboscia curvirostris*	*Pyxidicula zabelinae*	*Rhizosolenia hebetata* f. *hiemalis*	*Rouxia californica*	*Stephanopyxis horridus*	*Stephanopyxis turris*	*Thalassionema nitzschioides*	*Thalassionema schraderi*	*Thalassiosira antiqua*	*Thalassiosira gravida*	*Thalassiosira jouseae*	*Thalassiosira latimarginata*	*Thalassiosira nidulus*	*Thalassiosira oestrupii*	*Thalassiosira praeoestrupii*	*Thalassiosira yabei*	*Thalassiothrix longissima*	*Chaetoceros* spp. (resting spores)
186	1151	A	70	R	CC	16	18	732.14	*N. kamtschatica*	7A	late Miocene	G	C				R		R		F				r									R					R			F	C													
186	1151	A	71	R	CC	15	17	747.10	*N. kamtschatica*	7A	late Miocene	M	F				R				F				r									R					R			F	R	R												
186	1151	A	72	R	CC	14	18	755.44	*N. kamtschatica*	7A	late Miocene	M	A							T	C				r						T			R					R				R	R												
186	1151	A	73	R	CC	17	21	767.11	*N. kamtschatica*	7A	late Miocene	M	F				R				F													R				T		R				R												
186	1151	A	74	R	CC	18	21	774.79	*N. kamtschatica*	7A	late Miocene	M	C		r		R				C	r			r									F						T	F	F	R												
186	1151	A	75	R	CC	0	4	784.18	*N. kamtschatica*	7A	late Miocene	M	C		r		R			R	C								r					R					R			C	T		R	R		R									
186	1151	A	76	R	CC	18	22	794.56	*N. kamtschatica*	7A	late Miocene	M	F				R	T			F													R																					
186	1151	A	77	R	CC	18	22	800.62	*N. kamtschatica*	7A	late Miocene	M	C		R						F											R		R																					
186	1151	A	78	R	1	70	73	806.10	*R. californica*	7A	late Miocene	G	C								F				r									R					R	R			T												
186	1151	A	78	R	CC	12	16	814.52	*R. californica*	7A	late Miocene	M	C						R		F			r	r							R									R													
186	1151	A	79	R	1	70	73	815.70	*R. californica*	7A	late Miocene	M	C					R			F											R		R				R	F				T										
186	1151	A	79	R	CC	0	5	816.95	*R. californica*	7A	late Miocene	M	F								F																							T											
186	1151	A	80	R	1	73	77	825.33	*T. schraderi*	6B	late Miocene	G	C				R				F				r					r		R		R								F	R											
186	1151	A	80	R	3	70	74	828.30	*T. schraderi*	6B	late Miocene	G	C								F				r							R		R								F	R											
186	1151	A	80	R	CC	14	16	834.47	*T. schraderi*	6B	late Miocene	M	C						R		C											R		R								R	F											
186	1151	A	81	R	CC	14	17	836.94	*T. schraderi*	6B	late Miocene	M	C								C											R							R				R	R											
186	1151	A	82	R	CC	20	22	850.93	*T. schraderi*	6B	late Miocene	M	C	T							C											R							R				R	F											
186	1151	A	84	R	CC	16	19	872.05	*T. schraderi*	6B	late Miocene	M	C				R				F																							F	F											
186	1151	A	85	R	CC	2	5	882.45	*T. schraderi*	6B	late Miocene	M	F		R		R	R			F																			R			T	F	C											
186	1151	A	86	R	CC	7	9	886.60	*T. schraderi*	6B	late Miocene	M	C				R				C										T								R				R	R											
186	1151	A	87	R	CC	18	21	897.70	*T. schraderi*	6B	late Miocene	M	C		T		R				F									F										T				R	F											
186	1151	A	88	R	CC	0	3	911.06	*T. schraderi*	6B	late Miocene	M	C				F				R									R										R	R			R	C											
186	1151	A	89	R	CC	13	16	920.99	*T. schraderi*	6B	late Miocene	M	C				R				F									R							R					R	R	F											
186	1151	A	90	R	2	71	74	923.01	*T. schraderi*	6A	late Miocene	M	C	T	F						R				T									T								R	T											
186	1151	A	90	R	CC	22	25	926.10	*T. schraderi*	6A	late Miocene	M	C		F			T			F				R					T					T						R	T											
186	1151	A	91	R	1	70	73	931.10	*T. schraderi*	6A	late Miocene	M	F		T						F				F										T							F	R											
186	1151	A	91	R	3	70	73	934.10	*T. schraderi*	6A	late Miocene	M	F				T				F			r	R																	R		F	T										
186	1151	A	91	R	5	70	73	937.10	*D. katayamae*	6A	late Miocene	M	F				T				R				R					R											R			F	R										
186	1151	A	91	R	CC	21	23	939.54	*D. katayamae*	6A	late Miocene	M	C	T	R		T				F				R					R											T	R		F	R										
186	1151	A	92	R	2	70	73	942.21	*D. dimorpha*	5D	late Miocene	G	C		F									C	C					F													F											
186	1151	A	92	R	4	70	73	945.04	*D. dimorpha*	5D	late Miocene	M	C		R						R			F	R					F													F											
186	1151	A	92	R	CC	27	31	948.09	*D. dimorpha*	5D	late Miocene	G	C		R						R			F						F													R	C											
186	1151	A	93	R	1	70	73	950.40	*D. dimorpha*	5D	late Miocene	G	C		R		T				F			C	r					F													F											
186	1151	A	93	R	CC	22	26	953.73	*D. dimorpha*	5D	late Miocene	G	A		R		F	T						C	T					C													R	C											
186	1151	A	94	R	1	70	73	960.00	*D. dimorpha*	5D	late Miocene	P	R								R			R	r					T													F											
186	1151	A	94	R	CC	18	21	962.76	*D. dimorpha*	5D	late Miocene	M	C	T			T				F			F						F													C											
186	1151	A	95	R	1	70	73	969.60	*D. dimorpha*	5D	late Miocene	M	C								F			C						R													F											
186	1151	A	95	R	CC	0	3	970.00	*D. dimorpha*	5D	late Miocene	G	A				R				F			C						F			T										C											
186	1151	A	96	R	1	72	77	979.32	*T. yabei*	5C	late Miocene	G	C		R				R		R									F													F											
186	1151	A	96	R	CC	21	24	982.34	*T. yabei*	5C	late Miocene	G	C		F				T		R									C												R	F											

Table T7 (continued).

Leg	Site	Hole	Core	Type	Section	Top (cm)	Bottom (cm)	Depth (mbsf)	Diatom zones	NPD	Geological Age	Group abundance	Preservation	*Actinocyclus ellipticus*	*Actinocyclus ingens*	*Actinocyclus oculatus*	*Actinoptychus senarius*	*Aulacoseira* spp.	*Cavitatus jouseanus*	*Cocconeis costata*	*Coscinodiscus marginatus*	*Crucidenticula nicobarica*	*Delphineis simonsenii*	*Denticulopsis dimorpha*	*Denticulopsis hyalina*	*Denticulopsis katayamae*	*Denticulopsis lauta*	*Denticulopsis praedimorpha*	*Denticulopsis praelauta*	*Denticulopsis simonsenii*	*Fragilariopsis doliolus*	*Hemidiscus cuneiformis*	*Ikebea tenuis*	*Kieselviella carina*	*Koizumia tatsunokuchiensis*	*Neodenticula kamtschatica*	*Neodenticula koizumii*	*Neodenticula seminae*	*Nitzschia fossilis*	*Nitzschia reinholdii*	*Nitzschia rolandii*	*Paralia sulcata*	*Proboscia barboi*	*Proboscia curvirostris*	*Pyxidicula zabelinae*	*Rhizosolenia hebetata* f. *hiemalis*	*Rouxia californica*	*Stephanopyxis horridus*	*Stephanopyxis turris*	*Thalassionema nitzschioides*	*Thalassionema schraderi*	*Thalassiosira antiqua*	*Thalassiosira gravida*	*Thalassiosira jouseae*	*Thalassiosira latimarginata*	*Thalassiosira nidulus*	*Thalassiosira oestrupii*	*Thalassiosira praeoestrupii*	*Thalassiosira yabei*	*Thalassiothrix longissima*	*Chaetoceros* spp. (resting spores)
186	1151	A	97	R	1	69	72	988.89	*T. yabei*	5C	late Miocene	M	C		F						R	r								C																			R	F											
186	1151	A	97	R	CC	21	24	995.83	*T. yabei*	5C	late Miocene	M	C		F		R				F				r					C													R																		R
186	1151	A	98	R	1	68	70	998.48	*T. yabei*	5C	late Miocene	M	C	R	C			T			F									C													R							F											R
186	1151	A	98	R	CC	18	21	1003.72	*T. yabei*	5C	late Miocene	M	C	R	F															F												R	T						R	F										R	F
186	1151	A	99	R	1	69	72	1008.09	*T. yabei*	5C	m. Miocene	M	F						R											R																				R											R
186	1151	A	99	R	CC	17	20	1009.53	*T. yabei*	5C	m. Miocene	M	F				R				F									F																			R										R		R
186	1151	A	100	R	1	66	69	1017.66	*D. praedimorpha*	5B	m. Miocene	G	C		R						F	R						C	r	F																				F											
186	1151	A	100	R	CC	20	23	1020.57	*D. praedimorpha*	5B	m. Miocene	M	C		R						R	R			R			C		F																				F											F
186	1151	A	101	R	1	71	73	1027.31	*D. praedimorpha*	5B	m. Miocene	M	A		F						C	T	C		F			F																						F										R	R
186	1151	A	101	R	1	90	91	1027.50	*D. hustedtii*	4Bb	m. Miocene	M	C		R							F			C					T																			F	R											R
186	1151	A	101	R	2	62	64	1028.33	*D. hustedtii*	4Bb	m. Miocene	G	A		C							F			C		R			T																			R	R									R		
186	1151	A	101	R	CC	18	21	1028.78	*D. hustedtii*	4Bb	m. Miocene	G	C		C						F	F			F		R																							R											R
186	1151	A	102	R	1	69	72	1036.89	*D. hustedtii*	4Bb	m. Miocene	M	C		C			T				R			C		F			R																															R
186	1151	A	102	R	2	72	75	1038.42	*D. hyalina*	4Ba	m. Miocene	M	C		F						R	R			C		F																																		R
186	1151	A	102	R	CC	16	19	1039.51	*D. hyalina*	4Ba	m. Miocene	M	C		C		R				R	R			F		R																							R											
186	1151	A	103	R	1	66	69	1046.56	*D. hyalina*	4Ba	m. Miocene	M	F		R						R				F																									R											R
186	1151	A	103	R	CC	18	20	1048.85	*D. hyalina*	4Ba	m. Miocene	M	F		F			T							F		R															T								R											R
186	1151	A	104	R	1	70	73	1056.30	*D. hyalina*	4Ba	m. Miocene	M	C		C			T			R				F		R																							R											R
186	1151	A	104	R	CC	16	18	1061.21	*D. lauta*	4A	m. Miocene	M	C		C			T	T		R						T							r																R											T
186	1151	A	105	R	2	90	91	1067.70	*D. lauta*	4A	m. Miocene	M	F		F			R									R															R																			
186	1151	A	105	R	CC	19	21	1074.44	*D. lauta*	4A	m. Miocene	M	C		C				R								R		r													R								F											
186	1151	A	106	R	3	70	73	1078.70	*D. lauta*	4A	m. Miocene	P	F		F						R						T															R																			
186	1151	A	106	R	CC	19	21	1083.11	*D. lauta*	4A	m. Miocene	M	F		F				R								R							r								R								F											R
186	1151	A	107	R	3	72	74	1088.20	*D. lauta*	4A	m. Miocene	P	F		F				T		R						T																							T											T
186	1151	A	107	R	CC	24	26	1093.97	*D. lauta*	4A	m. Miocene	M	F		F				R								R															T								R										T	
186	1151	A	108	R	4	56	58	1099.19	*D. lauta*	4A	m. Miocene	M	F		R						R						R		F																																R
186	1151	A	108	R	CC	20	22	1104.08	*D. praelauta*	3B	m. Miocene	M	F		F				R		R								F																				T	R											T
186	1151	A	109	R	4	71	75	1108.81	*D. praelauta*	3B	m. Miocene	M	F		R						R								R																				T	R											R
186	1151	A	109	R	CC	10	13	1113.46	*D. praelauta*	3B	m. Miocene	M	F		F			T	T		R								F																					F											R

Notes: NPD = North Pacific diatom zones, A = abundant, G = good, R = rare, F = few, T = trace, C = common, P = poor, M = moderate, r = reworking, VG = very good. This table is also available in **ASCII format**.

Table T8. Distribution and relative abundances of selected diatom species, Holes 1151C and 1151D.

Leg	Site	Hole	Core	Type	Section	Top (cm)	Bottom (cm)	Depth (mbsf)	Diatom zones	NPD	Preservation	Group abundance	*Actinocyclus curvatulus*	*Actinocyclus oculatus*	*Actinoptychus senarius*	*Azpeitia nodulifera*	*Bacterosira fragilis*	*Coscinodiscus marginatus*	*Denticulopsis katayamae*	*Denticulopsis simonsenii*	*Fragilariopsis doliolus*	*Neodenticula koizumii*	*Neodenticula kamtschatica*	*Neodenticula seminae*	*Nitzschia reinholdii*	*Paralia sulcata*	*Proboscia barboi*	*Proboscia curvirostris*	*Rhizosolenia hebetata*	*Stephanopyxis turris*	*Thalassionema nitzschioides*	*Thalassiosira antiqua*	*Thalassiosira gravida*	*Thalassiosira jouseae*	*Thalassiosira latimarginata*	*Thalassiosira lineata*	*Thalassiosira oestrupii*	*Thalassiothrix longissima*	*Chaetoceros* spp. (resting spores)
186	1151	C	1	H	CC	13	18	2.10	*N. seminae*	12	G	A					R							C				R		F		F		R	R	R		C
186	1151	C	2	H	CC	23	28	12.10	*N. seminae*	12	G	C	F				R							C				R		F		F	r	R	R			R
186	1151	C	3	H	CC	20	25	21.44	*N. seminae*	12	G	A					F				F			C					F	F		F		F		R		A
186	1151	C	4	H	4	70	70	26.43	*P. curvirostris*	11	M	A												R				R	R	R	R		C	R		R		F
186	1151	C	4	H	CC	39	44	31.58	*P. curvirostris*	11	G	A	R	r		T					F			F				R		R	F		F	T				C
186	1151	C	5	H	CC	8	13	40.31	*P. curvirostris*	11	G	A	R					R			R		r	C				F			R		F	R		R		C
186	1151	C	6	H	CC	13	18	50.10	*P. curvirostris*	11	G	A	R		R						T			F	R						F		C	T		R		C
186	1151	C	7	H	CC	15	20	59.46	*P. curvirostris*	11	G	A	R		T						R			C				R			R		C	F				C
186	1151	C	8	H	CC	27	32	69.30	*P. curvirostris*	11	M	C			T									F					R		F		F	F		R		F
186	1151	C	9	H	5	70	70	75.40	*P. curvirostris*	11	G	C					R	R	r					R	T			R					F	F	R			F
186	1151	C	9	H	CC	19	24	78.38	*A. oculatus*	10	G	A	R	F	R			R					r	F	T			R			F		F	F	R		R	C
186	1151	C	10	H	CC	29	34	88.38	*A. oculatus*	10	G	A		C				R						F	R		R	R	R				F	F				F
186	1151	C	11	H	4	70	70	92.90	*A. oculatus*	10	G	A	R	F										C			R	T		F	F		F			F		F
186	1151	C	11	H	CC	13	18	97.55	*N. koizumii*	9	G	A		F			R					F		C		R		T	R	R	F			F	R			C
186	1151	D	1	H	CC	25	30	7.51	*N. seminae*	12	G	A	R				T							F					C	F	F		R		F	R	R	F
186	1151	D	2	H	CC	23	28	17.44	*N. seminae*	12	G	A	F								F			F						F	R		C		R	R	R	F
186	1151	D	3	H	4	70	70	22.20	*N. seminae*	12	G	C	R											F							R		R	F		T		F
186	1151	D	3	H	CC	25	30	26.88	*P. curvirostris*	11	G	C					T	R		r	R			R				T			R		F	F	T		R	R	C
186	1151	D	4	H	CC	24	28	36.42	*P. curvirostris*	11	G	A	R					R			R			F				R	R		F		C	F	R		R		A
186	1151	D	5	H	CC	23	28	45.71	*P. curvirostris*	11	G	C	R								R			R	T				R	F	R		F	F					F
186	1151	D	6	H	CC	23	28	55.37	*P. curvirostris*	11	G	C									T			F				R	R	R	F		F	R					C
186	1151	D	7	H	CC	7	12	64.56	*P. curvirostris*	11	G	A	F											C	R			R			F		F		R		R		C
186	1151	D	8	H	CC	24	29	74.63	*P. curvirostris*	11	G	A	R				F	C						F	R			F			F		R	F				R	F
186	1151	D	9	H	CC	24	28	83.43	*A. oculatus*	10	G	A		F				R						F	R						F			F	T		R		F
186	1151	D	10	H	CC	16	20	93.27	*N. koizumii*	9	G	C	R	F	T							F		F	R	R	F			R	F	T		R					C

Notes: NPD = North Pacific diatom zones, G = good, M = moderate, A = abundant, R = rare, C = common, F = few, r = reworking, T = trace. This table is also available in **ASCII format**.

Table T9. Stratigraphic occurrences and chronology of datum levels of diatoms, Site 1151.

Datum event	Zone (base)	Age (Ma)	Upper sample		Lower sample		Upper sample		Lower sample		Upper sample		Lower sample	
			Core, section, interval (cm)	Depth (mbsf)	Core, section, interval (cm)	Depth (mbsf)	Core, section, interval (cm)	Depth (mbsf)	Core, section, interval (cm)	Depth (mbsf)	Core, section, interval (cm)	Depth (mbsf)	Core, section, interval (cm)	Depth (mbsf)
			186-1151A-		186-1151A-		186-1151C-		186-1151C-		186-1151D-		186-1151D-	
LO *Thalassiosira jouseae*		0.30					3H-CC	21.44	4H-4, 70	26.43	2H-CC	17.44	3H-4, 70	22.20
LO *Proboscia curvirostris*	NPD 12	0.30					3H-CC	21.44	4H-4, 70	26.43	3H-4, 70	22.20	3H-CC	26.88
LO *Nitzschia reinholdii*		0.62*					5H-CC	40.31	6H-CC	50.10	4H-CC	36.42	5H-CC	45.71
LCO *Actinocyclus oculatus*	NPD 11	1.01-1.46	3R-CC	92.50	4R-2, 138-142	96.18	9H-5, 70	75.40	9H-CC	79.38	8H-CC	74.63	9H-CC	83.43
LO *Neodenticula koizumii*	NPD 10	2.0	5R-CC	105.90	6R-1, 70-72	113.30	11H-4, 70	92.90	11H-CC	97.55	9H-CC	83.43	10H-CC	93.27
LCO *Neodenticula kamtschatica*	NPD 9	2.61-2.68	11R-CC	168.86	12R-3, 140-144	174.60								
FO *Neodenticula koizumii*	NPD 8	3.53-3.95	14R-CC	199.19	15R-4, 72-74	204.42								
FO *Thalassiosira latimarginata*		5.07	29R-CC	344.01	30R-CC	353.56								
FO *Thalassiosira oestrupii s.l.*	NPD 7Bb	5.49	38R-1, 70-73	421.30	38R-CC	426.21								
LCO *Rouxia californica*	NPD 7Ba	6.65	66R-1, 70-73	690.50	66R-CC	693.43								
LO *Cavitatus jouseanus*		6.7-6.8	69R-CC	725.77	70R-CC	732.14								
FCO *Neodenticula kamtschatica*		7.3-7.4	77R-CC	800.62	78R-1, 70-73	806.10								
LO *Thalassionema schraderi*	NPD 7A	7.6	79R-CC	816.95	80R-1, 73-77	825.33								
LO *Denticulopsis katayamae*		8.5	89R-CC	920.99	90R-2, 71-74	923.01								
LCO *Denticulopsis simonsenii*	NPD 6B	8.6	91R-3, 70-73	934.10	91R-5, 70-73	937.10								
LO *Denticulopsis dimorpha*	NPD 6A	9.16	91R-CC	939.54	92R-2, 70-73	942.21								
FO *Thalassiosira schraderi*		9.5	91R-CC	939.54	92R-2, 70-73	942.21								
FO *Denticulopsis dimorpha*	NPD 5D	9.9	95R-CC	970.00	96R-1, 72-77	979.32								
LCO *Denticulopsis praedimorpha*	NPD 5C	11.5	99R-CC	1009.53	100R-1, 60-69	1017.66								
LO *Crucidenticula nicobarica*		12.5	99R-CC	1009.53	100R-1, 60-69	1017.66								
FO *Denticulopsis praedimorpha*	NPD 5B	12.9	101R-1, 71-73	1027.31	101R-1, 90-91	1027.50								
FCO *Denticulopsis simonsenii*	NPD 5A	13.1	101R-1, 71-73	1027.31	101R-1, 90-91	1027.50								
FO *Denticulopsis simonsenii*	NPD 4Bb	14.1-14.6	102R-1, 69-72	1036.89	102R-2, 72-75	1038.42								
FO *Denticulopsis hyalina*	NPD 4Ba	14.9	104R-1, 70-73	1056.30	104R-CC	1061.21								
FO *Denticulopsis lauta*	NPD 4A	15.9	108R-4, 56-58	1099.19	108R-CC	1104.08								
FO *Denticulopsis praelauta*	NPD 3B	16.3	109R-CC	1113.46										

Notes: LO = last occurrence, LCO = last common occurrence, FO = first occurrence, FCO = first common occurrence. * = an age revealed in the eastern equatorial Pacific (Shackleton et al., 1995). This table is also available in **ASCII format**.

Table T10. NRM and ARM results from the NP2 magnetometer before and after AF demagnetization.

Leg	Site, Hole	Core	Section	Interval (cm)	Depth (mbsf)	Susceptibility	Jn MDF (mT)	Ja MDF (mT)	Jn/Ja (20 mT)	Jn/Ja (10 mT)	Jn/Ja (0 mT)	Susc/Jn	Inc. (20 mT)	Dec. (20 mT)	ErrIC	Log (Jn) (0 mT)	Log (Jn) (10 mT)	Log (Jn) (20 mT)	Log (Jn) (30 mT)
186	1151A	2	3	26	81.26	25.0	32.36	22.19	0.24	0.23	0.23	0.35	54.2	49.6	8.9	–5.681	–5.776	–5.902	–5.917
186	1151A	3	6	28	91.48	12.9	40.00	22.51	0.14	0.12	0.04	0.76	–59.1	340.1	12.7	–6.602	–6.167	–6.320	–6.126
186	1151A	4	5	11	98.91	16.2	23.12	23.24	0.05	0.05	0.05	1.05	–48.3	190.3	67.7	–6.401	–6.458	–6.640	–6.838
186	1151A	5	2	11	104.51	13.8	5.37	21.67	0.09	0.05	0.18	2.19	–34.3	308.7	23.9	–6.131	–6.692	–6.633	–6.960
186	1151A	6	4	30	117.40	23.2	3.55	17.77	0.29	0.07	0.38	0.61	37.5	264.8	13.7	–5.695	–6.542	–6.176	–6.242
186	1151A	7	3	20	125.40	19.5	12.86	21.50	0.04	0.09	0.10	1.43	27.0	6.1	25.8	–6.010	–6.163	–6.681	–6.449
186	1151A	8	4	20	136.50	7.0	3.96	19.89	0.07	0.02	0.10	3.30	–56.4	42.0	41.8	–6.308	–7.068	–6.771	–6.685
186	1151A	9	4	20	146.10	12.8	40.00	22.04	0.08	0.05	0.05	1.95	–64.4	336.9	17.4	–6.583	–6.686	–6.675	–6.513
186	1151A	10	5	31	157.31	11.0	33.11	20.88	0.09	0.12	0.09	1.14	–31.7	212.1	22.9	–6.431	–6.356	–6.689	–6.707
186	1151A	11	5	7	166.67	4.6	40.00	20.64	0.12	0.07	0.10	1.65	–48.3	344.6	72.9	–6.573	–6.745	–6.755	–6.799

								Principal axes of AMS (°)							Log Ja (Z-axis only)				
Leg	Site, Hole	Core	Section	Interval (cm)	Depth (mbsf)	Log Jn (40 mT)	Log Susc.	Max. Inc.	Max. Dec.	Int. Inc.	Int. Dec.	Min. Inc.	Min. Dec.	qn	(0 mT)	(10 mT)	(20 mT)	(30 mT)	(40 mT)
186	1151A	2	3	26	81.26	–6.193	–6.354	–35.7	132.7	–21.5	239.1	–46.4	353.5	1.773	–5.038	–5.130	–5.280	–5.549	–7.087
186	1151A	3	6	28	91.48	–6.276	–6.436	–14.3	53.8	–62.9	173.6	–22.5	317.7	2.239	–5.241	–5.239	–5.464	–5.776	–7.377
186	1151A	4	5	11	98.91	–6.567	–6.621	–13.2	38.3	–66.1	276.4	–19.6	133.1	–1.292	–5.115	–5.185	–5.308	–5.642	–6.189
186	1151A	5	2	11	104.51	–6.668	–6.294	–72.4	335.8	–2.8	237.0	–17.4	146.1	0.090	–5.381	–5.418	–5.610	–6.040	–7.117
186	1151A	6	4	30	117.40	–6.288	–6.390	–51.8	47.1	–25.7	174.8	–26.2	278.5	–1.302	–5.278	–5.361	–5.642	–6.425	–7.289
186	1151A	7	3	20	125.40	–6.366	–6.525	–65.8	199.6	–22.3	355.8	–8.8	89.4	0.783	–5.023	–5.099	–5.267	–5.646	–6.912
186	1151A	8	4	20	136.50	–6.828	–6.252	–58.4	226.2	–27.5	78.5	–14.4	340.8	0.611	–5.303	–5.385	–5.606	–5.868	–7.431
186	1151A	9	4	20	146.10	–6.621	–6.385	–50.1	116.9	–37.5	320.2	–11.6	221.1	1.030	–5.322	–5.341	–5.567	–5.844	–6.771
186	1151A	10	5	31	157.31	–6.788	–6.631	–28.1	43.3	–50.9	272.3	–24.8	147.6	–0.372	–5.382	–5.419	–5.651	–6.005	–7.055
186	1151A	11	5	7	166.67	–6.855	–6.537	–56.5	50.1	–28.0	266.7	–16.9	167.4	1.793	–5.562	–5.582	–5.849	–6.073	–6.705

Notes: Jn = NRM intensity; Ja = ARM intensity; Jn/Ja = the ratio of the NRM to the ARM, where the level of demagnetization of both the ARM and NRM is given in parentheses; AMS = anisotropy of magnetic susceptibility; Inc. = inclination; Dec. = declination; Max. = maximum AMS axis; Int. = intermediate AMS axis; Min. = minimum AMS axis; qn = anisotropy shape factor. All intensities are given as log values in kA/m units. Only a portion of this table appears here. The complete table is available in **ASCII format.**

Table T11. Age control points for Site 1151 datum events and sedimentation rates.

Datum number		Datum events	Depth (mbsf)	Age (Ma)	Sedimentation rate (m/m.y.)
		Top	0.0	0.00	
					73
1	LO	*Proboscia curvirostris*	(22)	0.30	
					119
2	B	C1n (Brunhes)	(79)	0.78	
					33
3	LCO	*Actinocyclus oculatus**	94 (75)	1.24	
					20
4	LO	*Neodenticula koizumii**	110 (93)	2.00	
					90
5	B	C2r (Matuyama)	162	2.581	
					152
6	FO	*Neodenticula kamtschatica*	171.73	2.65	
					34
7	FO	*Neodenticula koizumii*	201.81	3.53	
					114
8	T	C3n.1n	276	4.18	
					113
9	FO	*Thalassiosira oestrupii* s.l.	423.76	5.49	
					65
10	T	C3An.1n	450	5.89	
					238
11	B	C3An.2n	610	6.57	
					247
12	FO	*Neodenticula kamtschatica*	803.36	7.35	
					71
13	LO	*Thalassionema schraderi*	821.14	7.6	
					112
14	LO	*Denticulopsis katayamae*	922	8.5	
					29
15	LO	*Denticulopsis dimorpha*	940.88	9.16	
					46
16	FO	*Denticulopsis dimorpha*	974.66	9.9	
					24
17	LCO	*Denticulopsis praedimorpha*	1013.60	11.5	
					10
18	FO	*Denticulopsis praedimorpha*	1027.41	12.9	
					0
19	FCO	*Denticulopsis simonsenii*	1027.41	13.1	
					8
20	FO	*Denticulopsis simonsenii*	1037.66	14.4	
					38
21	FO	*Denticulopsis hyalina*	1058.76	14.9	
					43
22	FO	*Denticulopsis lauta*	1101.635	15.9	
23		bottom (calculated)	1113.46	(16.18)	

Notes: LO = last occurrence, LCO = last common occurrence, B = base, FO = first occurrence, T = top, * = diatom datums from Hole 1151A sediment. In Holes 1151C and 1151D, these diatom datums were ~20 m shallower. Values in parentheses are from Holes 1151C and 1151D. This table is also available in **ASCII format**.

Table T12. Headspace concentrations of light hydrocarbons, Site 1151.

Leg	Site	Hole	Core	Type	Section	Top (cm)	Bottom (cm)	Depth (mbsf)	C_1 (%)	C_2 (ppmv)	C_1/C_2
186	1151	A	2	R	3	0	5	81.00	6.15	10.90	5645
186	1151	A	3	R	3	0	5	86.70	3.09	6.86	4500
186	1151	A	4	R	3	0	5	96.30	2.81	5.51	5095
186	1151	A	5	R	2	0	5	104.40	0.93	2.20	4206
186	1151	A	6	R	3	0	5	115.60	1.29	2.60	4950
186	1151	A	7	R	3	0	5	125.20	3.22	6.20	5192
186	1151	A	8	R	3	0	5	134.80	3.08	5.90	5222
186	1151	A	9	R	3	0	5	144.40	3.92	7.10	5528
186	1151	A	10	R	3	0	5	154.00	3.33	6.80	4892
186	1151	A	11	R	3	0	5	163.60	2.77	4.90	5660
186	1151	A	12	R	3	0	5	173.20	3.48	4.90	7097
186	1151	A	13	R	3	0	5	182.80	3.62	6.40	5660
186	1151	A	14	R	3	0	5	192.50	4.16	6.70	6204
186	1151	A	15	R	4	0	5	203.70	2.47	4.60	5360
186	1151	A	16	R	4	0	5	213.40	3.22	6.00	5372
186	1151	A	17	R	3	0	5	221.50	2.37	5.00	4749
186	1151	A	18	R	4	0	5	232.60	1.73	3.50	4956
186	1151	A	19	R	4	0	5	242.20	2.81	5.40	5211
186	1151	A	20	R	3	0	5	250.30	2.82	5.40	5228
186	1151	A	21	R	4	0	5	261.40	1.72	3.80	4533
186	1151	A	22	R	4	0	5	271.10	1.65	3.60	4590
186	1151	A	23	R	4	0	5	280.70	2.02	4.10	4934
186	1151	A	24	R	4	0	5	290.40	0.53	1.50	3520
186	1151	A	25	R	4	0	5	300.10	1.15	2.50	4596
186	1151	A	26	R	3	0	5	308.30	0.85	2.30	3696
186	1151	A	27	R	3	0	5	317.90	1.68	3.90	4320
186	1151	A	28	R	4	0	5	329.10	0.92	1.90	4856
186	1151	A	29	R	4	0	5	338.70	1.56	3.70	4205
186	1151	A	30	R	4	0	5	348.40	0.72	1.80	3987
186	1151	A	31	R	3	0	5	356.60	1.21	3.00	4021
186	1151	A	32	R	2	0	5	364.70	1.56	3.20	4860
186	1151	A	33	R	2	0	5	374.40	1.81	3.90	4630
186	1151	A	34	R	2	0	5	384.00	0.37	1.10	3374
186	1151	A	35	R	2	0	5	393.60	0.72	2.00	3602
186	1151	A	36	R	2	0	5	402.90	0.67	1.50	4443
186	1151	A	37	R	2	0	5	412.50	0.86	2.30	3749
186	1151	A	38	R	2	0	5	422.10	1.09	2.20	4973
186	1151	A	39	R	2	0	5	431.80	4.65	6.70	6935
186	1151	A	40	R	2	0	5	441.40	0.59	1.40	4213
186	1151	A	41	R	2	0	5	451.00	3.93	6.70	5863
186	1151	A	42	R	2	0	5	460.70	3.52	6.60	5332
186	1151	A	43	R	2	0	5	470.30	2.69	5.00	5387
186	1151	A	45	R	2	0	5	489.50	1.80	4.50	3997
186	1151	A	46	R	2	0	5	499.10	4.14	7.80	5306
186	1151	A	47	R	4	0	5	511.70	2.52	4.90	5142
186	1151	A	48	R	2	0	5	518.30	4.19	9.00	4651
186	1151	A	49	R	2	0	2	527.90	3.18	5.80	5476
186	1151	A	50	R	2	0	2	537.50	3.16	5.00	6319
186	1151	A	51	R	2	0	2	547.20	2.92	4.30	6801
186	1151	A	52	R	4	0	5	559.90	2.12	4.20	5059
186	1151	A	53	R	4	0	5	569.60	1.50	3.20	4692
186	1151	A	54	R	4	0	2	579.20	1.48	3.00	4921
186	1151	A	55	R	CC	0	2	584.30	2.33	3.90	5964
186	1151	A	57	R	4	0	2	608.00	2.03	3.70	5497
186	1151	A	58	R	4	0	2	617.70	1.58	3.30	4777
186	1151	A	59	R	5	0	2	628.90	2.09	3.80	5509
186	1151	A	60	R	4	0	5	637.00	2.04	3.50	5829
186	1151	A	61	R	3	0	5	645.10	0.60	1.40	4279
186	1151	A	62	R	1	0	2	651.60	2.12	3.20	6625
186	1151	A	63	R	2	0	2	662.70	1.01	2.20	4582
186	1151	A	64	R	1	0	2	670.80	1.64	2.90	5645
186	1151	A	65	R	3	0	2	683.20	2.22	3.70	6003
186	1151	A	66	R	2	0	2	691.30	3.85	6.50	5917
186	1151	A	67	R	3	0	2	702.20	2.47	5.20	4751
186	1151	A	68	R	3	0	2	712.00	1.41	3.20	4392
186	1151	A	69	R	2	0	2	720.10	3.97	7.90	5023

Note: Only a portion of this table appears here. The complete table is available in **ASCII format.**

Table T13. Results of interstitial water analyses, Site 1151.

Leg	Site	Hole	Core	Type	Section	Top (cm)	Bottom (cm)	Depth (mbsf)	pH	Alkalinity (mM)	Salinity	Cl^- (mM)	SO_4^{2-} (mM)	Na^+ (mM)	Mg^{2+} (mM)	Ca^{2+} (mM)	K^+ (mM)	NH_4^+ (mM)	Sr^{2+} (µm)	Li^+ (µm)
186	1151	A	2	R	2	145	150	80.95	7.67	31.11	32.0	530.63	0.90	440.2	32.92	3.59	10.52	-	100.7	20.84
186	1151	A	5	R	1	145	150	104.35	7.39	24.36	30.0	499.76	0.68	425.0	25.20	2.55	9.29	3.91	114.2	35.10
186	1151	A	8	R	2	145	150	134.75	7.42	22.58	30.0	498.77	1.65	422.9	25.13	2.89	9.15	3.90	117.2	43.87
186	1151	A	11	R	2	145	150	163.55	7.22	21.43	29.0	498.77	0.37	421.6	24.33	3.00	8.66	4.16	123.4	60.32
186	1151	A	14	R	2	145	150	192.45	7.11	20.37	29.0	499.76	0.86	429.7	25.36	3.52	9.16	4.47	123.9	71.29
186	1151	A	17	R	2	145	150	221.45	7.04	19.65	29.0	499.76	0.12	425.6	25.52	4.06	9.40	4.55	124.5	80.06
186	1151	A	20	R	2	145	150	250.25	7.00	17.85	29.0	504.74	1.37	426.1	25.74	4.23	8.32	4.85	121	88.84
186	1151	A	23	R	3	145	150	280.65	7.24	18.80	29.0	497.77	0.88	424.3	25.12	4.34	8.59	5.23	126.2	104.19
186	1151	A	26	R	2	145	150	308.25	6.98	19.17	28.0	495.78	0.93	432.0	25.84	4.36	8.59	5.46	123.9	133.61
186	1151	A	29	R	3	140	150	338.60	7.05	20.30	28.0	486.82	0.41	415.3	24.72	3.96	7.99	5.62	123.4	156.90
186	1151	A	32	R	1	140	150	364.60	6.90	22.12	28.0	481.85	0.36	412.6	24.82	4.31	7.73	5.33	122.6	174.06
186	1151	A	35	R	1	140	150	393.50	7.13	23.20	30.0	477.86	1.57	410.8	24.59	4.04	7.56	5.74	113.2	190.00
186	1151	A	38	R	1	140	150	422.00	7.09	24.56	27.0	462.93	0.52	399.0	22.62	3.89	7.48	6.05	115.2	225.55
186	1151	A	41	R	1	140	150	450.90	7.17	24.22	26.0	452.97	0.72	389.1	21.48	4.23	7.29	6.34	113.5	261.10
186	1151	A	44	R	1	140	150	479.80	6.99	22.13	26.0	448.00	0.00	383.7	20.60	4.41	6.95	6.30	108.5	281.94
186	1151	A	47	R	3	140	150	511.60	7.05	21.67	26.0	429.08	1.10	377.3	19.41	4.52	6.96	6.26	106.3	305.22
186	1151	A	50	R	1	140	150	537.40	7.07	20.22	26.0	430.07	0.77	371.3	18.74	4.35	6.79	5.92	103	306.45
186	1151	A	53	R	3	140	150	569.50	6.94	19.64	24.0	417.13	0.00	322.6	15.62	4.20	5.92	5.95	106.3	393.48
186	1151	A	56	R	1	73	83	594.63	6.94	16.25	24.0	407.18	0.00	352.3	15.07	4.27	6.77	6.11	105.2	424.13
186	1151	A	59	R	4	140	150	628.80	6.88	16.20	23.0	397.22	0.00	340.9	14.15	5.12	6.29	5.54	112.9	442.52
186	1151	A	63	R	1	140	150	662.60	6.97	14.99	22.0	382.29	0.41	214.1	9.12	4.11	4.06	5.12	122.3	462.13
186	1151	A	66	R	1	140	150	691.20	7.15	12.83	22.0	375.32	0.45	324.8	11.54	6.44	7.37	4.80	126.7	465.81
186	1151	A	69	R	1	140	150	720.00	7.26	9.34	22.0	364.37	0.31	311.8	10.17	6.74	6.24	4.60	141	467.03
186	1151	A	72	R	2	116	128	750.06	7.37	10.61	21.0	359.39	0.85	303.9	9.85	7.94	6.10	4.18	150.5	481.29
186	1151	A	75	R	2	140	150	779.40	7.23	9.22	20.0	359.39	0.19	303.6	10.05	8.29	6.11	3.83	148.2	460.65
186	1151	A	78	R	3	140	150	809.80	7.20	8.84	20.0	349.44	0.00	292.4	9.10	9.02	5.92	3.65	171.2	473.55
186	1151	A	81	R	1	140	150	835.60	7.07	7.97	20.0	346.45	0.46	292.5	8.69	9.99	5.72	3.22	181.4	468.39
186	1151	A	84	R	3	140	150	867.50	6.98	7.27	19.0	341.47	0.00	284.4	8.45	10.77	5.52	2.81	187.9	458.06
186	1151	A	87	R	2	140	150	894.80	7.35	6.46	19.0	338.49	0.50	278.5	7.97	11.50	5.64	2.87	195.4	450.32
186	1151	A	90	R	1	140	150	922.20	6.98	4.99	18.0	330.52	0.00	272.9	7.61	12.10	5.64	2.53	206.6	433.55
186	1151	A	93	R	2	123	133	952.31	7.50	4.03	18.0	323.55	0.15	264.8	7.03	12.86	5.16	2.46	212.6	415.48
186	1151	A	97	R	3	140	150	992.60	7.40	3.43	18.0	324.55	0.00	266.8	6.87	14.37	5.64	2.10	212.3	366.45
186	1151	A	102	R	2	100	110	1038.70	7.63	2.24	18.0	320.57	0.06	254.9	5.83	16.86	5.23	1.73	226.5	307.10
186	1151	A	106	R	3	140	150	1079.40	7.78	3.03	18.0	302.65	0.14	241.5	3.97	18.15	4.89	1.57	232.6	273.55

Notes: - = Not determined. This table is also available in **ASCII format**.

Table T14. Thermal conductivity, Hole 1151A.

Core, section, interval (cm)	Depth (mbsf)	Average thermal conductivity (W/[m·K])
186-1151A-		
2R-1, 52	78.52	0.861
3R-3, 75	87.45	0.359
4R-3, 75	97.05	0.730
5R-2, 75	105.15	0.670
6R-3, 75	116.35	0.783
7R-2, 75	124.45	0.551
8R-3, 75	135.55	0.642
9R-3, 75	145.15	0.553
10R-3, 75	154.75	0.688
11R-3, 75	164.35	0.594
12R-3, 75	173.95	0.616
13R-3, 75	183.55	0.654
14R-3, 70	193.20	0.630
15R-3, 75	202.95	0.687
16R-3, 10	212.00	0.725
17R-3, 69	222.19	0.611
18R-3, 86	231.96	0.746
19R-3, 80	241.50	0.643
20R-3, 80	251.10	0.622
21R-3, 75	260.65	0.613
22R-3, 75	270.35	0.706
23R-3, 75	279.95	0.701
24R-3, 75	289.65	0.414
25R-3, 75	299.35	0.589
26R-3, 75	309.05	0.525
27R-3, 75	318.65	0.435
28R-3, 75	328.35	0.549
29R-3, 70	337.90	0.650
30R-3, 75	347.65	0.579
31R-3, 75	357.35	0.755
32R-2, 75	365.45	0.629
33R-3, 75	376.65	0.660
34R-3, 75	386.25	0.722
35R-2, 75	394.35	0.595
36R-3, 75	405.15	0.547
37R-2, 75	413.25	0.714

Note: This table is also available in **ASCII format**.

Table T15. *P*-wave velocity and anisotropy, Hole 1151A.

Core, section, interval (cm)	Depth (mbsf)	*P*-wave velocity (m/s)			Anisotropy		
		V_X	V_Y	V_Z	A_{Hh}	A_{HV}	A_{hV}
186-1151A-							
2R-2, 61	80.11	—	—	1454	0.00	0.00	0.00
2R-3, 58	81.58	—	—	1473	—	—	—
20R-1, 3	247.33	3405	3186	3155	0.07	0.08	0.01
26R-1, 3	305.33	1569	—	—	—	—	—
26R-2, 3	306.83	1546	—	—	—	—	—
26R-3, 74	309.04	1569	—	—	—	—	—
27R-1, 71	315.61	1558	—	—	—	—	—
28R-1, 62	325.22	1577	—	—	—	—	—
28R-2, 26	326.36	1558	—	—	—	—	—
28R-3, 57	328.17	1566	—	—	—	—	—
29R-1, 57	334.77	1557	—	—	—	—	—
29R-2, 95	336.65	1571	—	—	—	—	—
29R-3, 33	337.53	1568	—	—	—	—	—
30R-1, 48	344.38	1551	—	—	—	—	—
30R-2, 134	346.74	1541	—	—	—	—	—
31R-1, 12	353.72	1590	—	—	—	—	—
32R-1, 136	364.56	1580	—	—	—	—	—
32R-2, 18	364.88	1583	—	—	—	—	—
33R-1, 85	373.75	1581	—	—	—	—	—
33R-2, 114	375.54	1587	—	—	—	—	—
33R-3, 93	376.83	1560	—	—	—	—	—
34R-1, 43	382.93	1572	—	—	—	—	—
34R-2, 61	384.61	1578	—	—	—	—	—
34R-3, 29	385.79	1562	—	—	—	—	—
35R-1, 26	392.36	1567	—	—	—	—	—
35R-2, 29	393.89	1570	—	—	—	—	—
35R-3, 13	395.23	1600	—	—	—	—	—
36R-1, 28	401.68	1596	—	—	—	—	—
36R-2, 60	403.50	1589	—	—	—	—	—
36R-3, 55	404.95	1595	—	—	—	—	—
37R-1, 106	412.06	1582	—	—	—	—	—
37R-2, 92	413.42	1575	—	—	—	—	—
38R-1, 135	421.95	1611	1626	1565	0.01	0.04	0.03
38R-2, 63	422.73	1607	1601	1583	0.00	0.01	0.01
38R-3, 82	424.42	1616	1600	1577	0.01	0.02	0.01
38R-4, 27	425.37	1643	—	—	—	—	—
39R-1, 46	430.76	1631	1615	1588	0.01	0.03	0.02
39R-2, 86	432.66	1597	1594	1571	0.00	0.02	0.01
39R-3, 35	433.35	1606	1597	1575	0.01	0.02	0.01
40R-1, 84	440.74	1620	1632	1578	0.01	0.03	0.03
40R-2, 140	442.80	1679	1661	1644	0.01	0.02	0.01
40R-3, 20	443.10	1659	1632	1574	0.02	0.05	0.04
41R-1, 29	449.79	1621	1612	1585	0.01	0.02	0.02
41R-2, 47	451.47	1669	—	—	—	—	—
41R-3, 17	452.67	1637	1630	1554	0.00	0.05	0.05
41R-4, 59	454.59	1613	1614	1574	0.00	0.03	0.02
42R-1, 25	459.45	1605	1597	1569	0.00	0.02	0.02
42R-2, 143	462.13	1611	1617	1579	0.00	0.02	0.02
42R-3, 29	462.49	1676	1658	1622	0.01	0.03	0.02
43R-1, 26	469.06	1625	1604	1585	0.01	0.03	0.01
43R-2, 29	470.59	1598	1595	1579	0.00	0.01	0.01
43R-3, 106	472.86	1629	1621	1629	0.00	0.00	0.00
44R-1, 3	478.43	1652	1621	1615	0.02	0.02	0.00
44R-2, 31	480.21	1618	1631	1612	0.01	0.01	0.00
44R-3, 43	481.83	1799	1624	1592	0.10	0.12	0.02
44R-4, 59	483.49	1628	—	—	—	—	—
44R-5, 126	485.66	1717	1622	1567	0.06	0.09	0.03
44R-6, 31	486.21	1609	1619	1582	0.01	0.02	0.02
45R-1, 102	489.02	1617	1625	1596	0.01	0.02	0.01

Notes: V_X, V_Y, horizontal velocity; V_Z, vertical velocity; A_{Hh}, anisotropy of maximum vs. minimum horizontal velocity; A_{HV}, anisotropy of maximum horizontal velocity vs. vertical velocity; A_{hV}, anisotropy of minimum horizontal velocity vs. vertical velocity. — = not measured. Only a portion of this table appears here. The complete table is available in **ASCII format.**

Table T16. Index properties, Hole 1151A samples.

Core, section, interval (cm)	Depth (mbsf)	Salinity	Pore water density (g/cm^3)	Water content of total mass (%)	Water content of mass solids (%)	Bulk density (g/cm^3)	Dry density (g/cm^3)	Grain density (g/cm^3)	Porosity (%)	Void ratio
186-1151A-										
2R-1, 58-60	78.58	0.032	1.023	58	136	1.36	0.58	2.45	77	3.27
2R-2, 59-61	80.09	0.032	1.023	46	85	1.51	0.82	2.54	68	2.12
2R-3, 56-58	81.56	0.032	1.023	48	94	1.48	0.76	2.56	70	2.35
3R-1, 69-71	84.39	0.032	1.022	42	71	1.57	0.92	2.54	64	1.77
3R-2, 69-71	85.89	0.032	1.022	46	85	1.50	0.81	2.48	67	2.05
3R-3, 69-71	87.39	0.031	1.022	52	110	1.42	0.68	2.46	73	2.64
3R-4, 69-71	88.89	0.031	1.022	53	111	1.40	0.67	2.40	72	2.60
3R-5, 69-71	90.39	0.031	1.022	53	115	1.40	0.65	2.47	73	2.77
3R-6, 69-71	91.89	0.031	1.022	55	121	1.37	0.62	2.36	74	2.80
4R-1, 69-71	93.99	0.031	1.022	55	120	1.40	0.63	2.51	75	2.96
4R-2, 69-71	95.49	0.031	1.022	50	102	1.44	0.72	2.47	71	2.46
4R-3, 69-71	96.99	0.031	1.022	54	119	1.39	0.63	2.45	74	2.86
4R-4, 69-71	98.49	0.031	1.022	48	92	1.46	0.76	2.41	68	2.16
4R-5, 29-31	99.09	0.030	1.021	53	113	1.39	0.65	2.36	72	2.60
5R-1, 70-72	103.60	0.030	1.021	54	116	1.40	0.65	2.48	74	2.81
5R-2, 65-67	105.05	0.030	1.021	55	123	1.39	0.62	2.49	75	3.01
6R-1, 64-66	113.24	0.030	1.021	44	77	1.53	0.86	2.51	66	1.90
6R-2, 61-63	114.71	0.030	1.021	50	99	1.44	0.73	2.42	70	2.34
6R-3, 109-111	116.69	0.030	1.021	43	74	1.55	0.89	2.51	65	1.83
6R-4, 78-81	117.88	0.030	1.021	40	66	1.58	0.95	2.48	62	1.61
7R-1, 90-92	123.10	0.030	1.021	57	130	1.37	0.59	2.44	76	3.10
7R-2, 90-92	124.60	0.030	1.021	48	91	1.49	0.78	2.54	69	2.26
7R-3, 90-92	126.10	0.030	1.021	47	88	1.49	0.79	2.50	68	2.16
8R-1, 98-100	132.78	0.030	1.021	46	84	1.49	0.81	2.43	67	2.00
8R-2, 98-100	134.28	0.030	1.021	45	83	1.50	0.82	2.47	67	2.02
8R-3, 98-100	135.78	0.030	1.021	56	127	1.37	0.60	2.41	75	2.99
9R-1, 80-82	142.20	0.030	1.021	50	101	1.43	0.71	2.41	70	2.38
9R-2, 80-82	143.70	0.030	1.021	52	110	1.42	0.68	2.49	73	2.67
9R-3, 80-82	145.20	0.030	1.021	49	95	1.47	0.75	2.50	70	2.33
9R-4, 80-82	146.70	0.030	1.021	55	122	1.38	0.62	2.41	74	2.88
10R-1, 80-82	151.80	0.029	1.021	46	84	1.49	0.81	2.45	67	2.02
10R-2, 80-82	153.30	0.029	1.021	50	101	1.44	0.71	2.44	71	2.42
10R-3, 80-82	154.80	0.029	1.021	50	99	1.45	0.73	2.46	70	2.38
10R-4, 80-82	156.30	0.029	1.021	53	113	1.40	0.66	2.45	73	2.72
10R-5, 80-82	157.80	0.029	1.021	51	102	1.43	0.71	2.42	71	2.42
11R-1, 112-114	161.72	0.029	1.020	52	110	1.41	0.67	2.44	72	2.63
11R-2, 112-114	163.22	0.029	1.020	55	120	1.38	0.63	2.38	74	2.80
11R-3, 112-114	164.72	0.029	1.020	53	114	1.40	0.65	2.41	73	2.70
11R-4, 112-114	166.22	0.029	1.020	53	115	1.39	0.65	2.36	73	2.65
11R-5, 112-114	167.72	0.029	1.020	54	117	1.40	0.64	2.47	74	2.84
12R-1, 60-62	170.80	0.029	1.020	51	103	1.42	0.70	2.37	71	2.40
12R-2, 60-62	172.30	0.029	1.020	53	114	1.39	0.65	2.35	72	2.62
12R-3, 60-62	173.80	0.029	1.020	50	100	1.41	0.70	2.26	69	2.21
12R-4, 60-62	175.30	0.029	1.020	47	88	1.45	0.77	2.28	66	1.96
12R-5, 60-62	176.80	0.029	1.020	46	85	1.45	0.79	2.26	65	1.88
12R-6, 60-62	178.30	0.029	1.020	44	79	1.44	0.80	2.12	62	1.64
12R-7, 60-62	179.80	0.029	1.020	49	95	1.40	0.72	2.14	67	1.99
13R-1, 90-92	180.70	0.029	1.020	55	122	1.38	0.62	2.41	74	2.89
13R-2, 90-92	182.20	0.029	1.020	47	90	1.45	0.76	2.33	67	2.06
13R-3, 90-92	183.70	0.029	1.020	48	92	1.43	0.75	2.29	67	2.06
13R-4, 90-92	185.20	0.029	1.020	51	105	1.39	0.68	2.26	70	2.32
13R-5, 90-92	186.70	0.029	1.020	39	65	1.56	0.95	2.38	60	1.51
14R-1, 50-52	190.00	0.029	1.020	52	108	1.41	0.68	2.41	72	2.54
14R-2, 50-52	191.50	0.029	1.020	56	130	1.35	0.59	2.31	75	2.94
14R-3, 50-52	193.00	0.029	1.020	45	82	1.48	0.81	2.33	65	1.87
14R-4, 50-52	194.50	0.029	1.020	53	112	1.40	0.66	2.43	73	2.67
14R-5, 50-52	196.00	0.029	1.020	55	122	1.37	0.62	2.34	74	2.79
14R-6, 50-52	197.50	0.029	1.020	50	100	1.42	0.71	2.34	70	2.31
14R-7, 50-52	199.00	0.029	1.020	53	114	1.40	0.65	2.41	73	2.68
15R-1, 69-71	199.89	0.029	1.020	48	93	1.45	0.75	2.37	68	2.15
15R-2, 69-71	201.39	0.029	1.020	45	83	1.48	0.80	2.35	66	1.93
15R-3, 69-71	202.89	0.029	1.020	49	97	1.43	0.73	2.32	69	2.20

Notes: Values shown are corrected for in situ salinity and density of pore water. Only a portion of this table appears here. The complete table is available in **ASCII format**.

Table T17. Summary of Hole 1151D logging operations.

	Logging string	Depth (mbsf)	Time (local)	Date (1999)
Run 1	FMS-LSS (pass 1)	871	2130 hr to 0235 hr	11 August
	FMS-LSS (pass 2)	870	0235 hr to 0720 hr	12 August
Run 2	Triple combo + LDEO-TAP	868	0720 hr to 1500 hr	12 August

Notes: FMS = Formation MicroScanner, LSS = long-spaced sonic imager, Triple combo = triple combination logging tool, LDEO-TAP = Lamont-Doherty Earth Observatory temperature/acceleration/pressure tool. See Figure **F8,** p. 44, in the "Explanatory Notes" chapter for explanation of the configuration of tool strings.

Table T18. Summary of in situ temperature measurements at Site 1151.

Hole, core	Depth (mbsf)	Tool	Equilibrium temperature (°C)	Comments
186-				
1151C	Mudline	APC	1.96 ± 0.1	
1151C-4H	30.70	APC	2.93 ± 0.1	
1151A-18R	228.10	DVTP	—	Bad data
1151A-20R	247.30	DVTP	—	Bad data
1150A-33R	372.90	DVTP	15.38 ± 0.1	

Note: APC = APC (advanced hydraulic piston core) Adara temperature tool, DVTP = Davis-Villinger temperature probe.

Table T19. Instrument package deployment, Site 1151.

Step	Date (Aug 1999)	Time (local)	Total Time	Description
				Install cable reel stands and rig sheaves in moonpool; make up stinger to strainmeter; make up lifting eyes and landing brackets to strainmeter
1	7	11:30	0	Move strainmeter/stinger assembly to rig floor
2	7	11:45	0:15:00	Make up 4.5-in casing joint to seismometer, horizontal on deck
3	7	12:15	0:45:00	Make up seismometer to strainmeter; pick up instrument package and remove strainmeter landing brackets
4	7	12:45	1:15:00	Slowly lower to moonpool; make up instrument cable connections in moonpool
5	7	13:00	1:30:00	Begin strapping and wrapping cables
6	7	13:15	1:45:00	Run 39 joints (~454 m) of 4.5-in casing, install circulating sub, 51 joints (594 m) of 4.5-in casing
7	7	22:00	10:30:00	Run in hole with two more joints of 4.5-in casing
8	7	22:30	11:00:00	Move hanger/riser onto rig floor
9	7	23:30	12:00:00	Make up hanger/riser to 4.5-in casing
10	7	23:45	12:15:00	Cut cables to length
11	8	0:15	12:30:00	Raise hanger/riser feeding free end of cables into subsea shop
12	8	0:30	13:00:00	Make up cable terminations
13	8	12:30	25:00:00	Install G-Box
14	8	14:45	27:15:00	Remove, troubleshoot, and reinstall MEG
15	8	18:45	31:15:00	Test VIT over riser/hanger
16	8	19:15	31:45:00	Run in hole/deploy VIT
17	8	21:45	34:15:00	Wash to total depth/land hanger/riser in reentry cone
18	9	0:45	37:15:00	Lower VIT/check installation
19	9	1:00	37:30:00	Pump 80 bbl 16 lb/gal (~1900 kg/m^3) cement slurry/drop dart
20	9	3:30	40:00:00	Prepare battery frame in moonpool
21	9	6:15	42:45:00	Deploy battery frame
22	9	9:00	45:30:00	Battery frame land in cone
23	9	9:00	45:30:00	Release/recover log line/pull out of hole/VIT
24	9	12:15	48:45:00	J-joint disconnected
25	9	17:15	53:45:00	Pull out of hole

Notes: Extra time due to contingency 8 Aug 14:45–18:45 (4 hr). MEG = multiple-access expandable gateway, VIT = vibration isolated television.

Table T20. Number of deformational structures, Hole 1151B.

Leg	Site	Hole	Core	Depth (mbsf)	Recovered length (m)	Normal fault (Number/ core)	Normal fault (Number/ recovered m)	Reverse fault (Number/ core)	Reverse fault (Number/ recovered m)	Strike slip fault (Number/ core)	Strike slip fault (Number/ recovered m)	Fault (Number/ core)	Fault (Number/ recovered m)	Total of faults (Number/ core)	Total of faults (Number/ recovered m)
186	1151	B	36	401.40	5.12	0	0.0	0	0.0	0	0.0	0	0.0	0	0.0
186	1151	B	37	411.00	4.46	0	0.0	0	0.0	0	0.0	0	0.0	0	0.0
186	1151	B	38	420.60	5.64	0	0.0	0	0.0	0	0.0	0	0.0	0	0.0
186	1151	B	39	430.30	3.37	0	0.0	0	0.0	0	0.0	0	0.0	0	0.0
186	1151	B	40	439.90	5.49	2	0.4	0	0.0	0	0.0	0	0.0	2	0.4
186	1151	B	41	449.50	5.53	0	0.0	0	0.0	0	0.0	0	0.0	0	0.0
186	1151	B	42	459.20	5.28	0	0.0	0	0.0	0	0.0	0	0.0	0	0.0
186	1151	B	43	468.80	4.52	0	0.0	0	0.0	0	0.0	0	0.0	0	0.0
186	1151	B	44	478.40	8.90	0	0.0	0	0.0	0	0.0	0	0.0	0	0.0
186	1151	B	45	488.00	4.26	0	0.0	0	0.0	0	0.0	0	0.0	0	0.0
186	1151	B	46	497.60	8.20	0	0.0	0	0.0	0	0.0	2	0.4	2	0.4
186	1151	B	47	507.20	8.98	0	0.0	0	0.0	0	0.0	0	0.0	0	0.0
186	1151	B	48	516.80	7.73	0	0.0	0	0.0	0	0.0	1	0.2	1	0.2
186	1151	B	49	526.40	7.17	1	0.2	0	0.0	0	0.0	1	0.2	2	0.4
186	1151	B	50	536.00	5.98	1	0.2	1	0.2	0	0.0	1	0.2	3	0.6
186	1151	B	51	545.70	8.97	0	0.0	0	0.0	0	0.0	0	0.0	0	0.0
186	1151	B	52	555.40	8.63	0	0.0	0	0.0	0	0.0	0	0.0	0	0.0
186	1151	B	53	565.10	8.22	0	0.0	0	0.0	0	0.0	0	0.0	0	0.0
186	1151	B	54	574.70	8.10	3	0.6	0	0.0	0	0.0	0	0.0	3	0.6
186	1151	B	55	584.30	0.13	0	0.0	0	0.0	0	0.0	0	0.0	0	0.0
186	1151	B	56	593.90	2.61	0	0.0	0	0.0	0	0.0	0	0.0	0	0.0
186	1151	B	57	603.50	6.38	6	1.2	0	0.0	0	0.0	0	0.0	6	1.2
186	1151	B	58	613.20	9.79	0	0.0	0	0.0	0	0.0	0	0.0	0	0.0

Leg	Site	Hole	Core	Depth (mbsf)	Recovered length (m)	Joints (Number/ core)	Joints (Number/ recovered m)	Total of faults and joints (fractures) (healed fractures) (Number/ core)	Total of faults and joints (fractures) (healed fractures) (Number/ recovered m)	Healed fractures + open fractures (Number/ core)	Healed fractures + open fractures (Number/ recovered m)	Open fractures (Number/ core)	Open fractures (Number/ recovered m)
186	1151	B	36	401.40	5.12	0	0.0	0	0.0	3	0.6	3	0.6
186	1151	B	37	411.00	4.46	0	0.0	0	0.0	0	0.0	0	0.0
186	1151	B	38	420.60	5.64	0	0.0	0	0.0	0	0.0	0	0.0
186	1151	B	39	430.30	3.37	0	0.0	0	0.0	7	1.4	7	1.4
186	1151	B	40	439.90	5.49	0	0.0	2	0.4	2	0.4	0	0.0
186	1151	B	41	449.50	5.53	1	0.2	1	0.2	1	0.2	0	0.0
186	1151	B	42	459.20	5.28	0	0.0	0	0.0	8	1.6	8	1.6
186	1151	B	43	468.80	4.52	0	0.0	0	0.0	0	0.0	0	0.0
186	1151	B	44	478.40	8.90	0	0.0	0	0.0	0	0.0	0	0.0
186	1151	B	45	488.00	4.26	0	0.0	0	0.0	0	0.0	0	0.0
186	1151	B	46	497.60	8.20	1	0.2	3	0.6	12	2.3	9	1.8
186	1151	B	47	507.20	8.98	14	2.7	14	2.7	25	4.9	11	2.1
186	1151	B	48	516.80	7.73	1	0.2	2	0.4	25	4.9	23	4.5
186	1151	B	49	526.40	7.17	1	0.2	3	0.6	36	7.0	33	6.4
186	1151	B	50	536.00	5.98	6	1.2	9	1.8	34	6.6	25	4.9
186	1151	B	51	545.70	8.97	1	0.2	1	0.2	58	11.3	57	11.1
186	1151	B	52	555.40	8.63	7	1.4	7	1.4	36	7.0	29	5.7
186	1151	B	53	565.10	8.22	12	2.3	12	2.3	60	11.7	48	9.4
186	1151	B	54	574.70	8.10	0	0.0	3	0.6	17	3.3	14	2.7
186	1151	B	55	584.30	0.13	0	0.0	0	0.0	0	0.0	0	0.0
186	1151	B	56	593.90	2.61	0	0.0	0	0.0	13	2.5	13	2.5
186	1151	B	57	603.50	6.38	12	2.3	18	3.5	63	12.3	45	8.8
186	1151	B	58	613.20	9.79	4	0.8	4	0.8	30	5.9	26	5.1

Notes: Depths are measured at top of interval. Only a portion of this table appears here. The complete table is available in **ASCII format.**

Table T21. Orientations of healed fractures, Hole 1151A.

Core, section, interval (cm)	Depth (mbsf)	Paleomagnetic direction		Core coordinates		Geographic coordinates	
		Dec. (°)	Inc. (°)	Dip azimuth (°)	Dip angle (°)	Dip azimuth (°)	Dip angle (°)
186-1151A							
46R-1, 65	498.25	233.20	65.60	286	71	53	71
46R-1, 65	498.25	233.20	65.60	85	75	212	75
46R-2, 50	499.60	121.00	54.20	85	70	324	70
46R-3, 5	500.65	12.30	21.40	78	24	66	25
47R-3, 140	511.60	274.40	51.40	254	65	340	65
48R-4, 5	521.35	219.80	–52.30	313	47	273	47
48R-4, 15	521.45	219.80	–52.30	78	41	38	41
50R-4, 80	541.30	338.70	–55.90	268	74	109	74
57R-3, 130	596.92	339.68	–17.71	53	56	253	56
57R-3, 140	597.02	135.24	–70.96	80	80	125	80
58R-3, 70	616.90	22.66	–20.37	42	73	200	73
59R-1, 10	623.00	379.50	–54.80	264	55	64	55
59R-5, 30	623.20	287.50	–21.40	84	65	337	65
59R-5, 100	623.90	287.50	–21.40	329	73	221	73
59R-4, 30	627.70	246.40	–77.77	204	64	138	64
60R-5, 105	639.55	92.70	–61.80	106	69	193	69
60R-6, 10	640.10	239.08	31.50	263	47	204	47
61R-4, 90	647.50	307.21	–73.94	95	68	328	68
61R-5, 65	648.75	93.40	–52.28	145	68	231	68
65R-2, 30	682.00	230.36	–15.10	234	75	183	75
66R-1, 75	690.55	178.10	46.30	261	40	83	40
67R-1, 140	700.80	78.30	44.90	64	48	346	48
68R-5, 50	715.50	187.40	46.70	37	62	209	62
69R-1, 10	718.70	27.90	55.50	186	40	158	40
69R-2, 55	720.65	15.70	53.30	227	71	212	71
69R-2, 55	720.65	15.70	53.30	144	71	128	71
69R-4, 85	723.65	139.20	52.80	228	75	89	75
69R-4, 90	723.70	139.20	52.80	306	36	167	36
69R-5, 20	724.50	25.80	49.20	236	64	211	64
69R-5, 20	724.50	25.80	49.20	20	38	355	38
69R-5, 40	724.70	25.80	49.20	288	41	263	42
69R-5, 40	724.70	25.80	49.20	131	62	105	62
70R-2, 20	730.00	306.80	48.10	96	71	150	71
71R-1, 20	738.20	136.17	–7.00	232	25	276	25
71R-1, 140	739.40	336.62	–63.00	294	57	137	57
71R-4, 40	742.90	329.00	40.30	242	63	273	63
71R-4, 75	743.25	329.00	40.30	217	54	249	54
72R-1, 80	748.50	82.08	–61.00	52	70	150	70
72R-2, 10	749.00	95.80	15.70	245	53	149	53
72R-2, 15	749.05	95.80	15.70	260	30	164	30
72R-2, 35	749.25	95.80	15.70	113	42	17	42
72R-2, 40	749.30	95.80	15.70	186	40	90	40
72R-2, 70	749.60	95.80	15.70	166	85	70	85
72R-2, 80	749.70	95.80	15.70	202	62	106	62
72R-2, 95	749.85	95.80	15.70	215	60	120	60
72R-6, 10	754.58	291.30	35.10	49	62	118	62
72R-6, 55	755.03	291.30	35.10	52	25	121	25
73R-1, 5	757.35	319.00	44.50	291	71	332	71
73R-1, 15	757.45	319.00	44.50	80	75	121	75
73R-1, 30	757.60	319.00	44.50	220	57	261	57
73R-2, 30	759.10	265.70	50.00	313	71	47	71
73R-3, 115	761.45	303.30	15.20	285	41	342	41
73R-3, 120	761.50	303.30	15.20	239	54	295	54
73R-4, 5	761.85	281.90	53.70	249	47	327	47
73R-4, 25	762.05	281.90	53.70	244	50	322	50
73R-5, 50	763.80	307.80	50.80	309	42	1	42
73R-5, 55	763.85	307.80	50.80	77	51	129	51
73R-5, 100	764.30	307.80	50.80	74	71	126	71
73R-6, 45	765.25	23.20	46.50	351	72	328	72
73R-6, 50	765.30	23.20	46.50	351	67	328	67
74R-1, 20	767.10	71.30	54.10	236	14	165	14

Notes: Only a portion of this table appears here. The complete table is available in ASCII format.

Table T22. Orientations of open fractures, Hole 1151A.

Core, section, interval (cm)	Depth (mbsf)	Paleomagnetic direction (°)		Core coordinates (°)		Geographic coordinates (°)	
		Dec.	Inc.	Dip azimuth	Dip angle	Dip azimuth	Dip angle
186-1151A							
42R-3, 45	462.65	337	18	88	55	110	55
42R-3, 50	462.70	337	18	88	60	111	60
42R-3, 50	462.70	337	18	74	66	96	66
45R-1, 10	488.10	316	42	39	66	84	66
45R-1, 52	488.52	316	42	327	66	12	66
45R-1, 55	488.55	316	42	331	61	15	62
46R-1, 90	498.50	233	66	114	56	241	57
46R-2, 20	499.30	121	54	306	46	185	46
46R-5, 110	504.70	128	59	321	79	194	79
47R-2, 140	510.10	300	41	328	80	28	80
47R-5, 10	513.30	334	41	156	71	182	71
47R-5, 15	513.35	334	41	162	66	188	66
48R-4, 140	522.70	321	–79	200	67	59	67
48R-5, 10	522.90	320	–61	217	54	78	54
48R-5, 70	523.50	320	–61	284	59	144	59
48R-6, 20	524.30	265	–71	336	72	250	72
49R-1, 40	526.80	171	–41	103	51	112	51
49R-1, 55	526.95	171	–41	123	68	132	68
51R-1, 95	546.65	227	–70	278	14	231	14
51R-4, 80	551.00	163	–63	80	84	97	84
51R-4, 90	551.10	256	–59	303	60	227	60
51R-4, 140	551.60	163	–63	256	57	273	57
52R-1, 10	551.80	66	–71	130	47	243	47
52R-1, 130	553.00	66	–71	219	67	333	67
53R-1, 30	565.40	332	–70	211	63	59	64
53R-1, 110	566.20	263	–61	98	83	15	83
53R-2, 5	566.65	275	–58	102	43	7	43
53R-2, 28	566.88	275	–58	78	43	343	43
53R-2, 60	567.20	68	–67	103	69	215	69
53R-2, 135	567.95	271	–55	332	63	242	63
53R-3, 30	568.40	324	–66	297	77	152	77
53R-4, 20	569.80	78	–29	308	55	50	55
53R-4, 80	570.40	260	–65	302	73	222	73
53R-5, 25	571.35	146	–59	196	64	230	64
54R-1, 35	575.05	170	51	198	82	28	82
54R-1, 85	575.55	170	51	28	78	217	78
54R-2, 20	576.40	269	44	150	55	242	55
54R-2, 105	577.25	149	50	69	71	280	71
56R-1, 15	594.05	66	49	307	56	241	56
56R-1, 30	594.20	66	49	111	74	45	74
56R-1, 50	594.40	66	49	312	48	246	48
56R-1, 60	594.50	66	49	235	60	169	60
56R-3, 10	595.72	256	85	348	52	91	52
56R-3, 20	595.82	120	10	314	67	194	68
56R-3, 35	595.97	115	37	4	50	249	50
57R-3, 45	596.07	325	53	46	75	82	75
57R-3, 60	596.22	325	53	102	61	137	61
57R-3, 70	596.32	325	53	219	66	255	66
57R-4, 20	608.20	69	32	77	51	8	51
57R-4, 20	608.20	69	32	216	71	147	71
57R-4, 40	608.40	145	68	60	44	276	44
57R-4, 60	608.60	274	68	222	61	308	61
57R-4, 60	608.60	274	68	146	33	232	33
57R-4, 65	608.65	4	0	14	76	191	76
58R-1, 85	614.05	33	–46	247	62	34	62
58R-1, 105	614.25	33	–46	60	59	207	59
58R-1, 140	614.60	33	–46	246	57	33	57
58R-3, 40	616.60	331	–52	265	80	114	80
58R-4, 50	618.20	153	–62	242	63	269	63
58R-4, 60	618.30	153	–62	324	45	352	45
58R-4, 105	618.75	153	–62	149	73	176	73

Notes: Only a portion of this table appears here. The complete table is available in **ASCII format**.

Table T23. Orientations of bedding planes, Hole 1151A.

Core, section, interval (cm)	Depth (mbsf)	Paleomagnetic direction (°)		Core coordinates (°)		Geographic coordinates (°)	
		Dec.	Inc.	Dip azimuth	Dip angle	Dip azimuth	Dip angle
186-1151A-							
50R-1, 36	535.64	88.00	–67.00	90	2	182	2
50R-3, 39	538.61	101.23	–73.42	346	8	65	8
53R-1, 47	564.63	3.00	–67.00	14	8	191	8
54R-1, 23	574.47	170.00	51.00	202	5	32	5
61R-3, 70	644.40	137.71	–78.76	180	0	222	0
71R-1, 3	737.97	29.94	–45.20	212	9	2	9
71R-6, 105	744.45	81.00	–47.00	169	5	268	5
75R-2, 7	777.93	153.00	45.00	180	1	27	1
76R-2, 28	787.32	47.00	46.00	149	12	102	12
76R-4, 12	790.48	77.00	40.30	191	10	114	10
86R-1, 42	881.88	151.59	50.76	264	20	113	20
86R-1, 105	881.25	336.00	63.00	51	19	75	19
88R-1, 75	900.55	54.50	45.80	111	9	56	9
88R-2, 10	903.00	128.80	55.80	229	18	100	18
88R-3, 45	904.15	119.40	55.00	213	14	94	14
88R-4, 42	905.68	12.20	50.10	124	7	112	7
88R-5, 84	906.76	117.60	48.60	202	5	84	5
89R-1, 42	910.78	23.20	56.50	172	7	149	7
91R-1, 53	929.87	106.80	54.00	187	15	81	15
91R-2, 17	931.73	340.70	45.10	56	18	75	18
91R-3, 77	932.63	5.50	44.70	84	18	78	18
92R-1, 17	939.93	26.60	61.00	106	19	79	19
92R-2, 24	941.27	34.60	51.60	113	26	79	26
92R-2, 114	940.37	34.60	51.60	111	26	77	26
92R-4, 14	944.20	327.30	48.00	133	18	166	18
94R-1, 27	959.03	29.10	55.60	122	9	93	9
94R-1, 73	958.57	29.10	55.60	154	11	125	11
94R-3, 5	961.86	88.10	62.60	124	18	36	18
94R-3, 52	961.38	88.10	62.60	125	12	37	12
95R-1, 51	968.39	204.90	66.30	279	13	74	13
102R-1, 49	1035.71	8.60	58.80	69	14	60	14
102R-1, 122	1034.98	8.60	58.80	61	10	52	10
102R-2, 82	1036.88	–54.90	57.20	36	28	91	28
103R-1, 104	1044.86	–15.70	61.10	110	15	126	15
103R-2, 52	1046.88	–38.10	62.40	115	12	153	12
105R-1, 126	1064.04	192.50	61.40	281	28	88	28
105R-3, 14	1068.16	181.20	59.30	231	19	49	19
105R-3, 58	1067.72	181.20	59.30	250	15	69	15
105R-6, 61	1072.20	83.10	59.70	147	14	64	14
105R-6, 67	1078.14	83.10	59.70	128	16	45	16
106R-2, 70	1075.80	–52.20	65.40	44	17	97	17
106R-2, 98	1075.52	–52.20	65.40	32	13	84	13
106R-4, 52	1078.98	152.77	–13.08	45	14	72	14
106R-5, 123	1079.77	13.40	60.50	82	15	69	15
106R-5, 145	1079.55	13.40	60.50	82	21	68	21
106R-6, 20	1082.30	–3.10	55.40	111	14	114	14
107R-1, 30	1084.30	43.60	57.90	104	21	61	21
107R-1, 110	1083.50	43.60	57.90	128	25	85	25
107R-2, 3	1085.95	248.20	61.40	349	25	101	26
107R-6, 5	1091.49	230.80	58.90	304	18	74	18
107R-6, 140	1090.14	172.60	58.20	264	20	92	20
107R-7, 55	1092.49	169.90	58.50	266	30	96	30
109R-4, 26	1092.78	56.60	68.00	116	21	59	21
109R-6, 75	1110.23	3.50	55.60	54	17	50	17
109R-7, 40	1112.08	149.30	61.60	243	22	93	22

Notes: Only a portion of this table appears here. The complete table is available in **ASCII format**.